

Measurement of Displacements in Granular Systems in
Response to Penetration and Compaction



John Addiss

Department of Physics

Trinity College, University of Cambridge

A thesis submitted for the degree of

Doctor of Philosophy

November 2009

Acknowledgements

The research reported in this thesis was performed in the Fracture and Shock Physics group at the Cavendish Laboratory, Cambridge, between October 2006 and November 2009, under the supervision of Dr William Proud. I would like to thank Bill Proud for supervising my research.

I also wish to thank the other members of the Fracture group, particularly Dr David Williamson, Dr Stephen Walley and David Chapman for their help and guidance over the years. Professor John Field and Dr Stephen Walley deserve thanks for proof-reading this thesis and for making helpful suggestions to improve it.

I would like to thank the staff of the Cavendish Workshop and the Cavendish Students' Workshop for making or helping to make various parts of the experimental set-up including, but not limited to, the catch-chamber, sample holder and the projectiles.

I am grateful to the European Office of Aerospace Research and Development for funding the dynamic penetration experiments discussed in Chapters 4 and 5, under grant number 063057. The flash X-ray system used throughout was kindly supplied by QinetiQ and the Phantom high-speed video camera used in some of the dynamic penetration experiments was provided by the Atomic Weapons Establishment.

I am very grateful to the Engineering and Physical Sciences Research Council for funding my PhD studies and to Trinity College, Cambridge, and the American Physical Society, US, for their financial support for attendance at conferences.

I would like to thank Adam Collins for his help with the practicalities of performing the dynamic penetration experiments discussed in Chapters 4 and 5. The penetration simulations discussed in Chapter 8 were performed by Florin Bobaru and his student Konlayut Promratana, while on a sabbatical at the Cavendish. The interpretation and discussion of the simulation results, and the comparison to the experimental data, is my own. I am also very grateful to Vitali Nesterenko for his advice regarding the experiments discussed in Chapter 9, and for his more general support during my studies, and to his student David Benson who performed the simulations discussed in that chapter. Again, the interpretation of the simulation results is my own.

I would like to thank my girlfriend Fay for proof-reading my thesis and for making helpful suggestions to improve it and for all of her love and support over the last three years. I am also grateful to my parents for all of their support during my time at Cambridge and to my friends, both in and out of the lab, for making Cambridge a fun place to live.

Declaration

This dissertation is my own work and contains nothing which is the outcome of work done in collaboration with others, except as specified in the text and Acknowledgments.

This dissertation is not substantially the same as any other that I have submitted for a degree or diploma or qualification at this or any other University. No part of this thesis has already been, or is currently being, submitted for any degree, diploma or other qualification.

I can confirm that the word limit of 60,000 words set by the Degree Committee for the Faculty of Physics and Chemistry has not been exceeded.

John Addiss,
November 2009

Abstract

The research reported in this thesis is concerned with the flow of granular systems in response to penetration and compaction. The technique of Digital Speckle Radiography (DSR), which involves analysis of flash X-ray images, has been applied to measure the internal displacement fields within large opaque granular samples. Large samples are desirable as the measured displacements are more representative of the bulk.

Current DICC algorithms were found to be unsuitable for analysis of X-ray images of large samples. The large contrast variations present in such X-ray images, due to the X-ray beam profile, sample geometry and the high X-ray absorbance of metal penetrators, are shown to cause significant errors in the calculated displacement fields. A study of image normalisation techniques was carried out, and the effect of each technique on the accuracy of the measured displacements was investigated. A new DICC algorithm for use in DSR was produced which includes image normalisation techniques to correct for uneven contrast in the images. This new DICC algorithm was shown to be far more effective at analysing X-ray images of large samples.

This improved DSR technique was applied to measure the internal displacements within a large sample of sand during penetration by projectiles with different nose-shapes (flat, ogive-2 and hemispherical) and at different rates (1.5 mm/min to 200 ms⁻¹). The improved technique was found to provide high-resolution displacement data illustrating the response of the material. The dominant material response at low rates (1.5 mm/min) was found to be splitting of the material ahead of the projectile tip, followed by bulk reverse-flow of

material towards the penetration face. At the higher rates (200 ms^{-1}), the dominant response was compaction of the material ahead of the projectile tip. The transition between the two regimes was found to occur between velocities of 5 and 19 ms^{-1} .

The streamlined ogive-2 projectile nose-shape was shown to be the most effective for penetration, in that it caused less disruption of the material ahead of the projectile, lost less energy during the early stages of penetration in the dynamic experiments and more effectively split the material ahead of the projectile tip, a process which was shown to be important at all rates of penetration.

The compaction properties of a particulate mixture and a granular material, including the effect of factors such as porosity, initial particle arrangement and force chain formation, were investigated. Samples which were conducive to the formation of force chains spanning the whole sample were discovered to have anomalously high strengths. Small amounts of added water were shown to increase the compactability, by lubricating the grain contact points, but larger amounts of water decreased the compactability.

Contents

Nomenclature	xiii
1 Introduction	1
1.1 Overview	1
1.2 Motivation	3
1.3 Properties of Granular Media	5
1.4 Penetration of Granular Media	11
1.5 Summary	16
References	22
2 Principles of Digital Image Cross Correlation	23
2.1 Introduction	23
2.2 DICCC Algorithms	26
2.2.1 Overview	26
2.2.2 Correlation Functions	30
2.2.3 Tracking Sub-Images	37
2.3 Problems With Contrast Variation	38
2.4 Conclusions	48
References	52
3 Producing a New DICCC Algorithm	53
3.1 Algorithm Features	53
3.2 Contrast Normalisation	56
3.2.1 Window Averaging	60
3.2.2 LOWESS	61

CONTENTS

3.2.3	RLOWESS	62
3.2.4	Median Filter	63
3.2.5	Comparison of the Techniques	63
3.2.6	Spatial DICC	75
3.2.7	Previous Example	79
3.2.8	Experimental Images	84
3.3	Tracking Deformed Sub-Images	87
3.4	Testing of the DICC Algorithm	89
3.5	Conclusions	100
	References	103
4	Dynamic Penetration of Granular Media	105
4.1	Introduction	105
4.2	Experimental Method	106
4.2.1	Material Characterisation	106
4.2.2	Flash X-Ray System	109
4.2.3	Preliminary Experiments	112
4.2.3.1	Effect of the Lead Shot	114
4.2.4	Sample Design	116
4.2.5	Projectiles	116
4.2.6	The Light Gas-Gun	118
4.2.7	Impact Chamber	119
4.2.8	Alignment Rig	120
4.2.9	Sample Preparation	120
4.2.10	Experimental Procedure	123
4.3	Results and Discussion	125
4.3.1	Longitudinal Displacements	134
4.3.2	Lateral Displacements	139
4.3.3	Decay of the Displacements	143
4.3.4	High-Speed Video	149
4.3.5	Penetration Velocity	151
4.4	Summary	154
	References	157

5	Effect of Projectile Nose Shape	159
5.1	Introduction	159
5.2	Results and Discussion	160
5.2.1	Penetration Velocity Profiles	170
5.3	Summary	173
	References	175
 6	 Quasi-Static Penetration	 177
6.1	Introduction	177
6.2	Experimental Setup	178
6.3	Penetration by Flat-Ended Projectiles	180
6.3.1	Longitudinal Displacements	187
6.3.2	Lateral Displacements	191
6.3.3	Decay of the Displacements	193
6.3.4	Extent of Compaction	195
6.4	Penetration by Ogive-Tipped Projectiles	197
6.5	Summary	201
	References	202
 7	 Intermediate Rate Penetration	 203
7.1	Introduction	203
7.2	Drop-Weight Experiments	205
7.3	Light Gas-Gun Experiments	208
7.4	Summary	216
 8	 Simulation and Comparison with Other Materials	 219
8.1	Comparison with Other Materials	219
8.1.1	Gelatine	220
8.1.2	Concrete	226
8.1.3	Comparison	228
8.2	Computational Simulations	230
8.2.1	Simulation Details	230
8.2.2	Close-Packed, Mono-Disperse Samples	233
8.2.3	Randomly-Packed, Poly-Disperse Sample	235

CONTENTS

8.2.4	Randomly-Packed, Mono-Disperse	236
8.2.5	Discussion	237
8.2.6	Modelling Conclusions	238
8.3	Summary	242
	References	244
9	High Strain-Rate Behaviour of PTFE/Al/W Composites	245
9.1	Introduction	245
9.2	Experimental Method	248
9.2.1	Cavendish Drop-Weight Machine	248
9.2.2	Soft Drop-Weight Experiments	250
9.2.3	Validation of the Soft Drop-Weight Technique	255
9.2.4	Interrupted Experiments	258
9.3	Results	259
9.3.1	Porous Samples with Fine W Particles	259
9.3.2	Porous Samples with Coarse W Particles	262
9.3.3	Dense Samples with Coarse W Particles	266
9.4	Discussion	266
9.5	Simulations	269
9.6	Conclusions	274
9.7	Summary	275
	References	279
10	Compaction of Soils	281
10.1	Introduction	281
10.2	Sample Characterisation and Preparation	282
10.3	Experimental Method	288
10.4	Preliminary Results	289
10.5	Results	292
10.5.1	Comparison of Dry Materials	292
10.5.2	The Effect of Water	294
10.6	Discussion	298
10.7	Conclusions	302
	References	304

11 Conclusions	305
11.1 Future Work	307
A	309
A.1 Published Papers	309
A.2 Lists of Experiments	310

CONTENTS

Nomenclature

Roman Symbols

C Silt

CCS A mixture of two thirds silt and one third sand

CS A mixture of one half sand and one half silt

CSS A mixture of one third silt and two thirds sand

S Sand

W Tungsten

Acronyms

DEM Discrete Element Method

DICC Digital Image Cross Correlation

DSR Digital Speckle Radiography

FEM Finite Element Method

LOWESS Locally Weighted Scatter-Plot Smoothing

PTFE Polytetrafluoroethylene

RLOWESS Robust Locally Weighted Scatter-Plot Smoothing

SEM Scanning Electron Microscopy

TMD Theoretical Maximum Density

CONTENTS

Chapter 1

Introduction

1.1 Overview

The research presented in this thesis is concerned with the internal flow of granular systems in response to penetration and compaction. The research can be split into three main areas:

1. Optimisation of the technique of Digital Speckle Radiography (DSR) so that significant improvements are achieved in the resolution and accuracy of the measured displacement fields.
2. An experimental investigation of the internal flow of material within a sample of sand during penetration using the optimised DSR algorithm, including the effect of penetration velocity, projectile nose-shape and comparison with simulations.
3. An investigation of the effect of particle size, density and water content on the mechanical behaviour of granular systems and particulate composites during compaction.

In this chapter, the motivation for this research and a review of the properties of granular materials are presented. Previous experiments investigating the penetration of granular materials and their limitations in considering only the external consequences of the penetration or the terminal state of the system are discussed.

1. INTRODUCTION

In the following two chapters, the techniques of Digital Image Cross Correlation (DICC) and Digital Speckle Radiography (DSR), which allow measurement of internal displacements within opaque granular materials through analysis of X-ray images, are introduced and discussed. Current DICC algorithms are found to be unsuitable for DSR studies on large samples. The large contrast variations present in experimental X-ray images, due to the X-ray beam profile, sample geometry and the presence of a metal penetrator, are shown to cause significant problems with the correlation. A number of different approaches for improving the contrast in X-ray images are discussed and their effect on the success of the correlation and the subsequent accuracy of the measured displacements is investigated.

In Chapters 4 and 5, this improved technique is applied to an investigation of the penetration of sand by long-rod projectiles at 200 ms^{-1} . The displacement fields are mapped at high resolution, allowing quantitative measurement of how the displacements are transmitted through the granular material. The temporal progression of the penetration is investigated for a number of different projectile nose-shapes. The dominant material response at these rates is compaction of the material ahead of the projectile.

A series of lower-rate penetration experiments (1.5 mm/min to 5 ms^{-1}) are discussed in Chapters 6 and 7. The response of the granular material is markedly different at lower rates of penetration. The dominant material response changes to bulk flow of material towards the impact face. The velocity at which this transition occurs is investigated through a series of intermediate velocity penetration experiments.

In Chapter 8, the observed behaviour of the sample is contrasted with that observed for hydrodynamic materials or inhomogeneous solids. The experimental data is compared to combined Discrete Element Method and Finite Element Method simulations of penetration of a granular medium. Some strong similarities are observed between the experimental results and the results of the simulations.

Chapters 9 and 10 move on to consider the uniform compaction of granular or particulate materials. In Chapter 9, the dynamic compaction response of mixtures of metal and PTFE powders are discussed. The experiments illustrate the importance of a number of factors, including porosity, initial particle arrangement

and the effect of force chain formation on the strength of a sample. In Chapter 10, the compaction behaviour of mixtures of sand, silt and water is investigated. The influence of water in lubricating or strengthening a granular material is discussed, as are the effect of porosity and particle size on the compactability of granular materials.

1.2 Motivation

Granular materials are some of the most widely occurring materials in nature and are heavily exploited in industry. Well-known natural examples of granular materials include sand, gravel and soil. Examples of granular materials and granular flow in industry include pills being transported in pharmaceutical factories, the flow of nuts, grains or potatoes in food processing and transport and the use of soils and grouts in construction [1]. The flow and equilibrium properties of these granular materials are central to the design of the equipment for handling and transporting them. Sand and silt are also major components of concrete, one of the most widely used building materials in the world. In order to fully understand the behaviour of an aggregate such as concrete, it is necessary to first have a better understanding of the behaviour and properties of the constituent granular materials.

Understanding the behaviour of these materials, in particular how they respond to stimuli in the form of vibration, uniform loading or localised loading (penetration), is of great importance to diverse fields such as excavation, construction, geomechanics, seismology, mining and oil and gas extraction. A greater understanding of the basic interactions between grains within a granular material should lead to more physically realistic computational models of such materials. These could then be used to make predictions about important phenomena, such as the formation and behaviour of landslides [2] or the flow of granular materials through various openings.

Since the field of granular materials is of such economic importance, extensive research is currently being carried out into the properties of granular materials. Much of this research is concerned with trying to produce more realistic computational models that consider the grain-level interactions and applying them

1. INTRODUCTION

to consider processes such as vibration [3], penetration [4] and granular flow [5]. Due to the difficulty of quantitatively measuring the motion of granular materials, particularly the internal motions within an opaque granular material, there is little experimental data available regarding the flow of material or the interactions between individual grains.

The aim of the research reported in this thesis is to add to the current knowledge about flow and compaction of granular materials in response to localised loading (in the form of penetration) and uniform loading, by performing experiments in which the internal displacement fields are measured. Currently, the mechanisms of penetration in granular materials at low-to-medium impact speeds are not well understood. The effect on these mechanisms of factors such as the impact velocity [6], projectile shape and the properties of the granular system [7], all of which may significantly influence penetration, is not known in any detail.

High resolution data on the displacements generated during dynamic penetration would be useful in a number of fields. Such knowledge could be used to increase understanding of the mitigation of fragments thrown from a blast, for example by sand bags. Currently the placement and type of sand bags used as simple ballistic shields is based more on empirical experience than the results of controlled experiments. Detailed data regarding the internal flow of a granular material during penetration would allow penetration by fragments to be modelled more successfully and for more effective arrangements to be designed. Conversely, such data could also be used to optimise the properties of a projectile designed to penetrate through soil or concrete. Performing penetration experiments on small samples, and using the data to optimise computational simulations, should significantly reduce the number of large scale trials required and therefore save time and money. Such simulations require data on the interactions between particles and the way in which forces are transmitted through the bulk. Detailed information on the internal response of a granular material during penetration should provide such data.

Penetration of granular materials is also currently of considerable interest to the planetary science community. There is interest in firing penetrators into the surface layers of celestial bodies. Planets such as Mars are generally covered by a layer of dust and debris, generated during asteroid impacts and deposited by

frequent dust storms. By embedding sensors into the surface of a planet, it should be possible to investigate the local chemical composition, physical properties, and the extent of any heat flow from the interior. To achieve this, it would be necessary to embed detectors into the surface at a depth of a few metres. This could most simply be achieved by impacting the surface with a penetrator containing the required diagnostic instruments [8]. One such project, MoonLITE, proposed by the British National Space Centre, plans to fire four penetrators weighing approximately 40 kg into the surface of the moon at 300 ms^{-1} , from an orbiting satellite. This will provide a network of seismometers and heat sensors at a depth of 2 - 3 m, allowing the internal structure of the Moon to be probed, as well as exploring the frequency and origin of moonquakes [9].

At lower rates of penetration of granular materials (of the order of millimetres per minute to a few metres per second) the data is relevant to situations in which a soft, sandy material experiences a localised load. Such situations occur frequently in the construction industry when heavy machinery or vehicles bearing heavy loads may have to travel on soil or sandy ground, or when pile drivers are used to drive rods into the ground at velocities of a few metres per second. A knowledge of how granular materials respond to these localised loads would be useful in determining safe working conditions. A better understanding of how the response of the material changes with the penetration velocity should provide an interesting insight into the underlying processes.

Before discussing in more detail the experiments carried out for this thesis, it is useful to review the properties of a granular system, and the challenges they pose to experimental diagnostics or attempts to simulate their behaviour.

1.3 Properties of Granular Media

A granular material is a conglomeration of discrete solid particles. The particles generally range in size from micrometres (particles smaller than this are subject to thermal motion fluctuations) to centimetres, although the behaviour of some larger bodies, such as icebergs, can also be understood using granular physics [10]. The forces between the grains are generally purely repulsive, and there is negligible cohesion.

1. INTRODUCTION

Granular materials present a number of problems for modelling. They exhibit behaviour consistent with both solids and liquids, depending on the situation [10]. When the average kinetic energy of the grains is low, such that the relative movement of the grains is small compared to their size, a granular material behaves as a solid, in that the material can maintain its shape under an applied load, such as gravity [11]. Even at rest, granular materials can exhibit some unusual behaviour. A column of a solid material, such as a metal, displays a height dependent pressure relationship, such that the pressure experienced at the bottom of the column increases with the total height and therefore the mass of the column. When a granular material, such as sand, is held in a cylindrical container the pressure at the base of the column initially increases with height, but eventually plateaus at a constant value. This is because the contact forces, and the friction between grains and the sides of the container, cause the container walls to support some of the weight of the column [12].

Granular materials at rest can behave anisotropically, due to the inhomogeneous arrangement of particles. Of significance in explaining the behaviour of granular materials are force chains. These occur where the stresses within a sample become localised due to the load being born by a chain of particles in contact, rather than the whole sample homogeneously bearing the load at a uniform stress. Figure 1.1 shows the location of force chains within a two dimensional pile of photoelastic disks at rest. Viewed through crossed polars, the force chains, along which the majority of the load is being born, are clearly visible as bright areas [13]. Different particle arrangements will enable or disrupt the formation of force chains to differing extents. As a consequence, repeated experiments on granular samples with the same mass, density and shape will give somewhat different results, due to the variations in how the samples transmit the applied load [14]. This variation has been noted by a number of experimenters when compacting granular materials [15] or when trying to measure the transmission of sound through granular materials. In the latter case the transmitted intensity and arrival time is found to be extremely sensitive to the arrangement of particles [16].

When a larger amount of energy is fed into a granular system, for example by vibration or the release of gravitational potential energy during a landslide,

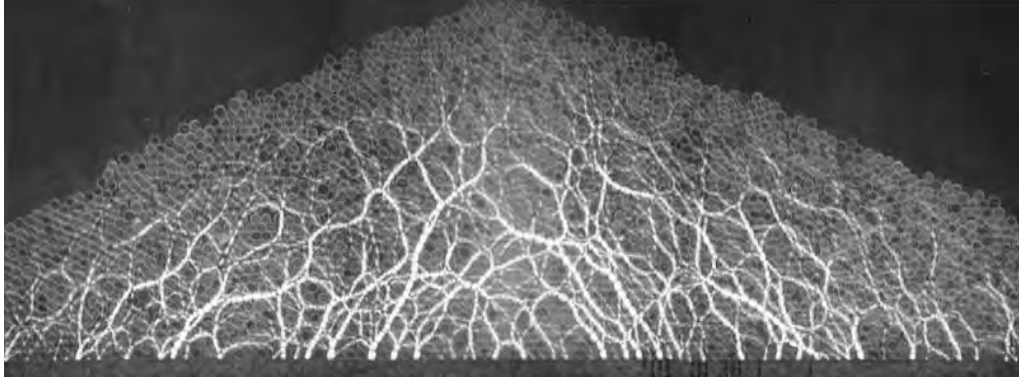


Figure 1.1: Figure taken from [13]. A two dimensional pile (height 30 cm, base length 130 cm) of photoelastic disks, viewed between crossed polarizers. Bright regions in the image correspond to high stresses. The formation of chains of localised stress (and therefore force), representing chains of particles in contact that are bearing a large proportion of the load, is clearly visible in the image.

a granular material can enter a fluid like state [17]. Granular materials can flow like liquids and exhibit fluid like properties such as convection [18, 19]. When a granular material is poured into a container, it assumes the shape of the container, as with a liquid. Hou *et al.* determined that when a steel ball-bearing accelerating from rest due to gravity impacts a bed of loose fine granules (hollow cenospheres were used) the behaviour of the bed during impact is similar to a fluid [19]. The penetration velocity during the early stages of impact was explained by considering the viscous damping and hydrostatic drag forces of the bed. In particular, as shown in Figure 1.2, when the ball bearing impacts the surface a ‘granular splash’, consisting of a narrow jet of particles moving upwards, is generated. Very similar behaviour is observed during ball bearing impacts into fluids.

Attempts to understand the flow of granular materials on the basis of a continuum fluid mechanics approach, as with the Navier Stokes equations for hydrodynamics, lead to significant problems and instabilities in the equations. In reality the flow of granular materials is often not very fluid-like in nature, as illustrated in Figure 1.3 which shows three images of the flow of small grass seeds

1. INTRODUCTION

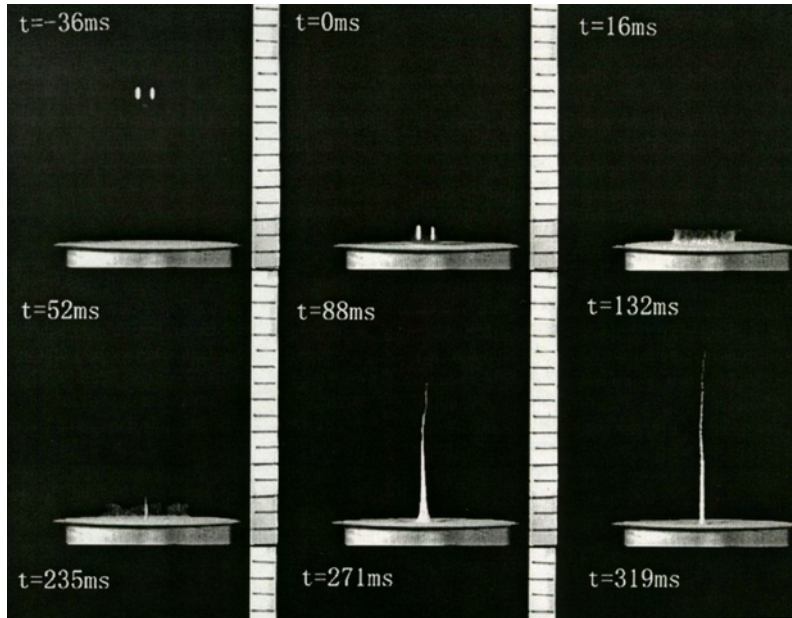


Figure 1.2: Jet formation after the impact of a small steel ball ($R=5$ mm) released from a height of 10 cm on loose fine granules (0.074-0.1 mm). The ball is impacting from above. Image taken from [19].

approximately 0.5 mm in size through the opening of a silo, taken from [20]. The material behaves quite differently to a fluid. The motion mainly occurs in the column of material directly above the opening. There is a cone shaped area of material, with the opening at the point, where material has been disturbed. The material outside this cone remains at rest, even 2.6 s after opening the silo.

There are clearly important differences between the flow of granular materials and the flow of homogeneous liquids. Since granular materials are inhomogeneous and contain a range of particle sizes, they frequently behave anisotropically. They present collective phenomena, such as heap formation or the ability to lock together and form a blockage when flowing through a narrowing, such as the neck of a funnel or an egg-timer. This is not physically possible for a homogeneous liquid.

The properties of a granular material can vary with time. For example, when a granular material consisting of a range of particle sizes is shaken, size segrega-

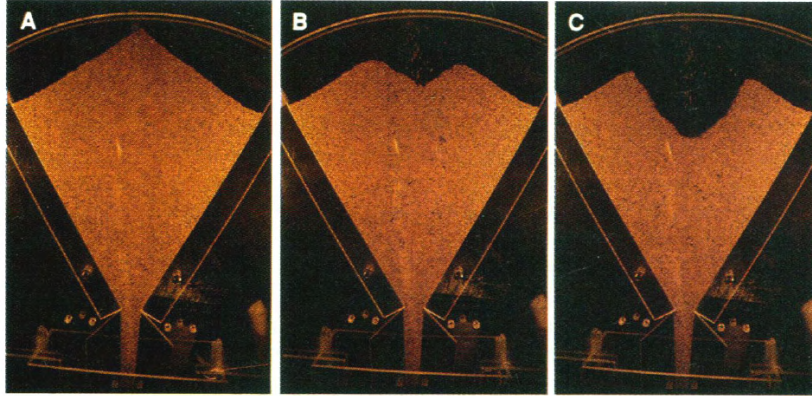


Figure 1.3: The flow of grass seeds through the opening of a silo (a) immediately after opening, (b) 0.6 s and (c) 2.6 s after opening. The flow is localised to a cone of material with the opening of the silo at its point. The material outside this cone remains undisturbed 2.6 s after flow began. Figure taken from [20].

tion, in which the different sizes respond differently and separate out, can occur. The material becomes increasingly inhomogeneous as the shaking continues. The Brazil nut effect is an example of this [21]. Vibrations due to transport cause mixtures of Brazil nuts with other grains/nuts to stratify according to size, with the larger nuts unexpectedly rising to the top [21]. When considering the attenuation of sound waves of a particular frequency in a granular material, the fluctuations in the magnitude of the signal can be as large as the average magnitude of the signal itself [22]. This is thought to be due to particle rearrangement and the activation and subsequent destruction of force chains within the structure.

If the grains in a granular material become well separated, such that inter-grain contact is infrequent, the material could be said to be behaving in a gaseous state [17, 23]. In contrast to an ideal gas however, the energy scale, $k_B T$, is insignificant and so thermodynamic arguments are not applicable. Also, collisions between grains are inherently inelastic, so that energy is dissipated in each collision between particles [12].

Different regions of a granular body can behave in very different ways. For example, when a stationary sand pile is tilted, such that the slope is greater than a critical angle (called the angle of repose, whose value depends on a number of

1. INTRODUCTION

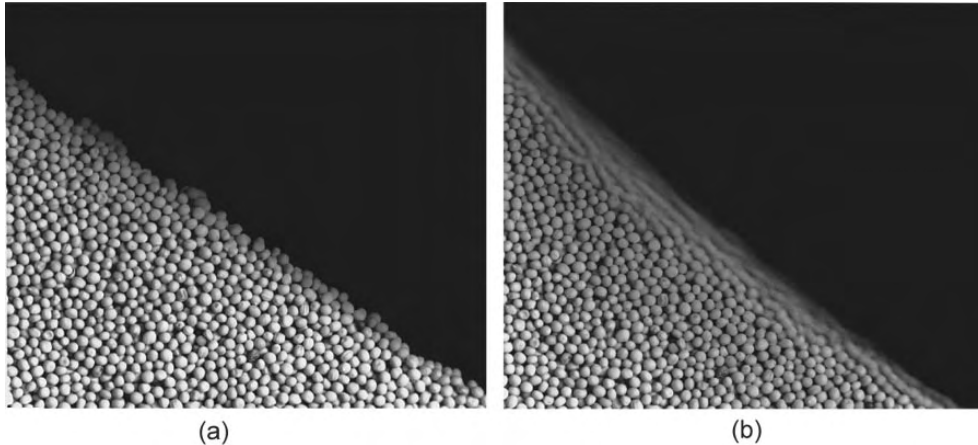


Figure 1.4: (a) A pile of mustard seeds at rest, with a slope angle less than the angle of repose. (b) The same pile tilted so that the angle of the slope is slightly greater than the angle of repose. Granular flow is occurring but is localised to only the first few upper layers of seeds (the blurry region). These images are taken from [12].

factors including internal friction, particle morphology, water content [24]), some of the material begins to flow [12]. However, this flow is localised to the boundary layer at the pile's surface. The bulk of the material remains at rest and behaves as a solid. This effect is illustrated in Figure 1.4 for a pile of mustard seeds [12].

During dynamic penetration experiments, a granular material's behaviour most closely resembles that of a fluid. Hydrodynamic approximations, in which the material is treated as a fluid, have been successfully used to predict a variety of experimental parameters during penetration, including the penetration depth and the variation of the projectile velocity during the penetration process [25, 26]. Hydrocode modelling, in which more detailed information such as the equation of state and temperature effects can be included, has also been applied to this area [27, 28]. Again, however, there is the limitation of treating the material as a continuum.

Current modelling efforts are directed towards determining the forces experienced by individual particles in a granular material and their subsequent dynamics. It is this grain level response of the material that is important in causing

the variability in the results of experiments on granular materials, and the other effects mentioned. A difficulty with this approach is that real granular materials may contain millions of particles which cannot be individually tracked. Instead, simulations are generally run on a few hundred particles and are used to give information on the form of deformation that occurs, assuming that the determined properties are scalable to larger systems [4, 29]. A second problem with predictive models of single particle dynamics is that the fundamental mechanics of the interaction between a penetrator and the granular media, as well as the subsequent dynamics of the granular material, are not well understood.

Figure 1.5 shows plots of the von-Mises stress calculated during penetration of a granular material, using a code by Dwivedi *et al.* [30]. This code is a Lagrangian explicit parallel finite element code that can analyse grain-grain and grain-penetrator interactions using a contact algorithm, with or without friction. The model was able to predict phenomena such as projectile instability during the penetration process. The main source of this instability, and the ensuing trajectory change in the penetration simulations, was found to be the inhomogeneous loading of the projectile due to the heterogeneities and randomness inherent in the granular sand. The simulations also demonstrated the importance of considering the elastic properties of the projectile and sand grains. Variations in these parameters strongly affected the calculated stresses, as shown in Figure 1.5.

1.4 Penetration of Granular Media

Quantitatively assessing the penetration of a granular material by a projectile can be difficult. High-speed photography is not generally suitable as the materials are often opaque. Stress or strain gauges can be embedded into the bulk of the material, but these only give information at a single point. Gauges are also very vulnerable to disruption or destruction during the experiment by the action of sharp sand grains moving across their surfaces.

In order to determine penetration depth as a function of time, for conical-nosed projectiles, Allen *et al.* used a specially developed photographic-electronic chronograph [31, 32]. This consisted of a series of wooden plates, covered in fine metal wire mesh, mounted in the sand along the path of the projectile. When

1. INTRODUCTION

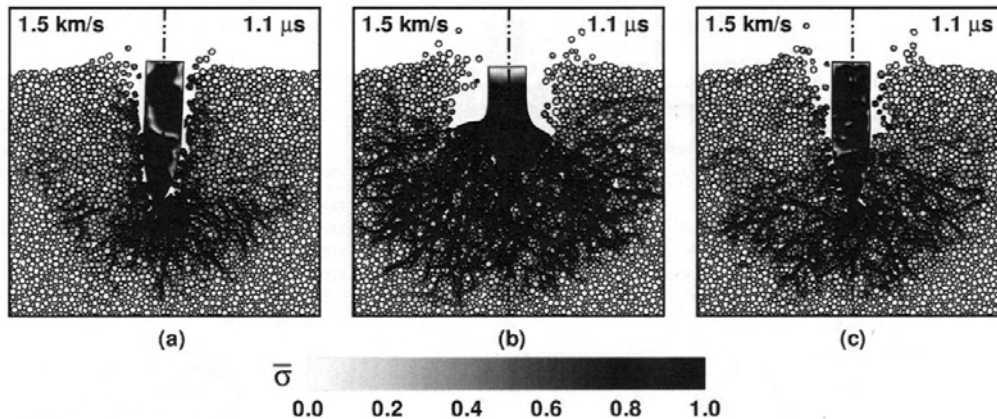


Figure 1.5: The predicted von-Mises stresses generated during penetration of sand by a projectile at 1.5 km s^{-1} . (a) An elastic projectile and inelastic sand grains (b) Inelastic projectile and elastic sand grains (c) Elastic projectile and elastic sand grains. There are significant variations in the simulation results, depending on whether the elasticity of the projectile and the grains is included.

the projectile penetrated the wire mesh, a capacitor discharged through a bank of neon bulbs mounted behind a fixed slit. The resulting signal was recorded by a high-speed camera. In this way the penetration depth as a function of time at a series of discrete points was measured.

Penetrators 5 inches in length and 0.5 inches in diameter were fired into a sand target 6 ft long. The depth as a function of time results were used to test a number of suggested projectile penetration depth theories. They concluded that the deceleration of the projectile could be represented by the following equation,

$$-\frac{dv(t)}{dt} = \alpha v^2(t) + \beta v(t) + \gamma, \quad (1.1)$$

where $v(t)$ is the velocity of the projectile and α , β and γ are constants. They postulated that there is a critical velocity, v_c , such that $\beta = \gamma = 0$ for $v(t) > v_c$ and $\alpha = 0$ for $v_c > v(t) > 0$. This critical velocity was thought to be the transition between inelastic and quasi-elastic impact, and occurred at a velocity of approximately 100 ms^{-1} . A clear flaw in this method is that the flow of sand within the target and the flight of the projectile were restricted by the presence of wooden sheets.

An alternative approach is to use X-ray imaging to produce a series of images of the rod during the penetration process. A flash X-ray system can be used to produce a number of different time delayed X-ray images, showing the spatial progression of the projectile through the sample [33]. This technique has the advantage of giving similar data to the technique of Allen *et al.* (i.e. penetration depth as a function of time), but uses a non-invasive measuring system.

Other experimenters investigating the penetration depth have considered the final depth achieved by a projectile impacting a large body of sand, at speeds of up to 4 kms^{-1} [4, 34]. The obvious disadvantage of looking only at the terminal penetration is that this provides only one depth versus time measurement, which has limited use for understanding the penetration process or validating models.

A better method for obtaining data on the linear flight of a projectile is to embed wireless accelerometers into the body of the projectile. This provides detailed information about the projectile velocity and the extent of penetration with time. Such a setup has been used by Forrestal *et al.* to validate mathematical models of the force experienced by the projectile [35, 36]. It would also be possible to embed accelerometers into the sand material itself to probe the forces felt by the material and to measure the resultant deformation. However, this would only give data at a limited number of discrete points and the presence of accelerometers is likely to affect the flow of the material.

Another variable that has been considered by some authors is the role of the projectile nose shape on its penetration properties. Simulations of the final penetration depth achieved by tungsten rods, for various nose shapes penetrating metal targets, suggest that those with sharpened ends penetrate up to three times further than those with flat ends [37].

All of these methods involve investigating the velocity profile or, even if indirectly, the force experienced by the projectile during the penetration process. They are unable to provide much information about how this resistive force is generated by the granular material. This would require mapping the force or displacement fields within the material during penetration. Some qualitative measure of the force on the grains can be obtained by looking for fractured grains in the wake of the projectile. This method has been used to estimate the min-

1. INTRODUCTION

imum force experienced, and also to identify the route taken by the projectile through the material [31].

In order to investigate in detail the response of a granular material to penetration, it would be useful to map the local displacements within the material, allowing local density changes to be calculated and for estimates of the energy deposited into the material to be determined. Such data would help in understanding the temporal progression of the penetration and why different projectile shapes behave so differently.

The technique of Digital Image Cross Correlation (DICC), and more specifically Digital Speckle Radiography (DSR), is particularly suited to the study of granular materials as it allows unobtrusive and high resolution measurement of displacements. DICC is a technique for determining full-field displacement measurements on the surface of a material through analysis of optical images [38]. DSR is the extension of the technique to measuring displacement in internal planes through analysis of X-ray images [39]. The techniques work by tracking the displacement of small sub-sections of a material between images taken before and after some deformation has occurred. How this process works is discussed in more detail in Chapter 2. DICC using optical images is an established technique which has been applied to a wide range of problems, including the measurement of velocity in seeded flows [40], the measurement of strain fields around crack tips [41], impact mechanics [42] and a variety of other applications [14, 43–45].

The technique of DSR has already been applied to some experiments looking at the penetration or compaction of granular materials, including the impact of concrete samples by spherical impactors [46]. It was found to provide interesting data regarding the internal flow field around the impactor. The samples used in the experiments were relatively small ((50×50) mm plan view, 30 mm thick). Small specimens were used due to their relative transparency to X-rays and to avoid issues with the intensity profile of the X-ray beam. Once a penetration depth of a few centimetres had been reached, the deformation could no longer be usefully studied as significant interaction between the compaction fronts and the boundaries had occurred.

Some preliminary studies of long rod penetration of sand and concrete using DSR have been carried out by Grantham *et al.* [14, 39, 47, 48]. These involved

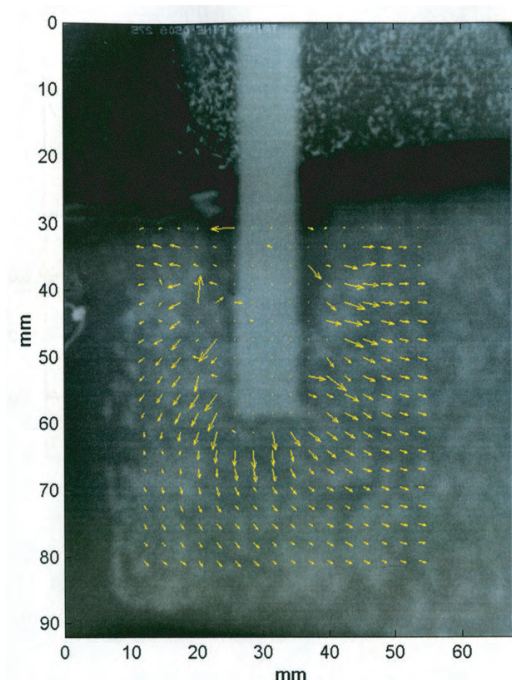


Figure 1.6: A plot of the displacements measured during a penetration experiment, superimposed on an X-ray of the penetration process. The sample size is $(70 \times 60 \times 30)$ mm. The general flow of material away from the projectile can be observed, but there are problems visible such as rotation of the sample. Figure taken from [14].

firing 80 mm long, 9.2 mm diameter, projectiles into the side of a square target of sand with a plan view size of (60×70) mm and with a vertical depth of 30 mm. DSR was used to determine the displacements in a horizontal plane within the material. An example image of the displacements calculated from such a penetration experiment is shown in Figure 1.6.

There are a number of potential problems with using a sample that is small relative to the size of the penetrator. Since the depth of the sample is only 30 mm, the projectile penetrates only a small distance into the sample before the compaction waves reach and begin to significantly interact with the sides of the container, after which the material behaviour can no longer be considered to be representative of the bulk material. There are also problems associated with

1. INTRODUCTION

using a rectangular geometry as the effect of the boundary conditions imposed by the confinement is difficult to model. The boundary conditions with a cylindrical symmetry would be much simpler and would consist mainly of hoop stresses around the cylindrically symmetric confinement.

Figure 1.6 shows that there also appears to have been some global rotation of the sample during the penetration (the arrows towards the bottom of the image tend to the right more than those higher up). This global translation and rotation significantly disrupts our view of the deformation process within the material, such rotation and translation is visible in many of the displacement plots in [14].

It is clear that there is still a significant need for improved data showing the internal displacements during penetration of a granular material. In particular, it is essential to use a larger sample so that the measured displacements are more representative of the bulk behaviour of the material. This can be achieved by ensuring that the displacements are not affected by the boundaries of the sample until as late on in the penetration as possible. If a cylindrical confinement is used, the penetration can be followed yet further as the effects of the confinement become relatively simple to model in terms of hoop stresses.

In Chapters 4 to 7 DSR (discussed in more detail in Chapters 2 and 3) is used to investigate the response of a large cylindrical sample of sand (100 mm diameter, 150 mm length) to penetration by long rods at a variety of rates. The effect of variables including the projectile nose shape, the projectile width, and the penetration velocity are investigated. These experiments illustrate the localised internal response of a granular material to penetration and provide significant amounts of data on the subsequent dynamics of the granular material.

1.5 Summary

In summary:

- Granular materials are very widely used and are important in a large number of applications, but their behaviour in response to applied loads is not well understood.

- Granular materials can behave as solids or in a fluid-like manner depending on the situation. Different sections of a granular body can behave differently (e.g. fluid-like flow localised to the surface areas).
- Hydrodynamic or hydrocode modelling have limitations when applied to granular materials since they do not account for collective phenomena such as heap formation or locking of the particles.
- Modelling single particle dynamics is more appropriate, but the fundamental mechanics of the dynamic behaviour of granular materials are not well understood. In particular there is little information about the interaction between a penetrator and the material.
- Detailed data on the internal response of granular materials to stimuli is required to increase understanding of their behaviour and to facilitate more appropriate and accurate computational models.
- Such data will be more useful if a sample that is large relative to the projectile width is used, so that significant interaction with the confinement does not occur until late in the penetration process.
- Standard experimental techniques, such as high-speed photography or the use of gauges and accelerometers, are unable to effectively probe the internal displacements in an opaque material.
- DSR, discussed in Chapter 2, is ideally suited to this problem. It is a non-intrusive measuring technique that can provide high-resolution displacement data within an internal plane of an opaque granular material.

References

- [1] Schadschneider, A., Kuhne, R. and Wolf, D.E., *Traffic and Granular Flow '05*, Springer, US (2007)

REFERENCES

- [2] Ren, D., Leslie, L.M. and Karoly, D., “Landslide Risk Analysis using a New Constitutive Relationship for Granular Flow”, *Earth Interaction*, **12**, (2008), 108–114
- [3] Promratana, K., *Granular Materials Behavior under Dynamic Excitations*, Phd, University of Nebraska-Lincoln (2008)
- [4] Borg, J.P. and Vogler, T.J., “Mesoscale simulations of a dart penetrating sand”, *Int. Journal of Impact Engineering*, **35**, (2008), 1435–1440
- [5] Lin, D.G., Hsu, S.Y. and Chang, K.T., “Numerical simulations of flow motion and deposition characteristics of granular debris flow.”, *Natural Hazards*, **50(3)**, (2009), 623–650
- [6] Siddiqui, N.A., Kahn, F.H. and Umar, A., “Reliability of underground concrete barriers against normal missile impact”, *Computer and Concrete*, **6(1)**, (2009), 79–93
- [7] Kantak, A.A., Hrenya, C.M. and Davis, R.H., “Initial rates of aggregation for dilute, granular flows of wet particles”, *Physics of Fluids*, **21(2)**, (2009), 301–305
- [8] Surkov, Y.A. and Kremnev, R.S., “Mars-96 mission: Mars exploration with the use of penetrators”, *Planet Space Science*, **46(11/12)**, (1998), 1689–1696.
- [9] Crawford, I.A., Ball, A.J., Wilson, L., Smith, A. and Gao, Y., “MOON-LITE: The Scientific Case”, *Proceedings of the Lunar and Planetary Science Conference*
- [10] Duran, J. and Reisinger, A., *Sands, Powders and Grains: An Introduction to the Physics of Granular Materials*, Springer-Verlag New York (1999)
- [11] Zhang, Y. and Campbell, C.S., “The interface between fluid-like and solid-like behaviour in two-dimensional granular flows”, *J. Fluid Mech.*, **237**, (1992), 541–568

REFERENCES

- [12] Jaeger, H.M., Nagel, S.R. and Behringer, R., “Granular solids, liquids and gases”, *Review of Modern Physics*, **68(4)**, (1996), 1259–1273
- [13] Geng, J., Longhi, E., Behringer, R.P. and Howell, D.W., “Memory in two-dimensional heap experiments”, *Physical Review E*, **64**, (2001), 060,301:1–4
- [14] Grantham, S.G., *Digital Speckle Radiography*, Phd, University of Cambridge (2002)
- [15] Cai, J., Nesterenko, V.F., Vecchio, K.S., Herbold, E.B., Benson, D.J., Jiang, F., Addiss, J.W., Walley, S.M. and Proud, W.G., “The influence of metallic particle size on the mechanical properties of PTFE-Al-W powder composites”, *J. Appl. Phys.*, **104**, (2008), 103,903
- [16] Liu, C., “Spatial patterns of sound propagation in sand”, *Phys. Rev. B*, **50(2)**, (1994), 782–794
- [17] Pudasaini, S.P. and Hutter, K., *Avalanche Dynamics: Dynamics of Rapid Flows of Dense Granular Avalanches*, Springer-Verlag New York (2007)
- [18] Knight, J.B. and Nagel, S.R., “Vibration-induced size separation in granular media: The convection connection”, *Phys. Rev. Lett.*, **70(24)**, (1993), 3728–3731
- [19] Atwell, J. and Olafsen, J.S., “Anisotropic Dynamics in a Shaken Granular Dimer Gas Experiment”, *Phys. Rev. E*, **71**, (2005), 062,301
- [20] Jaeger, H.M. and Nagel, S.R., “Physics of the Granular State”, *Science*, **255(5051)**, (1992), 1523–1531
- [21] Mobius, M.E., Benjamin, E., Lauderdale, S.R.N. and Jaeger, H.M., “Size separation of granular particles”, *Nature*, **414**, (2001), 270
- [22] Liu, C.H. and Nagel, S.R., “Sound in a granular material: Disorder and nonlinearity”, *Phys. Rev. B*, **48**, (1993), 15,646–15,650
- [23] Atwell, J. and Olafsen, J.S., “Anisotropic Dynamics in a Shaken Granular Dimer Gas Experiment”, *Phys. Rev. E*, **71**, (2005), 062,301

REFERENCES

- [24] Julien, P.Y., *Erosion and Sedimentation*, Cambridge University Press, UK (1998)
- [25] Tate, A., “A theory for the deceleration of long rods after impact”, *J Mech Phys Solids*, **22(5)**, (1967), 551–557
- [26] Grove, B., “Theoretical consideration on the penetration of powdered metal jets”, *International Journal of Impact Engineering*, **33**, (2006), 316–325
- [27] Fahrenthold, E.P., “Shock physics simulation using a hybrid particle-element method”, *Shock Compression of Condensed Matter*, (2005), 483–486
- [28] Grady, D.E., A., W.N., Kerley, G.I., T., W.L. and Kuhns, L.D., “Computational modeling and wave propagation in media with inelastic deforming microstructure”, *J Phys IV*, **10**, (2000), 15–20
- [29] Addiss, J.W., Collins, A., Bobaru, F., Promratana, K. and Proud, W.G., “Dynamic behavior of granular materials at impact”, *DYMAT 2009, not yet published*
- [30] Dwivedi, S.K., Teeter, R.D., Felice, C.W. and Gupta, Y.M., “Two Dimensional Mesoscale Simulations of Projectile Instability During Penetration in Dry Sand”, *Journal of Applied Physics*, **104**, (2008), 083,502–1
- [31] Allen, W.A., Mayfield, E.B. and Morrison, H.L., “Dynamics of a Projectile Penetrating Sand”, *Journal of Applied Physics*, **28(3)**, (1957), 370–376
- [32] Allen, W.A., Mayfield, E.B. and Morrison, H.L., “Dynamics of a Projectile Penetrating Sand Part II”, *Journal of Applied Physics*, **28(11)**, (1957), 1331–1336
- [33] Gooch, W.A., Burkins, M.S., Kingman, P., Hauver, G., Netherwood, P. and Benck, R., “Dynamic x-ray imaging of 7.62-mm APM2 projectiles penetration boron carbide”, *18th Int. Symposium on Ballistics*, (1999), 901–908
- [34] Savvateev, A.F., Budin, A.V., Kolikov, V.A. and Rutberg, P.G., “High-Speed Penetration into Sand”, *Int. Journal of Impact Engineering*, **26**, (2001), 675–681

REFERENCES

- [35] Forrestal, M.J. and Luk, V.K., “Penetration into Soil Targets”, *Int. Journal of Impact Engineering*, **12(3)**, (1992), 427–444
- [36] Forrestal, M.J., Frew, D.J., Hickerson, J.P. and Rohwer, T.A., “Penetration of concrete targets with deceleration-time measurements”, *Int. Journal of Impact Engineering*, **28**, (2003), 479–497
- [37] Rosenberg, Z. and Dekel, E., “On the role of nose profile in long-rod penetration”, *Int. Journal of Impact Engineering*, **22(3)**, (1999), 551–557
- [38] Sjudahl, M. and Benckert, L.R., “Electronic speckle photography: analysis of an algorithm giving the displacement with subpixel accuracy”, *Applied Optics*, **32(13)**, (1993), 2278–2284
- [39] Grantham, S.G., Goldrein, H.T., Proud, W.G. and Field, J.E., “Digital speckle radiography - a new ballistic measurement technique”, *Imaging Sci. J.*, **51**, (2003), 175–186
- [40] Peters, W.H., Zheng-Hui, H., Sutton, M.A. and Ranson, W.F., “Two-dimensional fluid velocity measurements by use of digital speckle correlation techniques”, *Experimental Mechanics*, **24**, (1984), 117–121
- [41] Peters, W.H., Ranson, W.F., Kalthoff, J.F. and Winkler, S.R., “A study of dynamic near crack tip fracture parameters by digital image analysis”, *J. Phys. IV*, **5**, (1985), 631–638
- [42] Russel, S.R. and Sutton, M.A., “Image correlation quantitative NDE of impact and fabrication damage in a glass fiber reinforced composite system”, *Journal of Material Evaluation*, **47**, (1989), 102–108
- [43] Hild, F., Fayolli, X., Rethore, J. and Roux, S., “Recent progress in digital image correlation: from measurement and control to mechanical identification”, *Proceedings of the International Symposium on Optical Metrology in Industrial, Medical and Daily Life Applications*, (2008), 117–124
- [44] Rethore, J., Hild, F. and Roux, S., “Extended digital image correlation with crack shape optimisation”, *Int. J. Num. Meth. Eng.*, **73**, (2008), 248–272

REFERENCES

- [45] Grantham, S.G. and Proud, W.G., “Digital speckle x-ray flash photography”, *Shock Compression of Condensed Matter*, (2001), 803–806
- [46] Synnergren, H., Goldrein, T. and Proud, W.G., “Application of digital speckle photography to flash x-ray studies of internal deformation fields in impact experiments”, *Applied Optics*, **38(19)**, (1999), 4030–4036
- [47] Grantham, S.G., Proud, W.G. and Field, J.E., “Internal Displacements in Cement During Ballistic Impact”, *Shock Compression of Condensed Matter*, **706**, (2003), 1335–1338
- [48] Grantham, S.G. and Forsberg, F., “Measurement of granular flow in a silo using digital speckle radiography”, *Powder Technology*, **146**, (2004), 56–65

Chapter 2

Principles of Digital Image Cross Correlation

2.1 Introduction

Digital Image Cross Correlation (DICCC) is essentially a pattern tracking technique. Such techniques work by tracking the motion of a pattern, such as a grid pattern or a particular arrangement of spots. Using a grid approach, a fine grid is printed onto the surface of a material. When the material deforms, the arrangement of the grid lines is disturbed. By comparing the deformed grid with the original grid, the localised strains can be determined from the resulting moiré interference pattern [1]. This approach gives accurate strain and displacement data but necessitates including a grid pattern on the sample. While this is generally simple to achieve on the surface of a solid, it is almost impossible to achieve for a granular material, such as those discussed in this thesis. For such materials, it is more appropriate to use a random variation in contrast as the pattern to be tracked, commonly referred to as a speckle pattern [2]. It is also often easier, in terms of application and analysis, to use such a random pattern when considering the deformation of solid materials [3].

The contrast variation pattern may be due to inherent variability within the sample, such as the variable microstructure within a granular material (e.g. see [2] and [4]). Alternatively, an artificial variation in contrast can be achieved, either by spraying a random pattern of paint onto the surface of the material

2. PRINCIPLES OF DIGITAL IMAGE CROSS CORRELATION

[3, 5, 6] or by adding a number of ‘tracker particles’. In the case of optical photography of granular materials, adding fine graphite particles can provide a suitable variation in contrast [7], although care must be taken to keep the volume fraction sufficiently low so as to not alter the bulk properties of the sample. When X-ray imaging is used to obtain the images, a layer of randomly distributed lead particles within the bulk of the material can provide a suitable contrast variation [8–10].

The main advantage of using a random pattern when investigating granular materials is that randomly including tracker particles, such as graphite, minimises the influence of the technique on the response of the material. Additionally, if the tracker particles are of a similar size and shape to the material being studied and are randomly included on the surface or within an internal layer, they are more likely to behave in the same manner as the bulk material and therefore more accurately reflect the underlying displacements. Because of this, DICCC is a technique that is ideally suited to studying the deformation of granular materials.

The first stage of the DICCC process is to take an image of the sample before any deformation has occurred. This reference image shows the initial arrangement of the speckle pattern. The speckle pattern appears as a variation in intensity, giving a range of light and dark areas in the image. In an idealised speckle pattern, the distribution of these light or dark areas over the sample is entirely random. This means that each sub-section of the image contains a pattern of contrast variation which is unique within the larger image. A subsequent image of the sample is taken after some deformation has occurred. Where the material has deformed, the speckle pattern will have moved and changed.

The spatial resolution of the displacement field obtained using DICCC is determined by the smallest size sub-image which can be tracked between the two images. Various suggestions have been made as to what constitutes the minimum traceable area. Lecompte *et al.* suggest that areas of the order of three times the speckle size are necessary [11], although it is unclear whether this applies to all types of speckle pattern. Others have taken a more quantitative approach to choosing the optimal speckle pattern and smallest traceable area, including Lane *et al.* who derived a grey level co-occurrence matrix [12]. In order to achieve a good spatial resolution the spatial scale of the contrast variations should be small

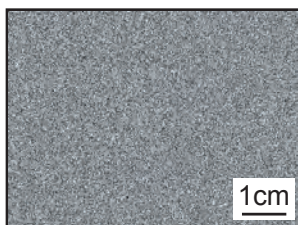


Figure 2.1: An ideal, computer generated, speckle pattern consisting of a random arrangement of black dots on a white background.

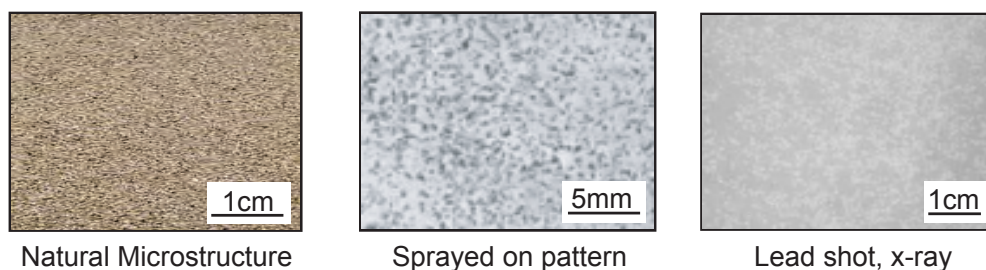


Figure 2.2: Examples of various types of speckle patterns. The left image shows the contrast variation formed by the natural microstructure of a material. The centre image shows a pattern formed by spraying paint onto a sample surface. The right image is an X-ray image showing a speckle pattern made up of lead particles.

relative to the size of the area that is being tracked between the two images. This ensures that the pattern of contrast variation is unique within the larger image. Clearly, the achievable spatial resolution is dependent on the size of the light or dark areas, referred to as the speckle size (for example the size of the particles of the added graphite or lead).

Figure 2.1 shows an example of an idealised computer generated speckle pattern. Real experimental speckle patterns often differ considerably from the idealised form. The spatial scale of the contrast variations can be relatively large, and there is often blurring or distortion of the images. This can lead to errors in the correlation process and is discussed in detail in [13] and [14]. Examples of speckle patterns experimentally obtained by the author are shown in Figure 2.2.

2. PRINCIPLES OF DIGITAL IMAGE CROSS CORRELATION

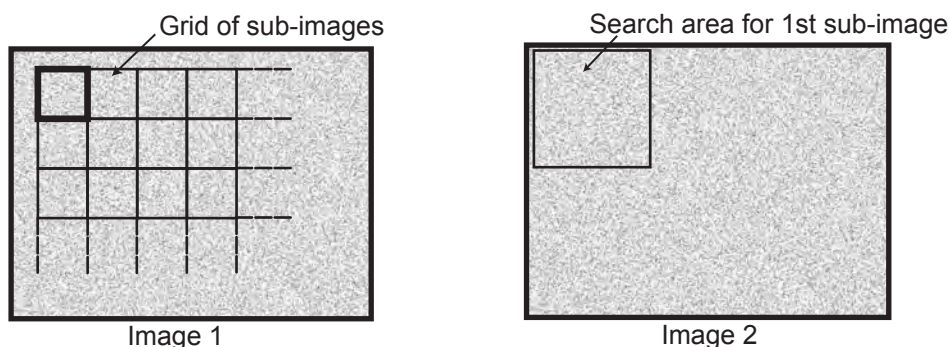


Figure 2.3: Setting up a mesh for digital image cross correlation. The first image is split up into a grid of sub-images (the sub-images can also be arranged so that they overlap to some extent). For each sub-image, a search area is identified in the second image.

In the second stage of the DICC process, the images are input to a computer, either directly, in the case of digital images, or by transmissive scanning for X-ray film. The initial reference image, Image 1 in Figure 2.3, is divided into a grid of squares (sub-images) of size $(L \times L)$ pixels. The algorithm extracts the pixel intensity distribution of a particular sub-image. This is the pattern that will be searched for in the second image, taken after the deformation, in order to find its position and therefore its displacement between the images. In order to reduce computing time and to increase the chance of a successful correlation, the algorithm does not search through the entirety of the second image. Instead, a suitably sized search area is identified, as illustrated in Image 2 of Figure 2.3. The way in which the sub-image is located in the second image, in order to determine its displacement, differs between DICC algorithms. The two main techniques are discussed in the following section.

2.2 DICC Algorithms

2.2.1 Overview

The majority of DICC algorithms can be separated into two groups. In the first, particularly represented by the work of Sutton *et al.* [15–19], the sub-

image being tracked between the two images can be located even if it has been sufficiently deformed through compaction or shearing that a direct correlation is no longer possible. The assumption is made that the sub-images are sufficiently small that they distort homogeneously and that the distortion can therefore be represented by six parameters $\left(u, v, \frac{\partial u}{\partial x}, \frac{\partial u}{\partial y}, \frac{\partial v}{\partial x}, \frac{\partial v}{\partial y}\right)$, such that the coordinates of the sub-image in the first reference image (x_i, y_i) and the second deformed image (x_i^*, y_i^*) are related by equations (2.1) and (2.2),

$$x_i^* = x_i + u + \frac{\partial u}{\partial x} \Delta x + \frac{\partial u}{\partial y} \Delta y, \quad (2.1)$$

$$y_j^* = y_j + v + \frac{\partial v}{\partial x} \Delta x + \frac{\partial v}{\partial y} \Delta y. \quad (2.2)$$

Here, u and v are the extent of displacement of the centre of the sub-image in the x - and y -directions respectively, and Δx and Δy are the distances from the centre of the sub-image to a point in the sub-image at (x, y) . The correlation value is therefore a function of the displacement components and the displacement gradients. By maximising the correlation coefficient between the original sub-image, and potential locations in the second image, with respect to these six parameters, the displacement, strain and the extent of shear and rotation of each sub-image can be determined.

Sutton's approach has the advantage of providing detailed information regarding the localised strain and the extent of shearing and rotation within the sample, in addition to the displacement data. However, there are disadvantages associated with this method. Due to the large number of variables being investigated, and the accuracy with which they are determined, naive implementations of this approach can be computationally heavy. The artificial distortion of the sub-image through the application of the distortion parameters $\frac{\partial u}{\partial x}, \frac{\partial u}{\partial y}, \frac{\partial v}{\partial x}, \frac{\partial v}{\partial y}$, representing compaction, shear and rotation, can lead to systematic errors. The speckle pattern must be isotropic and well-defined, something which is not necessarily true for non-ideal, experimental speckle patterns.

Looking for distorted sub-images in this manner is not applicable in all DICC applications. The technique is particularly unsuitable when dealing with a relatively coarse grained speckle pattern in which the speckles themselves do not

2. PRINCIPLES OF DIGITAL IMAGE CROSS CORRELATION

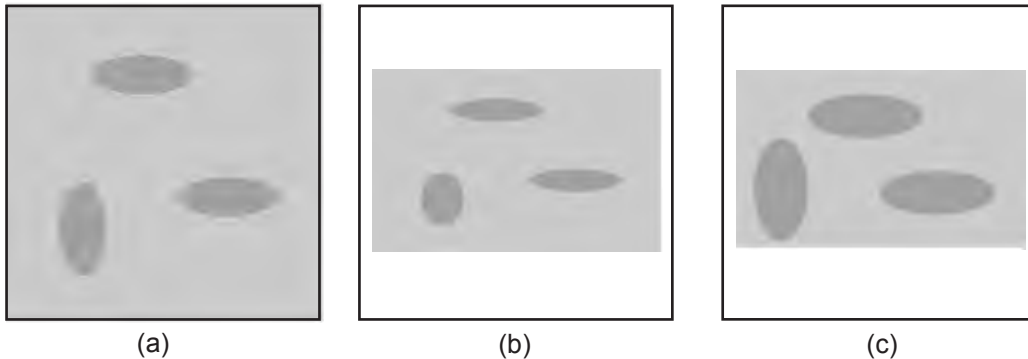


Figure 2.4: (a) An example of a sub-image containing incompressible speckles, for example an X-ray image showing the location of pieces of lead. (b) Computationally simulated image of how the image in (a) would look after compaction according to the Sutton method [16]. (c) How the image in (a) would look if compacted experimentally. The speckle particles have not deformed as in (b) but have instead become more concentrated.

deform. This is the case when using lead shot to produce the speckle pattern or when using the coarse micro-structure of a granular material in optical speckle (even if the grains deform they are unlikely to do so in the same way as the surrounding material). Figure 2.4 (a) shows an example of a sub-image containing incompressible speckle particles. If the sub-image were compacted computationally, as in the Sutton approach, to simulate compaction of the material, the sub-image in (b) would result. The speckle particles themselves are assumed to have deformed with the surrounding material.

In reality, the experimentally compacted sub-image would look more like image (c), in which the speckles have not changed shape and have instead become more concentrated as the volume of the sub-image has decreased. A similar effect occurs when considering shearing of the material. Falsely assuming that the speckles themselves deform in the same way as the underlying material can therefore lead to errors for coarse grained speckle patterns - patterns where the speckles are large relative to the sub-image size, for example the speckle size is greater than around a quarter of the sub-image size.

In the second main class of DIC algorithms [20], the assumption is made that

the local strain in the material is small, relative to the size of the sub-images, such that the global deformation can be represented as a series of simple rigid-body translations of sub-images. Unlike in the Sutton approach, each sub-image is assumed to have only been displaced to some extent in the x - and y -directions between images. It is assumed that no rotation, shearing or compaction of the sub-image has occurred during the deformation process. More global shearing, rotation or compaction of the material can be accounted for by the translation of a series of rigid-body sub-images. This approach has been adopted by a number of researchers, particularly for studying materials in which the global strain is small [14, 20–22].

The main advantage of this approach is that the correlation can be performed in the Fourier domain, rather than the spatial domain, which can significantly decrease the computational time of the algorithm, due to the smaller number of calculations required [14, 21]. This method also directly calculates the displacement field within the sample, without additional errors caused by considering compaction, shearing and rotation of the sub-images, rather than the strain field. For a granular material the concept of a displacement field is potentially more appropriate than a strain field, as there is often bulk flow of material. The main disadvantage of this approach is that for significant strains (greater than around 5%), the sub-image size must be small in order for the assumption of rigid-body motion to hold. This introduces some experimental problems as a suitably fine speckle pattern must be generated such that each sub-image encompasses at least 3-4 speckles [11].

In penetration experiments, such as those discussed in Chapters 4 and 5, there is considerable variation in the extent of the compaction and shearing throughout the sample [13]. This means that small sub-images would also be required for the Sutton approach, so that the assumption of homogeneous deformation of the sub-images holds, as considerable gradients in the displacements are found in the immediate vicinity of a projectile penetrating a granular material [23]. The achievable spatial resolution of the displacements in the main areas of interest, i.e. those directly around the projectile, is therefore likely to be similar with both approaches (the spatial resolution of the displacements is determined by the

2. PRINCIPLES OF DIGITAL IMAGE CROSS CORRELATION

sub-image size). However, the rigid-body approach has the advantage of being less computationally intensive and more straight-forward to implement.

For these reasons, the rigid-body approach is used in this thesis. The success of this approach in analysing images from penetration experiments is clear from the displacement contour plots included in the later chapters of this thesis. Generally, only sub-images which have been entirely destroyed by the penetration, mainly those which overlap the area directly penetrated by the projectile, fail to correlate. As the speckle pattern in this region is destroyed, no DICC algorithm will be able to determine the displacements in this area. The suitability of the assumption that the distortion of the material can be approximated as a series of rigid-body translations is confirmed in the next chapter, suggesting that the quality of the displacement data would be no better with the Sutton approach.

The position of a sub-image within the second image is determined by performing a two-dimensional correlation. In the next section, the basic theory behind such correlations is discussed.

2.2.2 Correlation Functions

DICC algorithms involve finding the correlation between two matrices of data, in order to determine the position of the pixel intensity distribution of the sub-image in the search area of the second image. The correlation coefficient $r_{x,y}$ between two single random variables x and y with expectation values μ_x and μ_y and standard deviations σ_x and σ_y is defined as

$$r_{x,y} = \frac{\text{cov}(x,y)}{\sigma_x\sigma_y}, \quad (2.3)$$

$$= \frac{\text{E}((x - \mu_x)(y - \mu_y))}{\sigma_x\sigma_y}, \quad (2.4)$$

where E is the expected value operator and $\text{cov}(x,y)$ represents the covariance of x and y [24].

If instead of a single random variable we have a series of n measurements of x and y , $X = x_1, x_2, \dots, x_n$, and $Y = y_1, y_2, \dots, y_n$, then the correlation of the two sets of data is best given by the Pearson product moment correlation coefficient

[25]. Equation (2.3) can be rewritten as

$$r_{X,Y} = \frac{E((X - \mu_X)(Y - \mu_Y))}{\sigma_X \sigma_Y}, \quad (2.5)$$

$$= \frac{E(XY) - E(X)E(Y)}{\sigma_X \sigma_Y}, \quad (2.6)$$

$$= \frac{\sum_0^n x_i y_i - n\bar{x}\bar{y}}{n\sigma_X \sigma_Y}, \quad (2.7)$$

$$= \frac{\sum (x_i - \bar{x})(y_i - \bar{y})}{n\sigma_X \sigma_Y}, \quad (2.8)$$

which is the Pearson product moment correlation coefficient. This equation corresponds to a simple spatial cross-correlation between the two sets of data, after normalisation, based on the mean and standard deviation of the data sets [26]. For example, if a vector of data X is correlated with the same set of data displaced by four places (see data sets X and Y in Table 2.1) there will be an associated correlation value. As the data sets do not line up well, the correlation will be low. If the data in data set Y are shifted relative to X there will be a different correlation value. If the shifting is repeated for a range of shifts there will be a peak in the correlation coefficient at a shift of six, for which the data are perfectly aligned. A graph of the correlation value of the data sets X and Y in Table 2.1 relative to the shift of data set Y is shown in Figure 2.5. The correlation peak at a shift of six is clearly visible. The correlation value of one represents perfect correlation.

X	3	9	6	3	7	1	4	8	7	2
Y	4	8	7	2	3	9	6	3	7	1

Table 2.1: Two vectors of data. Vector Y is equal to vector X shifted left by 6 steps, provided the elements wrap around so that the numbers leaving the left of the vector re-appear on the right.

Extending the idea from 1D to 2D, in the case of two matrices of random values $X(x, y)$ and $Y(x, y)$ of size $(m \times n)$, the correct form of the Pearson product moment correlation is given by the extension of equation (2.5) into two

2. PRINCIPLES OF DIGITAL IMAGE CROSS CORRELATION

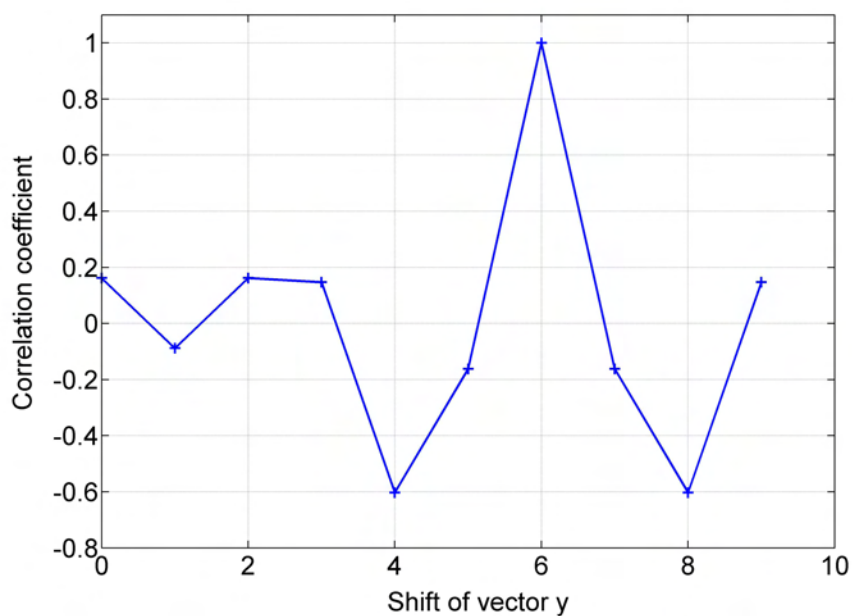


Figure 2.5: Correlation values for the two vectors in Table 2.1. The value at a shift of zero corresponds to directly correlating the vectors. The other values are obtained by shifting the elements in vector Y by the required shift value (and assuming wrapping of the elements), and then correlating the shifted vector with vector X . A correlation value of one shows perfect alignment of the two vectors.

dimensions

$$r_{X,Y} = \sum_{x=0}^m \sum_{y=0}^n \left[\frac{X - \bar{X}}{\sigma_X} \frac{Y - \bar{Y}}{\sigma_Y} \right], \quad (2.9)$$

where \bar{X} and \bar{Y} are the mean values for X and Y and σ_X and σ_Y are the standard deviations.

As an example, consider the two matrices shown in Table 2.2. The second matrix is equal to the first matrix, offset by two elements in the vertical direction and two elements in the horizontal direction, assuming that the data are ‘wrapped’ as they move off the bottom and right hand edges so that they reappear at the top or left side respectively. Equally, the first matrix is equal to the second shifted by three elements in both the vertical and horizontal directions. If the two matrices are correlated using equation (2.9), there will be an associated correlation value, which will be low, as the matrices are not aligned. If the second matrix is shifted in steps in the vertical and the horizontal directions, a matrix of correlation values is generated with a peak value of one at a shift of three in both the vertical and horizontal directions - corresponding to perfect alignment. A surface plot showing how the correlation value changes as the matrix elements are shifted is shown in Figure 2.6. There is a clear correlation peak at a shift of (3,3) with a value of one, corresponding to perfect correlation.

4	7	2	9	3	8	4	3	6	4
3	8	6	5	8	6	9	2	7	4
8	3	8	9	1	9	3	4	7	2
3	6	4	8	4	5	8	3	8	6
2	7	4	6	9	9	1	8	3	8

Table 2.2: Two five by five matrices. The right matrix is equal to the left matrix off-set by two elements in both the x - and y -directions (assuming that elements reappear at the left or top when they leave the right or bottom respectively). The right matrix needs to be shifted by three elements horizontally and vertically to equal the first.

Correlation in the spatial domain, as represented by equation (2.9), represents the most accurate method for determining the correlation between two matrices.

2. PRINCIPLES OF DIGITAL IMAGE CROSS CORRELATION

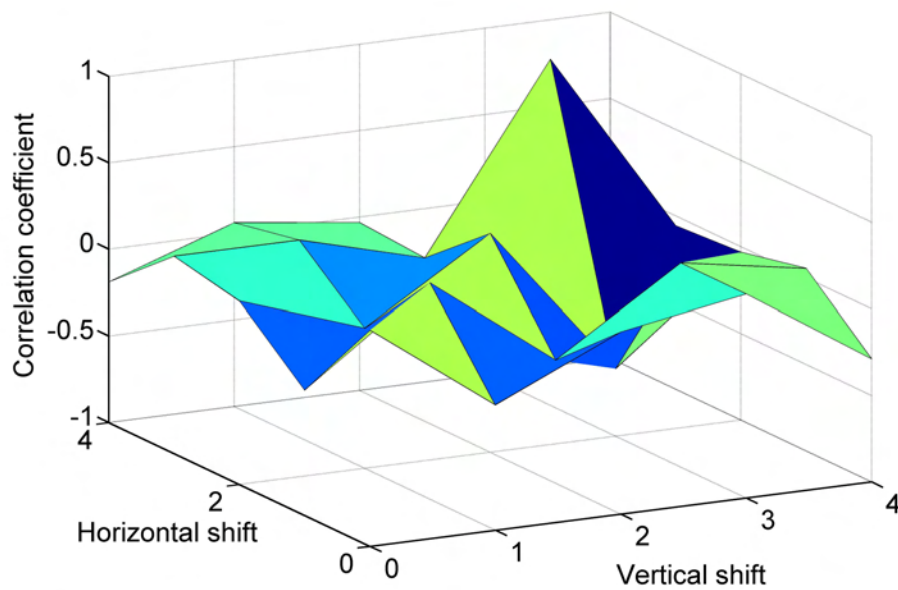


Figure 2.6: A surface plot of the correlation values for the two matrices in Table 2.2. The value at $(0,0)$ corresponds to directly correlating the matrices. The other correlation values are generated by shifting the elements of the second matrix by the required number in the horizontal and vertical directions and then correlating with the first matrix. The correlation value of one at $(3,3)$ represents perfect alignment of the matrices.

However, this approach involves a large number of calculations and is therefore somewhat time-consuming. When correlating two $(m \times n)$ matrices, $(m \times n)$ calculations are required, excluding the normalisation calculations. When attempting to find the position of a sub-image of $(L \times L)$ pixels within a larger image of $(m \times n)$ pixels, approximately $((m - L)(n - L)L^2)$ calculations are required. This technique therefore rapidly becomes prohibitively time-consuming when attempting to locate large numbers of sub-images in large search areas (search areas of two to three L are common). When performing DICC in the spatial domain on images of the order of 2000 by 2000 pixels, with a sub-image size of (100×100) pixels, the analysis can take up to 24 hours (with a search area of (300×300) pixels in the second image, using a 1.8 GHz Dual-Core Processor and 1 GB of RAM).

The calculation speed can be increased by performing the correlation in the spectral domain (Fourier space), rather than the spatial domain. The process illustrated in Table 2.2 and Figure 2.6, in which the second matrix, matrix Y , was shifted in stages relative to the first matrix, matrix X , to produce a matrix of correlation values, can be summarised as equation (2.10) [20].

$$r(k, l) = \frac{\sum_{x=0}^m \sum_{y=0}^n [X'(x, y) Y'(x + k, y + l)]}{\sigma_X \sigma_Y}, \quad (2.10)$$

$$k = 0, 1, \dots, m - 1,$$

$$l = 0, 1, \dots, n - 1.$$

where $X' = X - \bar{X}$ and $Y' = Y - \bar{Y}$.

Equation (2.11) represents the circular discrete convolution of two periodic matrices f and g , limited to the interval $[0, 0]$ to $[m, n]$ [27].

$$[f * g](i, j) = \sum_{x=0}^m \sum_{y=0}^n f(x, y) g(x - i, y - j). \quad (2.11)$$

Comparing equation (2.11) with the numerator of equation (2.10), it can be seen that equation (2.10) represents a normalised convolution.

The convolution theorem states that under suitable conditions (the functions f and g must be point-wise continuous and their integrals must be absolutely

2. PRINCIPLES OF DIGITAL IMAGE CROSS CORRELATION

convergent between $\pm\infty$), the Fourier transform of the convolution of two functions f and g is equal to the point-wise multiplication of the Fourier transforms of f and g , or, in equation form

$$\mathcal{F}[f * g] = \mathcal{F}(f) \otimes \mathcal{F}(g), \quad (2.12)$$

where \mathcal{F} represents the Fourier transform. Therefore, the convolution can be determined by carrying out such a point-wise multiplication of Fourier transforms and then taking the inverse Fourier transform, as shown in equation (2.13).

$$[f * g] = \mathcal{F}^{-1}(\mathcal{F}(f) \otimes \mathcal{F}(g)), \quad (2.13)$$

where \mathcal{F}^{-1} represents the inverse Fourier transform and \otimes represents point-wise multiplication (the outer product of the two matrices), rather than matrix multiplication.

Applying equation (2.13) to equation (2.10) gives

$$r(k, l) = \frac{[X' * Y']}{\sigma_X \sigma_Y}, \quad (2.14)$$

$$= \frac{\mathcal{F}^{-1}(\mathcal{F}(X') \otimes \mathcal{F}(Y'))}{\sigma_X \sigma_Y}, \quad (2.15)$$

where \mathcal{F} represents the two dimensional discrete Fourier transform, defined as

$$F(r, s) = \frac{1}{mn} \sum_{k=0}^{m-1} \sum_{l=0}^{n-1} \left\{ X(k, l) \exp \left[-2\pi i \left(\frac{rk}{m} + \frac{sl}{n} \right) \right] \right\}, \quad (2.16)$$

$$r = 0, 1, \dots, m - 1,$$

$$s = 0, 1, \dots, n - 1.$$

Equation (2.14) demonstrates that the matrix correlation can be carried out in Fourier space, which requires far fewer calculation steps than correlation in the spatial domain and therefore is considerably faster computationally. The two dimensional Fourier Transform of a matrix of size $(m \times n)$ requires roughly $(m \times n)$ calculations. When performing the correlation in the Fourier domain, two Fourier transforms and one inverse Fourier transform are required for the calculation to locate the sub-image within the search area. This involves far fewer calculations than the repeated correlation calculations required in the spatial

domain. When performing DICC in the Fourier domain, on images of the order of 2000 by 2000 pixels with a sub-image size of 100 by 100 pixels, the analysis will take around 10 minutes, rather than the hours required for correlation in the spatial domain (with a search area size of (300×300) pixels in the second image, using a 1.8 GHz Intel Dual Core T2350 Processor - 533 MHz bus speed, 2 MB L2 cache, and 1 GB of RAM).

When performing the correlation in the Fourier domain it is assumed that as elements leave the bottom or right side of the matrix they reappear at the top or left side respectively. This is referred to as wrapping of the data and it assumes periodic boundary conditions. This effect can lead to some unexpected results and can introduce large errors when analysing real experimental speckle data in which wrapping does not occur [28]. By padding the two matrices with zeros, these wrapping errors can be avoided, as when the zeros wrap around they do not contribute to the correlation factor.

2.2.3 Tracking Sub-Images

The previous section discussed the application of image correlation to two equally sized matrices or images. In this section, we focus on using such algorithms to determine the position of sub-images within a larger image. In experimental situations, we are interested in determining the displacements of a whole series of sub-images between two images, in order to determine full-field displacement maps. This involves determining the position of a small section of the first image in a subsequent image.

The idealised method for determining the position of a sub-image in a larger image is shown in Figure 2.7. A suitably sized search area is identified in the second image. This is done firstly to reduce the computing time relative to searching through the whole image. Secondly, in non-ideal speckle patterns, where the pattern is not entirely random or is blurred, the chance of a false correlation is reduced by using a smaller search area. If the speckle pattern is not sufficiently random, the sub-image may not be unique within the image. This could lead to the position of the sub-image being mis-identified and a false displacement being determined.

2. PRINCIPLES OF DIGITAL IMAGE CROSS CORRELATION

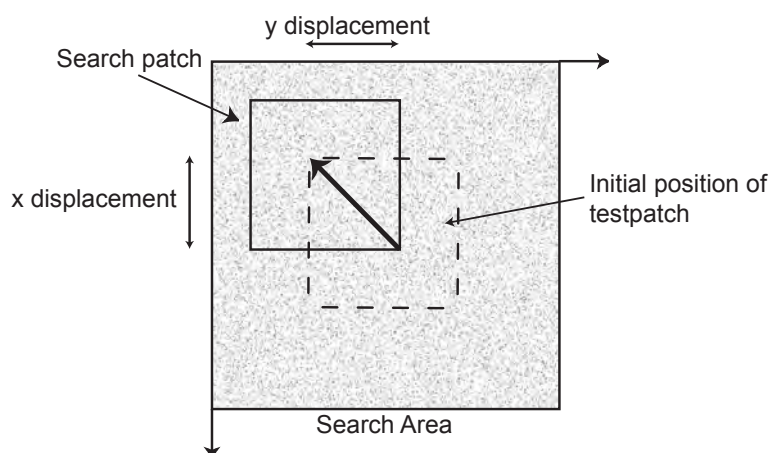


Figure 2.7: A search area in the second image is identified, centred on the original position of the sub-image. A section of the search area of equal size to the sub-image is extracted and the correlation value is determined. This is repeated for all possible sections of the search area to build up a matrix of correlation values.

The intensity distribution of a section of the search area of an equal size to the first sub-image is extracted and the two dimensional normalised correlation coefficient is determined using equation (2.9). This process is then repeated for every possible section of the search area by shifting in pixel increments the area being extracted. A matrix of correlation factors is built up showing the position in the second image at which there is the best correlation with the sub-image. The displacement of the sub-image is then the difference between the sub-image position in the reference image and the position of the best correlation in the dynamic image.

2.3 Problems With Contrast Variation

Considerable variations in contrast are caused during DSR experiments by the non-uniform profile of the X-ray beam. The X-ray beam has an approximately Gaussian profile which becomes more significant when the head to sample distance is small, which is unavoidable for X-ray images of large samples. Previous experiments using the X-ray system showed that the Gaussian profile results in

2.3 Problems With Contrast Variation

the correlation failing around the outside of the image at relatively small displacements [13]. The energy of X-rays produced by the X-ray system for a given charging voltage of the capacitor bank system is also somewhat variable, meaning that the reference and subsequent images can have different contrasts and even slightly different contrast variations. Similar problems arise with optical set-ups in which the shadows from a fixed light source can vary or give non-uniform and varying illumination of the sample [7].

If a standard, Fourier-based DIC algorithm, for example that of White *et al.* [2], is used to analyse flash X-ray images of penetration experiments on large granular samples, we find that the algorithm does not work entirely as expected. Consider the flash X-ray images shown in (a) and (b) of Figure 2.8. These X-ray images were taken during an experiment in which a cylindrical sample of sand (100 mm diameter) was impacted with a long rod projectile, a preliminary experiment to those which will be discussed in later chapters. The cylindrical nature of the sample means that the thickness of sand varies considerably over the cylindrical volume. This leads to a considerable variation in contrast across the image. In image (b), the rod projectile is clearly visible. As it is made of steel, it is considerably more opaque to X-rays than the surrounding sand and therefore appears as an area of high intensity (a white area in the image).

Image (c) is a quiver plot showing the displacements determined using the algorithm of White *et al.*, a standard Fourier based algorithm [21]. The displacements are shown as arrows with length proportional to the magnitude of the displacement. The quiver plot shows that there is a large area around the rod in which the correlation algorithm has not worked correctly. Large areas of sand around the rod have been identified as moving inwards towards the position of the rod, which is unphysical. Since these errors mostly occur in the region around the projectile it is likely that they are caused by the high intensity white area of the rod in image (b), coupled with the contrast effects of the beam profile and sample geometry.

The two X-ray images presented in Figure 2.9 are from a plate impact experiment carried out on a sand sample using the Cavendish Laboratory plate impact machine [29]. The first image (a) shows a plan view of the initial arrangement of the experiment. A sample of sand has been seeded with a plane of lead and

2. PRINCIPLES OF DIGITAL IMAGE CROSS CORRELATION

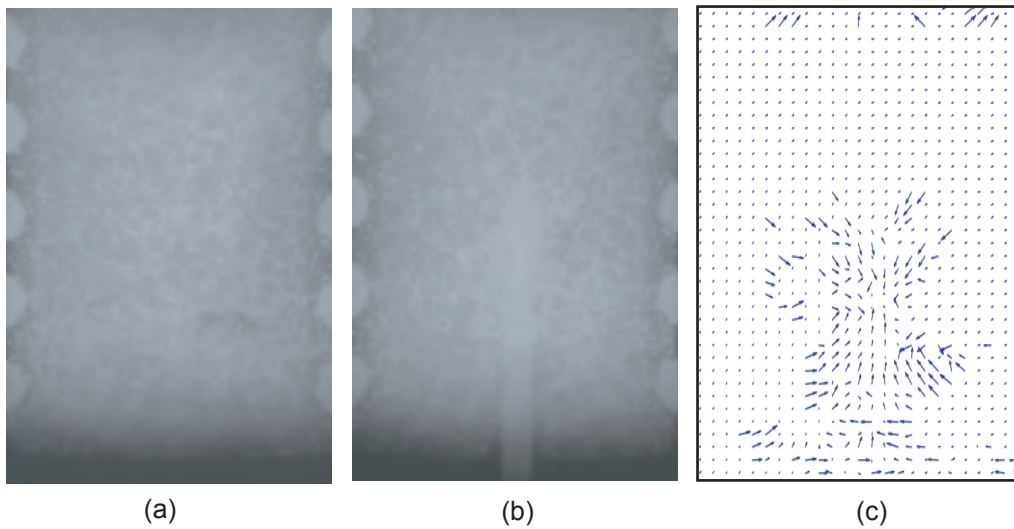


Figure 2.8: Image (a) is a reference X-ray image showing the speckle pattern formed by a randomly scattered layer of lead along the centre of a cylindrical sample of sand. Image (b) is a dynamic X-ray image taken at a later time showing the penetration of the sample by a long rod projectile, traveling at $(200 \pm 3) \text{ ms}^{-1}$. In image (c) the displacement field within the sample is shown as a quiver plot. The correlation algorithm of White *et al.* [2] has given spurious inwards displacements for large regions of material surrounding the projectile. This is thought to be due to the relative high intensity of the projectile on the X-ray image compared with the surrounding material.

2.3 Problems With Contrast Variation

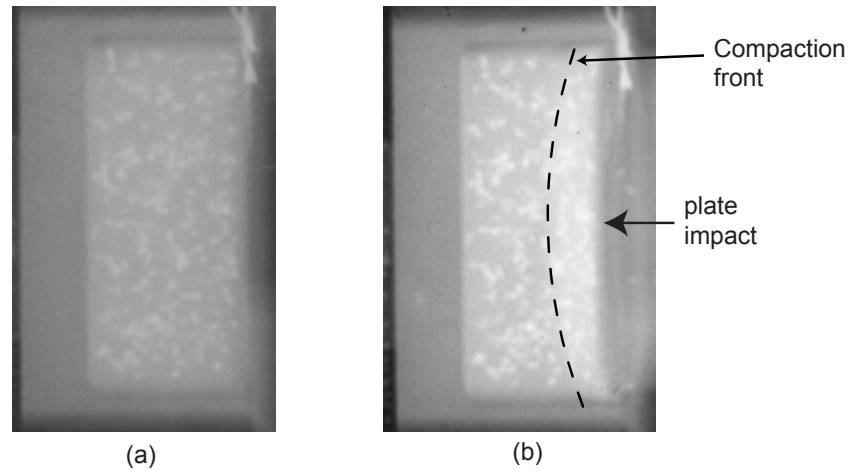


Figure 2.9: X-ray images showing a plan view of a sand sample containing a layer of scattered lead. Image (a) shows the initial arrangement of the lead speckle pattern. Image (b) shows the sample being impacted by a flat plate projectile from the right. In image (b) there is a change in contrast as the material is densified by the compaction wave. Experiment performed by Chapman [29].

is to be impacted by a flat plate projectile, impacting from the right in Figure 2.9. In the second X-ray image (b), a compaction wave is clearly present, behind which the contrast is considerably altered. This large change in contrast causes considerable errors when DIC is performed on the images (although in this case more significant errors are caused by the small number of speckles in the speckle pattern and the extent of the compaction).

The experimental images demonstrate that in DSR experiments, the speckle pattern is often far from ideal. The pattern is made up of large (as compared to a useful sub-image size) spots, or speckles, which do not deform in the same way as the surrounding material. The pattern is frequently blurred and the contrast between the speckles and the background material is often poor, making the speckle pattern indistinct. The sample shape, and the presence of a projectile or localised densification of the material, lead to significant variations in contrast which can cause large errors in the measured displacements. In some cases, these problems can be avoided by careful design of the experiment and choice of speckle

2. PRINCIPLES OF DIGITAL IMAGE CROSS CORRELATION

pattern. For example, with an optical setup, the lighting can be arranged to give a uniform illumination of the sample. Alternatively, if the displacements are small, a suitably small search area can be chosen such that the localised mean and variance are effectively constant across the search area (even if the overall image contains larger changes in contrast). For the majority of the experiments that compose the research presented in this thesis, both large displacements and considerable variations in contrast occur.

To better understand the effect of contrast variation and to look for possible solutions to the problem, it is useful to first consider a simple illustrative example. Consider the image shown in Figure 2.10. This image consists of two smaller square images surrounded by a rectangular region of zero pixel intensity (shown in black in the image). The left white square has a uniform pixel intensity of 400 and represents a bright section of an X-ray image, such as a projectile or area of densified material. The right image consists of five ellipses with pixel intensities of 255 on a background with a uniform pixel intensity of 220, representing a typical section of speckle pattern from an X-ray image. We can think of this simple image as being representative of a search area in the deformed image which contains significant variation in contrast, for example a search area which includes both a section of the speckle pattern and a section of the bright projectile.

Figure 2.11 shows the sub-image whose position in Figure 2.10 is to be determined. It is identical to the right square component of the image shown in Figure 2.10. Therefore, if it is correctly located within Figure 2.10, its position should be identified as being towards the right side of the image. More precisely, its position should be identified as being 71 pixels in the vertical direction and 291 pixels in the horizontal direction from the upper left corner of Figure 2.10. This represents the position of the upper left corner of the right square image within the larger image. The upper left corner of the left square image is at (71,71) pixels.

If the sub-image in Figure 2.11 is correlated with the search area shown in Figure 2.10 in the spatial domain, using the spatial correlation procedure discussed earlier and expressed for a sub-image and a section of the search area of equal size in equation (2.9), the correlation matrix displayed in Figure 2.12 results. This plot shows a clear peak in the correlation surface at (71,291) pixels.

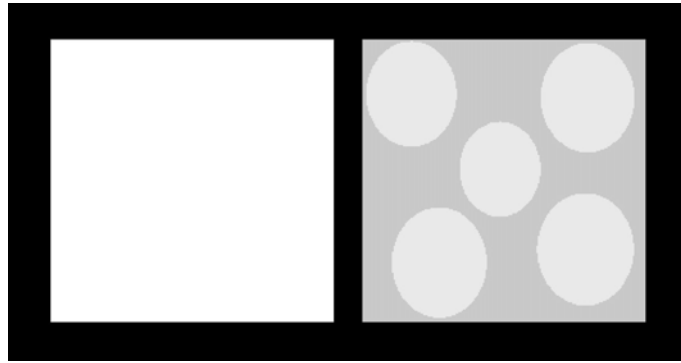


Figure 2.10: An image consisting of two smaller square images on a rectangular background of zero pixel intensity. The left white square has a uniform pixel intensity of 400 and represents a localised bright region in an X-ray image. The right square has five ellipses with pixel intensities of 255 on a background with a uniform pixel intensity of 220 and represents a section of speckle pattern from an X-ray image. The overall image represents a search area that contains large variations in contrast.

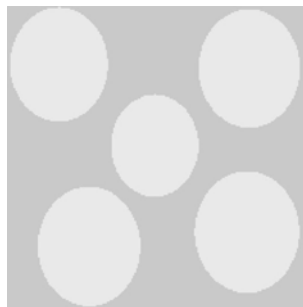


Figure 2.11: The sub-image whose position within Figure 2.10 is to be determined. The sub-image is identical to the right square within the image in Figure 2.10. In the following correlation calculations, this sub-image will be correlated with the entirety of the image shown in Figure 2.10, to see if it is possible to locate it in the presence of the bright region.

2. PRINCIPLES OF DIGITAL IMAGE CROSS CORRELATION

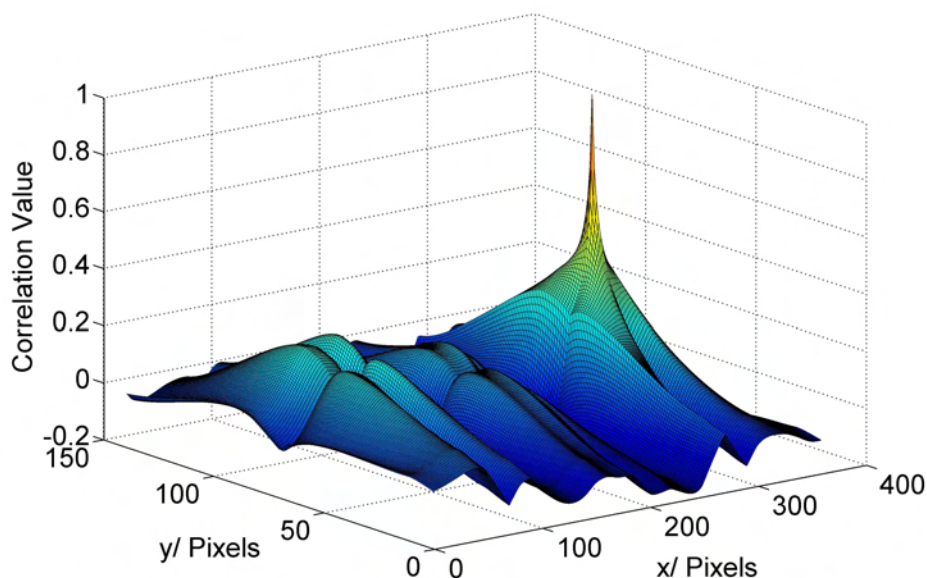


Figure 2.12: A surface plot of the correlation matrix obtained when correlating the sub-image in Figure 2.11 with the search area shown in Figure 2.10, in the spatial domain. The x - and y -axes correspond to the position of the upper left corner of the sub-image relative to the upper left corner of the search area for a given correlation step. The position of the sub-image has been correctly identified as (71,291) pixels.

This corresponds to the top left corner of the sub-image having to be shifted 71 pixels vertically and 291 horizontally, relative to the upper left corner of the search area, to overlap its position in the larger image. This correctly identifies the position of the sub-image within the search area.

Since the spatial correlation formula selects regions of the search area with a size equal to the sub-image, and normalises these smaller areas separately by subtraction of their mean and division by their variance, it is able to correctly differentiate between the two square images contained in Figure 2.10. Since the left square image in Figure 2.10 is uniform, its pixel intensities are reduced to near zero during the normalisation process (as the mean value is subtracted) and the correlation at this location is correspondingly small. The spatial correlation

2.3 Problems With Contrast Variation

process therefore appears to be able to correctly differentiate between an area of speckle and a region of higher than average pixel intensity in X-ray images. However, as discussed earlier, for larger and more realistic images, the spatial correlation method is computationally intensive.

Let us now consider the results of carrying out a similar correlation in the Fourier domain, using equation (2.14). The sub-image is padded with zeros to the same size as the search area shown in Figure 2.10, in order to avoid wrap around errors. Correlation in the Fourier domain is equivalent to calculating the sum of the products of the overlapping elements of the sub-image and search area, for every possible position of the sub-image within the search area. Let us firstly consider the case where the two matrices are correlated in Fourier space without normalisation through subtraction of their mean values. This results in the correlation matrix illustrated as a surface plot in Figure 2.13.

Figure 2.13 shows that the maximum correlation occurs at (71,71). This is the position of the left white square in figure 2.10. There is a considerably smaller secondary peak at (71,291), showing the actual position of the sub-image in the search area. With no normalisation applied, the Fourier algorithm incorrectly identifies the position of the sub-image. This is because the algorithm effectively multiplies the over-lapping pixel values and calculates the sum. The result will be highest when the sub-image is correlated with the left square image in Figure 2.10 (the white area), since this left image has a higher mean pixel intensity than the right smaller image (the speckle pattern). Therefore, with no normalisation applied to the search area or sub-image, the Fourier technique is unable to correctly locate a speckle pattern in the locality of a bright region of an X-ray image.

In reality, most DICCC algorithms working in the Fourier domain which use equation (2.14) normalise the images by the subtraction of their mean values before padding and correlation occurs. This is a subtly different situation from the spatial case. Rather than extracting a section of the search area of equal size to the sub-image and normalising this area (by subtraction of the mean and division by the variance), the *entire* search area is normalised in a single step by the subtraction of its mean value and division by its variance. The subsequent correlation is no longer identical to the ideal spatial correlation derived in equation (2.9). This can lead to some problems in carrying out the correlation if there is

2. PRINCIPLES OF DIGITAL IMAGE CROSS CORRELATION

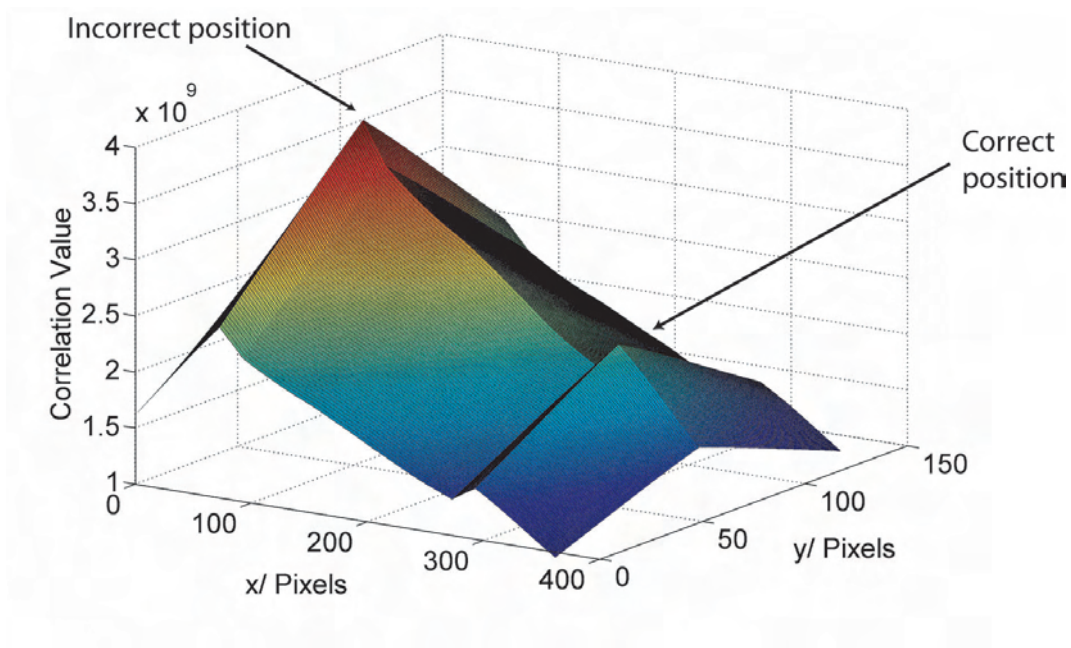


Figure 2.13: A surface plot of the correlation matrix obtained when correlating the sub-image in Figure 2.11 with the search area shown in Figure 2.10 in the Fourier domain with no normalisation applied (without subtracting the means from the two images). With no applied normalisation, the position of the sub-image has been incorrectly identified as (71,71) pixels. This corresponds to the position of the left, white square in 2.10.

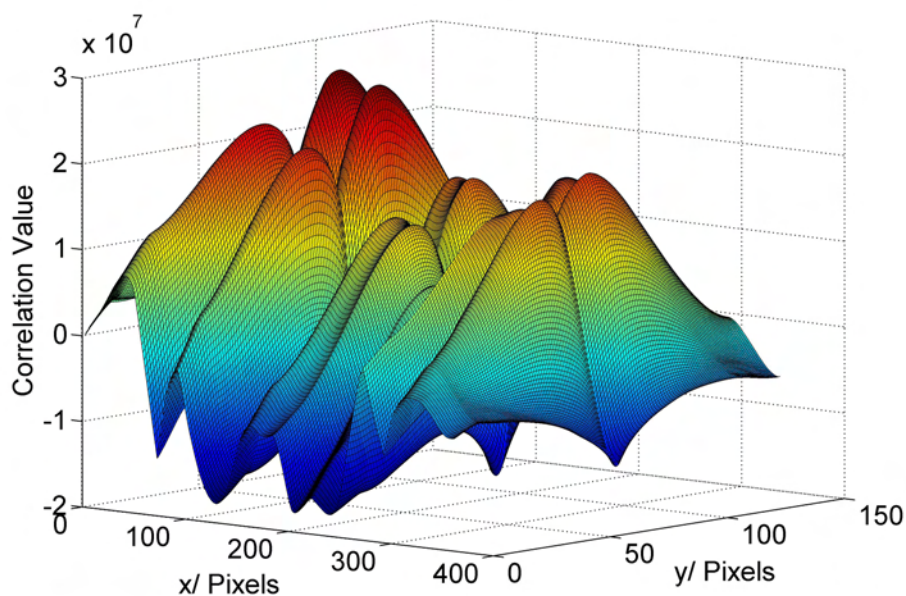


Figure 2.14: A surface plot of the correlation matrix obtained when correlating the sub-image in Figure 2.11 with the search area shown in Figure 2.10, in the Fourier domain (using equation (2.14)). With the basic normalisation included, there is a larger correlation value at the correct position of (71,291). However, the largest correlation value incorrectly identifies the position of the sub-image within Figure 2.10 as being in the region of the left, white square.

a noticeable variation in the mean across the search area, as in Figure 2.10. Applying this form of normalised Fourier correlation to the images in Figures 2.10 and 2.11 results in the correlation surface shown in Figure 2.14.

Figure 2.14 shows that with the ‘single-step’ normalisation applied there is now a considerably larger relative correlation peak at the correct position, compared with the results in Figure 2.13. However, the largest correlation value still incorrectly identifies the actual position of the sub-image in Figure 2.10. Normalising the entire search area in a single step is failing to correctly account for the localised area of high intensity (the white square in Figure 2.10). After normalisation, this area still has higher than average pixel intensity values and the correlation value at this position can still be greater than in the correct position.

2. PRINCIPLES OF DIGITAL IMAGE CROSS CORRELATION

Since the Fourier technique replaces the series of discrete correlation calculations used in the spatial approach with a series of Fourier calculations, it is not possible to normalise sections of the search area separately.

This simple example illustrates that standard Fourier based DICCC algorithms are unsuitable for situations where the speckle pattern is not ideal. If the image of the speckle pattern does not have a uniform mean and variance, and instead includes large variations in contrast as in Figure 2.10, errors can occur. Returning to the X-ray images shown in Figure 2.8, we can now confirm that the correlation errors have been caused by the appearance of the high intensity white area of the rod in image (b), coupled with the contrast effects of the beam profile and sample shape. The standard normalisation approach, in which the search areas are normalised in a single step, does not correctly account for the bright area and the correlation function is therefore giving spurious higher values when the sub-images around the rod are correlated with a patch of the rod, rather than their actual position in image (b). This leads to the large spurious displacements inwards towards the rod that are seen in the quiver plot.

These correlation problems mean that we are currently unable to determine the displacements in the areas we are most interested in – those directly ahead of, and around, the projectile. If DSR is to prove a suitable technique for investigating these kinds of penetration experiments, it will be necessary to improve the contrast normalisation process. This is the subject of the following chapter.

2.4 Conclusions

To summarise the conclusions of this chapter:

- DSR (the application of DICCC to X-ray images) is a technique ideally suited to the study of granular materials. If suitably chosen, randomly incorporated pieces of lead behave as the surrounding material, making DSR an unobtrusive measuring technique capable of providing high resolution displacement data.
- There are two main classes of DICCC algorithms - those that consider rotation, shearing and compaction of the sub-images (the Sutton approach) [15],

and those that consider rigid-body translation of sub-images and where the correlation is performed in the Fourier domain [20].

- The two main correlation approaches both work well for ideal speckle patterns where there is a high density of small, randomly distributed speckles.
- X-ray speckle images are often far from ideal. There can be significant blurring of the speckle pattern, poor contrast between the speckles and the surrounding material, and variable contrast across the image due to the sample geometry or denser regions of material. The speckle pattern is often fairly coarse, with large speckles.
- With such speckle patterns, in which the speckles are large and do not deform with the surrounding material, looking for compacted, rotated or sheared sub-images can introduce errors and is not necessarily appropriate.
- Using a Fourier approach instead produces a computationally fast algorithm, without compromising significantly on the success of the correlation (when there is little contrast variation).
- Unlike the direct spatial correlation approach, all Fourier based DICC algorithms involve normalising large areas of the second image in a single step. They are therefore unable to correct for large variations in contrast.
- The contrast variations found in real DSR experiments are significant enough to cause large correlation errors.
- In penetration experiments on large samples, such as those discussed in Chapter 4, the correlation fails in large areas around the rod due to the brightness of the rod in the images and the effects of the sample geometry and the Gaussian X-ray beam profile.
- A new approach to image normalisation is required if DSR is to prove a useful technique for investigating internal flow in large granular samples.

REFERENCES

References

- [1] Kafri, O. and Glatt, I., *The Physics of Moire Metrology*, Wiley, US (1990)
- [2] White, D.J., Take, W.A. and Bolton, M.D., “Soil deformation measurement using particle image velocimetry (PIV) and photogrammetry”, *Geotechnique*, **53**, **7**, (2003), 619–631
- [3] Williamson, D.M., Palmer, S.J., Proud, W.G. and Govier, R., “Brazilian disc testing of a UK PBX above and below the glass transition temperature”, *Proc. of Shock Com. of Cond. Matter*, **955**, (2007), 803–806
- [4] Grantham, S.G. and Forsberg, F., “Measurement of granular flow in a silo using digital speckle radiography”, *Powder Technology*, **146**, (2004), 56–65
- [5] Zdunek, J., Brynk, T., Pakiela, Z. and Kurzydowski, K.J., “Digital image correlation investigation of Portevin-Le Chatelier effect in aluminum alloy”, *Materials Characterisation*, **59**, (2008), 1429–1433
- [6] Siviour, C.R., Williamson, D.M., Grantham, S.G., Palmer, S.J.P., Proud, W.G. and Field, J.E., “Split Hopkinson bar measurements of PBXs”, *Shock Compression of Condensed Matter*, **1**, (2003), 804–807
- [7] Williamson, D., *DICC Workshop*, Internal report, University of Cambridge (2007)
- [8] Grantham, S.G., Proud, W.G. and Field, J.E., “Digital speckle radiography of explosives”, *12th International Detonation Symposium*, **1**, (2002), 49–54
- [9] Grantham, S.G., Proud, W.G. and Field, J.E., “The study of internal deformation fields in materials using digital speckle radiography”, *25th International Congress on high-speed photography and photonics*, **4948**, (2003), 592–597
- [10] Goldrein, H.T., Grantham, S.G., Proud, W.G. and Field, J.E., “The study of internal deformation fields in granular materials using 3D digital speckle x-ray flash photography”, *Shock Compression of Condensed Matter*, **1**, (2001), 1105–1108

REFERENCES

- [11] Lecompte, D., Smits, A., Bossuyt, S., Sol, H., Vantomme, J., Van Hemelrijck, D. and Habraken, A.M., “Quality assessment of speckle patterns for digital image correlation”, *25th International Congress on high-speed photography and photonics*, **4948**, (2003), 592–597
- [12] Lane, C., Burguete, R.L. and Shterenlikht, A., “An objective criterion for the selection of an optimal DIC pattern and subset size”, *Proceedings of the International Symposium on Optical Metrology in Industrial, Medical and Daily Life Applications*, (2008), 178–186
- [13] Grantham, S.G., *Digital Speckle Radiography*, Phd, University of Cambridge (2002)
- [14] Sjodahl, M., “Electronic speckle photography: increased accuracy by non-integral pixel shifting”, *Applied Optics*, **33**, (1994), 6667–6673
- [15] Sutton, M.A., McNeill, S.R., Helm, J.D. and Chao, Y.J., “Advances in Two-Dimensional and Three-Dimensional Computer Vision”, *Topics in Applied Physics - Photomechanics*, **77/2000**, (2000), 323–372
- [16] Sutton, M.A., Wolters, W.J., Peters, W.H., Ranson, W.F. and McNeill, S.R., “Determination of displacements using an improved digital correlation method”, *Image and vision computing*, **1(3)**, (1983), 133–139
- [17] Sutton, M.A., Wong, A.K. and Chao, Y.J., “Enhanced-displacement measurement using a generalized formulation for double-aperture specklegrams”, *Experimental Mechanics*, **23(3)**, (1983), 348–353
- [18] McNeill, S.R., Sutton, M.A., Miao, Z. and Ma, J., “Measurement of surface profile using digital image correlation”, *Experimental Mechanics*, **23(3)**, (1996), 13–20
- [19] Sutton, M.A., Bruck, H.A. and McNeill, S.R., “Determination of deformations using digital correlation with the Newton-Raphson method for partial differential corrections”, *Experimental Mechanics*, **29**, (1989), 261–268

REFERENCES

- [20] Sjodahl, M. and Benckert, L.R., “Electronic speckle photography: analysis of an algorithm giving the displacement with subpixel accuracy”, *Applied Optics*, **32(13)**, (1993), 2278–2284
- [21] White, D.J., Take, W.A. and Bolton, M.D., “Measuring soil deformation in geotechnical models using digital images and PIV analysis”, *10th Int. Conference on Computer Models and Advances in Geomechanics*, (1999), 997–1002
- [22] Chen, D., Chiang, F.P., Tan, Y.S. and Don, H.S., “Digital speckle-displacement measurement using a complex spectrum method”, *Applied Optics*, **32**, (1993), 1839–1849
- [23] Grantham, S.G. and Proud, W.G., “Digital speckle x-ray flash photography”, *Shock Compression of Condensed Matter*, (2001), 803–806
- [24] Riley, K.F., Hobson, M.P. and Bence, S.J., *Mathematical Methods for Physics and Engineering, Second Edition*, Cambridge University Press, UK (2002)
- [25] Lomax, R.G., *An introduction to statistical concepts*, Routledge, US (2007)
- [26] Cohen, J., *Applied Multiple Regression/correlation Analysis for the Behavioral Sciences*, Lawrence Erlbaum Associates, US (2003)
- [27] Brigham, E.O., *The Fast Fourier Transform and its Applications*, Prentice Hall, US (1988)
- [28] Prentice, H.J., *Development of Stereoscopic Speckle Photography Techniques for Studies of Dynamic Plate Deformation*, Phd, University of Cambridge (2006)
- [29] Chapman, D.J., Proud, W.G., Tsembelis, K. and Collins, A., *Hard Target Research: Final Progress Report*, Internal Report SP 1184, University of Cambridge (2007)

Chapter 3

Producing a New DICC Algorithm

3.1 Algorithm Features

In the previous chapter, it was demonstrated that current Fourier based DICC algorithms [1, 2] are not immediately applicable to DSR experiments, due to the problems associated with variable contrast. For penetration experiments of the type discussed in Chapter 4, large contrast variations are caused by the X-ray beam profile, the cylindrical nature of the samples and the appearance of the rod penetrator. These three factors combined mean that the correlation fails to work correctly for sections of the image, particularly those immediately around the projectile. To make DICC more applicable to DSR, an improved form of normalisation is required to correct for these contrast variations.

Because of the significant time investment required to produce a stable and user-friendly DICC algorithm, most commercial or freely available DICC programs are protected so that the source code cannot be accessed or modified. Such codes are also often programmed with a particular set of experiments in mind and are therefore not necessarily suitable for all applications. For example, a commercial program designed and optimised for the study of an ideal, high density, fine grained speckle pattern would be unsuitable for studying the poor quality speckle patterns obtained during DSR experiments on large samples. Some of these programs are also designed to produce ‘pretty’ strain maps,

3. PRODUCING A NEW DICC ALGORITHM

by using considerable levels of interpolation on the data. It is often hard, or impossible, to adjust these and other parameters.

Some codes have certain limits applied for their intended use. For example, the code by Sjordahl *et al.* [1] was written for low-strain experiments and will only correlate for displacements up to half the size of the sub-image, therefore making it unsuitable for experiments on granular materials, where larger displacements are expected.

To produce a speckle algorithm designed and optimised for DSR experiments on granular materials, it was decided to begin by programming a Fourier based DICC algorithm of the kind discussed in detail in the previous chapter. This provides a known foundation which can then be modified to include features such as a more effective contrast normalisation approach. Without knowing the precise features of other available DICC algorithms, such as any additional normalisation features they may include, it would be difficult to determine how such pre-processing of the images would affect the correlation.

The DICC algorithm written for, and used, in this thesis was programmed in MATLAB R2007a using the Fourier based approach discussed in Chapter 2. The implementation is similar to that discussed by Sjordahl *et al.* [1] and White *et al.* [3]. The reference image is first split into a series of equally sized square sub-images. The size of sub-image is set by the user, and needs to be carefully chosen to be appropriate for the experiment. Particularly, each sub-image must be large enough that it contains a minimum of three speckles, so that it is sufficiently unique within the larger image. The sub-images are arranged in a grid pattern and are set so that their separation is half of their size, causing them to overlap. This arrangement is chosen as it involves sampling the displacement data at half of the bandwidth (the sub-image size). This completely describes the displacement field. Sampling more frequently would generate superfluous data and add to the computing time [4]. This consideration applies only for a continuous displacement field. If the displacement is discontinuous, for example if a crack is present, more frequent sampling may be advisable [4].

For a given sub-image, the algorithm identifies an appropriate search area in the second image. This is done by selecting a section of the second image, centered on the original position of the sub-image, with sides equal in length to

the sub-image size plus twice the maximum expected displacement (this allows for this displacement in all directions). If this chosen search area extends beyond the bounds of the image, the extremes are instead set to be the edges of the image. Using a search area, rather than searching through the entire second image, significantly reduces the number of calculations required. It also leads to fewer errors when dealing with non-ideal speckle patterns. If the sub-image is not very unique within the larger image, due to a small number of speckles or significant blurring of the speckle pattern, the chances of its position being falsely identified are reduced by using a smaller search area. Both the search area and the sub-image are initially normalised in the standard manner by the subtraction of their respective mean values and division by their respective variances. The search area and the sub-image are then both padded with zeros to avoid any wrap-around errors during the correlation process.

The two-dimensional Fourier transforms of the sub-image and search area are generated. These matrices are then multiplied in a point-wise fashion (i.e. multiplication of corresponding elements rather than matrix multiplication). The inverse Fourier transform of the resulting matrix is calculated, and divided by the relevant variances, as discussed in Chapter 2 and described in equations (3.1) and (3.2).

$$r(k, l) = \frac{[X' * Y']}{\sigma_X \sigma_Y}, \quad (3.1)$$

$$= \frac{\mathcal{F}^{-1}(\mathcal{F}(X') \otimes \mathcal{F}(Y'))}{\sigma_X \sigma_Y}, \quad (3.2)$$

where \mathcal{F} represents the 2D Fourier transform, \mathcal{F}^{-1} represents the inverse 2D Fourier transform and X' and Y' represent the sub-image and search area after subtraction of their mean values and zero-padding. The highest correlation value in this correlation matrix gives, to the nearest pixel, the location within the search area where there is the best correlation with the sub-image. Taking into account the original position of the sub-image in image one, and the position of the search area in image two, the displacement of the sub-image between the two images can be determined.

To determine the position of the peak to a sub-pixel accuracy, a small area of the correlation surface around the main peak is extracted. A square area of

3. PRODUCING A NEW DICC ALGORITHM

size (10×10) elements, centred on the point of maximum correlation, is found to be suitably large. Bi-cubic interpolation is then used to determine the position of the peak to a sub-pixel accuracy [3]. The extent of interpolation can easily be altered. For the research in this thesis it is generally set to determine the peak to the nearest 0.02 pixels. Given the errors that are introduced during the scanning process and when correcting for rotation of the images, the real accuracy achieved is likely to be considerably worse than this. Repeating this whole correlation process for each of the sub-images in the reference image allows the displacement map for the whole sample to be generated.

The centre-point of each of the sub-images, (x, y) , is determined, as is the extent of the displacement in the x - and y -directions, (dx, dy) , at each of these points. The displacement data can be plotted as a quiver plot. At each centre point, a vector is drawn with length proportional to the magnitude of the displacement and pointing in the direction the sub-image has moved. Alternatively, the displacements in the x - and y -directions, or the total magnitude of displacement, can be plotted as a filled contour plot. In such a plot, the extent of the displacement at any point can be determined from the colour at that point (see Chapter 4 for examples).

3.2 Contrast Normalisation

Variable contrast in images is a problem that affects many different fields of research, including face recognition technologies [5], scanning of text and images [6] and image registration [7]. A number of techniques have been proposed to correct for uneven illumination and contrast variation. Global variations in contrast between images can be corrected for in some cases using Gamma Intensity Correction [5, 8]. Other techniques, such as Histogram Equalisation and Histogram Matching can be used to normalise the cumulative histogram of grey levels, in the latter case relative to a standard image [9].

These methods mainly correct for global variations in contrast, although they can be applied to sub-sections of images in some cases to deal with smaller scale contrast variations. For example, in region-based gamma intensity correction, the image is split into regions of effectively constant contrast. Regular gamma

intensity correction can then be applied to each of these areas [5]. The problem with these methods is that they often require some reference image or a knowledge of the contrast variation and so they are not appropriate in this situation.

An alternative approach is to apply some form of smoothing or blurring function to the image to determine the underlying variation in contrast across the image, so that it can then be subtracted. One such technique is to apply a Gaussian blur to the image. Mathematically this is equivalent to convolving the image with a Gaussian function. Subtracting the blurred image from the original will remove some of the underlying contrast variation [10].

A potentially more suitable technique for DSR images is the one proposed by Xie *et al.* to correct for uneven illumination in images used for face recognition techniques [11, 12]. This technique aims to normalise an image by subtracting the localised mean and dividing by the localised variance, so that the image is left with a local mean of zero and a local variance of one. This corresponds well to the requirements of an idealised speckle pattern, in which the mean and variance should be constant across the image. For an image $I(x, y)$, the normalised image, $I'(x, y)$, is given by

$$I'(x, y) = \frac{I(x, y) - M(x, y)}{\text{Var}(I(x, y))}, \quad (3.3)$$

where $M(x, y)$ and $\text{Var}(I(x, y))$ are matrices of the ‘local mean’ and ‘local variance’ respectively [11]. The local mean and variance of each pixel are representative values for the pixel intensity and the variance of a chosen number of surrounding pixels.

Xie *et al.* demonstrate that applying this filtering technique to images of human faces which contain varying illumination increases the recognition rate significantly (including the recognition of facial features), provided that a suitably sized averaging window is applied [11]. In their case, the local mean and variance were determined by calculating the mean intensity and the mean variance of a certain number of surrounding pixels, for each pixel in the image. It is not necessarily obvious that taking the mean is the most appropriate way of getting a representative value of the surrounding pixel intensity values and variance. Various possible alternative approaches will be discussed shortly.

3. PRODUCING A NEW DICC ALGORITHM

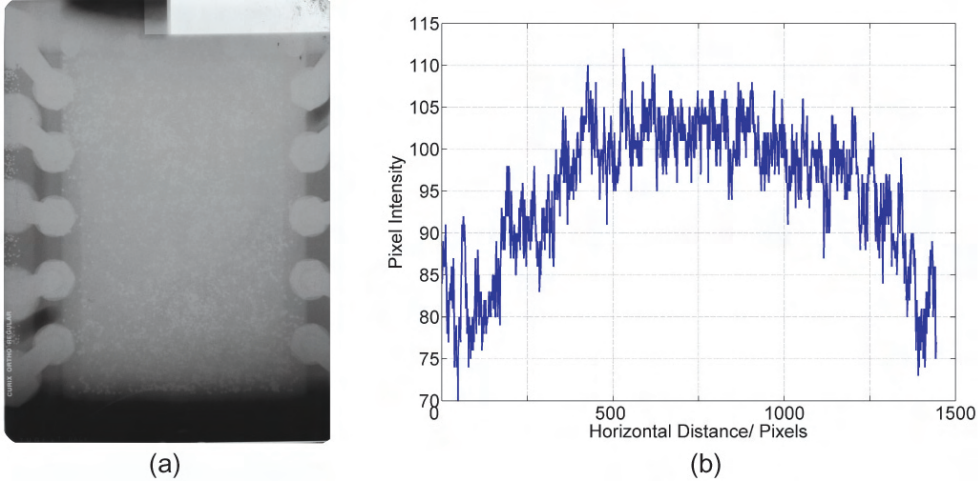


Figure 3.1: (a) An X-ray image of a cylinder of sand containing a seeded lead speckle pattern (b) a 1D slice showing the variation in pixel intensity across the sample for a horizontal line mid-way down the image (ignoring the parts of the image outside of the sample).

An image of a speckle pattern, I , can be considered as a speckle pattern, S , combined with an underlying contrast variation, C , provided by a combination of the surrounding material, the X-ray beam profile and the presence of any regions of high X-ray absorbance, such as metal projectiles or densified regions of material.

$$I(x, y) = S(x, y) + C(x, y). \quad (3.4)$$

This assumes that the speckle pattern component is independent of the contrast variation. Although this is unlikely to be entirely true in the case of DSR, where a varying beam intensity would be expected to cause small variations in the brightness of the speckles in a lead speckle pattern, experimentally the brightness of the lead speckles in the X-ray image is seen to remain relatively constant. To illustrate the kind of contrast variation that is present in DSR experiments, Figure 3.1 shows an X-ray image of a cylindrical sample of sand containing lead speckle, and a horizontal slice showing the considerable variation in pixel intensities across the image.

3.2 Contrast Normalisation

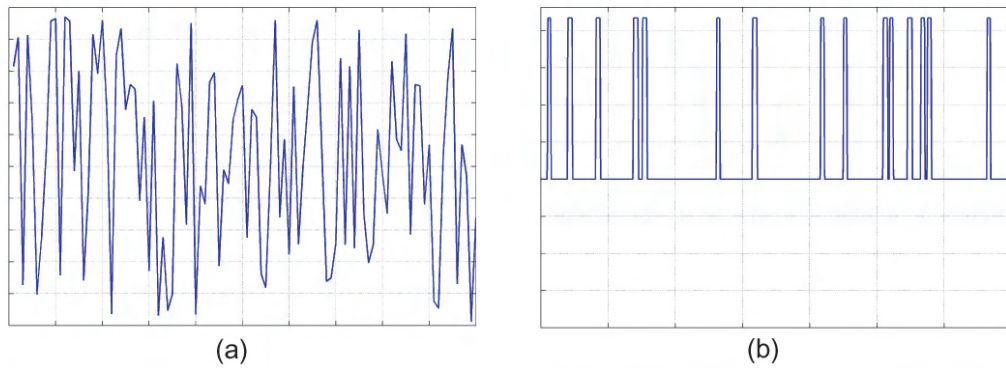


Figure 3.2: (a) A 1D signal consisting of random positive and negative noise. When averaged over a sufficiently large window of elements, the mean is zero. (b) a 1D slice through a random speckle pattern. Rather than random variation around a constant mean of zero, the signal consists of discrete, narrow positive pulses with a non-zero mean.

Any contrast normalisation technique needs to remove the contrast variation component, C , while affecting the speckle pattern component as little as possible. This is a similar problem to that encountered when attempting to remove high frequency or shot noise from a more slowly varying signal, or from an image, except that in this case it is the more slowly varying contrast variations which are to be removed. Therefore, it is possible that smoothing functions designed for noise removal will prove successful in correcting for the underlying contrast variations. The noise analogy is somewhat different however, since the speckle pattern does not consist simply of random positive and negative noise. Instead, as illustrated for a 1D slice in Figure 3.2, a speckle pattern consists of small regions of positive pixel intensity on a background of constant pixel intensity. Methods which cause random noise to be averaged to zero will therefore not necessarily be appropriate for an image of a speckle pattern.

There are a number of possible methods for dealing with noise which may prove useful in correcting for the contrast problems in the X-ray images. The most frequently used methods include window averaging, LOWESS filtering and median filtering [10]. These techniques, and their potential for calculating the

3. PRODUCING A NEW DICC ALGORITHM

representative values for the pixel intensity and variance for use with equation (3.3), are discussed below.

3.2.1 Window Averaging

Window averaging, used by Xie *et al.* to correct for uneven illumination in face recognition images [11], is a widely used technique for removing high frequency noise from a signal. It can be used in one dimension to remove random noise from a line trace, or in two dimensions to remove localised noise from photographic images, in which case the averaging filter is applied sequentially to each of the rows and columns of pixels in the image [10]. When this technique is applied to a signal, any purely random noise will average close to zero, provided a suitably sized averaging window is used, leaving the more slowly varying signal.

The localised mean map is calculated by replacing each pixel in the image with the average value of a certain number of surrounding values, in a procedure summarised by equation (3.5).

$$M(x, y) = \frac{\sum_{x-w}^{x+w} \sum_{y-w}^{y+w} I(x, y)}{w^2}, \quad (3.5)$$

where $M(x, y)$ is the matrix of localised means and w is the side-length of the square averaging window. This matrix is then subtracted from the original image, $I(x, y)$. The size of the window used when performing the averaging can be varied to suit the spatial scale of the contrast variations. It is important to carefully choose the window size when filtering the images in this way. For example, if the window size is too small, information on the speckle pattern itself will be removed. If, on the other hand, the window size is too large, localised areas of brightness, such as the presence of a rod in an X-ray image, may not be properly accounted for.

The variance of a single point in the image is determined by subtracting the localised mean at that point and squaring the result [11, 13],

$$V_1(x, y) = (I(x, y) - M(x, y))^2, \quad (3.6)$$

The local variance map is then determined in exactly the same manner as the local mean map, by replacing the variance of each pixel with the mean value of

3.2 Contrast Normalisation

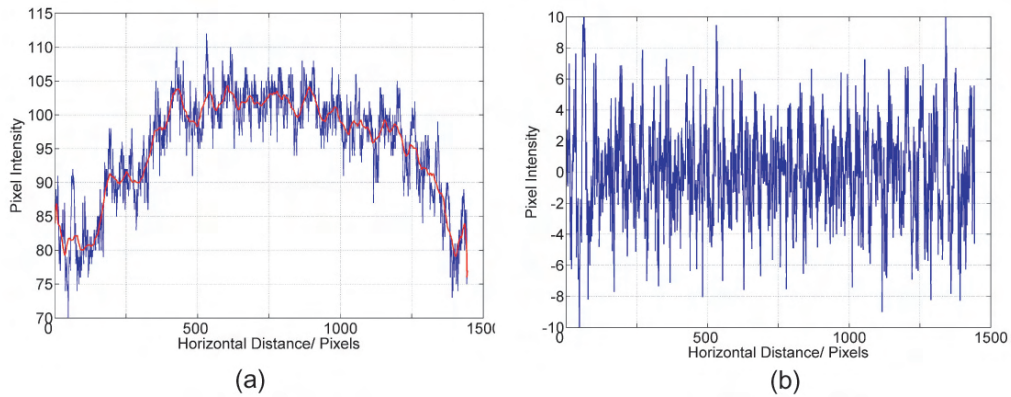


Figure 3.3: (a) The original intensity slice across the image in Figure 3.1 (blue), and the window averaged trace (red). An averaging window of 50 pixels was used. (b) The original trace with the filtered trace subtracted. The global variations in contrast have been removed, but the effect on the speckle component of the image is unknown.

the variance of a surrounding patch of pixels. Once the local mean and variance maps have been determined, the normalised image is produced by subtracting the local mean from the image and dividing by the local variance, as shown in equation (3.3) [11].

The resulting traces when this filtering technique is applied to the signal shown in (b) of Figure 3.1, with an averaging window of (50×50) elements, are shown in Figure 3.3. The resulting signal has a constant average, showing that the method has correctly removed the large scale contrast variation. It is not immediately clear what effect the filtering has had on the speckle pattern component. The intensity of the speckles will likely have been reduced as the averaging process does not remove them entirely. This will be considered in more detail later in this chapter.

3.2.2 LOWESS

Rather than using a window averaging algorithm, locally weighted scatter-plot smoothing (LOWESS) can be used to determine a representative localised intensity and local variance for use with equation (3.3). Using a LOWESS technique,

3. PRODUCING A NEW DICC ALGORITHM

local regression is performed on sub-sections of the data using a weighted linear least squares approach and a first degree polynomial model [14].

For each pixel, a given number of surrounding pixels is extracted. Once again, 1D filtering is applied sequentially to the columns and then the rows to achieve a 2D filtering effect. The problem is then to find the best straight-line fit to this section of the data, $f = \beta_1 + \beta_2 x$, such that the sum, S , of the squared residuals, r_i , is minimised.

$$S = \sum_{i=1}^n r_i^2, \quad (3.7)$$

and

$$r_i = y_i - f(x_i, \beta_1, \beta_2), \quad (3.8)$$

where y_i is the vector of pixel intensity values for the extracted set of pixels and $f(x_i, \beta_1, \beta_2)$ is the calculated intensity for each pixel from a straight-line fit with constants β_1 and β_2 . Once the best straight-line fit for the extracted set of data has been identified, it is used to determine a characteristic pixel intensity value for the original pixel of interest.

The matrix M in equation (3.3) can be determined by applying this technique to the pixels in each row and then each column of $I(x, y)$ sequentially. The matrix $\text{Var}(I(x, y))$ can be determined by doing the same to the matrix of the variance of each pixel, V_1 , given by

$$V_1(x, y) = (I(x, y) - M(x, y))^2. \quad (3.9)$$

The normalised image can then be calculated as before using equation (3.3).

3.2.3 RLOWESS

A more robust version of the LOWESS technique is the robust locally weighted scatter-plot smoothing (RLOWESS) technique. This technique is very similar to the LOWESS technique, but it assigns lower weight to outliers in the regression. Data outside of six mean absolute deviations are assigned a value of zero. This technique has potential as, depending on the relative intensities of the speckle pattern and the background, the speckles may be assigned lower values and therefore will be less influenced by the filtering process.

3.2.4 Median Filter

The previous three techniques discussed are all linear filtering techniques. An alternative non-linear filter is the median filter [10]. Median filtering works by replacing each element of a vector or matrix with the median value of a given number of surrounding elements. It is a technique that has been used successfully to remove ‘salt and pepper’ noise, consisting of randomly occurring white and black pixels, from photographic images [10]. This technique therefore appears well suited for correcting for larger scale contrast variations overlaid on a fine speckle pattern consisting of bright regions of a few pixels in size. However, this technique may struggle to filter out the considerably large speckles often found in DSR images, which can reach 20 pixels or more in size.

3.2.5 Comparison of the Techniques

In this section the success of the four techniques at correcting for the types of contrast problem observed in experimental X-ray images is investigated. However, using real experimental data, it would be difficult to assess what effect the smoothing functions have on the speckle pattern component of the image, S , since the actual background contrast variation (C) and original speckle pattern component (S) would be unknown. To quantitatively assess the performance of the four techniques in correcting for contrast problems in DSR images, it is necessary to test the methods on a simulated image composed of known speckle and background contrast components. The success of the smoothing can then be judged by performing a correlation calculation between the original speckle component and that recovered from the combined image after filtering.

The simulated speckle pattern component, S , was produced by randomly adding white circles (with a diameter of 14 pixels) to a background of pixels with zero intensity (which appear black) to a coverage of around 40%. The resulting speckle pattern is shown in Figure 3.4, although it will subsequently be scaled before adding to the contrast variation component.

To make the contrast variation component, C , representative of those seen in DSR experiments, it was produced experimentally by taking an X-ray image of a cylindrical sample of sand. The resulting image, shown in Figure 3.5, has a similar

3. PRODUCING A NEW DICC ALGORITHM

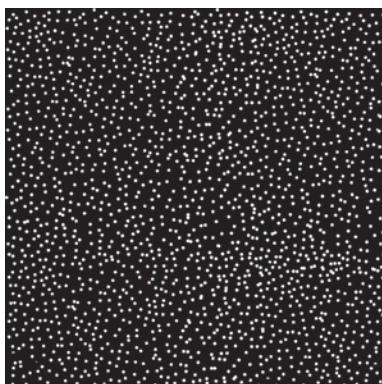


Figure 3.4: A simulated DSR speckle pattern consisting of white speckles (15 pixels in size) on a black background (with a pixel intensity of zero). The speckle pattern has no background contrast variation, and the size and distribution of the speckles is relatively representative of those found in DSR experiments.

contrast variation to that seen in experimental images, and will therefore allow testing of the filtering techniques on the types of image that will be discussed in this thesis. The contrast variation component is added to the speckle pattern component, suitable scaled, to produce the image shown in Figure 3.6. This image compares favourably to the types of images obtained during DSR experiments.

To compare the different filtering methods, each will be applied to the image shown in Figure 3.6 to produce a filtered image. This filtered image will then be correlated, using a Fourier DICC algorithm with no further normalisation, with the speckle pattern component shown in Figure 3.4 (scaled to the same extent as when it was combined with the contrast variation). If the contrast is entirely removed without affecting the speckle component, the correlation value will be one. If the speckle pattern has been distorted the correlation will be lower. Rather than simply correlating the entire images, sub-image tracking will be used to correlate small sub-sections of the speckle pattern in order to produce a matrix of correlation factors. This allows investigation of the success of local filtering of the contrast.

If the speckle image component in Figure 3.4 is correlated directly with the image in Figure 3.6, after scaling, the mean correlation value is 0.497, representing



Figure 3.5: An X-ray image of a cylindrical sample of sand (100 mm in diameter) showing the variations in contrast. This contrast variation will be combined with the speckle pattern in 3.4 to produce an artificial image.

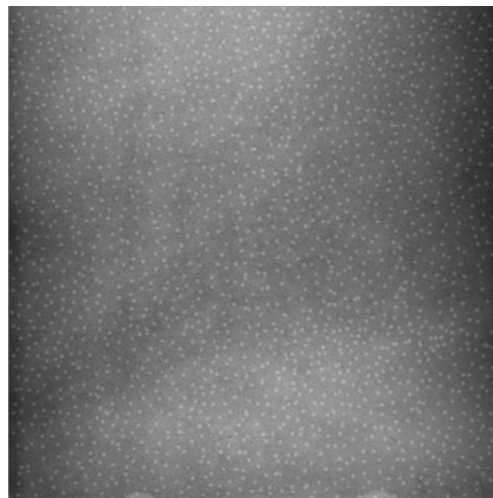


Figure 3.6: A simulated DSR image composed of the computer generated speckle pattern in Figure 3.4, suitably scaled, combined with the experimental image of contrast variation shown in Figure 3.5. The resulting image is similar to the experimental X-ray images of speckle patterns obtained during DSR experiments, but is composed of known speckle and contrast components.

3. PRODUCING A NEW DICC ALGORITHM

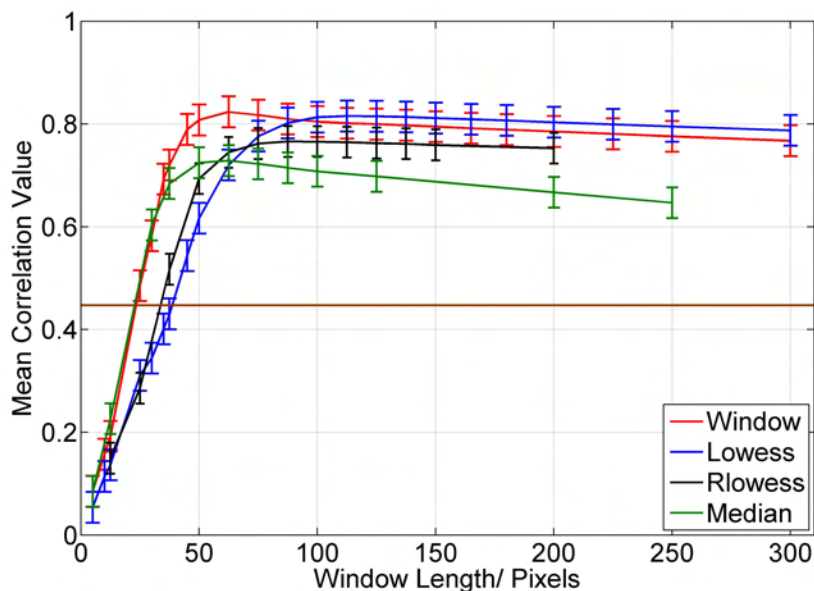


Figure 3.7: Comparing the success of the four filtering methods in removing the contrast variations from the image in Figure 3.6 as a function of the side-length of the filtering window. In each case, the filtered image is correlated with the original speckle pattern. All four methods show significant improvement relative to the value of 0.497 achieved with no filtering of the images (shown in brown) for window sizes of 50 and above. The window averaging approach is the most successful, leading to an 80% increase in the correlation value.

a fairly poor correlation due to the significant contrast variations. For each of the methods, the effect of varying the side length of the window over which the smoothing function is applied will be investigated. In each case a sub-image size of (100×100) pixels and a search area of (300×300) pixels are used. In Figure 3.7, the average correlation factor achieved for the four methods is plotted against the side-length of the windowing function.

All four methods show considerable success in removing the contrast variations and significantly increasing the correlation value. The window averaging technique is the most successful, leading to a correlation value of 0.82 when an averaging window (63×63) pixels in size is applied. This represents an 80% increase in the success of the correlation relative to direct correlation with no

filtering. As expected, with a small filtering window the correlation value is significantly lower, since the speckle component of the image is being significantly reduced. Interestingly, in all three cases, once the peak in correlation value has been passed the decline in the correlation value with window size is very gradual.

The least successful filtering approach is median filtering, where each element of the image is replaced with the median of a certain number of surrounding elements. Although this approach works well at removing ‘salt and pepper’ noise from images [10], it is less successful for the larger scale speckles in the X-ray images, which can reach tens of pixels in size. The LOWESS smoothing approach achieves a similar level of success to the window averaging approach, although the peak correlation value is smaller and occurs at a higher window size. However, the LOWESS technique is computationally intensive and takes up to 60 times longer than the window averaging approach.

Based on run-time considerations and the results shown in Figure 3.7, window averaging was chosen for the DICCC algorithm written for this thesis. Filtering an image (2000×2000) pixels takes roughly 15 s on a standard desktop computer (1.8 GHz Intel Dual Core T2350 Processor - 533 MHz bus speed, 2 MB L2 cache, and 1 GB of RAM). This technique can also be adjusted to a range of different scales of contrast variation by adjusting the range over which the local mean and variance are calculated.

For elements less than than half the window size from the edge of the matrix, the window size is reduced to the distance of the element from the edge of the matrix, so that pixels on the very edge of the image remain unchanged. This inadequate normalisation near the image boundaries can introduce some problems, and generally it is preferable to use an image greater in size than the area of interest so that the edges can be ignored after normalisation.

The improvement in the correlation values can be understood in more detail by studying the effect of the filtering on the images and on the subsequent correlation surfaces. Figure 3.8 shows the correlation surface produced by correlating a sub-image from the centre of the simulated speckle pattern component shown in Figure 3.4 with a search area in the centre of the unfiltered simulated image in Figure 3.6. The maximum correlation value of 0.37 is low, showing that there is relatively poor correlation. It is also important to consider the ratio of the height

3. PRODUCING A NEW DICC ALGORITHM

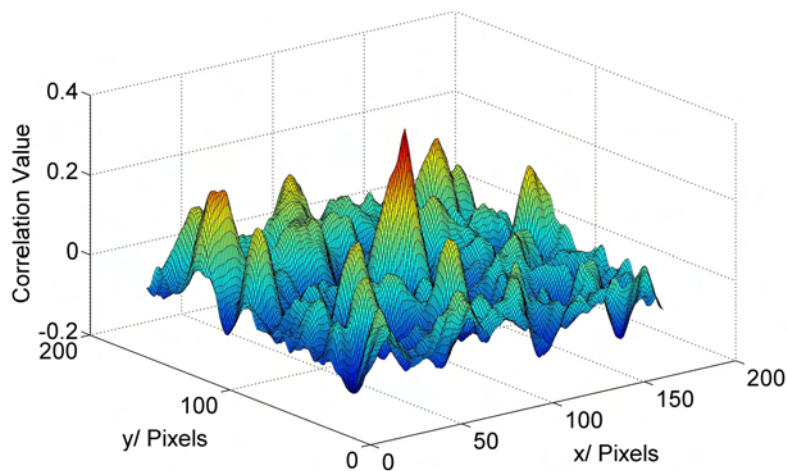


Figure 3.8: The correlation matrix obtained when correlating a sub-image from the centre of Figure 3.4 with a search area in the centre of Figure 3.6 with no filtering of the images. The peak correlation value of 0.37 is low, as is the peak to noise ratio of 1.5.

of the main peak to the height of the surrounding peaks, as this tells us how well the sub-image has been differentiated from the surrounding speckle pattern. In this case the ratio is 1.5, which shows that it is relatively difficult to tell the sub-image apart from the surrounding speckle pattern.

Figure 3.9 shows, from the top to the bottom, three images showing the effect of filtering the simulated image in Figure 3.6 with averaging windows of size (27×27) , (63×63) and (301×301) pixels using the window averaging technique and equation 3.3. The correlation surface achieved by correlating the same sub-image as in Figure 3.8 with the filtered images is shown to the right of each filtered image.

Figure 3.9 shows that using a small window size removes a large amount of information about the speckle pattern and leads to a very low correlation value, although note that the ratio of the peak to the surrounding noise is 1.9 which is actually a slight improvement on the original value. With a window of size (63×63) pixels the filtered image bears a strong resemblance to the original

speckle pattern shown in Figure 3.4. The location of the speckles is clearly visible and the contrast is approximately constant across the image. These factors contribute to a significantly higher peak correlation value. The ratio of the peak to the surrounding noise is also increased to a factor of 2.15, showing that the sub-image is more successfully located. Increasing the window size further leads to a more patchy appearance of contrast variation, and parts of the speckle pattern become less clear. This is because a large averaging window averages out the small scale contrast variations, meaning that they are not subsequently removed when the mean matrix is subtracted from the original image. These factors lead to a marginally lower correlation value of 2.04 and a reduced peak to noise ratio of 1.8. These images, and the plots in Figure 3.7, show that using an averaging window (63×63) pixels in size is optimal for this speckle pattern and sub-image size, but that window sizes much larger than this would also give adequate correlation.

Extrapolating this information to other sub-image sizes and other similar speckle patterns, it can be suggested that a window size of at least two thirds the sub-image size is required to provide a suitable level of filtering. The plots in Figure 3.7 suggest that larger window sizes of up to twice the sub-image size continue to provide acceptable levels of filtering.

It is also necessary to confirm that the window average filtering approach can deal with the effects of a more localised high intensity region, such as that caused by the presence of a metal projectile or an area of higher density. Figure 3.10 shows the previous artificial speckle image shown in Figure 3.6 with a brighter region added to represent the presence of a projectile.

Figure 3.11 shows a quiver plot of the displacement data calculated when correlating the images in Figures 3.4 and 3.10 using the standard Fourier based normalisation approach discussed in Chapter 2. There is no displacement between the two images so the displacements should all be zero, apart from the small area covered by the rod where spurious values will be given as the speckle pattern is obscured. Instead, Figure 3.11 shows that a large area of the speckle pattern around the rod has failed to correlate correctly. A large number of sub-images have been mis-identified as moving inwards towards the position of the rod. These spurious displacements are due to the higher correlation values obtained when correlating with a region of the image that contains the rod. The

3. PRODUCING A NEW DICC ALGORITHM

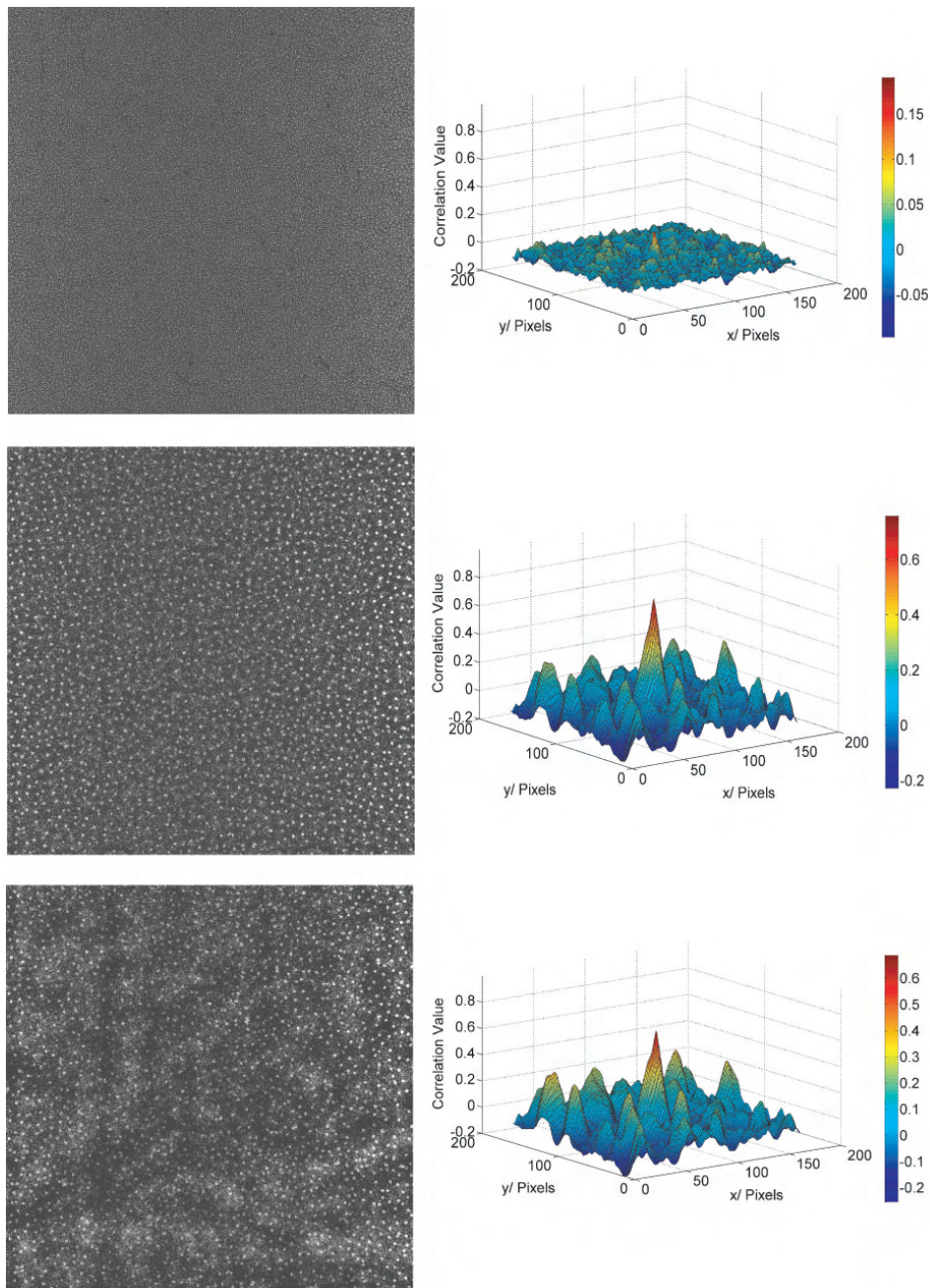


Figure 3.9: The image in Figure 3.6 filtered with averaging windows of (27×27) , (63×63) and (301×301) pixels and the corresponding correlation surface for a sub-image in the centre of the image

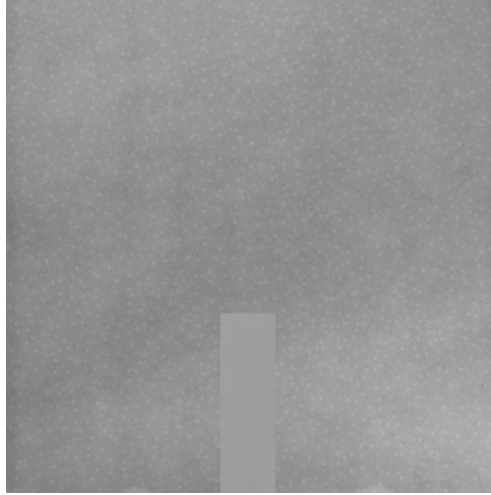


Figure 3.10: The artificial speckle image shown in Figure 3.6 with a bright region added to represent a metal projectile (or it could equally represent a densified region).

standard approach of subtracting the mean from the search area fails to correct for this localised bright spot.

When a (63×63) pixel window averaging filter is applied to the image in Figure 3.10, the image shown in Figure 3.12 results. The majority of the brightness of the rod has been removed during the filtering process, leaving an area with close to zero pixel intensity. Only the edges of the rod are still visible as white lines with a similar intensity to the surrounding speckles. If this filtered image is correlated with the speckle pattern in Figure 3.4, the displacements shown in Figure 3.13 are calculated. Once again the sub-images have not moved so all the recorded displacements should be zero.

Comparing the calculated displacements displayed in Figures 3.13 and 3.11, we see that filtering the image has increased the success of the correlation. When performing correlation with the filtered image, only sub-images from the first image that overlap the position of the rod in the second image fail to correlate. This is because the speckle pattern in this region of the second image is obscured by the rod, meaning a match for the original sub-image no longer exists. False correlation of the sub-images around the rod, leading to spurious inwards dis-

3. PRODUCING A NEW DICC ALGORITHM

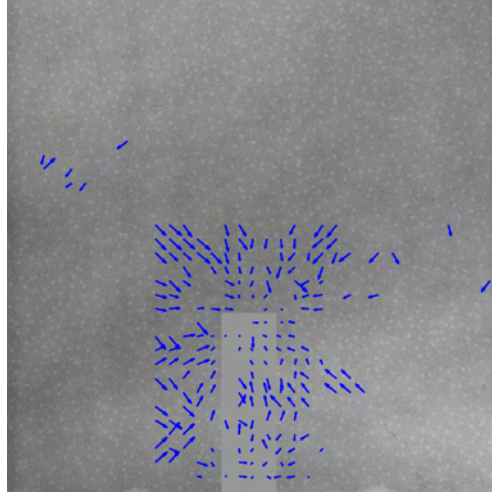


Figure 3.11: A quiver plot showing the displacements calculated when correlating the images in Figures 3.10 and 3.4 with no pre-normalisation applied to the images. The displacements should be zero as the images are the same apart from the bright region. Instead we see that a large area around the bright region has incorrectly been identified as moving inwards towards it.

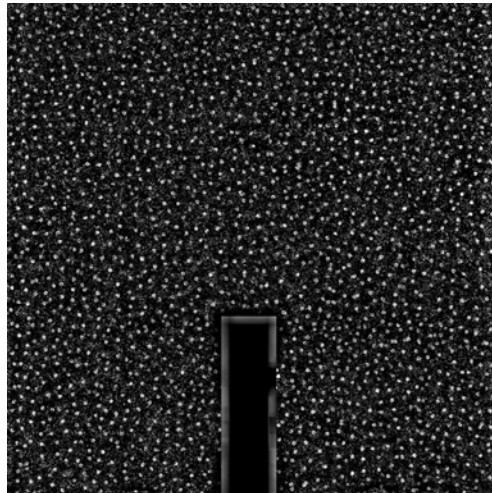


Figure 3.12: The image shown in Figure 3.10 after applying a (63×63) pixel window averaging filter. The brightness of the rod has been almost entirely removed, leaving only a bright outline.

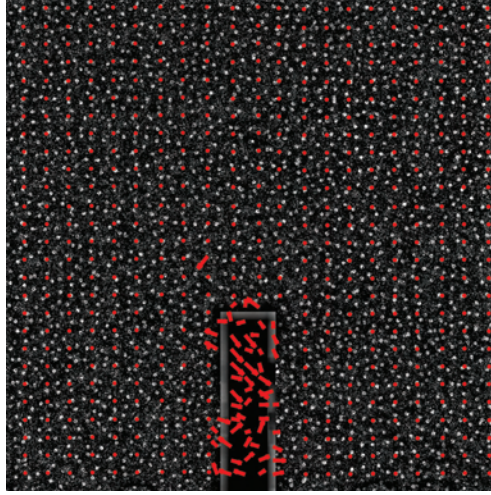


Figure 3.13: A quiver plot showing the displacements calculated when correlating the images in Figures 3.12 and 3.4. The correlation has been much more successful with the normalised image. Only sub-images which directly overlap the area of speckle pattern obscured by the projectile have failed to correlate correctly. The other sub-images have been correctly identified as having not moved (zero displacement - shown as circles).

placements, has been drastically reduced. This is due to the intensity of the rod being significantly reduced in the filtered image.

The filtering process, in particular the effect of the filtering on the higher frequency speckle component of the images, can be understood in more detail by considering the effect of the filter on different frequency components of the image. A moving average filter is a finite impulse response filter (FIR), meaning that the filter's response to a Kronecker delta function input falls to zero in a finite number of sample intervals [15].

A general FIR filter has the following form:

$$y[n] = \sum_{a=0}^N b_a x[n-a], \quad (3.10)$$

where $y(n)$ is the filter output, b_a are constants and $x(n)$ is the input vector. The filter output is a weighted sum of the current value and a certain finite number of

3. PRODUCING A NEW DICC ALGORITHM

preceding elements. The impulse response of the filter, $h[n]$, the response of the filter to a single frequency impulse - a Kronecker delta function, can be calculated as:

$$h[n] = \sum_{a=0}^N b_a \delta[n-a], \quad (3.11)$$

$$= b_n. \quad (3.12)$$

In Fourier space, the frequency response, $H(\omega)$, is

$$H(\omega) = \sum_{-\infty}^{\infty} h[n] e^{-i\omega n}, \quad (3.13)$$

where ω is the frequency. For a square moving average filter with a window length of L , the impulse response is

$$h[n] = \frac{1}{L}, \text{ for } n = 0, 1, \dots, L-1, \quad (3.14)$$

$$h[n] = 0, \text{ otherwise.} \quad (3.15)$$

Therefore the frequency response in Fourier space simplifies to

$$H(\omega) = \frac{1}{L} \sum_{n=0}^{L-1} e^{-i\omega n}. \quad (3.16)$$

Using the formula for the sum, s , of a geometric series in terms of a variable r ,

$$s = \sum_{n=0}^{L-1} r^n = \frac{1-r^L}{1-r}, \quad (3.17)$$

we can write the frequency response of the filter as

$$H(\omega) = \frac{1}{L} \frac{1-e^{-i\omega L}}{1-e^{-i\omega}}. \quad (3.18)$$

Figure 3.14 shows the effect on the frequency response of the window averaging filter of varying the window side-length, calculated using equation (3.18). The plots show that the frequency response shares some characteristics with a low-pass filter, in that a constant component (zero frequency) passes through the filter unattenuated while higher frequency components are more heavily attenuated.

For all averaging window sizes, certain frequencies are eliminated entirely by the filtering process. Unlike an ideal low-pass filter however, higher frequency components are passed with varying amounts of attenuation by the filter. With a filtering window of (10×10) elements, up to 20% of the amplitude of the higher frequency components is passed. This explains why with a small size of averaging window significant information is removed from the speckle component of the image, which contains significant high frequency components.

For larger window sizes there is considerably more attenuation of the amplitude at higher frequencies. The high frequency response of the filter with window sizes of (63×63) elements and (125×125) elements is very similar. In both cases, the high frequency components are attenuated to a few percent of their original amplitude. This similarity in the high frequency behaviour explains the slow drop off in correlation success with window sizes above (80×80) pixels, observed in the plots in Figure 3.7. Above a window size of around (80×80) pixels, increasing the window size further makes little difference to the extent of filtering of the high frequency components, where most of the information about the speckle pattern component, S , is contained.

3.2.6 Spatial DICC

We have concentrated thus far on the effect of the image filtering on the correlation values determined using the Fourier based DICC algorithm written for this thesis. As discussed in Chapter 2, there is a second major group of DICC algorithms that involve performing the correlation in the spatial domain and which can consider factors such as compaction, shearing and rotation of the sub-image. To assess the applicability of the window average filtering technique to this second class of DICC algorithm, the effect of the window average filtering process on the direct spatial correlation values was investigated using equation (3.19), which was discussed in Chapter 2.

$$r_{X,Y} = \sum_{x=0}^m \sum_{y=0}^n \left[\frac{X - \bar{X}}{\sigma_X} \frac{Y - \bar{Y}}{\sigma_Y} \right], \quad (3.19)$$

where X is the matrix of pixel intensities for the sub-image and Y is the matrix of pixel intensities of a section of the search area of equal size. This equation is

3. PRODUCING A NEW DICC ALGORITHM

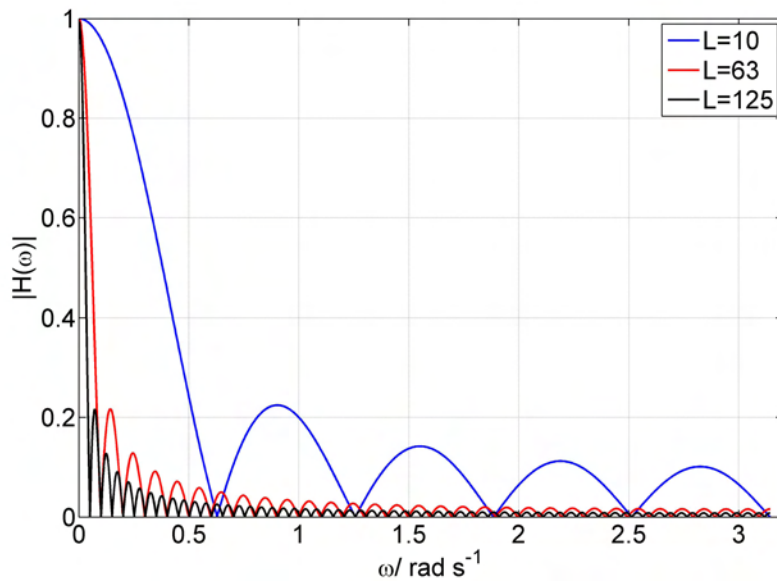


Figure 3.14: The frequency response of the window averaging process for three different window sizes. All three cases resemble a low-pass filter to some extent, as the higher frequency components are significantly attenuated. With a window size of (10×10) (blue), significant high frequency components are passed, meaning that considerable information will be removed from the speckle component. With larger window sizes the higher frequency components are more significantly attenuated.

applied to every possible section Y of the search area to build up a correlation matrix. As before, the speckle pattern in Figure 3.4 and the combined speckle and contrast image in Figure 3.6 were correlated. Rather than directly correlating the two images, sub-image tracking was again used to build up a matrix of correlation values for a series of sub-images in the first image, so that an average value could be calculated.

Figure 3.15 shows the effect on the direct spatial correlation value (similar to the approach used by Sutton) of applying a window averaging filter to the image in Figure 3.6, for a range of different window sizes. When the images in Figures 3.4 and Figure 3.6 are correlated directly using a spatial algorithm the mean correlation value is 0.66, considerably higher than with the Fourier technique, but substantially less than the peak of 0.82 achieved with the Fourier technique and the filtered image. The peak to noise ratio for this correlation, for the same sub-image as in the Fourier case, is 1.55, again higher than for the standard Fourier technique. Figure 3.15 demonstrates that the filtering approach used in this thesis is equally applicable to spatial correlation algorithms, such as that developed by Sutton [16]. The correlation value increases from 0.66 to a peak of 0.84 with a window size of 63 pixels. This represents an increase in the success of the correlation of 30%.

The improvement in the correlation values can be seen in the two contour plots shown in Figure 3.15, where a sub-image from Figure 3.4 (the same as with the Fourier technique discussed previously) is correlated with a search area in Figure 3.6. The left plot shows the correlation matrix with no filtering applied to the images. The right plot shows the same correlation when an averaging window of size (63×63) pixels is used on the combined simulated image in Figure 3.4. The intensity of the central peak has noticeably increased in the right plot and the relative intensity of the surrounding peaks has been reduced. The peak to noise ratio has been increased to 2.05, representing a significant increase in the identifiability of the sub-image relative to the surrounding speckle pattern. Despite the slightly higher correlation value, this peak to noise ratio is actually slightly lower than the value of 2.15 obtained with the Fourier technique for the same extent of filtering.

3. PRODUCING A NEW DICC ALGORITHM

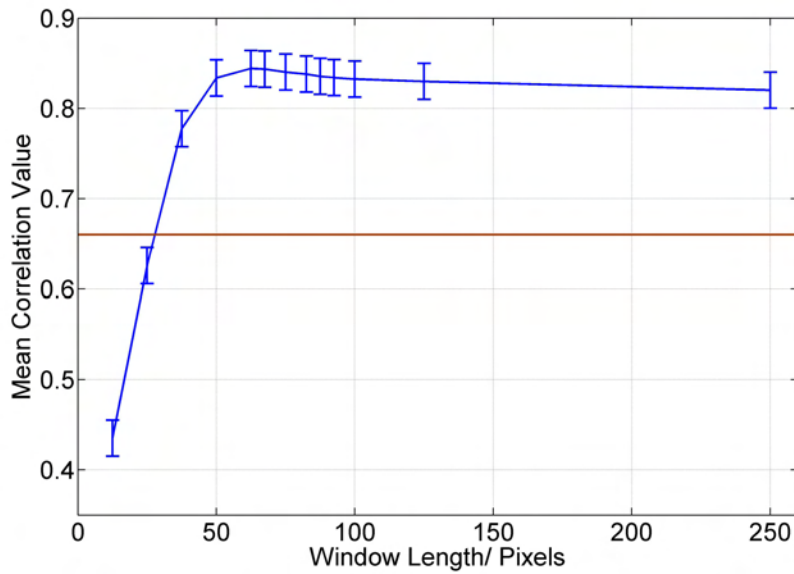


Figure 3.15: The effect of the side length of the square averaging window used in the image filtering on the correlation value when performing the correlation process in the spatial domain rather than the Fourier domain (blue line). The correlation value of 0.66 with no filtering applied to the images is shown in brown. An improvement of 27% in the correlation value is achieved. This demonstrates that the image filtering is equally applicable to the Sutton DICC approach when dealing with less than ideal speckle patterns.

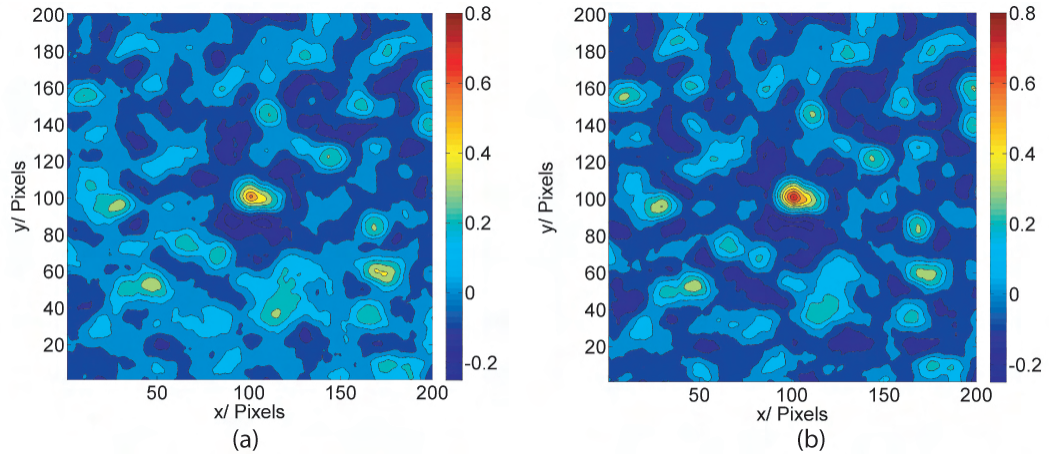


Figure 3.16: Contour plots showing the correlation matrices obtained when correlating, in the spatial domain, a sub-image in the centre of Figure 3.4 with (a) a search area in the centre of Figure 3.6 (b) the same search area after the image has been normalised with an averaging window with a size of (63×63) pixels. In (b) the correlation peak is larger (by 27%) and the peak to noise ratio is greater (by 38%).

It is clear therefore that the filtering approach used in this thesis is equally applicable to the spatial correlation approach used by Sutton and others. Such an approach will prove useful when using any DICCC program on non-ideal speckle patterns that contain significant variations in contrast. It is clear also that, for this sub-image at least, the Fourier based approach with this normalisation procedure correlates to a similar or better extent than the spatial correlation approach with the same normalised images. As previously discussed the Fourier approach also has the advantage of being computationally faster and more straight-forward to implement.

3.2.7 Previous Example

Let us briefly return to the example we discussed earlier in Chapter 2, involving the search area repeated here in Figure 3.17 and a sub-image which is identical to the right square section of this image. We saw that when this image and

3. PRODUCING A NEW DICC ALGORITHM

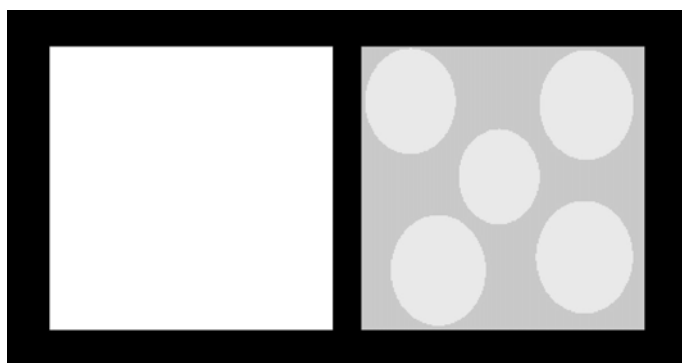


Figure 3.17: Two small square images on a background of zero pixel intensity. The right square represents a section of speckle pattern from an X-ray image. The left square represents a localised bright area in an X-ray image. The overall image represents a search area that contains large variations in contrast

the sub-image were correlated in Fourier space with the standard normalisation applied, namely subtraction of the mean values from the sub-image and search area, the position of the sub-image was incorrectly identified. If we now apply a window averaging filter (24×24) pixels in size to the search area and sub-image and perform the correlation in Fourier space, the correlation matrix displayed in Figure 3.18 results.

The surface plot shows a peak at (71,291), correctly identifying the position of the sub-image in the search area. The main peak is very sharp with little surrounding noise and the peak-to-noise ratio is 6.3. This demonstrates a very significant improvement on the standard Fourier correlation result, which is repeated here in Figure 3.19, for which the location of the sub-image was incorrectly identified.

The correlation now compares very favourably with the spatial correlation result, the plot of which is repeated here in Figure 3.20. Although the correlation value is slightly reduced, the peak to noise ratio is again slightly better in the Fourier case, suggesting that the sub-image is easier to differentiate from the surrounding speckle pattern.

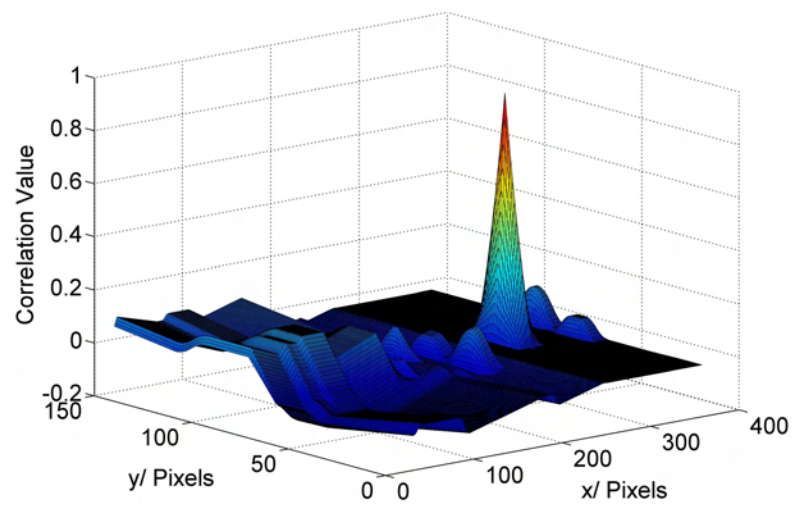


Figure 3.18: The correlation matrix obtained when the two images in Figures 2.11 and 2.10 are correlated in the Fourier domain after being normalised with an averaging window (24×24) pixels in size. The location has been correctly identified, which the standard Fourier DICCC algorithm was able to do. The peak size and peak to noise ratio (6.3) compare very favourably with the direct spatial correlation results shown previously in Figure 2.12.

3. PRODUCING A NEW DICC ALGORITHM

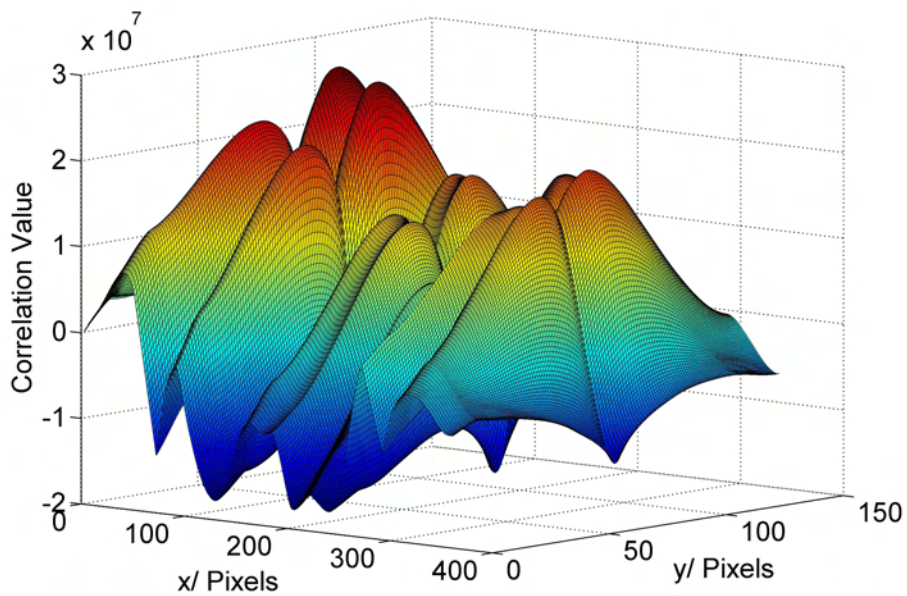


Figure 3.19: A surface plot of the correlation matrix obtained when correlating the sub-image in Figure 2.11 with the search area shown in Figure 2.10, in the Fourier domain (using equation (2.14)). With the basic normalisation included, there is a larger correlation value at the correct position of (71,291). However, the largest correlation value incorrectly identifies the position of the sub-image.

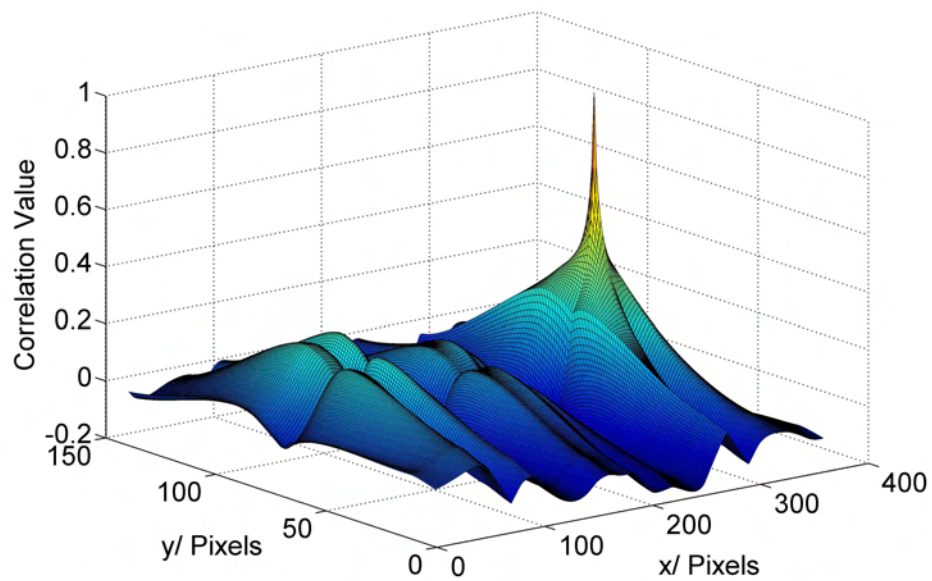


Figure 3.20: A surface plot of the correlation matrix obtained when correlating the sub-image in Figure 2.11 with the search area shown in Figure 2.10, in the spatial domain. The x - and y -axes correspond to the position of the upper left corner of the sub-image relative to the upper left corner of the search area for a given correlation step. The position of the sub-image has been correctly identified as (71,291) pixels.

3. PRODUCING A NEW DICC ALGORITHM

3.2.8 Experimental Images

We will now return to the experimental X-ray images in Figure 2.8 of Chapter 2, showing the penetration of a cylinder of sand by a rod projectile, repeated here in Figure 3.21. It was the correlation problems associated with the variation in contrast in these images that prompted the above investigation of image filtering techniques. In (c) of Figure 3.21, we see that the presence of the bright projectile, coupled with the effects of the sample geometry and X-ray beam profile, leads to spurious inwards displacements that obscure the areas of main interest - those directly around the projectile, showing the interaction with the surrounding material.

If we now apply equation (3.3) using the window averaging filter algorithm discussed above to these images, with an averaging window of (100×100) elements, the normalised images shown in (a) and (b) of Figure 3.22 result. The contrast across the images has been successfully normalised, so that the resulting speckle pattern has a uniform mean contrast and is clearly visible. The relative intensity of the rod in the second image has been significantly reduced. The resulting correlation of these normalised images, performed using the DICC algorithm described in this chapter, with a sub-image size of (100×100) pixels, is shown in the quiver plot in (c) of Figure 3.22. With the normalised images the correlation has been much more successful. There is still a narrow region around the projectile for which the correlation has failed, caused by the destruction of the sub-images in this location. However, this region is substantially smaller than the area of failed correlation in Figure 3.21, and none of the surrounding areas have incorrectly correlated inwards towards the rod. This demonstrates that using the normalisation approach included in the algorithm written for this thesis dramatically improves the success of the correlation. Considerably more displacement data are provided about the areas of main interest.

We can also see the success of the image normalisation process in correcting for densified material by applying it to the earlier plate impact facility [17] experimental X-ray images, one of which is shown in (a) of Figure 3.23. In the normalised image, shown in (b), we can see that the higher intensity of the densified material behind the compaction wave has been reduced so that the whole

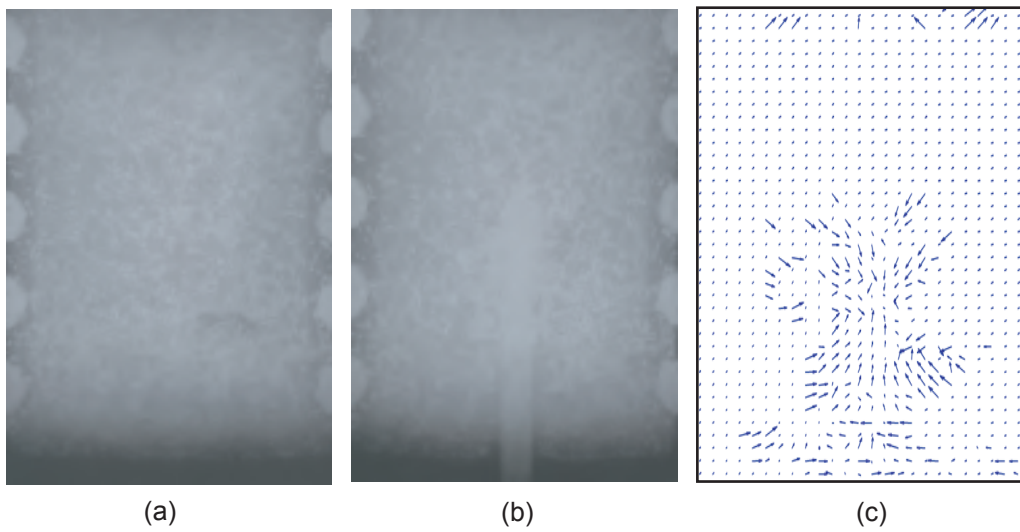


Figure 3.21: Image (a) is a reference X-ray image showing the speckle pattern. Image (b) is a dynamic X-ray image showing the penetration of the sample by a long rod. In image (c) the displacement field within the sample is shown, calculated using a sub-image size of (100×100) pixels and a search area of (300×300) pixels. The correlation algorithm of White *et al.* [3] has given spurious inwards displacements for large areas of material surrounding the projectile. This is thought to be due to the relative high intensity of the projectile on the X-ray image compared with the surrounding material.

3. PRODUCING A NEW DICC ALGORITHM

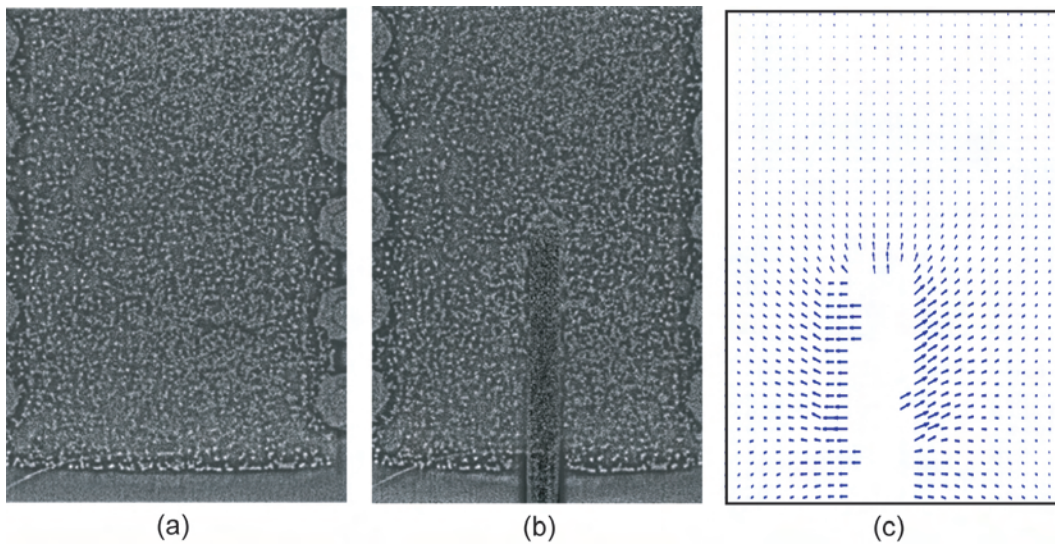


Figure 3.22: (a) The lead speckle pattern (reference image) shown in Figure 3.21, after being normalised by removal of the local mean and division by the local variance using equation (3.3) and a window averaging approach. The resulting image has a uniform mean contrast. (b) Normalised image of sample during rod penetration (dynamic image), the intensity of the rod has been significantly reduced. (c) Quiver plot of displacements calculated using the optimised DICC algorithm. Comparison with Figure 3.21 demonstrates the improved correlation.

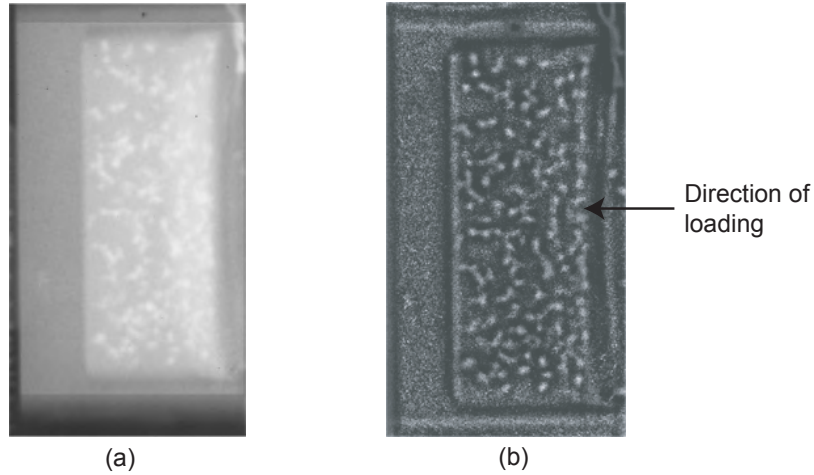


Figure 3.23: (a) Original X-ray image taken during a plate impact experiment on a sand sample. (b) The normalised image. The change in contrast behind the compaction wave has been successfully corrected for.

sample now has a uniform background intensity.

3.3 Tracking Deformed Sub-Images

To confirm the assumption that, provided suitably small sub-images are chosen, the global displacement can be considered as a series of rigid body translations, compaction of the sub-images was considered. The rigid body approach begins to fail when the strain reaches roughly 10%, although this depends to some extent on the characteristics of the speckle pattern.

To account for simple compaction, in which the global compaction can be split into two perpendicular scaling factors, the algorithm was modified to include tracking of deformed sub-images (this adds significantly to the computing time). To simulate the deformation of a given sub-image, bi-cubic interpolation is used. Consider the image of a cross shown in Figure 3.24. This image is (90×90) pixels. If we scale this image by factors of 0.5 vertically and 0.8 horizontally, the resulting image is (45×72) pixels. Bi-cubic interpolation is used to determine the pixel intensities in the matrix with the reduced dimensions. Figure 3.24 (b)

3. PRODUCING A NEW DICC ALGORITHM

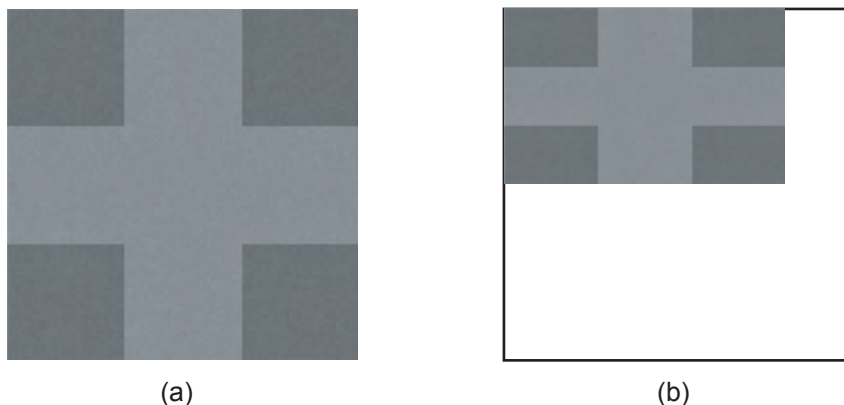


Figure 3.24: (a) A (90×90) image of a cross shape. (b) The same image scaled by a factor of 0.8 horizontally and 0.5 vertically. The pixel intensities in the scaled matrix are determined using bi-cubic interpolation.

shows an image of the cross with this deformation process applied.

When searching for a particular sub-image in a deformed image, the extent of the compaction is unlikely to be known. It is therefore necessary to try a series of different levels of compaction of the sub-image, correlate these different sub-images independently and determine which set of deformations produces the highest correlation factor. Each iteration adds to the overall computational time of the algorithm. Fairly coarse steps in the scaling factors can be used, as an image compacted by a factor of 0.85 will correlate successfully with the same image compacted by factors of 0.8 or 0.9.

If this modified algorithm is applied to X-ray images from a dynamic penetration experiment of the type shown in Figure 3.22, there is little change in the success of the correlation with a sub-image size of (100×100) . A few more sub-images directly ahead of the rod correlate successfully, but a few more errors are generated elsewhere in the correlation matrix. Contour plots of the extent of compaction in the longitudinal (parallel to the rod) and lateral directions are shown in (a) and (b) of Figure 3.25 respectively.

These diagrams show that the majority of the compaction is occurring around the projectile tip, and ahead of it, but that the extent of the compaction is small, with most of the material being compacted by a factor of 0.9 (shown as nine in

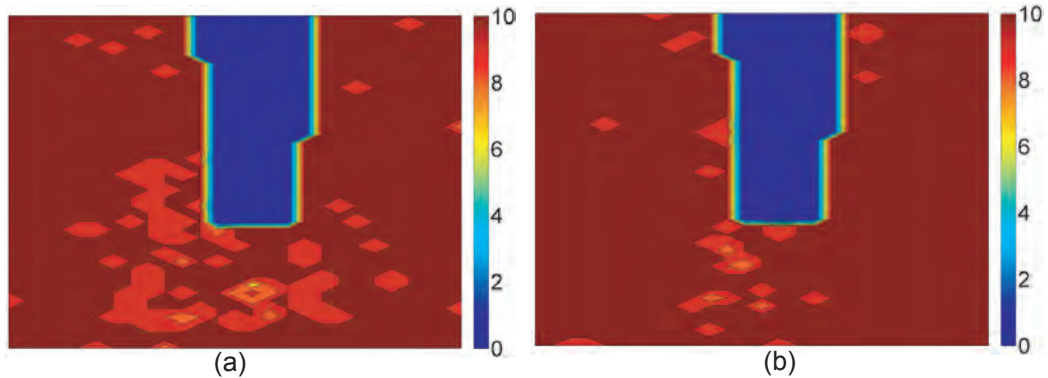


Figure 3.25: Contour plots showing the extent of compaction occurring during a penetration experiment of the type discussed in Chapter 4. The sub-image size is (7×7) mm. The longitudinal compaction (parallel to the rod) is shown in (a). The Lateral compaction is shown in (b). The colour bar represents the scale factor multiplied by ten. Most of the material is not being compacted on the scale of the sub-images.

the figure) at the most. This demonstrates that on the chosen size of the sub-images, (100×100) pixels, which corresponds to approximately (7×7) mm, the material is relatively incompressible.

These results confirm the applicability of the approach taken in the DICC algorithm written for this thesis. They show that the approximation that the material flow in penetration experiments can be represented by a series of rigid body translations of sub-images is appropriate for the chosen size of sub-images. Such an approach does not significantly impact the success of the correlation relative to other approaches. The correlation has only failed in the severely distorted region immediately around the rod, where all DICC algorithms would struggle.

3.4 Testing of the DICC Algorithm

Before using the DICC algorithm to analyse experimental displacements, it is important to investigate the accuracy with which the algorithm can determine

3. PRODUCING A NEW DICC ALGORITHM

displacements. It is also essential to investigate whether the window averaging contrast normalisation approach used in the algorithm affects the accuracy of the measured displacements. The accuracy of the algorithm will depend on a number of factors relating to the speckle pattern. In particular, the speckle size and the contrast of the images, taking into account effects like blurring, will have an effect. For a given speckle pattern, the chosen size of sub-image to be tracked and also potentially the size of the search area, will also influence the accuracy of the results. The size of the search area becomes important for non-ideal speckle patterns in which the pattern is not sufficiently random. In such a situation, various areas of the speckle pattern may resemble the sub-image that is being located, and there will no longer be a single sharp correlation peak.

The accuracy of Fourier based DICC algorithms when applied to perfectly random and sharp computer generated speckle patterns has been discussed in detail in the literature [1, 18]. Sjodahl and Benckert determined an empirical relationship between the standard deviation in a set of measurements, e , and speckle pattern parameters such as the speckle size σ , the sub-image size n , in pixels, and a ‘speckle decorrelation’ term δ ($0 \leq \delta \leq 1$) [1].

$$e \approx \frac{0.66\sigma}{n(1-\delta)^2}. \quad (3.20)$$

The speckle decorrelation factor represents deformation of the object surface and effects such as detector noise. This equation suggests that small speckles lead to smaller errors (all speckle points must be finite so the error is never zero) and that larger sub-images lead to more accurate displacement measurements. Such empirical equations are derived by investigating computer generated speckle patterns that are random and contain small speckles. Their applicability to the types of speckle pattern generated during DSR experiments, which contain large speckles and problems such as poor contrast and blurring, is not immediately obvious.

To determine the accuracy of the DICC algorithm written for this thesis when applied to DSR speckle images, it is more appropriate to test the algorithm on actual experimental speckle images rather than computer generated images.

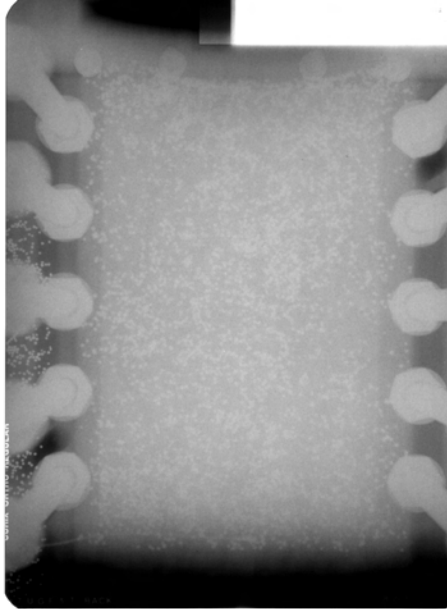


Figure 3.26: An X-ray image of a layer of randomly scattered lead shot (1 mm diameter) within a cylindrical sample of sand (100 mm diameter). The contrast has been artificially adjusted to make the speckle pattern more visible.

As an initial test of the algorithm, an X-ray image of a lead speckle pattern within a cylindrical sample of sand, shown in Figure 3.26, was produced. It can immediately be seen that this speckle pattern is non-ideal as the speckle size is large and the distribution of particles is not entirely random, since there is variation in the spatial density of speckles in the pattern.

The accuracy of the speckle algorithm when dealing with integer pixel displacements was investigated by shifting the image shown in Figure 3.26 by a chosen number of pixels in the x - and y -directions using Adobe Photoshop 7.0 and correlating it with the original to determine the displacement. Three different sub-image sizes were used, (100×100) , (60×60) and (40×40) pixels. Displacements of up to 200 pixels in a given direction were generated, giving a maximum total displacement of 250 pixels. In all cases the algorithm correctly determined the displacement. The error in measuring a single component of the displacement was 0.005 pixels in each case. This is set by the extent of interpolation used in the area around the peak in the correlation surface when determining the location of

3. PRODUCING A NEW DICC ALGORITHM

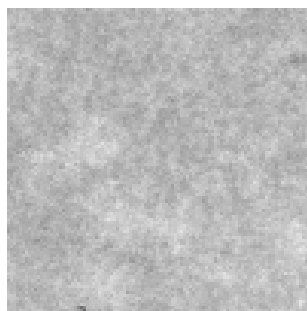


Figure 3.27: A sub-image (100×100) pixels in size taken from the speckle pattern shown in Figure 3.26. There are some brighter regions showing the location of speckles, but in general the pattern is very indistinct and blurred.

the peak to a sub-pixel accuracy.

This result demonstrates that looking for larger displacements, and therefore increasing the size of the search area in the second image, does not affect the accuracy of the measured displacements. This suggests that the speckle pattern shown in Figure 3.26 is sufficiently random for DICC to work. To investigate the minimum size of sub-image that can be used on the speckle pattern in Figure 3.26, the image was displaced by 95 pixels in the horizontal (x) direction and 75 pixels vertically (y -direction). DICC was performed using a variety of different square sub-images ranging from (10×10) pixels to (100×100) pixels in size. An example of a typical sub-image (100×100) pixels in size, extracted from the speckle pattern in Figure 3.26, is shown in Figure 3.27. Within this sub-image are 3-4 brighter regions showing the location of lead pieces. Further contrast on the images is caused either by the variability of the sand sample or noise generated during the detection and film developing process. It is clear that this sub-image bears little resemblance to an ideal speckle pattern, as discussed in Chapter 2.

A graph showing the fraction of sub-images (out of a sample size of 260 in each case) which correlate correctly, as a function of sub-image size, is shown in Figure 3.28. For a sub-image size greater than (20×20) pixels, all of the sub-images correlate correctly for integer pixel displacements. Even at a very low sub-image size of (10×10) pixels, 70% of the pixels correlate correctly with a search area of (200×200) pixels.

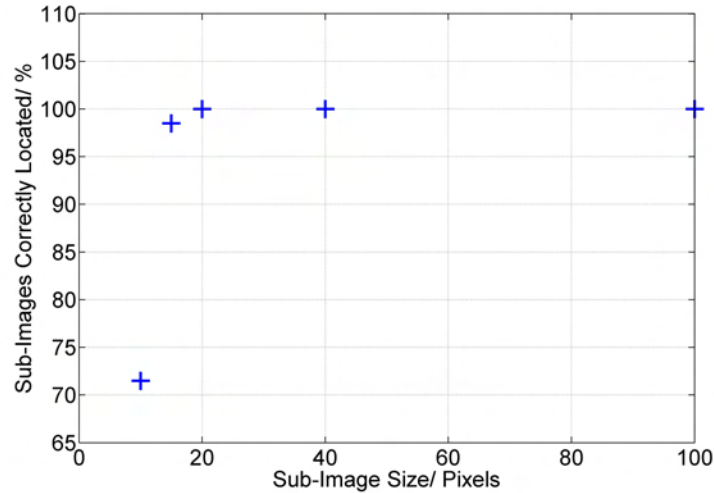


Figure 3.28: The percentage of sub-images which correctly correlate against sub-image size (for integer pixel displacements) when correlating Figure 3.26 with the same image displaced slightly. 100% of images correlate for sub-image sizes of (20×20) pixels and above.

It is clear that the accuracy of the algorithm when considering integer pixel displacements of a single image is very high. It is unlikely that this accuracy can be matched when considering two experimental X-ray images. Firstly, the experimental displacement of a sample is highly unlikely to lead to a translation of a whole number of pixels between the images. The intensity value recorded in each pixel of the scanned X-ray image represents the mean of the underlying continuous intensity structure contained within that pixel. A non-integer pixel translation will cause each pixel to sample a slightly different region of the underlying intensity distribution, which will have a slightly different mean value. There will no longer be an exact pixel by pixel match for a given sub-image in the second image and so the correlation peak will be broader and there may be a greater error in identifying the location of the sub-image. This also means that the speckles will be digitised in slightly different locations, leading to additional errors. Even if there is no translation of the speckle pattern the smallest of rotations, which are unavoidable in real large scale DSR experiments or during the scanning process, will lead to a re-sampling of the intensity distribution and will

3. PRODUCING A NEW DICC ALGORITHM

therefore reduce the correlation values.

To get a more realistic idea of the errors involved in measuring displacements between two different X-ray images, it is necessary to physically move the speckle pattern by some carefully controlled amount that leads to non-integer pixel translations between the X-ray images, and then see if the DICC algorithm can correctly determine the displacement. This approach also gives a more useful estimate of the error involved in analysing real experimental images as it will take into account errors caused by correcting for small rotations of the speckle pattern and in determining the scaling factor for the speckle pattern.

In order to test the DSR process on a sample similar to those that will be discussed in the following chapters, a column of sand 10 cm high with a horizontal plane of randomly scattered lead shot, with a particle size of approximately 1 mm and to a covering of 25 % by area, at a height of 5 cm, was produced. This sample was securely mounted onto a custom made translation stage, consisting of a platform that can be translated with an accuracy of 0.01 mm using a micrometer, as shown in Figure 3.29. A random pattern of lead shot was secured above the X-ray cassette to produce a second speckle pattern which did not move with the sample. This fiducial marker allows for correction of small misalignments of the X-ray cassette between successive X-rays. Although the X-ray cassette was carefully aligned manually, it is impossible to avoid some misalignment of the cassette, or indeed of the X-ray film within the cassette.

A reference X-ray image of the sample and the fiducial marker was taken and the sample was translated by a known amount before taking a second X-ray image. This process was repeated for a number of different translations. The graph in Figure 3.30 shows the displacements determined from the images by the DICC algorithm for a series of known translations. The graph shows that the DSR process has performed well at measuring the applied translation; there is little deviation between the line of perfectly measured displacements and the actual measured displacements. The errors shown on the graph are determined from the standard deviation of the measured displacement values. These errors include those inherent in the DICC process and those caused by slight misalignment of the X-ray film during the experiment or during the subsequent scanning.

3.4 Testing of the DIC Algorithm

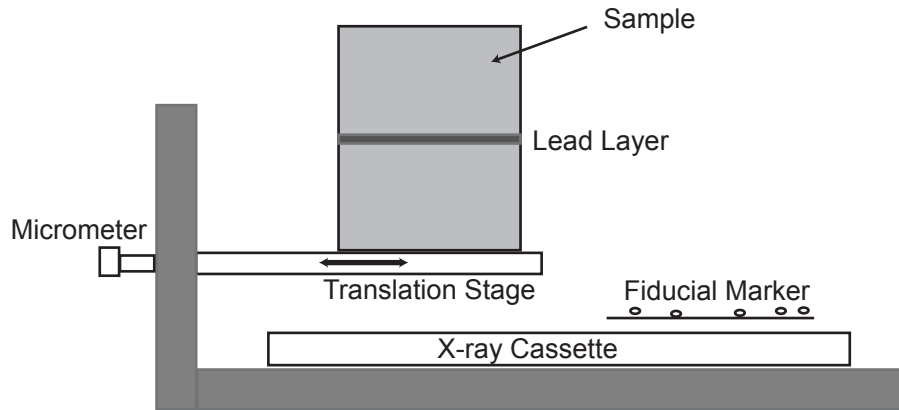


Figure 3.29: The translation stage used to accurately move the sample so that the accuracy of the speckle algorithm in measuring sub-pixel displacements can be determined.

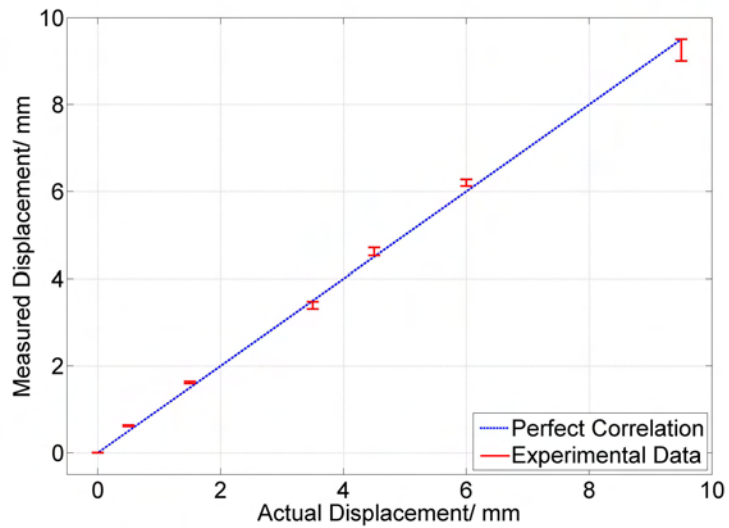


Figure 3.30: A plot of the measured displacement of the sample determined using DSR with a sub-image size of (100×100) pixels against the actual displacement of the sample measured using the micrometer on the translation stage. The algorithm accurately measures the displacement of the sample.

3. PRODUCING A NEW DICC ALGORITHM

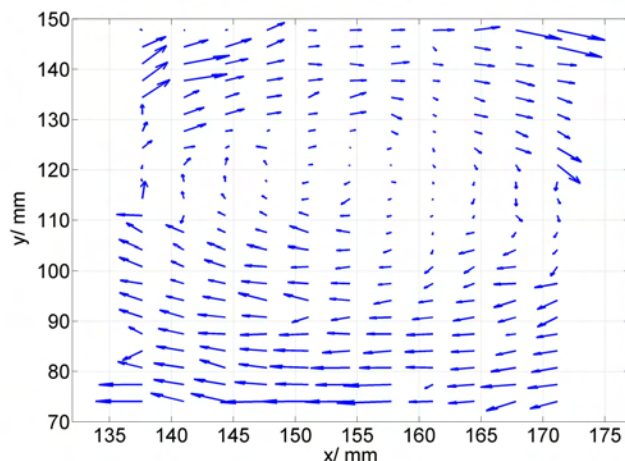


Figure 3.31: Displacements measured when correlating two X-ray images where, if the two pieces of film had been identically arranged within the cassette and there were no errors introduced during scanning, the displacements should all be zero. The displacements are scaled by a factor of ten to make the rotation more visible. It is clear that rotation of the film has occurred at some stage during the DSR process, giving errors of up to 0.4 mm.

Other errors may be introduced when estimating the scale factor in each case and correcting for small rotations. To illustrate the errors that can be introduced when loading the X-ray cassette with film, or when scanning the X-ray film, a random pattern of lead particles was attached to the front face of an X-ray cassette and an X-ray image was taken. The X-ray film in the cassette was then replaced with a second piece of film and a second X-ray image was then taken. The two different pieces of film were then carefully aligned in a scanner and were digitised. Ideally, when the two images are correlated the measured displacement should be zero, as the speckle pattern should be in exactly the same location and orientation in both images. Instead, when the two images were correlated the speckle pattern shown in Figure 3.31 resulted. The magnitude of the displacement arrows has been scaled by a factor of ten in this image to make the rotation more visible.

Figure 3.31 shows that the displacements are non-zero. The pattern of the displacements shows that rotation of one of the pieces of the film has occurred

3.4 Testing of the DICC Algorithm

during the loading or scanning process. The displacements due to this small rotation range from 0.01 mm to 0.4 mm. This demonstrates that even when being careful to correctly align the film at all stages, some small rotation or translation of the film is inevitable.

Correcting for rotation can be troublesome, given that the axis of rotation, and the extent of rotation, are generally both unknown. Small rotations can be corrected for using a plane fitting program [19]. The displacements due to the rotation can be considered as being made up of two different planes of displacement, one representing the lateral displacements, dx , and the other the longitudinal displacements, dy , as shown in equations (3.21) and (3.22),

$$dx = ax + by + c, \quad (3.21)$$

and

$$dy = dx + ey + f. \quad (3.22)$$

where the letters a to f represent constants and x and y are the lateral and longitudinal axes. By fitting planes to the two sets of displacement data, the variables a to f can be determined. Once this has been carried out for a set of fiducials, the displacements due to the rotation in the rest of the image, for example within a sample, can be calculated by extrapolation of these planes. If this process is applied to the displacement data shown in Figure 3.31, the displacements shown in Figure 3.32 result (once again the displacements have been scaled significantly). The majority of the rotation has been removed but other random errors have been introduced. These errors are smaller than the displacements caused by the rotation, the maximum being only around 0.08 mm in magnitude.

We discussed in Chapter 2 that the resolution of the displacement maps determined through DSR depends on the smallest size sub-image that can be tracked between the images. To investigate what this size is for non-integer pixel displacements of the sample, the translation stage was used to move a sample so that there was a displacement of (40.4 ± 0.6) pixels in one direction and (5.5 ± 0.4) pixels in a perpendicular direction. DICC was performed on X-ray images of the sample taken before and after the applied displacement, with a variety

3. PRODUCING A NEW DICC ALGORITHM

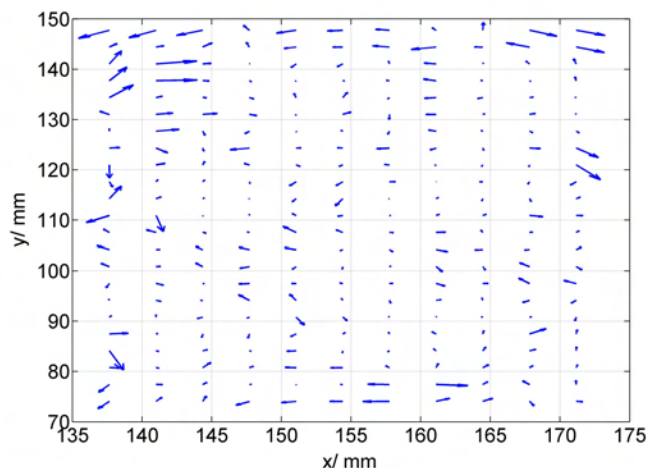


Figure 3.32: Displacements after correction for rotation using a plane fitting program. The rotation has been successfully removed leaving errors of up to 0.1 mm.

of different sizes of square sub-image. In each case the fraction of sub-images which had correctly correlated (defined as being within one half of a pixel of the correct displacement) is shown in Figure 3.33 as a function of the length of the sub-image.

Figure 3.33 shows that 100% of the sub-images correlate for sub-images larger than (72×72) pixels in size. The correlation remains moderately successful down to a sub-image size of (32×32) pixels, where 87% of the sub-images correctly correlate, but then there is a rapid drop off in the success of the correlation upon going to smaller sub-images, so that with a sub-image (22×22) pixels in size only 38% of sub-images correlate correctly. This result is unsurprising given that a piece of lead appears as a white area on the X-ray images with a size of roughly (10×10) pixels.

In order to achieve repeatable accuracy when performing DICC on DSR speckle images of this type, it seems appropriate to use a sub-image that is (82×82) pixels in size or greater. This represents a square physical area in the sample (depending on the extent of the magnification of the speckle pattern) with a side-length of between four and six millimetres. This level of accuracy should

3.4 Testing of the DICC Algorithm

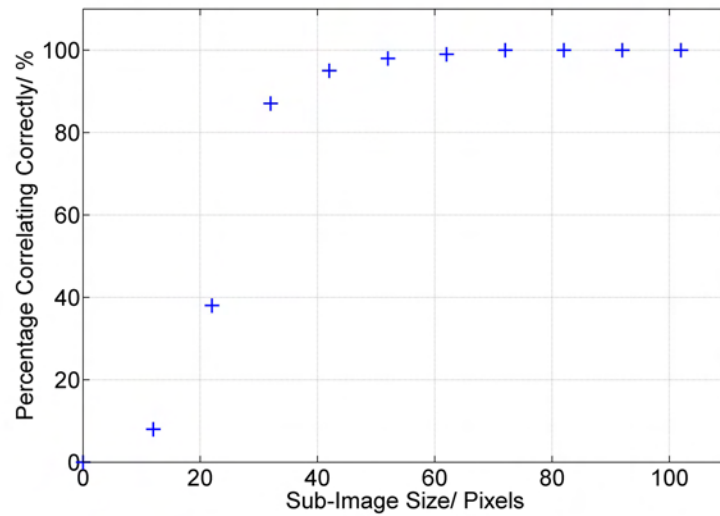


Figure 3.33: The percentage of the sub-images correctly correlating when measuring non-integer pixel displacement as a function of the sub-image length (for a displacement of 40.4 pixels in the x -direction and 5.5 pixels in the y -direction) for the experimentally displaced sample. 100% of the sub-images correlate successfully when a sub-image (72×72) pixels in size or greater is used. The success of the correlation falls dramatically for sub-images (32×32) pixels or smaller.

3. PRODUCING A NEW DICC ALGORITHM

prove sufficient for the dynamic penetration experiments which will be discussed in the following chapters.

3.5 Conclusions

To summarise:

- A Fourier based DICC algorithm has been produced and optimised for investigating the penetration and internal flow of large granular samples.
- Different image normalisation approaches were investigated. A window averaging approach provides the greatest improvement in both the absolute correlation values (an 80% increase) and the peak to noise ratio (a 45% increase).
- A window averaging approach corrects for both global variations in contrast and more localised bright areas, such as the presence of a projectile or densified material behind a compaction wave. A normalised speckle pattern with a uniform mean of zero and a uniform variance of one is produced by the filtering.
- The normalisation approach is equally applicable to the spatial DICC approach taken by Sutton and others [20]. An increase in the absolute correlation value (27%) and the peak to noise ratio (38%) was demonstrated. The signal to noise ratio with the Fourier technique and the filtered images is better than with the spatial correlation technique on the filtered images (2.15 versus 2.05).
- These improvements will allow larger samples, which produce less than ideal speckle patterns, to be investigated experimentally. This will ensure that the sample behaviour is representative of the bulk behaviour of the material and that the penetration can be followed to a greater penetration depth.
- The improvement in the success of the correlation was demonstrated for experimental penetration data (relative to a standard DICC algorithm).

Considerably more information was provided in the locality of the penetrator, which is the area of greatest interest.

- It was demonstrated that for DSR penetration experiments on large samples (of the type discussed in later chapters), the approximation of rigid-body translation of the sub-images is appropriate. For a sub-image size of (7×7) millimetres most of the sub-images did not experience any significant compaction.
- The algorithm was shown to accurately determine experimentally applied displacements of a sample of sand. The errors involved in the DSR process, including those involved in correcting for small rotations, determining scale factors and performing DICCC, generally amount to an error of less than 0.3 mm in the measured displacements.
- When performing DSR on X-ray speckle patterns made up of lead one millimetre in diameter, a sub-image size of (82×82) pixels or greater leads to very successful correlation, in that 100% of the sub-images correlated in the controlled displacement experiment. In the following chapters a sub-image size of (100×100) pixels is generally used to ensure the accuracy of the data.

References

- [1] Sjodahl, M. and Benckert, L.R., “Electronic speckle photography: analysis of an algorithm giving the displacement with subpixel accuracy”, *Applied Optics*, **32(13)**, (1993), 2278–2284
- [2] White, D.J., Take, W.A. and Bolton, M.D., “Measuring soil deformation in geotechnical models using digital images and PIV analysis”, *10th Int. Conference on Computer Models and Advances in Geomechanics*, (1999), 997–1002

REFERENCES

- [3] White, D.J., Take, W.A. and Bolton, M.D., “Soil deformation measurement using particle image velocimetry (PIV) and photogrammetry”, *Geotechnique*, **53**, **7**, (2003), 619–631
- [4] Jerri, A.J., “The Shannon sampling theorem - its various extensions and applications: A tutorial review”, *Proceedings of the IEEE*, **65**(**11**), (2005), 1565–1596
- [5] Arandjelovic, O. and Cipolla, R., “A pose-wise linear illumination manifold model for face recognition using video”, *Computer vision and image understanding*, **113**(**1**), (2009), 113–125
- [6] Meng, G., Zheng, N., Du, S., Song, Y. and Zhang, Y., “Shading extraction and correction for scanned book images”, *IEEE Signal Processing Letters*, **15**, (2008), 849–852
- [7] Chen, B., Cao, W. and Zhang, H., “An efficient algorithm on vehicle license plate location”, *Proc. IEEE International Conference on Automation and Logistics*, (2008), 1386–1386
- [8] Gonzalez, R. and Woods, R., *Digital Image Processing*, Addison-Wesley Publishing Company (1992)
- [9] Santamaria, M.V. and Palacios, R.P., “Comparison of Illumination Normalization Methods for Face Recognition”, *Third COST 275 Workshop - Biometrics on the Internet*, (2005), 27–30
- [10] Ross, J.C., *The Image Processing Handbook*, CRC Press (2007)
- [11] Xie, X. and Lam, K.M., “An efficient illumination normalization method for face recognition”, *Pattern Recognition Letters*, **27**(**6**), (2006), 609–617
- [12] Dong, S., He, B., Jiang, Q., Wang, H. and Huang, T., “A Half Face Recognition Scheme”, *Eighth ACIS International conference on Software Engineering*, (2007), 335–358

REFERENCES

- [13] Riley, K.F., Hobson, M.P. and Bence, S.J., *Mathematical Methods for Physics and Engineering, Second Edition*, Cambridge University Press, UK (2002)
- [14] Cleveland, W.S., “Robust Locally Weighted Regression and Smoothing Scatterplots”, *J. of the American Statistical Association*, **74(368)**, (1979), 829–836
- [15] Rabiner, L.R. and Gold, B., *Theory and Application of Digital Signal Processing*, Englewood Cliffs: Prentice-Hall Inc., US (1975)
- [16] Sutton, M.A., McNeill, S.R., Helm, J.D. and Chao, Y.J., “Advances in Two-Dimensional and Three-Dimensional Computer Vision”, *Topics in Applied Physics - Photomechanics*, **77/2000**, (2000), 323–372
- [17] Chapman, D.J., *Shock Compression of Distended Materials*, Phd, University of Cambridge (2009)
- [18] Sjodahl, M. and Benckert, L.R., “Systematic and random errors in electronic speckle photography”, *Applied Optics*, **32**, (1994), 7461–7471
- [19] Williamson, D., *DICC Workshop*, Internal report, University of Cambridge (2007)
- [20] Sutton, M.A., Wolters, W.J., Peters, W.H., Ranson, W.F. and McNeill, S.R., “Determination of displacements using an improved digital correlation method”, *Image and vision computing*, **1(3)**, (1983), 133–139

REFERENCES

Chapter 4

Dynamic Penetration of Granular Media

4.1 Introduction

In the Introduction to this thesis we discussed the need for precise data on the internal flow of material within a granular sample during penetration. Although some preliminary small-scale experiments have been carried out in this area [1], more useful data could be obtained by using a larger sample, as the response of a larger sample would be more representative of the bulk behaviour of the material. Furthermore, the boundary conditions would not become important until late in the penetration process, allowing the penetration to be studied to a greater depth. In the preliminary experiments by Grantham [1–3], a sample depth of only 30 mm was used, in order to avoid the correlation problems associated with non-ideal speckle patterns (which were discussed in detail in Chapters 2 and 3). In this chapter, a series of experiments are presented as part of a study of the response of a large (150 mm length, 100 mm diameter) cylindrically confined sample of sand to penetration by a rigid steel projectile (length 100 mm, diameter 10 mm).

DSR was used to determine the full field displacement within a cross-section of the cylindrical sample. The temporal progression of the penetration is followed through a series of time-delayed flash X-ray experiments. The effect of the nose

4. DYNAMIC PENETRATION OF GRANULAR MEDIA

shape of the projectile on the behaviour of the penetrator, and the response of the sand, is reported in the following chapter.

As discussed in the previous chapter, the Gaussian X-ray beam profile, cylindrical nature of the sample, and the presence of the bright rod in the second X-ray image mean that standard DIC algorithms perform relatively poorly at analysing these types of X-ray images. Using the algorithm discussed in Chapter 3 removes these contrast issues and significantly improves the correlation. This allows us to use a larger sample than would otherwise be possible.

4.2 Experimental Method

4.2.1 Material Characterisation

The sand used in the following experiments is a fine concrete sand provided by Cardigan Sand & Gravel Co Ltd (Penparc, Cardigan, Ceredigion, SA43 1RB). It was chosen as its relatively wide particle size distribution is representative of the types of material generally found in nature. The same sand has also been used for other experiments, including plate impact experiments [4]. Particle size data for the sand provided by the supplier is shown in Figure 4.1, showing that the sand grains range in size from 0.01 mm to approximately 4 mm. The average size is between 0.5 and 1 mm.

To check the particle size distribution of the supplied sand, the material was investigated using a Malvern Mastersizer 2000 laser particle sizer. The machine works by passing a suspension of the material in water across the path of a laser beam. The laser light is scattered by the collection of particles to a variety of angles that are directly related to the size of the particles. The scattered light is detected by a series of detectors and the signal is analysed to determine the sizes of the particles causing the scattering [5]. As part of the calculation, it is assumed that the particles are spherical. While this is not entirely true for the majority of the sand grains, it is a useful approximation to help determine the relative fraction of particles with a given particle size. The particle size data for the sand, averaged over three separate samples, are shown in Figure 4.2. The results show

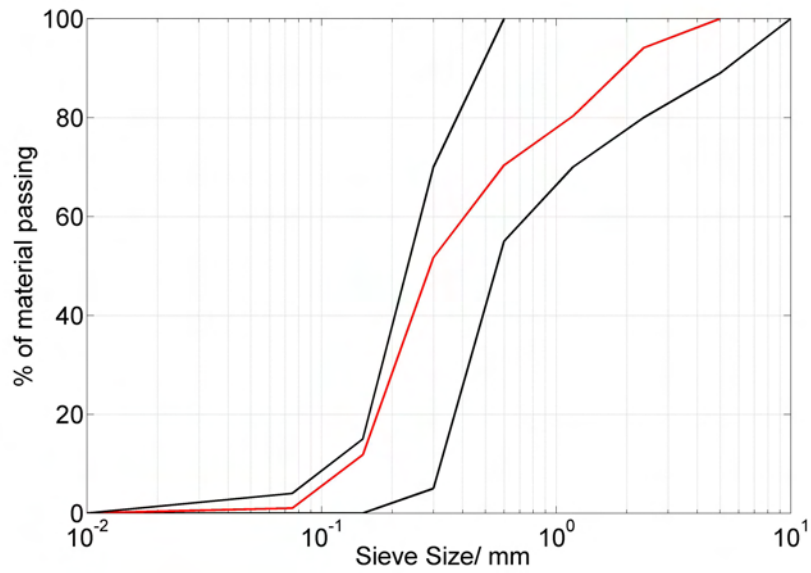


Figure 4.1: Particle size data for the sand provided by the manufacturer showing the minimum, average (red) and maximum fraction of the material passed by a sieve with holes of a given size. The average particle size is between 0.5 and 1 mm.

4. DYNAMIC PENETRATION OF GRANULAR MEDIA

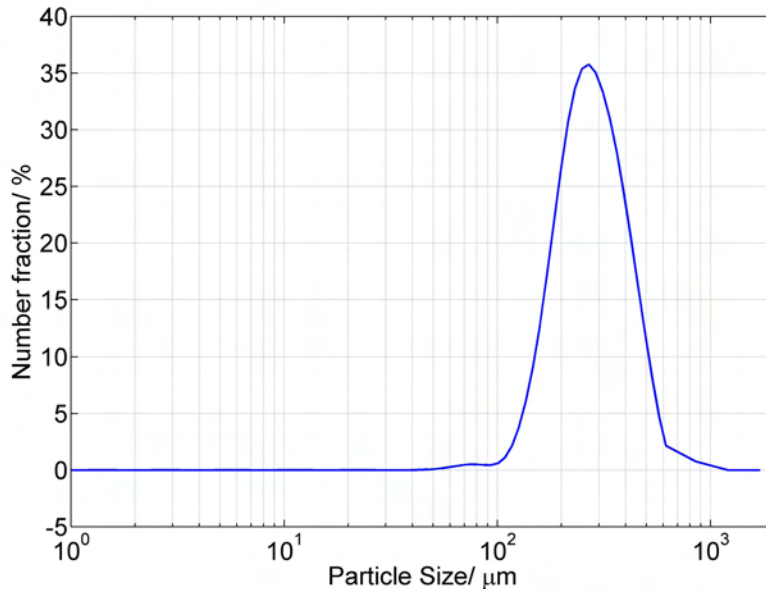


Figure 4.2: Particle size data for the sand measured using a Malvern Master-sizer 2000 machine. The distribution of particle sizes is Gaussian in appearance and the mean value is approximately 0.3 mm. The particles range in size from approximately 0.1 mm to 1.5 mm.

that the grains ranged in size from 0.1 mm to 1.5 mm with an average size of (0.29 ± 0.19) mm.

The grain morphology was investigated using scanning electron microscopy (SEM) [6]. A Phillips XL30 - SFEG SEM was used to image grains at magnifications ranging from 35x to 1148x. The two images presented in Figure 4.3 show a selection of grains at a magnification of 35 - 36x. The grains shown in (a) have an average Feret diameter, defined as the longest possible straight line between any two points on the perimeter, of (320 ± 90) μm . The grains are irregular in shape, with rough surface profiles. The circularity of the grains, defined as

$$\text{circularity} = 4\pi \left(\frac{A}{P^2} \right), \quad (4.1)$$

where A is the area of the grain and P is the length of the perimeter, ranges from 0.25 to 0.78. A value of one would correspond to a perfect circle while values approaching zero indicate an increasingly elongated polygon. The average

circularity of the grains shown in (a) is 0.6 ± 0.1 , suggesting that the grains are more elliptical than circular. In (b), a larger grain with a Feret diameter of 1.6 mm and a circularity of 0.59 is shown. Particles ranging in size from 0.25 mm to 1.6 mm are visible, illustrating the range of particle sizes found in the sand.

Figure 4.4 shows a sequence of images of a single grain of sand, at increasing levels of magnification, illustrating the surface features. In the first image, at a magnification of 287x, the irregular grain morphology is clear - there are a number of sharp out-croppings visible. Increasing the magnification to 574x and 1148x, we can see that the surface of the grain is rough. There are a number of pits and ridges visible on the surface ranging in scale from 50 μm down to less than 10 μm . These SEM images show that the grains have irregular shapes, with jagged edges and outcroppings, and rough surfaces, suggesting that at moderate to high densities friction between the grains is likely to be important.

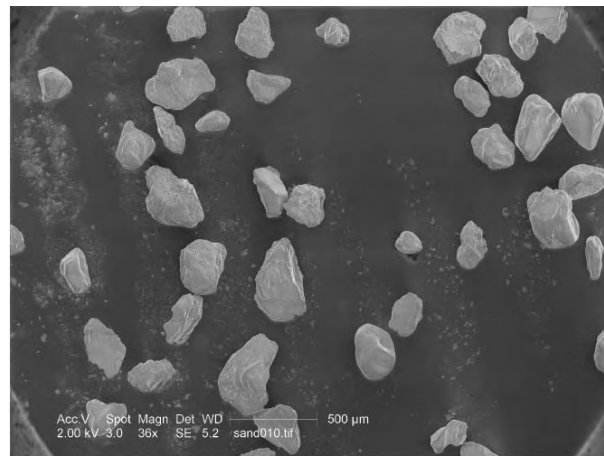
To ensure a uniform water content throughout the experiments, the sand was dried in an oven at a temperature of 80⁰C for 24 - 36 hours before each experiment. Previous experiments have shown that the water content can have a significant effect on the response of the sand to impact [1]. The tapped density of the dried sand, determined by gradually adding the sand to a cylindrical cavity and tapping the container to cause the material to settle, is $(1650 \pm 20) \text{ kgm}^{-3}$. The density of pure quartz is 2650 kgm^{-3} , suggesting that the tapped sand is 38% porous by volume.

4.2.2 Flash X-Ray System

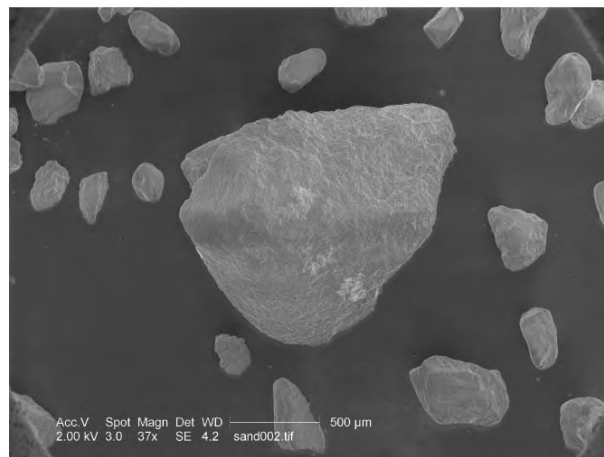
A flash X-ray system produces a very intense, short duration burst of X-rays ($< 100 \text{ ns}$ in duration). Such a system is ideally suited for studying high-speed events, such as objects moving at high velocity. The pulse of X-rays is produced by accelerating a very short intense pulse of electrons, produced by discharging a capacitor bank through a cathode, into a tungsten target.

A Scandiflash TA400 flash X-ray system was used here. It produces pulses of X-rays with a duration of approximately 70 ns and energies between 55 and 150 keV. Images are captured using X-ray cassettes (AGFA Curix Ortho Regular cassette). The cassettes contain two medical intensifier screens, consisting of a

4. DYNAMIC PENETRATION OF GRANULAR MEDIA



(a)



(b)

Figure 4.3: SEM images of the sand grains taken at a magnification of 36-37x. The grains are irregular in shape and are more elliptical than circular. Many of the grains have rough surface profiles with jagged out-croppings. In (b) particles ranging in size from 0.25 mm to 1.6 mm are visible, illustrating the range of particle sizes present.

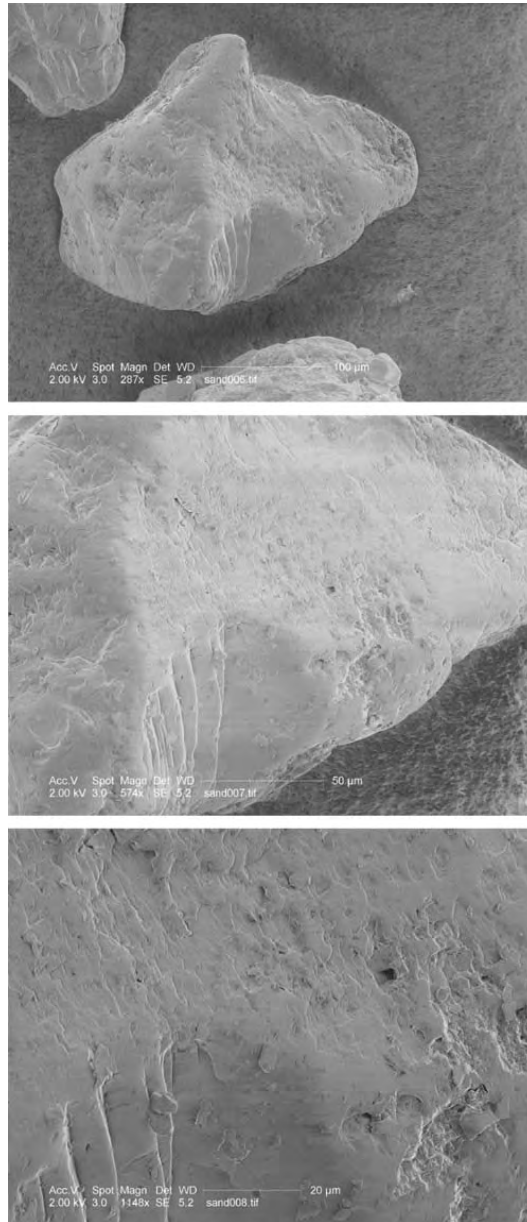


Figure 4.4: A sequence of SEM images of a single grain of sand, taken with increasing magnification (287x, 574x and 1148x). The irregular shape of the particles can be seen, as can the surface roughness and the presence of outcroppings and ledges. These surface features will increase the coefficient of friction between grains in contact.

4. DYNAMIC PENETRATION OF GRANULAR MEDIA

polyester base coated in a layer of rare earth phosphors. The image is recorded on X-ray film (AGFA Curix HT1.0006 Plus Medical X-ray film). The film is subsequently developed manually using Kodak developing products (Kodak RP X-OMAT LO Developer/replenisher and Fixer/replenisher). For each DSR experiment two separate X-ray cassettes are required, one for the reference X-ray image and the second for the ‘dynamic’ X-ray image.

4.2.3 Preliminary Experiments

A series of preliminary experiments was carried out to determine the optimal sample size and lead particle size combination. A number of conflicting requirements must be considered. The sample size should be large relative to the size of the grains of sand so that there is enough material to be representative of the bulk material. The sample also needs to be large relative to the diameter of the penetrator, so that compaction fronts do not reach the boundaries of the sample until as late as possible. However, as the sample size is increased, the contrast on the X-ray images reduces, as for a given size of lead particle the relative increase in X-ray absorption achieved by including the particle decreases with the thickness of sand. If the sample is too large, there will be insufficient contrast on the images to perform DICC [7]. To improve the contrast in large samples, it is necessary to use relatively large lead particles (around 1 mm in size) so that they absorb a greater fraction of the X-ray intensity, and show up more clearly. This in turn creates problems since the minimum size of sub-image required to encompass at least three speckles increases with the speckle size. If the sub-image size becomes too large, the resolution of the measured displacements is severely compromised.

To choose a sample size and lead particle size combination which is an acceptable compromise of these requirements, a wedge of sand was constructed and a series of different types of lead particle were applied to the bottom surface. The wedge had a maximum depth of 20 cm of sand. The lead ranged in diameter from 150 μm to around 1 mm. The details are given in Table 4.1.

X-ray images of this wedge showed the contrast achievable with the different types of lead particles for a given thickness of sand. For sand thicknesses greater

Lead Type	Manufacturer	Diameter
Shot	Sigma-Aldrich	1 mm
30 mesh	Aldrich	<0.6 mm
100 mesh	Aldrich	<0.25 mm
Granulated	Sigma-Aldrich	0.2 mm
Lead Powder	Goodfellow	150 microns

Table 4.1: The types of lead included on the sand wedge.

than 8 cm, only the lead shot was clearly visible - other sizes of lead particle did not provide sufficient contrast for DICC to be successful. The most suitable lead type for these experiments was therefore identified to be the lead shot. The lead shot is visible and the image is not significantly blurred at a sample thickness of 20 cm, suggesting that the contrast is sufficient for DSR for thicknesses of up to 20 cm (and possibly beyond). In reality the maximum thickness that can be used in the experiments will be less than this, since elements of the experimental setup will absorb X-rays. A sample size of around 10 cm at the thickest point proved optimal for the experimental setup. This provides adequate image contrast and is sufficiently large relative to the penetrator diameter to allow a significant depth of penetration before interactions between the compaction fronts and the confinement become significant.

The manufacturer's details give the average diameter of this lead shot as 1 mm. To verify this, a series of photographs of the lead were taken using an optical microscope. The images were analysed using the freely available ImageJ software [8], to determine the particle size distribution from over 500 particles. The results are shown in Figure 4.5. Ideally, the lead particle size should be closely matched to the size of the particles of sand, to ensure that the lead particles behave as part of the bulk material. In this case, the lead particles are slightly larger than the mean sand particle size, but not significantly so - the mean lead particle size is around 1 mm, the mean sand particle size is approximately 0.4 mm, with the maximum being approximately 3 mm.

4. DYNAMIC PENETRATION OF GRANULAR MEDIA

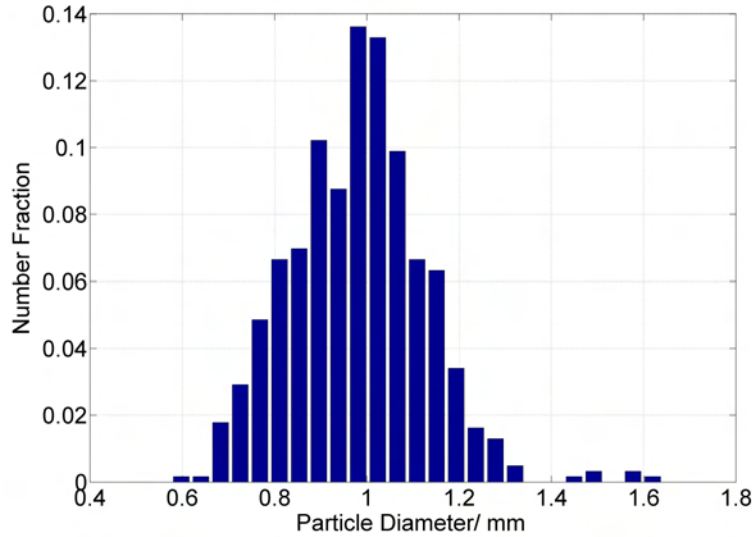


Figure 4.5: A histogram showing the fraction of the total number of particles of lead shot measured with given particle sizes. The mean particle size is around 1 mm, a little larger than the mean particle size of the sand.

4.2.3.1 Effect of the Lead Shot

To use DSR to investigate the material flow, it is essential that the presence of the lead shot does not significantly affect the material flow or response. To investigate this, preliminary experiments were performed to measure the force experienced by a projectile being slowly pushed into a box of sand, with and without a layer of randomly scattered lead. An Instron machine, discussed in more detail in Chapter 6, was used to push a flat-ended projectile (diameter 10 mm) into the centre of the box (100 mm cube) at a uniform rate of 4 mm/min. The Instron records the vertical force experienced by the projectile as a function of penetration depth. This experiment was performed a number of times on loosely packed sand, with and without a randomly seeded layer of lead shot covering 30% of a vertical plane. The results are shown in the graph in Figure 4.6.

Figure 4.6 shows that the effect of adding the layer of lead shot is smaller than the inherent natural variation between the samples, and so it is concluded that a coverage of up to 30% of lead can be used without interfering with the behaviour

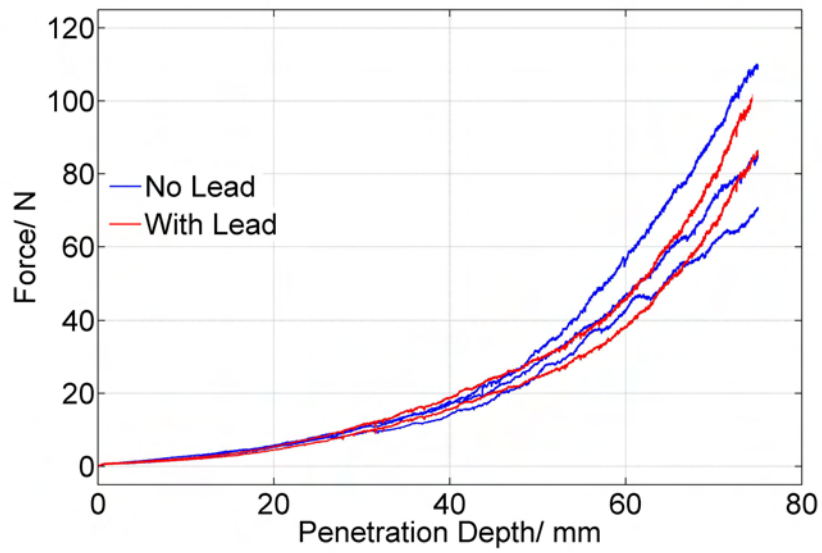


Figure 4.6: Vertical force as a function of penetration depth for Instron experiments on sand with a layer of randomly distributed lead (red) and without (blue). Any effect due to the inclusion of the layer of lead particles is smaller than the natural variability of the material.

4. DYNAMIC PENETRATION OF GRANULAR MEDIA

of the sand.

4.2.4 Sample Design

Producing a cylindrically confined and symmetric sample containing an internal plane of scattered lead poses a number of experimental challenges. Initial attempts involved the use of an extruded acrylic tube of internal diameter 100 mm. The tube was cut in half to allow the two sides to be independently filled with sand and to allow a scattering of lead shot to be applied to the surface of one half. The two halves were then recombined to form a cylinder. This approach was unsuccessful due to the release of hoop stresses (generated in the cylinder during formation) when the cylinder was cut in two. The release of these stresses deformed the two halves of the cylinder, such that the two sections no longer fitted together to make a perfect cylinder.

It was decided that the most accurate method of producing a uniform, symmetrical cylinder which could be separated into sections was to bore a cylindrical hole out of a solid block of polycarbonate. The sample holder design is shown in Figure 4.7. It has a length of 150 mm and the central bore has a diameter of 100 mm. The cylinder is split lengthwise into two sections. It is cut so that one of the sections is larger than the other (80 mm high compared to 60 mm). The purpose of this offset is to allow a layer of lead to be scattered over the central plane in the larger section, and to then be covered by a 10 mm layer of sand before the cylinder is reassembled. This minimises any disruption to the layer of lead when the cylinder is reassembled.

4.2.5 Projectiles

The projectiles used in these experiments are constructed from mild steel and have a diameter of 10 mm and a length of 100 mm. An aspect ratio of 10 makes the projectiles aerodynamically stable, both when flying through the air and when penetrating the sand. The diameter is one tenth the diameter of the target. This allows significant penetration to occur before compaction fronts significantly interact with the confinement.

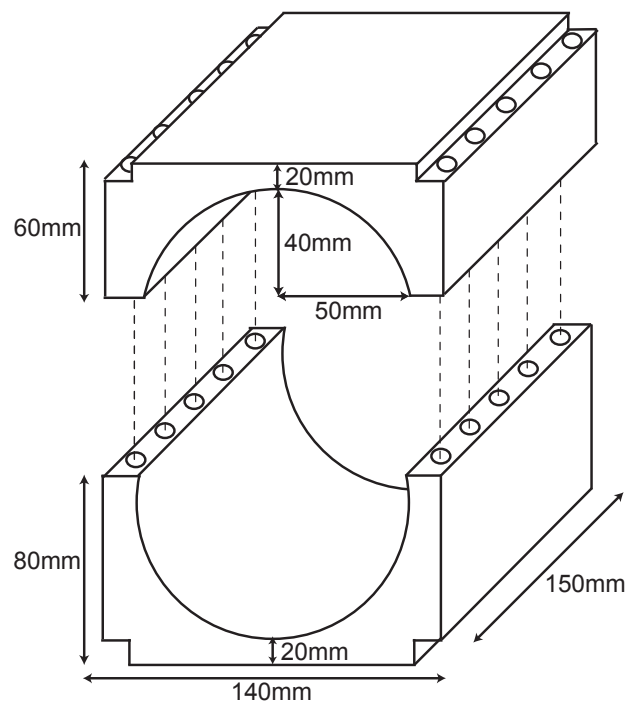


Figure 4.7: A diagram illustrating the main features of the sample holder. The central bore has a diameter of 100 mm and a length of 150 mm.

4. DYNAMIC PENETRATION OF GRANULAR MEDIA

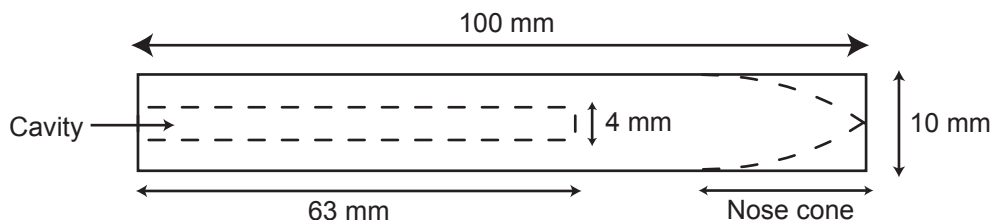


Figure 4.8: A schematic showing the main features of the projectiles. The cavity at the back-end of the projectile reduces the mass, leading to a higher velocity.

To lighten the projectiles so as to increase their velocity, whilst maintaining their strength and stability, cylindrical cavities (with diameter 4 mm and depth 63 mm) were bored into the rear section of the projectiles, as shown in Figure 4.8. The cavity reduces the projectile mass by 40% resulting in an average projectile mass of 55 g, with the centre of mass $\frac{3}{8}$ of the projectile length from the tip. Three different nose shapes were used for the research recorded in this thesis - flat-ended, hemispherical and ogive-2. In this chapter only the flat-ended projectiles are discussed, the details of the ogive-2 projectiles are given in the following chapter.

4.2.6 The Light Gas-Gun

The projectiles were fired using the light gas-gun at the Cavendish Laboratory. A more detailed description of the gun can be found in [9]. The light gas-gun is a single stage gun with a six litre firing reservoir. The gun uses Helium gas and can be fired at pressures of up to 80 bar. A smooth bore barrel with a diameter of (10.5 ± 0.2) mm and a length of 2 m was used to accelerate the projectiles. The velocity of the projectile upon leaving the barrel of the gun is measured using two light gates consisting of laser diodes and detectors and separated by 10 mm. Preliminary experiments showed that a velocity of (200 ± 3) ms⁻¹ could be reproducibly achieved using this setup. A photograph of the light gas gun with the attached barrel is shown in Figure 4.9

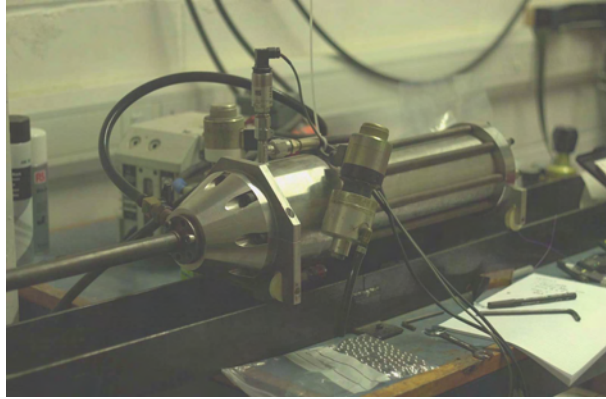


Figure 4.9: A photograph of the light gas-gun with the barrel attached. The catch-chamber is at the opposite end of the barrel.

4.2.7 Impact Chamber

The standard impact chamber used with the light gas-gun (and positioned at the end of the gun barrel) is designed primarily for strength and its ability to hold a low vacuum. Once an experiment has been set-up, it is very difficult to alter anything within the chamber. In DSR experiments, it is therefore very difficult to remove the X-ray cassette from beneath the sample, so that after taking the reference X-ray image a new cassette can be included to produce the second ‘dynamic’ X-ray image, without disrupting the sample alignment. If the sample alignment is altered between the reference image and second image, it is unlikely that the DICC algorithm will work effectively. If a rotation of more than 5 degrees is introduced relative to the position in the reference image, the errors in DICC become unacceptably large [1].

For these reasons a new impact chamber specifically designed for use in DSR experiments was designed and built. A side view of the new catch-chamber, with the side removed, is shown in Figure 4.10. Its main advantage over the standard chamber is an enclosure within the chamber for holding the X-ray cassette, which can be accessed directly through the side of the chamber. This allows the X-ray cassettes to be switched after taking the reference image without opening the chamber. The sides of the chamber can be easily removed, allowing a transparent side to be used if high-speed photography or video of the impact is required. The

4. DYNAMIC PENETRATION OF GRANULAR MEDIA

new chamber is designed to accept a detachable alignment rig which allows for easy and accurate alignment of the sample. A photograph showing the catch-chamber mounted at the end of the barrel, and ready for an experiment, is shown in Figure 4.11.

4.2.8 Alignment Rig

For reproducibility between experiments, it is necessary to precisely align the sample so that the same location can be impacted in each experiment. To achieve this as accurately as possible a rig was designed to allow alignment of the sample to an accuracy of a few millimetres. The alignment rig, pictured in Figure 4.12, consists of a turntable that can freely rotate 360 degrees, resting upon three screws. By adjusting these screws the sample can be made horizontal to within an accuracy of a few degrees.

A laser with a spot size of a few millimeters is shone down the central axis of the gas-gun barrel onto the front of the sample. This allows the centre of the front face to be aligned with the central axis of the barrel. A mirror fitted to the front of the sample can be used to further align the sample, such that the laser light is reflected back down the barrel. This ensures that the sample and the barrel are aligned uniaxially, and that the projectile will therefore penetrate along the central axis of the sample. Two photographs in Figure 4.13 show the sample being aligned, and the aligned sample with a make-trigger fitted (discussed later).

4.2.9 Sample Preparation

When preparing the sample the two sections of the sample holder were temporarily sealed at the ends using thin pieces of card, allowing them to be filled with sand. As the sand was added they were tapped regularly on a hard surface, to allow the sand to settle. The larger section was initially filled with sand up to the original centre line of the cylindrical bore, 10 mm below the lip. Lead shot was randomly scattered over the surface to a coverage of 30%. The section was then topped up with sand so that the surface was flush with the top of the section.

4. DYNAMIC PENETRATION OF GRANULAR MEDIA

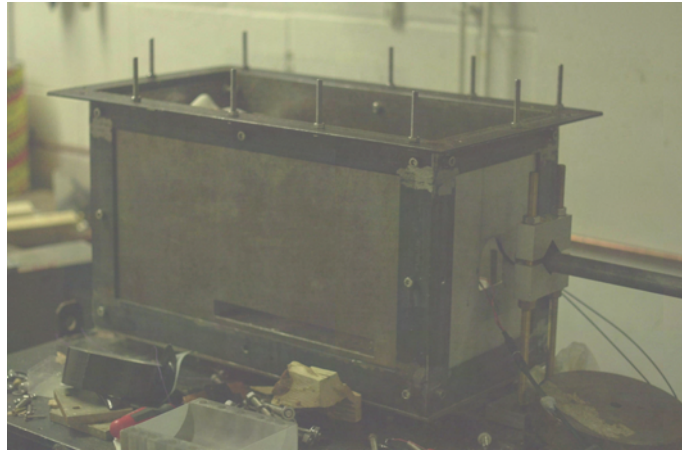


Figure 4.11: A photograph of the catch-chamber mounted on the end of the gun barrel. There is a slot on the side of the chamber through which the X-ray cassette enclosure can be accessed.

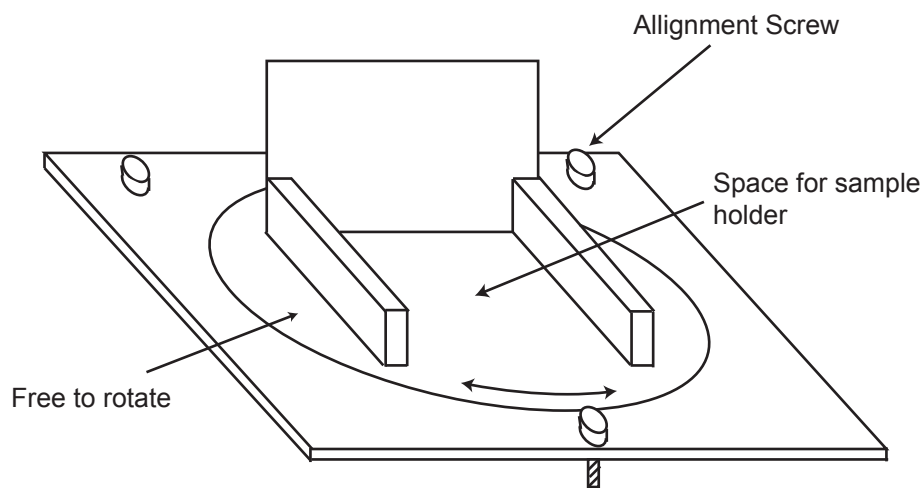


Figure 4.12: A diagram illustrating the main features of the sample alignment rig. The central turntable is free to rotate by 360 degrees. The rig can be made horizontal by adjusting the three screws.

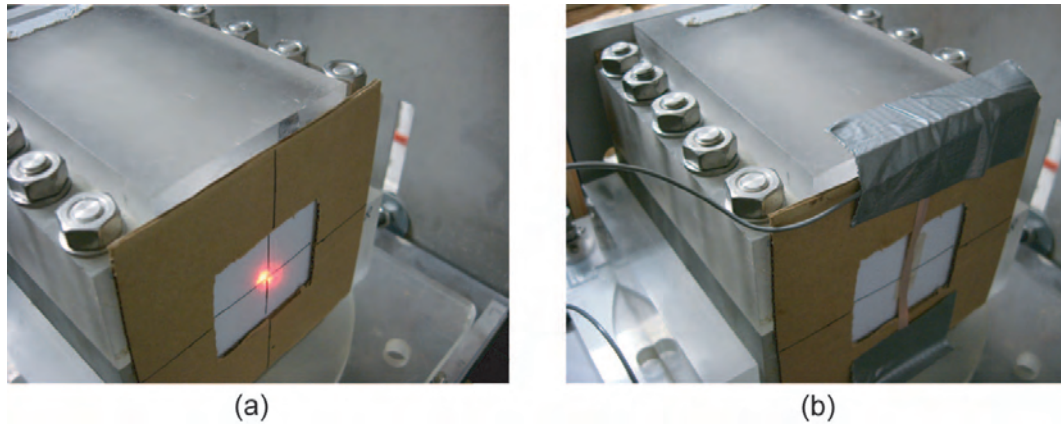


Figure 4.13: Photographs showing the front of the sample during the alignment process. In (a) a laser beam is used to align the front of the sample with the barrel. In (b) a make-trigger has been added to the impact face of the sample.

Once the smaller section was filled with sand, a Mylar sheet was secured over it to enclose the sand. A photograph showing the completed sections is shown in Figure 4.14. The smaller section was then turned over and placed on top of the larger section to complete the cylinder. The Mylar sheet was removed, and the two sections of the sample holder were bolted together. The temporary card was replaced with pieces of corrugated card, attached to the ends of the holder with epoxy. On the impact face, a section of the corrugated card was cut out and replaced with thinner card, in order to avoid slowing down or disturbing the flight of the projectile at the moment of impact (the brown corrugated card and the white thinner card can both be seen in Figure 4.13).

4.2.10 Experimental Procedure

Before performing an experiment the prepared sample was placed in the alignment rig, within the catch chamber, and was aligned. Figure 4.15 shows the inside of the chamber set up ready for an experiment. Pieces of wood and a steel plate are included in the chamber to decelerate and catch the projectile after impact.

The reference DSR X-ray image was taken after the chamber was closed and the lid fitted. During penetration a make-trigger fitted to the front of the sample

4. DYNAMIC PENETRATION OF GRANULAR MEDIA

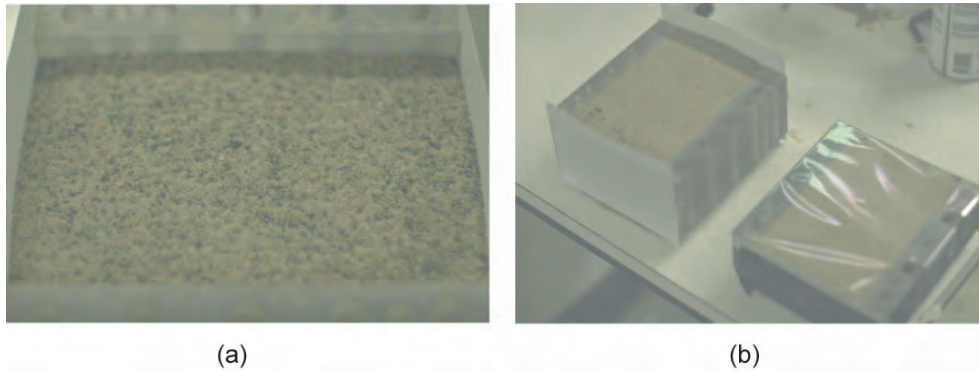


Figure 4.14: (a) The large section of the cylinder filled to 10 mm below the surface with sand and covered with a scattered layer of lead. (b) The two sections filled with sand ready for reassembly. The smaller section has a piece of Mylar secured over it.

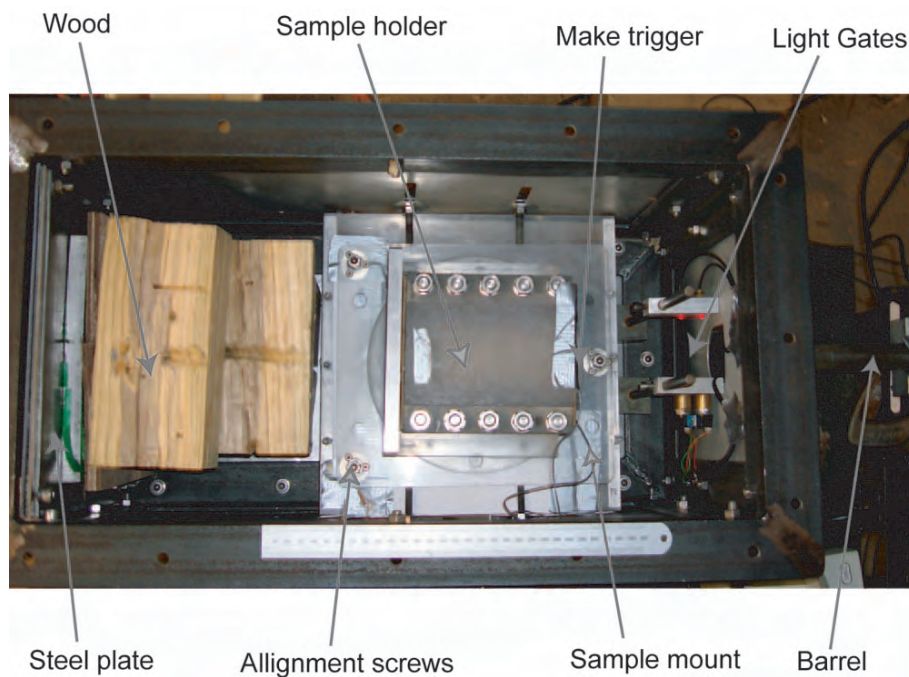


Figure 4.15: A photograph showing the inside of the catch-chamber when set-up in preparation for an experiment. Wood and steel plates are included behind the sample to stop the projectile. Light-gates are used to measure the projectile velocity at impact.

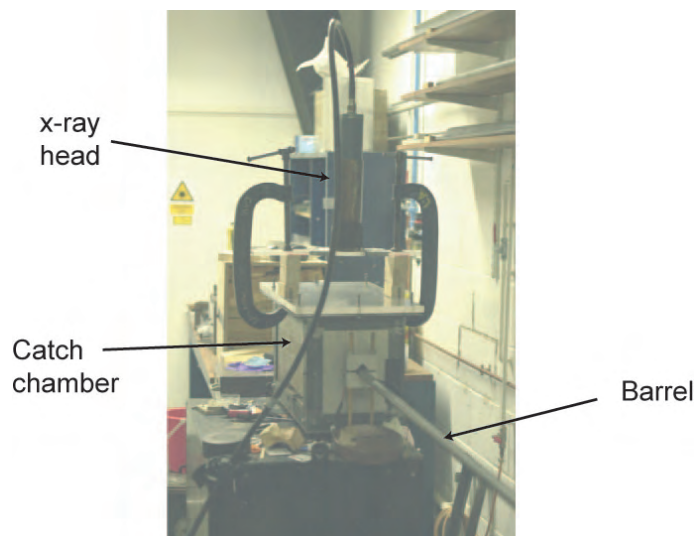


Figure 4.16: A photograph of the catch chamber set up for an experiment, with the lid on and the X-ray head mounted on top.

was used to trigger the X-ray system. The make-trigger consists of two sets of interleaved copper threads, such that there is no electrical contact across the trigger. When a metal projectile impacts the make-trigger, an electrical connection is made which triggers the X-ray system. Delays of varying length were added before firing the flash X-ray system, allowing X-ray images to be taken at various times after impact. This second X-ray image captures the penetration occurring.

The photograph in Figure 4.16 shows the catch-chamber set up ready for an experiment with the lid on and the X-ray head mounted. The gun barrel can be seen entering the front face of the catch-chamber.

4.3 Results and Discussion

To generate a sequence of images showing the temporal progression of the penetration process, experiments were performed with increasing X-ray delay times. For the flat-ended projectiles, delay times of 150, 250, 350, 450, 550, 750 and 1500 μs were used, which covered the whole penetration process. By 750 μs , the projectile is nearing the rear surface of the sample, and the compaction fronts

4. DYNAMIC PENETRATION OF GRANULAR MEDIA

have had sufficient time to interact with the boundaries. By $1500 \mu\text{s}$, the projectile has almost exited out of the back face of the sample. A list of all of the small-gun experiments performed, including those reported in the next chapter, is presented in the Appendix in Tables A.1, A.2 and A.3.

Examples of a reference and a dynamic X-ray image taken during an experiment are shown in Figure 4.17. The left (reference) image shows the arrangement of the lead speckle pattern when the sample is at rest. The right (dynamic) image shows the sample during penetration, $350 \mu\text{s}$ after the start of the penetration. The initial velocity of the projectile in this experiment was $(204 \pm 2) \text{ ms}^{-1}$. A second dynamic X-ray image, showing a sample at $1500 \mu\text{s}$ after impact, is shown in Figure 4.18. By this time, the projectile has partially exited the sample through the rear surface and the central void left behind the projectile has increased in size near the impact face (labelled as ‘larger void’ in the image).

Figure 4.19 shows an X-ray image of a sample taken from the side, showing the orientation of the layer of lead shot. The layer of lead is still relatively thin and flat, confirming that it was not been disrupted significantly during the sample preparation process.

Before analysis, the X-ray images are scanned into a computer at a resolution of 300 dots per inch using a transmissive scanner. DICC is performed on the images in order to determine the internal displacements. As discussed in Chapter 3, significant improvement in the success of the correlation can be achieved by using the DICC algorithm written for this thesis (which includes contrast normalisation of the images). In particular, more information can be obtained about the displacements in the immediate vicinity of the projectile.

An example of the displacement data measured from experimental X-ray images using the DICC technique, super-imposed on the relevant reference X-ray image, is shown in Figure 4.20. Where a sub-image has failed to correlate correctly, the displacement value has been set to zero. This occurs mainly in the area directly impacted by the projectile, in which the sub-images are deformed and sheared to such an extent that a direct correlation is no longer possible.

The displacements shown in Figure 4.20 are in pixels. To convert them to millimetres a scaling factor is required. Since the X-ray beam diverges, the X-ray images are magnified, and there will therefore be a depth-dependent scaling

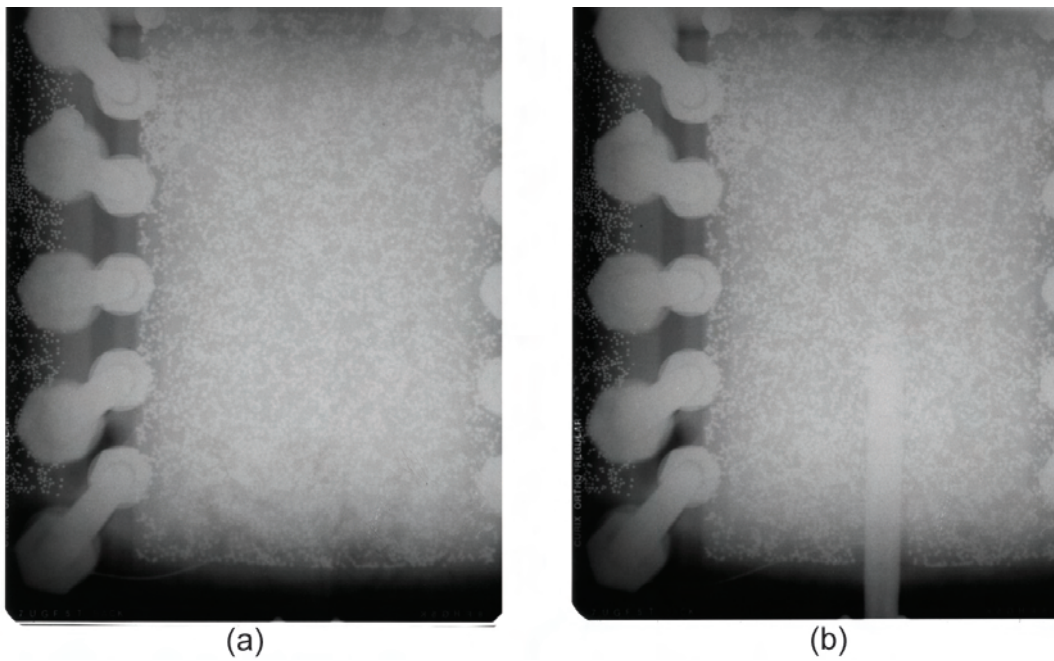


Figure 4.17: (a) A reference X-ray image showing a plan view of the sample and the lead speckle pattern. (b) An X-ray image taken at $350\mu s$ after impact. The projectile has penetrated to a depth of around 70 mm.

4. DYNAMIC PENETRATION OF GRANULAR MEDIA

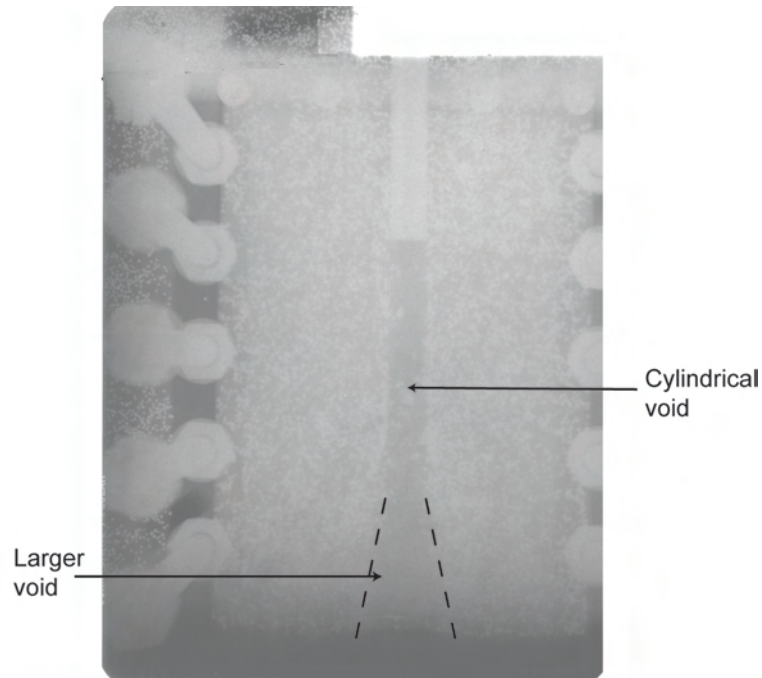


Figure 4.18: An X-ray taken $1500 \mu\text{s}$ after impact showing the deformation caused by the projectile motion. A larger void is forming at the impact face.

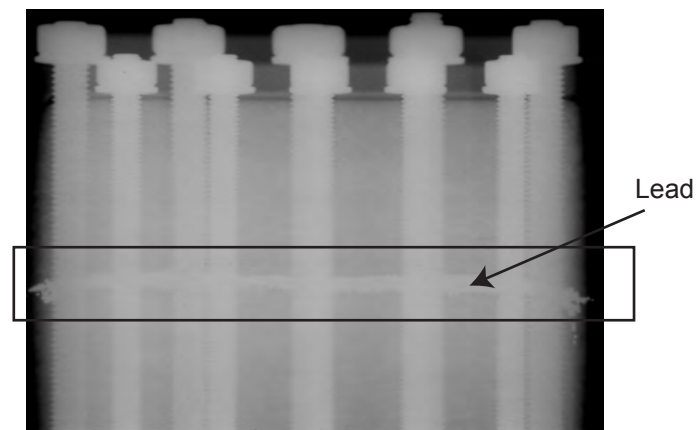


Figure 4.19: An X-ray image of a sample from the side, showing the layer of lead. It is clear that a relatively flat and thin layer of lead has been achieved.

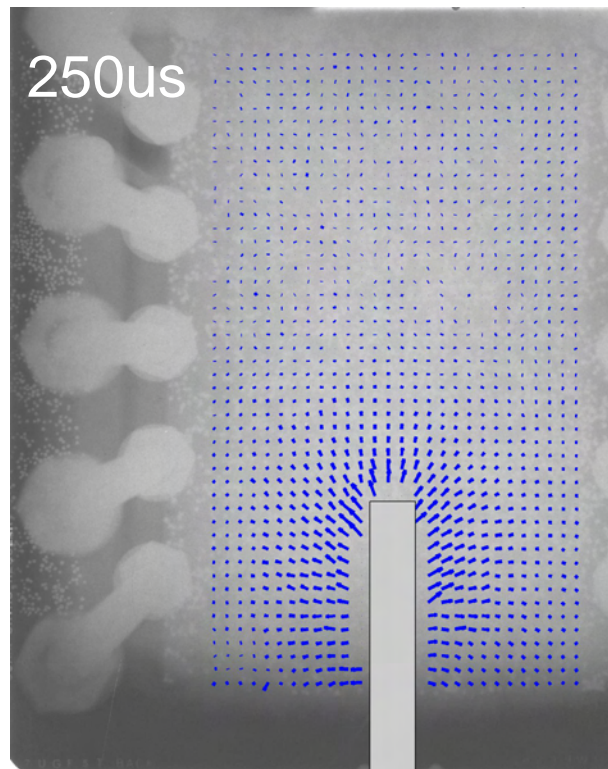


Figure 4.20: A quiver plot of the displacements calculated using the DIC algorithm written for this thesis, super-imposed on the reference X-ray image. Data from $250 \mu\text{s}$ after impact.

4. DYNAMIC PENETRATION OF GRANULAR MEDIA

factor. The scaling factor for the speckle pattern can be determined using the width of the projectile in the dynamic image, since the projectile penetrates directly through the plane of scattered lead at the same distance from the X-ray source. Scaled displacement quiver plots showing the measured displacement fields for penetration by flat-ended projectiles, with an initial velocity of $(200 \pm 4) \text{ ms}^{-1}$, at delay times ranging from 150 to 1500 μs after impact are shown in Figures 4.21, 4.22 and 4.23.

When discussing the measured displacements around the projectile we will discuss displacements parallel to the motion of the projectile, which we shall refer to as the longitudinal, dy , or forward displacements, and displacements perpendicular to the projectile motion, which we will refer to as lateral, sideways or dx displacements.

The quiver plots show that the response of the material is to flow away from the projectile. The material directly ahead of the projectile tip moves forward into the sample and spreads out laterally. The material to the sides of the projectile moves out sideways away from the projectile axis and on average moves forwards into the sample. The magnitude of the displacements decays with increasing distance from the projectile. As the penetration develops the quiver plots in Figure 4.21 and 4.22 show that a growing area of the material on the impact face, to the sides of the projectile axis, moves in the opposite direction to the projectile motion. This area first becomes apparent at 250 μs after impact, shown in the second image of Figure 4.21, and at this stage extends approximately 10 mm into the sample. By 750 μs , shown in the third image of Figure 4.22, approximately the first 30 mm or so of the material behaves in this manner.

The displacement fields are approximately symmetrical around the central axis of the penetrator, which is to be expected from the conservation of momentum. By 150 μs after impact, shown in the first image of Figure 4.21, the lateral displacement of the sand closest to the side of the projectile ranges from 0.8 to 1.2 mm. The magnitude of these displacements decays rapidly with lateral distance from the projectile axis, so that at 30 to 40 mm laterally from the projectile axis the material is at rest. There is also lateral displacement of the material occurring directly in front of the projectile tip, with a magnitude of approximately 1 mm. The material in this area is being split laterally.

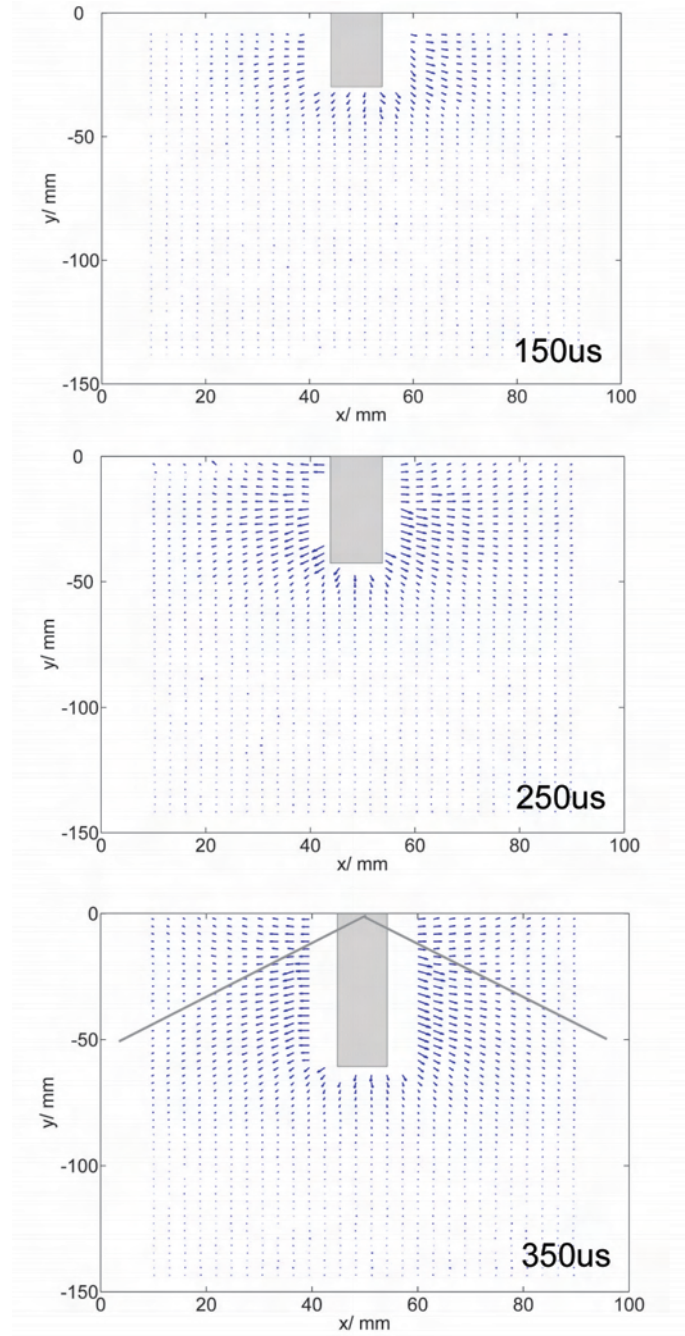


Figure 4.21: Quiver plots showing the displacements for penetration by a flat-ended rod at 150, 250 and 350 μs after impact. The grey lines in the third image show the area of material moving forward with the projectile (below the lines).

4. DYNAMIC PENETRATION OF GRANULAR MEDIA

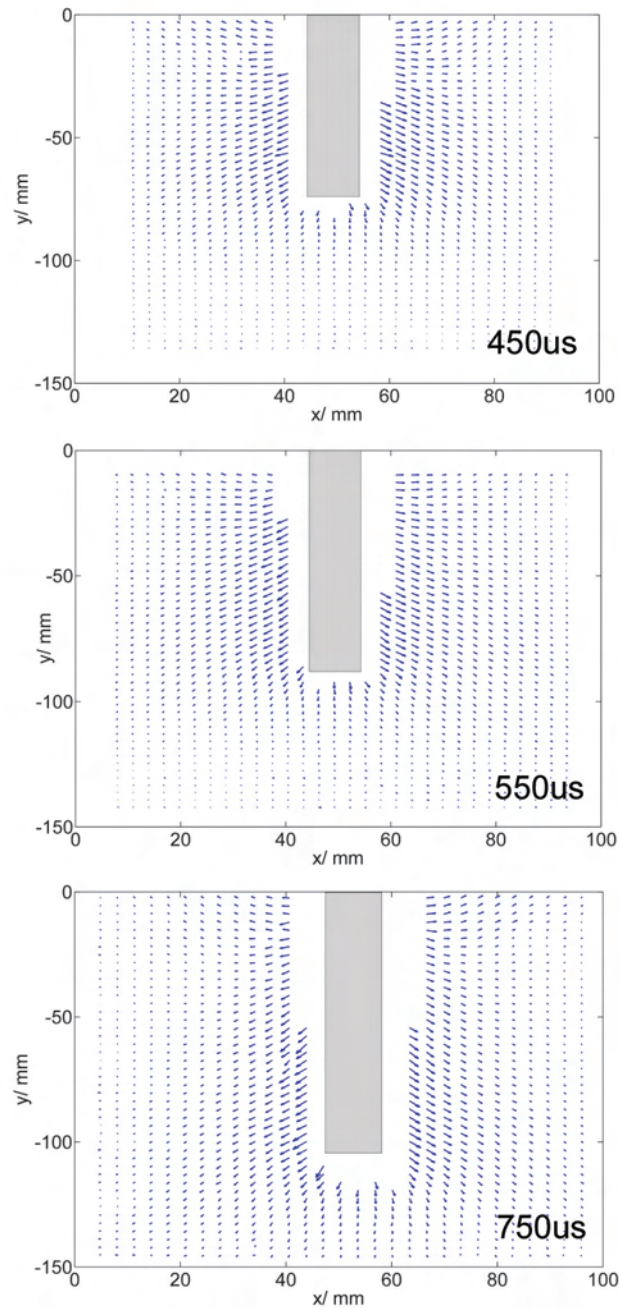


Figure 4.22: Quiver plots showing the calculated displacements for penetration of the sample by a flat-ended rod. The images show the situation at 450, 550 and 750 μs after impact.

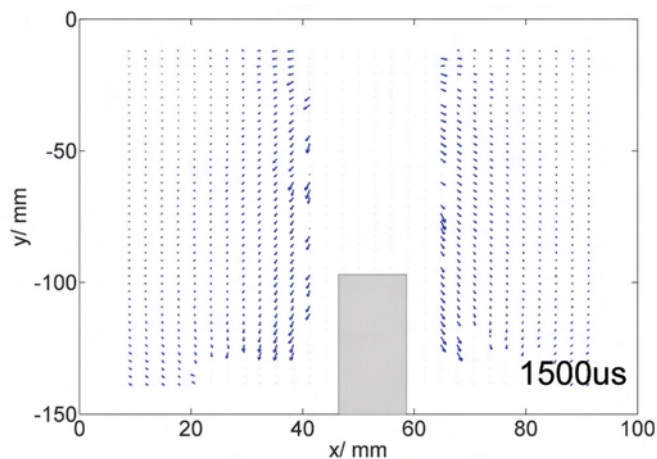


Figure 4.23: Quiver plot showing the calculated displacements for penetration of the sample by a flat-ended rod at $1500 \mu\text{s}$ after impact.

The largest longitudinal displacements at $150 \mu\text{s}$ after impact, shown in the first image of Figure 4.21, occur directly in front of the projectile tip and range in magnitude from 1.5 to 1.8 mm. The material in this region is being pushed forwards into the sample by the flat end of the projectile. The longitudinal displacements ahead of the projectile tip decay rapidly with distance from the tip, so that just 25 mm ahead of the projectile, the material is still largely undisturbed. A large amount of the material to the sides of the projectile is also moving forwards. The longitudinal displacements here reach 1.1 mm in magnitude. The quiver plot of the displacements at $150 \mu\text{s}$ after impact (the first image in Figure 4.21) shows evidence of a cone shaped area of material that is moving forwards into the sample. There appears to be a curved front, emanating from the point of impact with the front surface, behind which the material is moving longitudinally.

This cone shaped area becomes more apparent in some of the later quiver plots, for example the third plot in Figure 4.21, showing the measured displacements at $350 \mu\text{s}$ after impact. Grey lines marked on this quiver plot show the approximate boundary between material that is moving longitudinally in the direction of projectile motion (below the lines), and material that is not (above the lines). These boundaries emanate from the point of impact on the front surface and are joined by a curved front. In order to consider this feature in more detail

4. DYNAMIC PENETRATION OF GRANULAR MEDIA

Delay/ μs	Angle/ degrees
150 ± 2	39.5 ± 1.0
250	43.1
350	39.8
450	39.8
550	37.1

Table 4.2: The angle of the envelope of longitudinal displacements (the 0.2 mm contour) relative to the rod axis. The angle is constant at (40 ± 2) degrees.

it is helpful to plot the longitudinal displacements, showing motion parallel to the projectile motion (dy), and the lateral displacements, showing motion perpendicular to the projectile (dx), separately. This is shown in Figures 4.24 and 4.30 for X-ray delay times between 150 and 750 μs , and discussed in more detail in the following sections.

4.3.1 Longitudinal Displacements

The plots of the longitudinal component of the displacement in Figure 4.24 show a cone shaped region of material moving longitudinally. At 150 μs after impact, shown in (a) of Figure 4.24, the longitudinal displacements extend approximately 25 mm ahead of the projectile tip and have a maximum magnitude of approximately 1.8 mm. By 350 μs after impact, shown in (c) of Figure 4.24, the maximum longitudinal displacement increases to approximately 2.5 mm and the deformation precedes the projectile tip by around 40 mm. The general cone shape of this area remains the same throughout the sequence of images, although the absolute size of the cone changes. The edges of the curved front of the envelope are connected to the point of impact by approximately straight lines, as shown by the grey lines in the third image in Figure 4.21. These boundaries form a roughly constant angle with the rod axis through the sequence of images. The angle for each image, taken relative to the outside edge of the 0.2 mm displacement contour, is listed in Table 4.2.

The angle of the envelope remains constant at (40 ± 2) degrees during the penetration process. This supports the suggestion that there is a travelling front

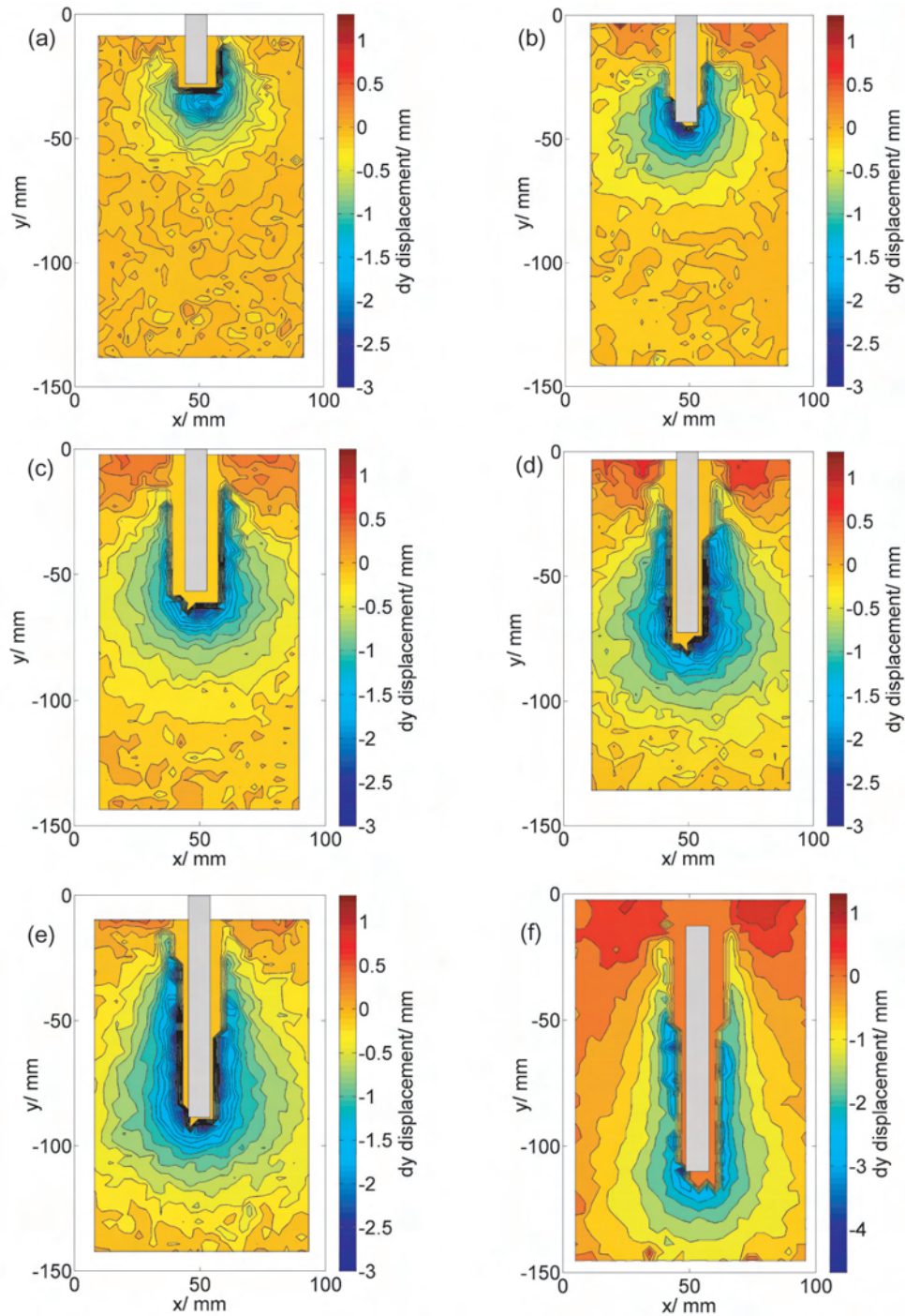


Figure 4.24: Contour plots of the longitudinal displacements at delay times of (a) 150, (b) 250, (c) 350, (d) 450, (e) 550 and (f) 750 μs after impact.

4. DYNAMIC PENETRATION OF GRANULAR MEDIA

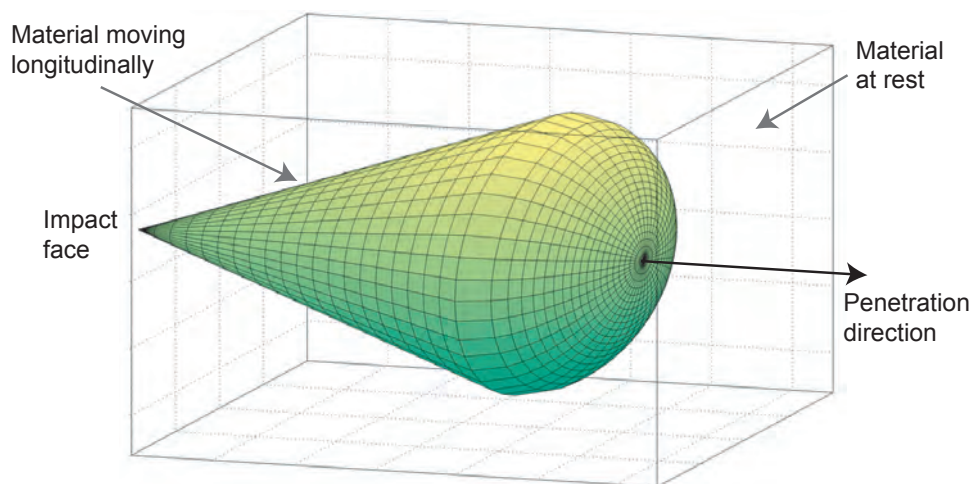


Figure 4.25: Illustration of the 3D envelope of material moving longitudinally, assuming axial symmetry, There is a cone shaped area with a curved travelling compaction front.

which has emanated from the point of impact and which precedes the projectile tip, behind which material has moved longitudinally. An illustration showing this envelope extended into three dimensions, assuming axial symmetry, is shown in Figure 4.25.

The extent of the longitudinal motion occurring directly in front of the projectile tip can be investigated by plotting the variation in magnitude of the longitudinal displacements along a line running directly from the projectile tip to the rear surface of the sample, as shown schematically in Figure 4.26. These displacements are plotted for five different X-ray time delays in Figure 4.27. The magnitude of the longitudinal displacement increases between 150 and 250 μs , but then remains relatively constant for the remainder of the penetration process. Some caution is required when interpreting this data as there is always an area directly in front of the projectile where the sub-images do not correlate, due to the excessive deformation. The maximum measured displacement is therefore likely to be slightly lower than the actual maximum. The magnitude of the longitudinal displacements directly ahead of the projectile decays rapidly with increasing distance from the projectile tip, so that even late on in the penetration

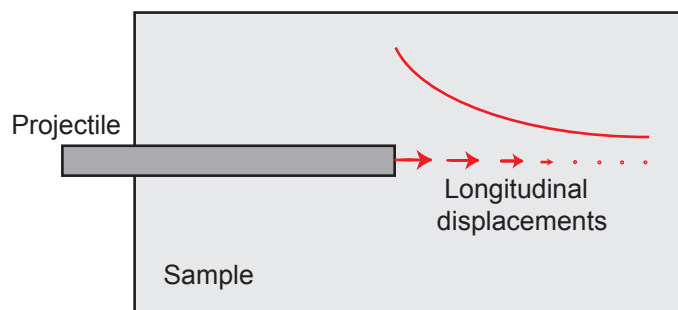


Figure 4.26: An illustration of the variation in longitudinal displacement along a line running from the projectile tip to the rear surface of the sample.

the material 40 mm or more ahead of tip is largely undisturbed.

The rapid decays in displacement shown in Figure 4.27 are well-fitted by single exponential functions. In Figure 4.28, exponential plots are fitted to the displacement profile curves. The fitted exponential curves have very similar decay constants, the mean being $(-0.070 \pm 0.010) \text{ mm}^{-1}$. The physics underlying this exponential decay will be discussed shortly.

When considering the total magnitude of the displacements - both lateral and longitudinal - as shown in Figure 4.29 at $450 \mu\text{s}$ after impact, the same exponential decay of the magnitude of the displacements ahead of the projectile tip is observed. In this case the exponential decay factor is $(0.065 \pm 0.011) \text{ mm}^{-1}$, which is consistent with the previous values.

The plots in Figure 4.24 also show the growth of the area of material on the impact face moving in the opposite direction to the projectile, shown in red. At $250 \mu\text{s}$ after impact, shown in (b) of Figure 4.24, the material to the sides of the projectile on the impact face has moved upwards by between 0.5 and 1 mm. By $450 \mu\text{s}$, shown in (d) of Figure 4.24, the size of this area has noticeably increased so that it extends to a depth of up to 30 mm and the magnitude of the displacement has increased to a maximum of 1.3 mm.

4. DYNAMIC PENETRATION OF GRANULAR MEDIA

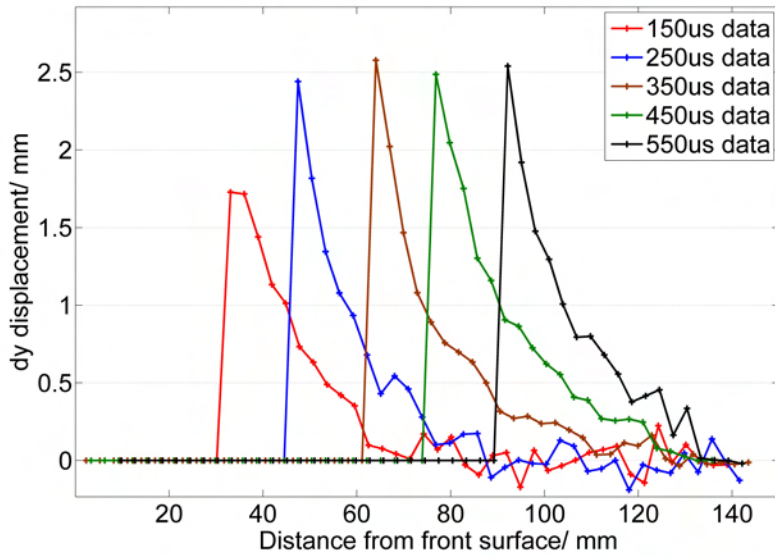


Figure 4.27: Plots showing how the longitudinal displacement varies with distance in front of the rod tip, for a series of different times since impact.

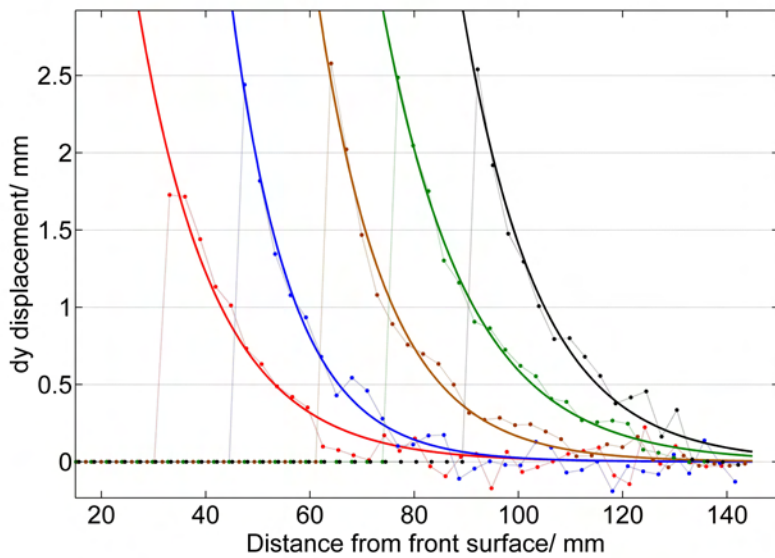


Figure 4.28: Exponential fits to the graphs shown in Figure 4.27.

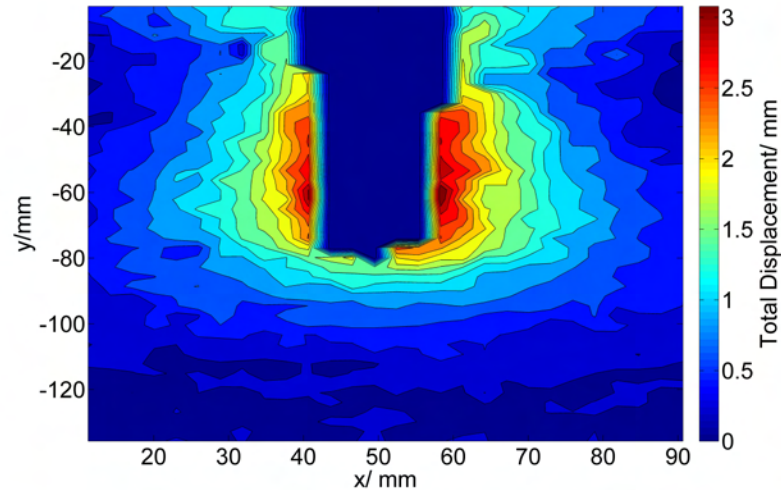


Figure 4.29: Contour plot of the total magnitude of displacement having occurred by $450\mu s$.

4.3.2 Lateral Displacements

We now move on to consider the lateral component of the displacements, shown in Figure 4.30. The maximum lateral displacements are generally found to the sides of the projectile, where displacements of up to 2.7 mm were measured. The lateral displacements have axial symmetry generally, but there are minor asymmetries due to the random granular nature of the material. The maximum lateral displacements measured at $150\mu s$, shown in (a) of Figure 4.30, range from 0.8 to 1.2 mm. The magnitude of these displacements decays rapidly upon moving away from the projectile axis, so that approximately 30 mm from the axis, the material is not moving laterally.

By $250\mu s$, shown in (b) of Figure 4.30, the maximum lateral displacements have increased to 2-3 mm and the displacements now extend to approximately 40 mm out from the projectile axis. The magnitude of the displacements is relatively uniform along the length of the shaft, although it reduces near the impact surface and near the tip of the rod. In all of the images shown in Figure 4.30 the lateral displacement extends ahead of the rod tip, separating the material directly ahead of the rod.

4. DYNAMIC PENETRATION OF GRANULAR MEDIA

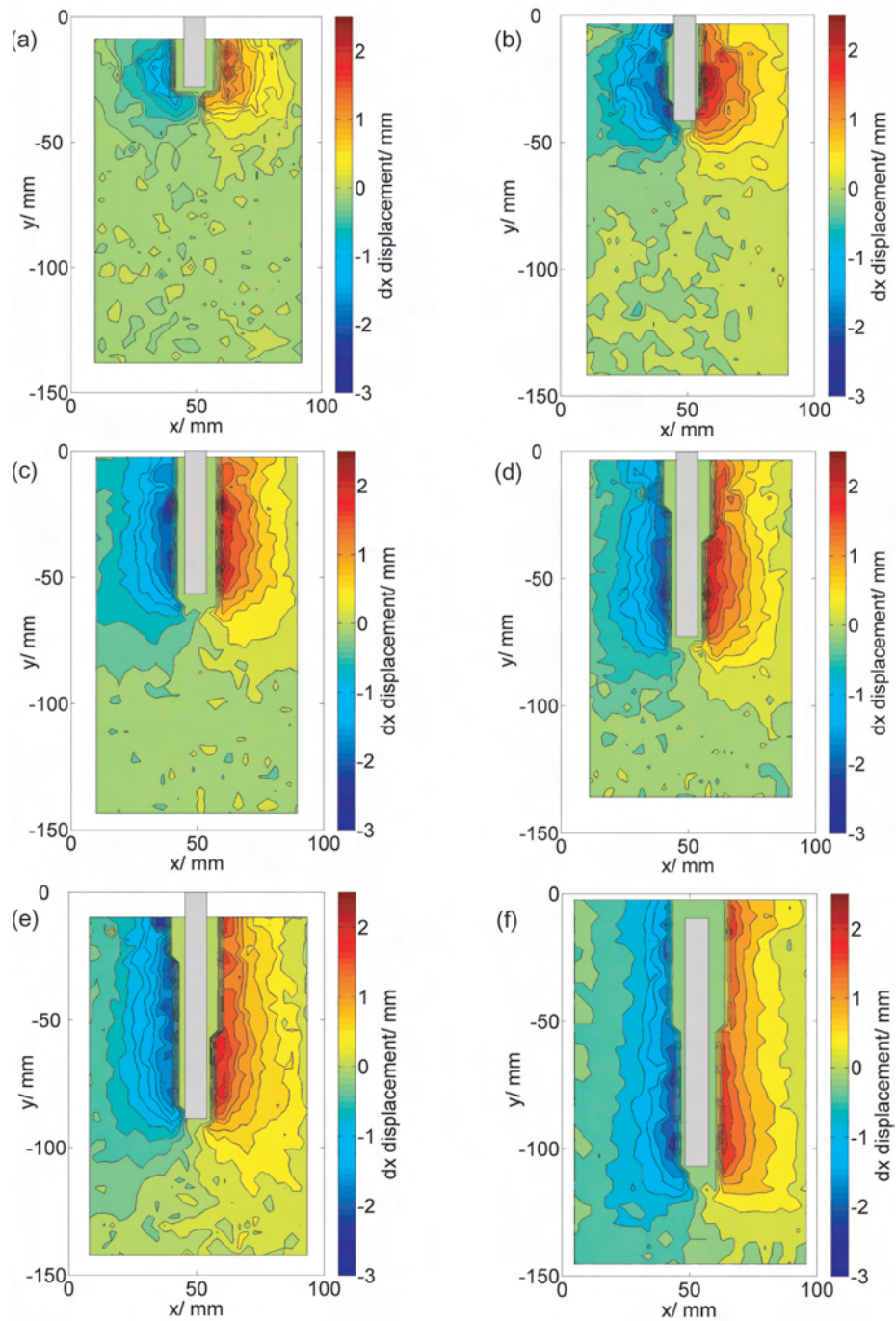


Figure 4.30: Contour plots of the lateral displacements at delay times of (a) 150, (b) 250, (c) 350, (d) 450, (e) 550 and (f) 750 μs after impact.

The images in Figure 4.30 show that the general shape and extent of the lateral displacement envelope does not change dramatically during the penetration. The average maximum lateral displacement, averaged along the length of the rod, remains fairly constant at around 2.1 mm from 250 μ s onwards, although localised maximum values of up to 2.5-3 mm are recorded. The extent to which the envelope of lateral displacements extends to the sides of the shaft also remains relatively constant at around 40 mm. This strongly suggests that most of the lateral displacement is caused by the splitting of the material directly ahead of the projectile tip. Once the projectile tip has passed there is little subsequent change in the lateral displacement.

The variation in magnitude of the lateral displacements to the side of the projectile axis can be considered by plotting the magnitude of the displacements as a function of the lateral distance from the projectile axis, along a horizontal line in the images in Figure 4.30. This variation is shown in Figure 4.31 for a horizontal line located at half the penetration depth from the impact face, as illustrated schematically in Figure 4.32, for three different times since impact. The three sets of displacement data are very similar. In each case, the displacements have a similar maximum value and decay rapidly to zero at a distance of around 40 mm from the projectile axis. No displacements are recorded around $x = 50$ mm as the correlation fails in the area covered by the projectile. Single exponential functions have been fitted to the data showing that, as with the decay of the longitudinal displacements, the magnitude of the lateral displacements decays exponentially with distance from the projectile axis. The similarity of the three data sets taken at increasing delay times again suggests that the majority of the lateral displacement is caused around the projectile tip.

Fitting single decaying exponentials to each set of lateral displacement data shows that the exponential decay constant is very similar in all cases, the average being $-0.063 \pm 0.006 \text{ mm}^{-1}$. The lateral displacements to the sides of the projectile and towards the middle of the penetration depth, D_+ for the displacements to the right of the shaft and D_- for the displacements to the left of the shaft, are therefore well described by the following equations (although the multiplication factors for the exponentials change somewhat along the length of the projectile

4. DYNAMIC PENETRATION OF GRANULAR MEDIA

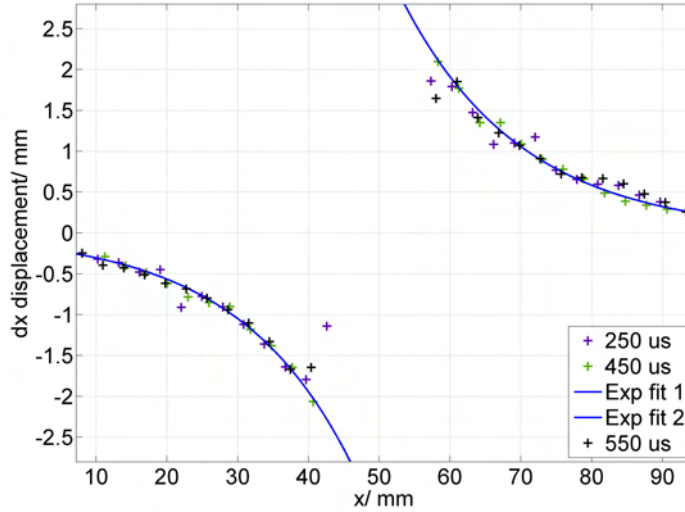


Figure 4.31: The variation of lateral displacement with distance laterally from the projectile axis during dynamic penetration (at 200 ms^{-1}) for three different delay times since impact. The displacement data are well-fitted by single decaying exponentials. No displacement data is recorded in the area occupied by the projectile, around $x = 50 \text{ mm}$.

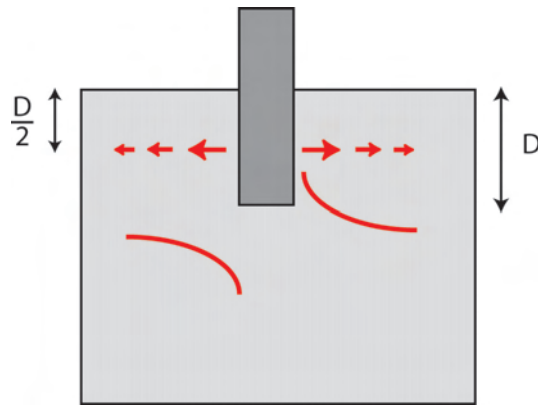


Figure 4.32: A schematic diagram showing the variation in lateral displacement as a function of the lateral distance from the projectile axis along a perpendicular line located at half the penetration depth from the impact face.

and there are anomalies and random variations present):

$$D_+ = (100 \pm 30) e^{(-0.062 \pm 0.006)x}, \quad (4.2)$$

$$D_- = (-0.17 \pm 0.09) e^{(0.064 \pm 0.006)x}. \quad (4.3)$$

Note that the pre-exponential factors are different since the displacements are centred around 50 mm (the position of the projectile) rather than zero, and displacements towards the right of the sample are considered positive while those towards the left are considered negative.

To investigate further how well-described by these equations the lateral displacements are, the measured lateral displacements, and those calculated using the above equations (applied along the length of the projectile), are compared in Figure 4.33 for an X-ray delay time of 350 μs after impact. The filled contour plots in Figure 4.33 demonstrate that 350 μs after impact, allowing for random variations due to the granular nature of the of the sample, the lateral displacements to the sides of the projectile are well described by the above equations. Looking at the residual lateral displacements in this case (the measured lateral displacements minus those determined using the exponential decay equations), shown as a contour plot in Figure 4.34, we see that the differences between the two reach 0.3 mm in magnitude (an error of 12%) and that the displacements immediately to the sides of the projectile are somewhat overestimated.

4.3.3 Decay of the Displacements

The exponential decay constant found for the lateral displacements to the side of the projectile, $(-0.063 \pm 0.006) \text{ mm}^{-1}$, is consistent with that found for the longitudinal displacements ahead of the projectile tip, which was $(-0.070 \pm 0.010) \text{ mm}^{-1}$. We will see in Chapter 6 that a similar exponential decay with a decay factor of $(-0.069 \pm 0.010) \text{ mm}^{-1}$ is observed for the longitudinal displacements ahead of the projectile tip during quasi-static penetration of the sample. The mean decay constant, determined using the lateral and longitudinal displacements (including at quasi-static rates), is $(0.067 \pm 0.011) \text{ mm}^{-1}$. The fact that these three values are consistent suggests that the material is responding in the same way to the applied forces in both locations and at the two different rates. As

4. DYNAMIC PENETRATION OF GRANULAR MEDIA

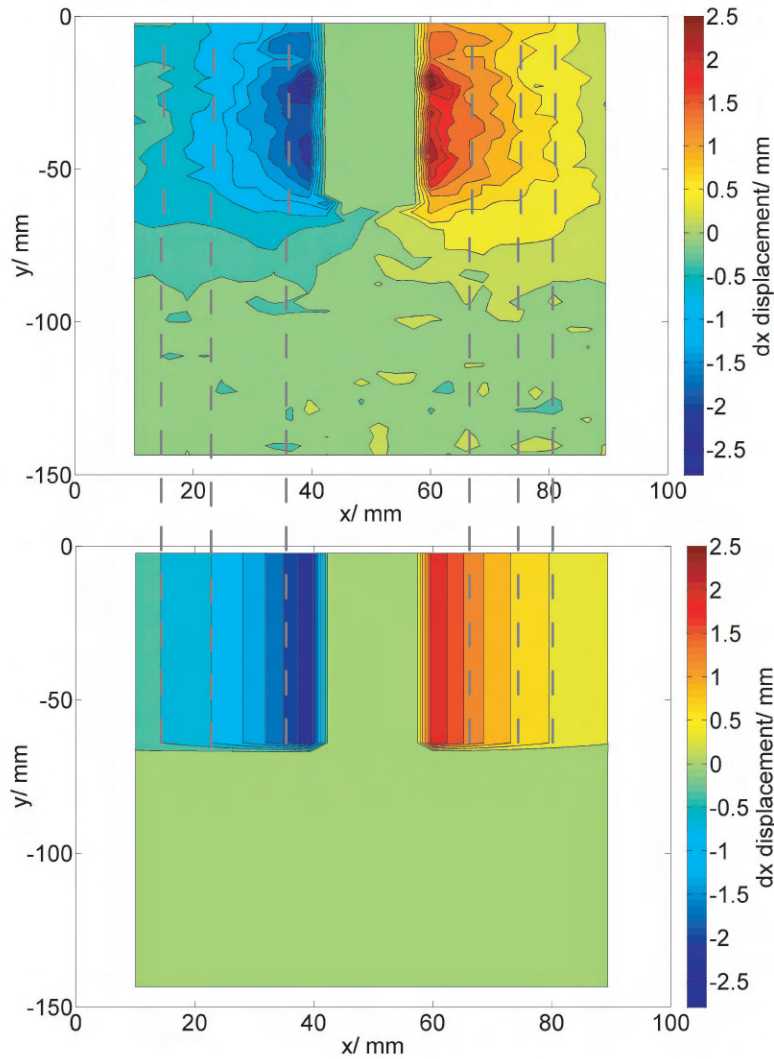


Figure 4.33: A comparison of the measured lateral displacements $350 \mu\text{s}$ after impact at 200 ms^{-1} and the displacements calculated using equations (1.2) and (1.3). There are strong similarities between the two plots suggesting that the lateral displacements are well described by these equations. The differences between the two plots are shown in Figure 4.34 where the residuals are plotted.

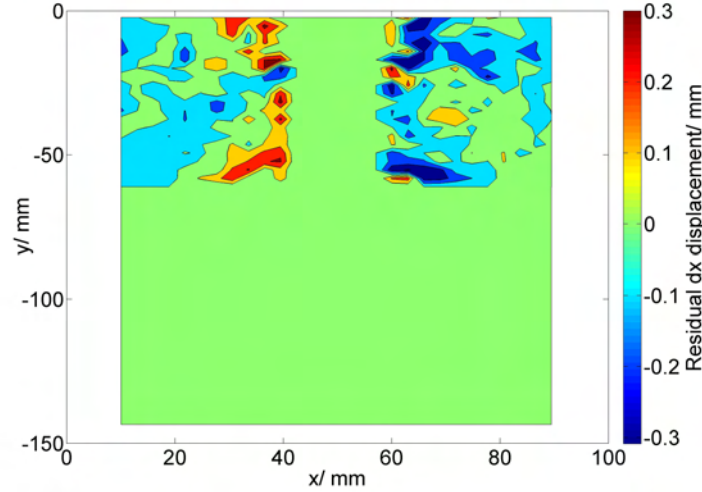


Figure 4.34: The measured lateral displacements shown in Figure 4.33 minus the lateral displacements predicted using equations (1.2) and (1.3). The differences reach 0.3 mm in magnitude (a difference of 12%) and the displacements close to the projectile appear to be somewhat overestimated.

the decay is exponential, we can identify a half-life distance, $d_{\frac{1}{2}}$, as the distance where the displacements have fallen to half of their original magnitude.

$$d_{\frac{1}{2}} = \frac{\ln(2)}{\lambda}, \quad (4.4)$$

where λ is the decay constant. The measured exponential factors give half-life distances ranging from (9.9 ± 1.0) to (11.1 ± 1.0) mm and a mean half-life distance of (10.5 ± 0.8) mm, showing that the displacements decay rapidly with distance from the projectile.

Similar exponential decay relationships are seen in processes such as the attenuation of gamma radiation by lead, the attenuation of light by an optical material or the attenuation of sound waves in dissipative media. Recent research looking at the attenuation of ultrasound pulses in sand saturated with water have shown that the amplitude of ultrasound signals decays exponentially with distance between a transmitter/receiver and a reflective target embedded in the sand [10].

4. DYNAMIC PENETRATION OF GRANULAR MEDIA

An exponential decay constant is a measure of how the material dissipates energy. For an ultrasound pulse, most of the energy is dissipated through two main processes - scattering of the pulse at inhomogeneities where there is a discontinuity in the impedance, and dissipation of energy within the sample. A granular material such as sand, which is composed of a porous mixture of grains of different materials, will scatter a high proportion of the ultrasound pulse. Dissipation of energy within the granular material occurs through processes such as compaction of the material and rotation and motion of the grains against the action of friction.

To determine whether it is the compaction of the column of material ahead of the projectile that leads to the observed exponential decay, a separate experiment was performed in which DSR was used to investigate low rate compaction of a column of sand by a uniform piston. A cubic sample of sand with a side length of 100 mm containing a vertical plane of randomly scattered lead was used. The sample was uniformly compacted by pushing in a square piston to a maximum depth of 20 mm, giving a maximum ‘strain’ of 0.05. The DIC algorithm was used to analyse images of the lead speckle pattern at various extents of compaction, allowing the variation of the vertical displacement with distance from the piston to be measured. An example of the measured displacements is shown as a quiver plot in Figure 4.35.

The displacement data for two different extents of compaction (2.5 mm and 4.7 mm displacement of the piston) are shown in Figure 4.36. For each set of data, the vertical displacements at each height were averaged across the width of the sample to remove the small variations in vertical displacement caused by inhomogeneities in the material. Linear relationships were fitted to the experimental data.

That the vertical displacements vary linearly in this manner is a surprise. It suggests that the sand sample is on average behaving in a similar manner to a uniform solid, in that the whole sample has been uniformly strained during the compaction. If a material is strained to a uniform strain ϵ , the definition of strain,

$$\epsilon = \frac{\Delta l}{l_0}, \quad (4.5)$$

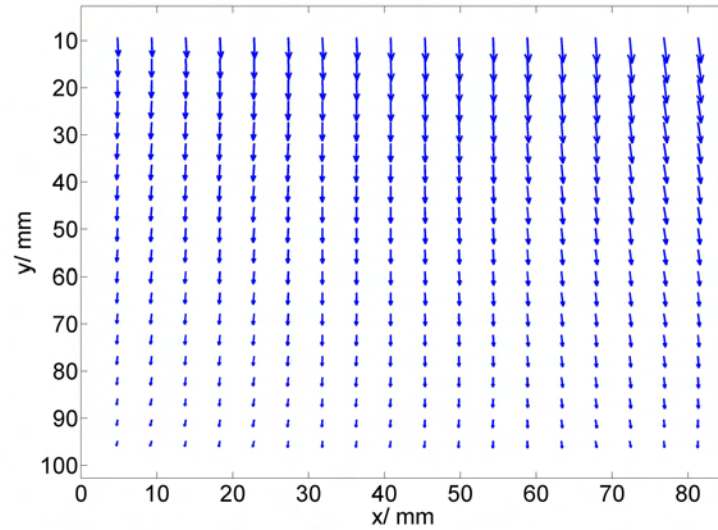


Figure 4.35: A quiver plot showing the measured displacements during uniform compaction of a column of sand.

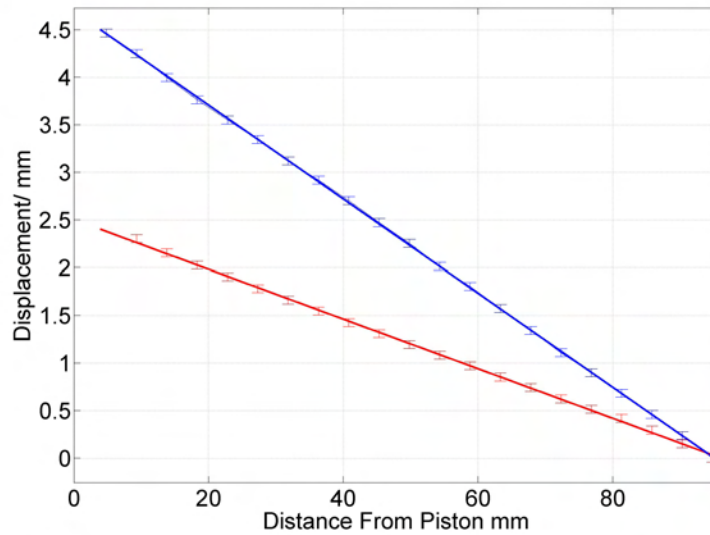


Figure 4.36: Plots showing how the longitudinal displacement varies with distance from the face of the piston during uniform compaction of a column of sand, for two different extents of compaction. Red = 2.5 mm displacement of the piston, Blue = 4.7 mm.

4. DYNAMIC PENETRATION OF GRANULAR MEDIA

where l_0 is the original height and Δl is the change in height, shows that the displacement at any height, Δl , will be linearly related to the height. For a uniform strain to occur the forces must be transmitted throughout the sample uniformly, so that the whole sample experiences the same compacting pressure. It appears that for this extent of compaction (greater than 2.5 mm) the porosity has been sufficiently reduced that the forces can be transmitted throughout the whole sample, leading to a uniform compaction. The red line shows the measured displacements after the piston has moved 2.5 mm into the material. This is comparable to the maximum longitudinal displacements measured ahead of the projectile tip during the penetration experiments.

This result suggests that the observed exponential decay of the displacements in the column of material directly ahead of the projectile tip cannot be explained solely by considering dissipation of energy through compaction of the material in this column. Unlike in the box example given above, the column of material ahead of the projectile is not part of a larger confined sample being uniformly compacted. Instead, it is surrounded by sand that is initially at rest and which does not provide a rigid confinement. In order to explain the decay of the displacements in the column of material ahead of the projectile tip we must consider some form of ‘scattering’ of the displacements into this surrounding material, in analogy to the scattering of the ultrasound pulse discussed earlier.

Scattering of the displacements can be understood as the inhomogeneous granular structure of the sand converting some of the longitudinal or lateral component of the displacement into the other perpendicular component, and through these displacements spreading out in three dimensions ahead of the projectile tip. As these displacements spread out through the sample ahead of the projectile tip the magnitude of the displacements in the column of material directly ahead of the projectile tip will fall. This is shown schematically in Figure 4.37, where a purely vertical displacement ahead of the projectile tip is dissipated across the sample through the generation of lateral displacements due to the random arrangement of grains (shown as spheres).

Therefore, in analogy to the decay of an ultrasound pulse in a granular material, the exponential delay in the magnitude of the displacements in the column of material directly ahead of the projectile tip is caused by the combined effects

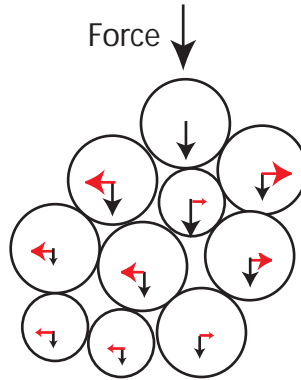


Figure 4.37: A schematic showing how a purely vertical displacement ahead of the projectile tip is 'scattered' by the transformation of some of the energy into horizontal displacement. Horizontal displacements are shown in red, vertical in black. As the displacement spreads out through the sample the measured force in the localised column of material ahead of the projectile will fall.

of energy dissipation through compaction of the material, and 'scattering' of the displacements into the surrounding material.

4.3.4 High-Speed Video

For some experiments, high speed video footage was taken using a Photsonics Phantom V4.3 high speed video camera. Figure 4.38 shows three images from a larger sequence showing the penetration of a sample by a flat-ended projectile. The images were taken at 16,000 frames per second (an inter-frame time of $63 \mu\text{s}$). While the projectile is entirely within the sample (middle image), there is no outward sign that the penetration is occurring. This suggests that the degree of deformation occurring ahead of the projectile is limited, although it is important to remember that the far side is constrained by card. When exiting the rear surface of the sample the projectile takes a cone of material with it. This is shown in the images in Figure 4.39, where the high-speed camera has been focused on the rear surface of the sample.

In some of the experiments discussed in the following chapter, high-speed video is used to measure the velocity of the projectile during penetration of the

4. DYNAMIC PENETRATION OF GRANULAR MEDIA

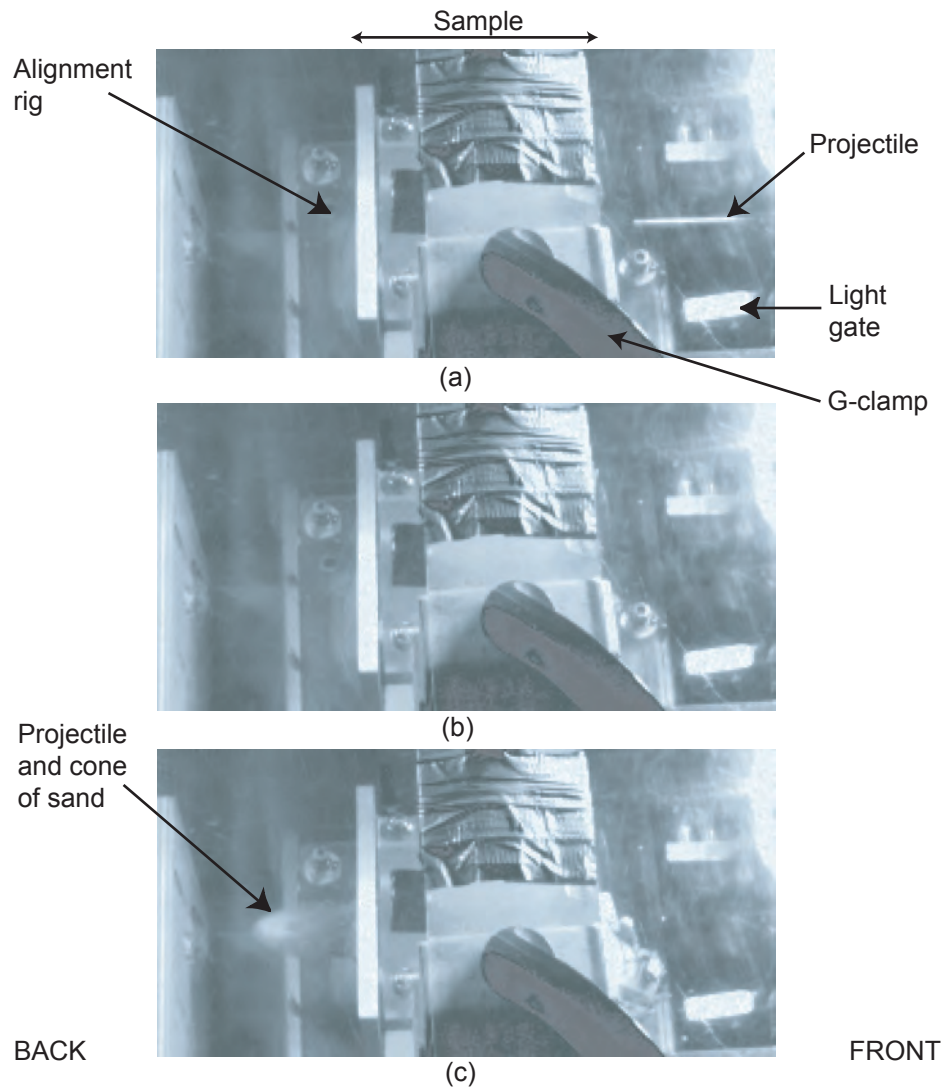


Figure 4.38: A sequence of high-speed video images showing a plan view of penetration of the sample by a flat-ended projectile. The images show: (a) The moment before impact. (b) The projectile entirely within the sample. (c) The projectile exiting the sample.

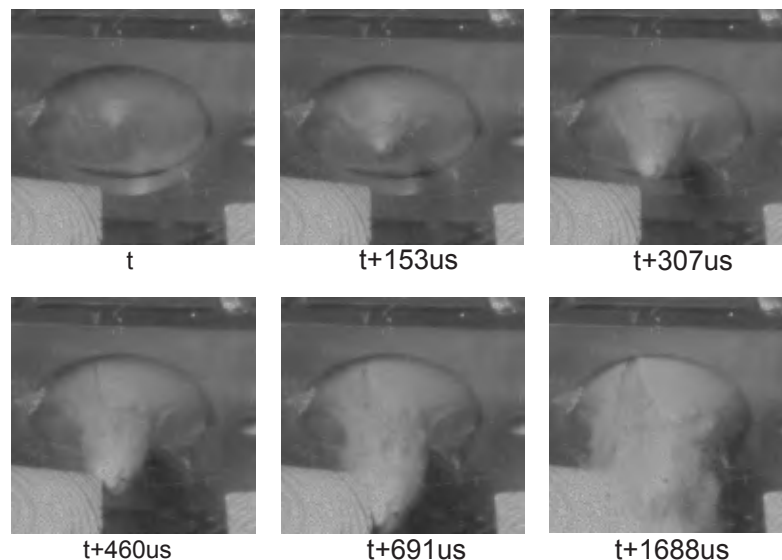


Figure 4.39: A sequence of high-speed video images, showing a flat-ended projectile exiting the back of the sample.

front surface.

4.3.5 Penetration Velocity

The depth of penetration of the projectile at a given time can be measured directly from the X-ray images. Care must be taken with some of the images, as there appears to be a cone of denser material at the projectile tip which can increase the difficulty of locating the projectile tip in the images (leading to relatively large errors in the velocity measurements). Figure 4.40 shows a graph of penetration depth of the flat-ended projectile as a function of the time since impact. There is an apparent change in gradient at $150 \mu\text{s}$ and a constant gradient for the remaining time. Using the measurements of penetration depth as a function of time, an estimate of the instantaneous velocity of the projectile can be made for a series of penetration depths, as shown in Figure 4.41. Each data point in Figure 4.41 represents a separate experiment. At each time delay the instantaneous velocity was approximated by comparing the depth of penetration with that recorded in the previous experiment at an earlier time. The average

4. DYNAMIC PENETRATION OF GRANULAR MEDIA

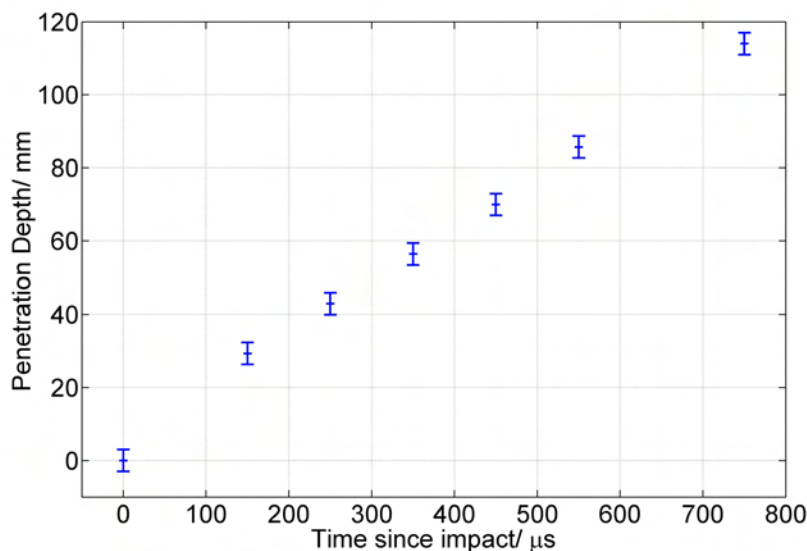


Figure 4.40: A plot of penetration depth as a function of time since impact for the flat-ended projectile. The errors are estimated from the difficulty in determining the position of the projectile tip in the X-ray images (where the contrast is often poor).

velocity of the projectile over the intervening time period, generally $100 \mu\text{s}$ for the earlier experiments, could then be calculated.

The velocity data show that there is a considerable decrease in the velocity of the penetrator between a depth of 20 - 40 mm (corresponding to between 150 and $250 \mu\text{s}$ after impact). The velocity falls from $(200 \pm 3) \text{ms}^{-1}$ to $(140 \pm 5) \text{ms}^{-1}$. What is then surprising is that the velocity of the projectile appears to change little after this initial decrease, remaining fairly constant around 140ms^{-1} up to $750 \mu\text{s}$. This suggests that the projectile feels a considerable force during the early stages of the penetration, but that after $250 \mu\text{s}$ the projectile experiences little subsequent force. At this time the projectile and the surrounding sand appear to have reached an equilibrium, such that little further energy is exchanged between them.

The velocity and displacement data combined suggest that the early stages of the impact cause a large body of sand to be set in motion. This is consistent with

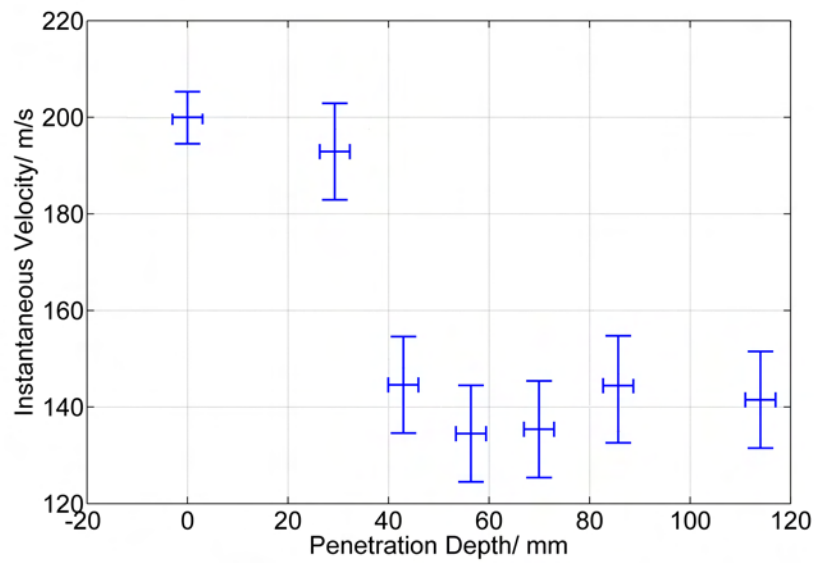


Figure 4.41: A plot of instantaneous velocity as a function of penetration depth for the flat-ended projectile. The instantaneous velocity at each time is calculated by comparing the extent of penetration with the previous X-ray image. The large errors are due to the difficulty in locating the position of the projectile in the X-ray images.

4. DYNAMIC PENETRATION OF GRANULAR MEDIA

the observed large area of disturbed material in the early plots of Figures 4.30 and 4.24, and with the large drop in the velocity of the projectile during the first 250 μs of the penetration shown in Figure 4.41. Beyond this, a second phase of motion occurs in which the extent to which the displacements stretch ahead of the projectile and the projectile velocity remain relatively constant. At this stage, the projectile is moving through material that has been disturbed and set in motion by the compaction front. This leads to significantly reduced resistive forces on the projectile relative to the early stages. For a period of time, a steady-state form of penetration is reached. If the penetration were followed further, dissipative processes such as compaction and shearing of the sand would slow the moving area of sand and the projectile would experience significant further resistive forces. This does not appear to have occurred to any great extent by 750 μs .

We will discuss these observations in more detail in the following chapter after considering the influence of projectile nose shape on the penetration.

4.4 Summary

To summarise the conclusions so far

- DSR, in conjunction with the DIC algorithm written for this thesis, has produced high resolution data on the displacement fields within a large sample of granular material experiencing penetration by a projectile.
- The data provide information about the response of the material to penetration and allow direct quantitative measurement of the resulting displacements.
- The lateral displacements (perpendicular to the rod) are roughly uniform along the length of the projectile. This suggests that the lateral displacement is caused by the movement of the projectile tip. Once it has passed, little further lateral displacement occurs.
- These lateral displacements to the side of the projectile decay exponentially with lateral distance from the projectile axis, with a decay constant of $(-0.063 \pm 0.006) \text{ mm}^{-1}$.

- The material directly ahead of the projectile tip is split laterally, reducing the amount of material pushed ahead of the rod.
- There is an expanding envelope behind which the material is in motion. This emanates from the point of impact and consists of an expanding cone with a curved front surface. The sides of this cone make a fixed angle of (40 ± 2) degrees to the projectile axis.
- The curved front of this area represents a travelling compaction wave generated in the material during impact.
- The displacements directly ahead of the projectile tip increase in magnitude between 150 and 250 μs , to around 2.5 mm, but then remain approximately constant.
- The displacements in the column of material ahead of the projectile tip decay exponentially, with a decay constant of $(-0.070 \pm 0.010) \text{ mm}^{-1}$. This value is consistent with the decay constant for the lateral displacements to the side of the projectile axis.
- The half-life distance for the displacements around the projectile, in which the magnitude of the displacement falls to half the original value, is $(10.5 \pm 0.8) \text{ mm}$.
- The exponential decay appears to be caused by the displacements spreading out in three dimensions into the surrounding material, leading to the conversion of longitudinal displacement to lateral displacement, and vice-versa.
- Energy is also dissipated through processes such as compaction and the motion and rotation of grains against the action of friction, causing work to be done.
- The initial impact (before 250 μs) of the projectile sets a body of sand in motion, generating a significant resistive force on the projectile and causing its velocity to fall sharply. This body of moving sand extends ahead of the projectile tip by up to 40 mm.

REFERENCES

- After the initial stages of the impact (after 250 μs), the projectile moves through a body of sand that is also moving. This leads to significantly reduced resistive forces relative to the early stages. For a period of time, the projectile and surrounding sand have entered a steady state, where little further energy is exchanged between them and the velocity therefore plateaus.
- If the penetration were followed further, dissipative processes such as compaction and shearing of the sand would slow the moving area of sand, and the projectile would experience further resistive force. This does not appear to have occurred to a significant extent by 550 μs .

References

- [1] Grantham, S.G., *Digital Speckle Radiography*, Phd, University of Cambridge (2002)
- [2] Grantham, S.G., Goldrein, H.T., Proud, W.G. and Field, J.E., “Digital speckle radiography - a new ballistic measurement technique”, *Imaging Sci. J.*, **51**, (2003), 175–186
- [3] Grantham, S.G., Proud, W.G. and Field, J.E., “The study of internal deformation fields in materials using digital speckle radiography”, *25th International Congress on high-speed photography and photonics*, **4948**, (2003), 592–597
- [4] Chapman, D.J., Proud, W.G., Tsembelis, K. and Collins, A., *Hard Target Research: Final Progress Report*, Internal Report SP 1184, University of Cambridge (2007)
- [5] McCave, I.N., Bryant, R.J., Cook, H.F. and Coughanower, C.A., “Evaluation of a laser-diffraction-size analyser for use with natural sediments”, *J. of Sedimentary Research*, **56(4)**, (1986), 561–564

REFERENCES

- [6] Goldstein, J., Newbury, D.E., Joy, D.C., Echlin, P., Lyman, C.E., Lifshin, E. and Sawyer, L., *Scanning electron microscopy and x-ray microanalysis*, Springer, US (2003)
- [7] Sjudahl, M. and Benckert, L.R., “Electronic speckle photography: analysis of an algorithm giving the displacement with subpixel accuracy”, *Applied Optics*, **32(13)**, (1993), 2278–2284
- [8] Abramoff, M.D., Magelhaes, P.J. and Ram, S.J., “Image Processing with ImageJ”, *Biophotonics International*, **11(7)**, (2004), 36–42
- [9] Hutchings, I.M. and Winter, R.E., “A simple small-bore laboratory gas-gun”, *E: Sci. Instrum*, **8**, (1975), 84–90
- [10] Seo, K., Shirakawa, T. and Sugimoto, T., “Ultrasonic exploration at extreme shallow underground in submerged soil.”, *Proceedings of Acoustic 08 Paris*, **1**, (2008), 6479–6483

REFERENCES

Chapter 5

Effect of Projectile Nose Shape

5.1 Introduction

An equivalent set of experiments to those discussed in the previous chapter was performed using a projectile with an ogive-2 nose shape (100 mm length to the tip, 10 mm diameter). Ogive projectiles have sharpened nose cones, such that the nose profiles are surfaces of revolution of a circular arc. The radius of curvature of the circular arc here was 20 mm, twice the diameter of the projectile. Figure 5.1 shows the design of the ogive projectiles. Ogive nose-cones are frequently found in bullets and missiles where they are intended to minimise drag [1]. An impact velocity of $(200 \pm 4) \text{ ms}^{-1}$ was used in the experiments, so as to be consistent with the previous experiments using flat-ended projectiles.

A series of experiments was also performed using projectiles with hemispherical nose cones. High-speed video was used to monitor the penetration of the front surface by hemispherical projectiles, to determine the velocity of the projectile during the penetration process. This provides an alternative method for measuring the velocity profile of the projectile during the penetration, for comparison with that obtained from measuring the position of the projectile on the X-ray images. Details of all the experiments performed are given in Tables A.1, A.2 and A.3 in Appendix A.

5. EFFECT OF PROJECTILE NOSE SHAPE

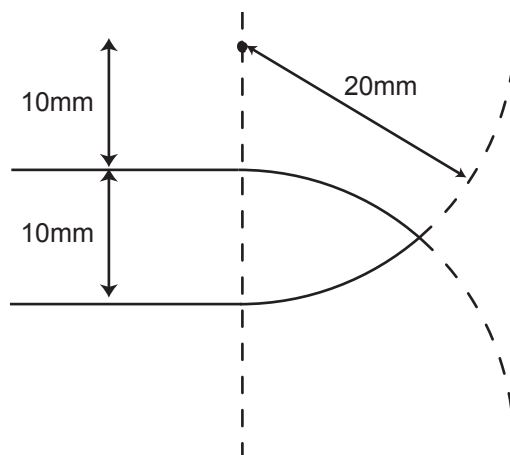


Figure 5.1: A schematic showing the main features of an ogive-2 nose shape. The ogive nose shape is a surface of revolution of a circular arc.

5.2 Results and Discussion

The measured displacement data for penetration by an ogive-2 projectile are shown as a series of quiver plots in Figures 5.2 and 5.3. Contour plots of the lateral and longitudinal components of the displacement are shown in Figures 5.4 and 5.5. The displacement data for penetration by a hemispherical projectile appeared indistinguishable from the data presented in these figures (and is therefore not shown), suggesting that there is little difference in the penetration properties of the two nose shapes. The effect of nose shape on the measured displacements will be discussed later in this chapter.

The displacement plots show that the pattern of the displacements is very similar to that observed for a flat-ended projectile. The maximum lateral displacements close to the projectile shaft range from 0.6 to 1.2 mm in magnitude at 150 μs after impact, shown in the second image of Figure 5.2. These increase to between two and three millimetres after 250 μs , shown in the third image, which is consistent with the corresponding displacements for the flat-ended projectile. The longitudinal displacements reach a maximum of 1.8 mm ahead of the projectile tip at 150 μs , before increasing further to approximately 2.5 mm at later times. These values are again consistent with those measured for a flat-ended

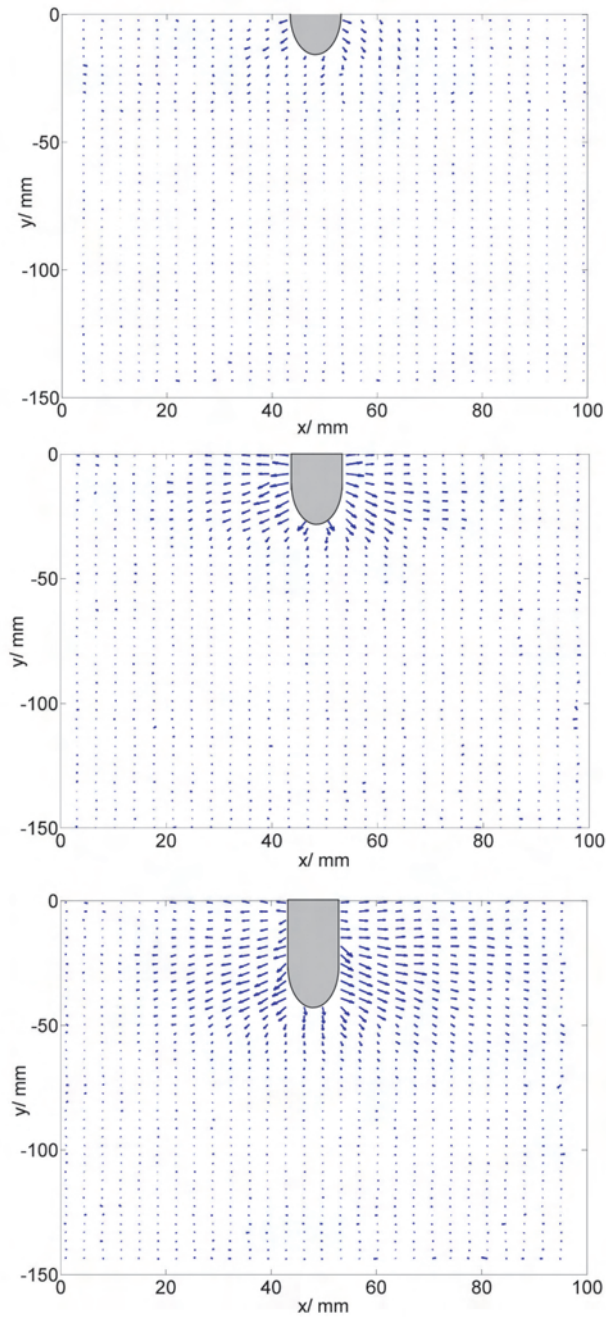


Figure 5.2: Quiver plots showing the displacements produced by penetration of the sample by an ogive tipped projectile, at 60, 150 and 250 μs after impact.

5. EFFECT OF PROJECTILE NOSE SHAPE

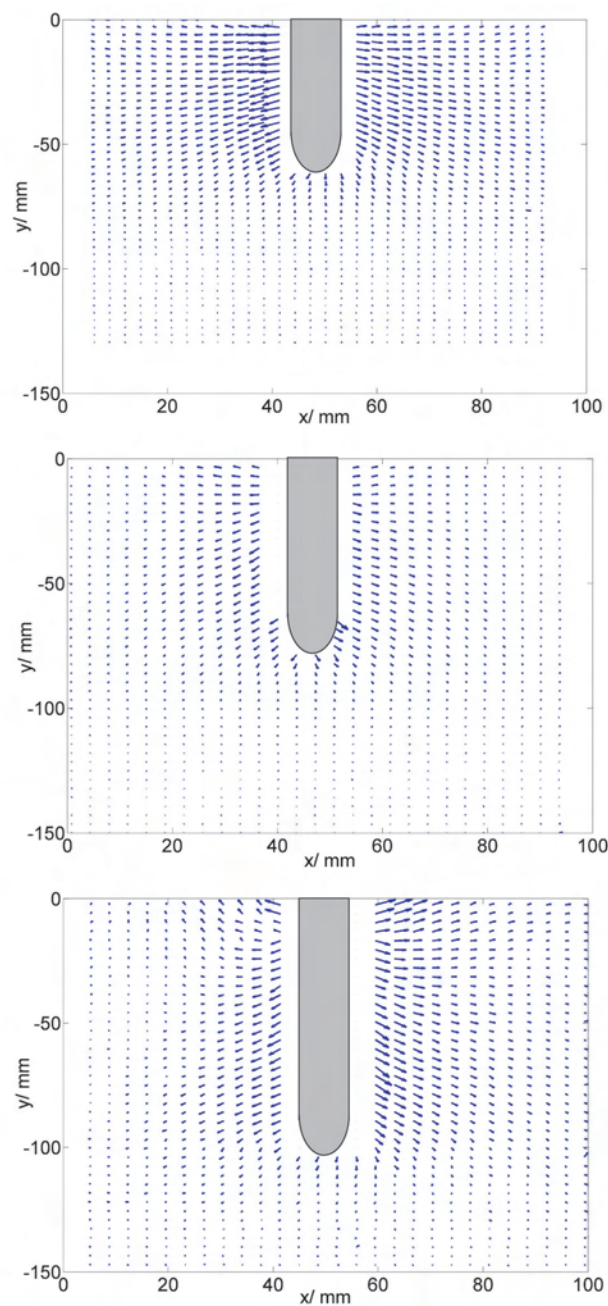


Figure 5.3: Quiver plots showing the displacements produced by penetration of the sample by an ogive tipped projectile at 350, 450 and 550 μs after impact.

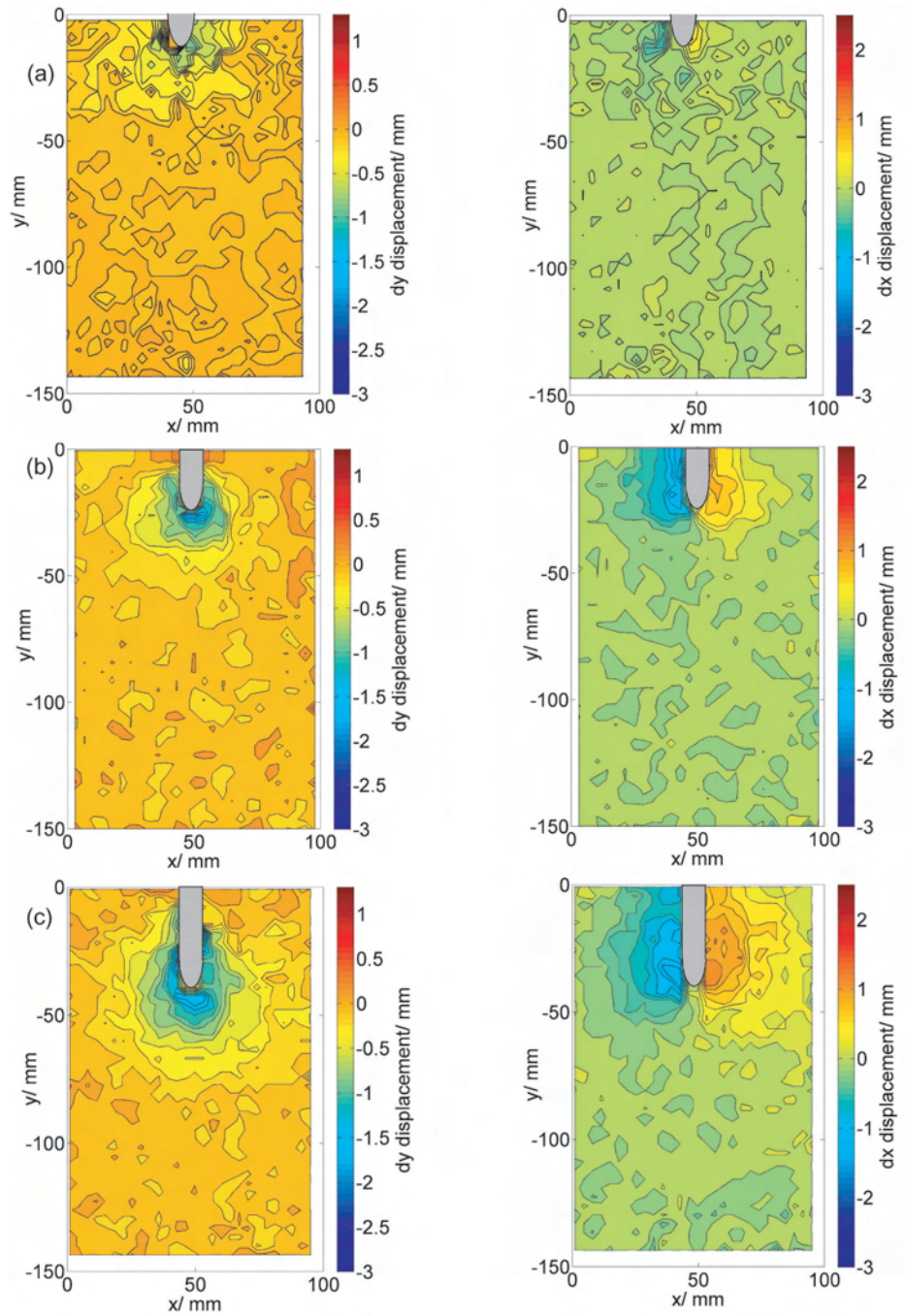


Figure 5.4: Contour plots of the dy displacements (left images) and dx displacements for delay times of (a) 60, (b) 150 and (c) 250 μs for penetration by ogive projectiles.

5. EFFECT OF PROJECTILE NOSE SHAPE

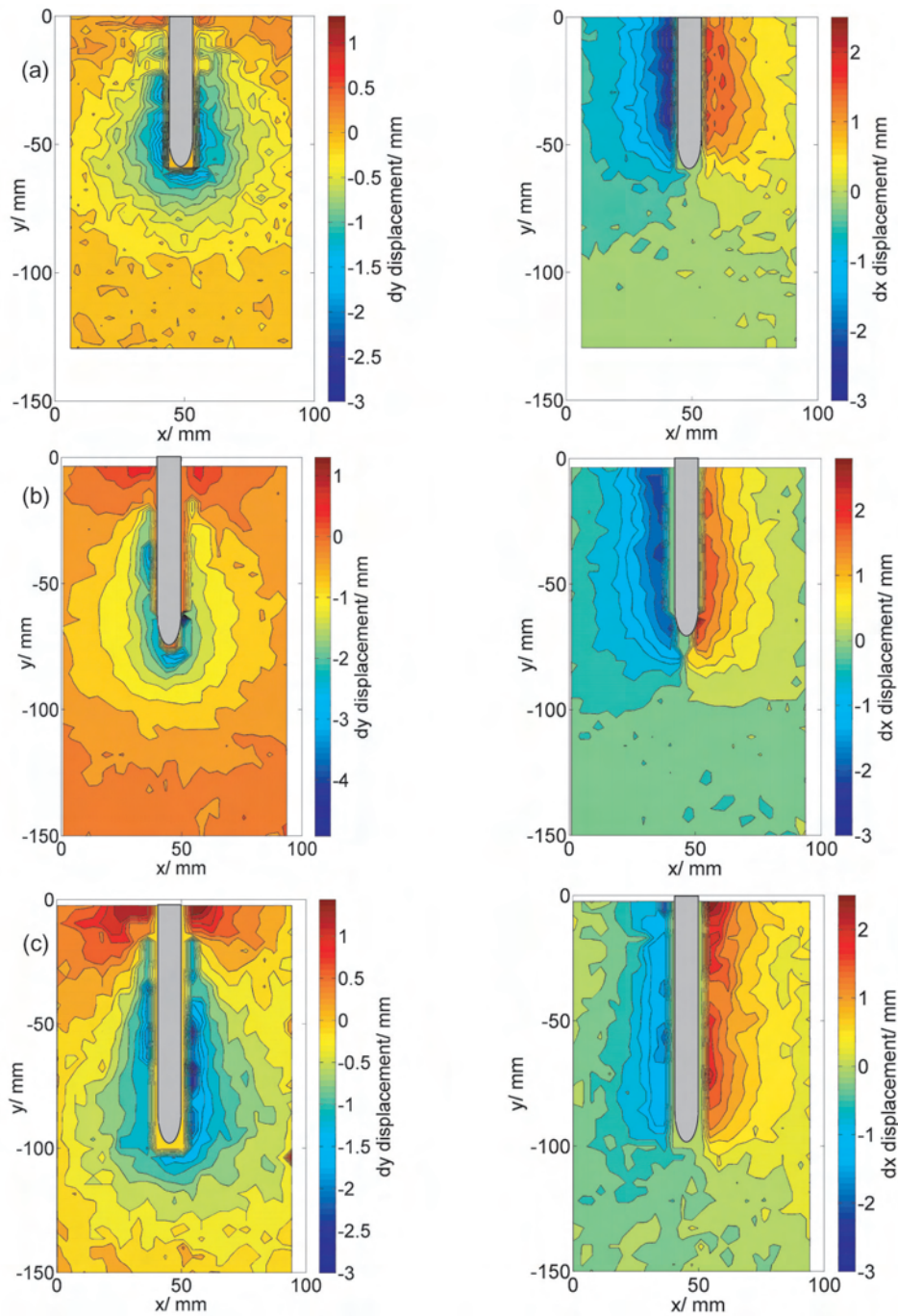


Figure 5.5: Contour plots of the dy displacements (left images) and dx displacements for delay times of (a) 350, (b) 450 and (c) 550 μs for penetration by ogive projectile.

projectile.

Comparing the plots of the displacement data with the equivalent plots presented in the previous chapter for penetration by flat ended projectiles (for example Figures 4.30 and 4.24), we see that the area directly around the projectile in which the correlation fails is narrower with the ogive projectile. This suggests that the extent of the deformation occurring in the area immediately around the rod is somewhat less severe in this case (the correlation fails when the sub-images have been subject to severe compaction, shearing or considerable rotation).

The general similarities in the sets of displacement data can be seen more clearly in Figure 5.6, in which the longitudinal (dy) and lateral (dx) components of the displacement are compared for penetration by ogive (left images) and flat-ended (right images) projectiles at $350 \mu s$ after impact. Although the displacement plots appear very similar, there is one important difference. The plot of the longitudinal displacements shows that the displacements extend further ahead of the tip of the projectile with a flat-ended projectile. For the flat-ended projectile the longitudinal displacements extend to approximately 50 mm ahead of the projectile tip, as compared to approximately 40 mm for the ogive case. This suggests that the flat-ended projectile causes more disruption to the material ahead of the projectile tip. There are no significant differences apparent in the plots of the lateral displacements.

To investigate in more detail the disruption being caused ahead of the projectile tip, it is helpful to plot the magnitude of the lateral (dx) and longitudinal (dy) displacements along a perpendicular line ahead of the projectile tip, as illustrated schematically in Figure 5.7. At a given distance along this perpendicular line (a certain x value) the magnitude of either the lateral or longitudinal displacement is recorded. These values are plotted in Figure 5.8 for a perpendicular line 15 mm ahead of the projectile tip for penetration by both flat-ended and ogive projectiles (again, the hemispherical results were consistent with those measured with an ogive projectile and are not shown).

Both the lateral (top image) and longitudinal displacements (bottom image) are larger ahead of the projectile for penetration by a flat-ended projectile (shown in blue). The longitudinal displacements are greater by almost a factor of two. The results confirm that a flat-ended projectile causes more disturbance in the

5. EFFECT OF PROJECTILE NOSE SHAPE

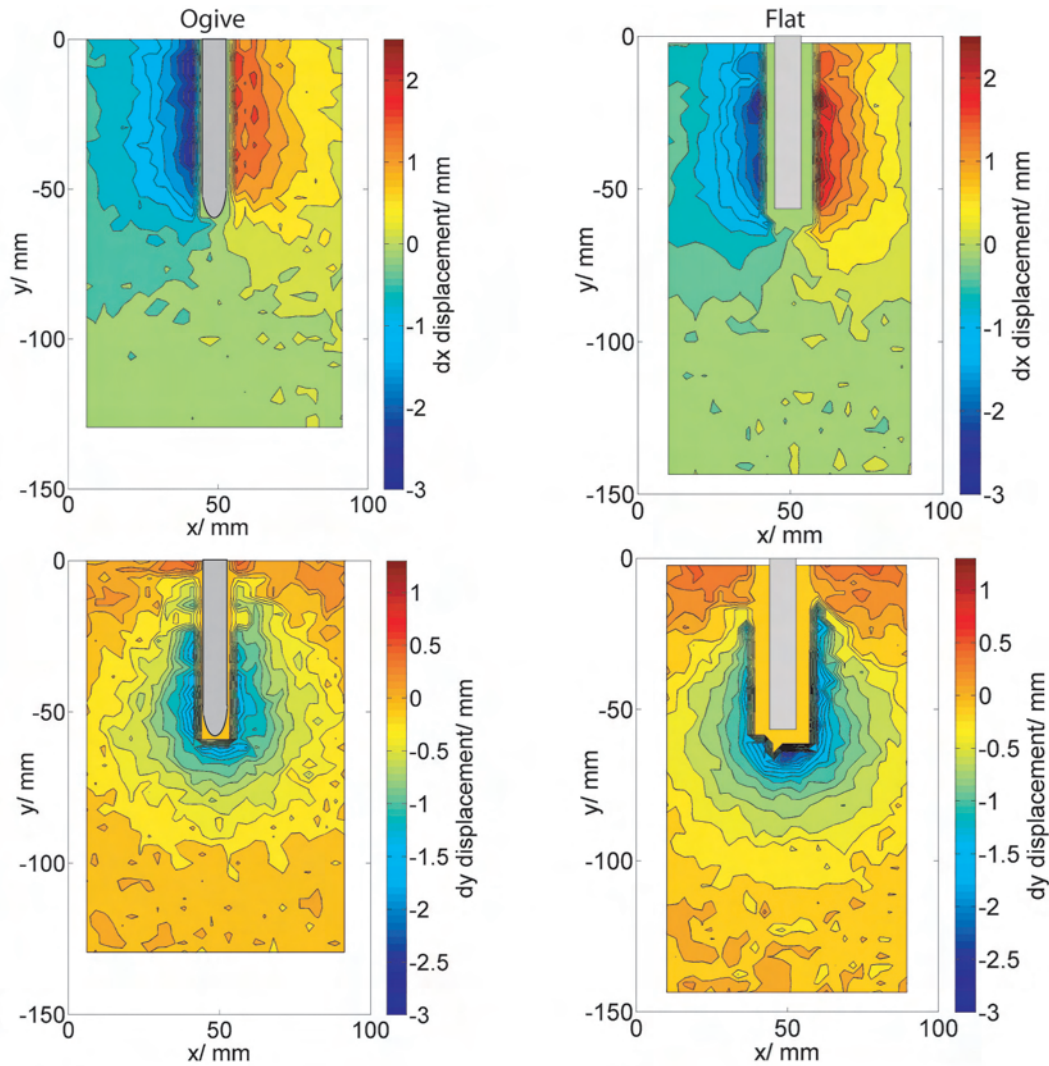


Figure 5.6: Comparing the lateral (top images) and longitudinal (bottom images) displacements, at $450 \mu\text{s}$ after impact, for penetration by an ogive (left images) and flat-ended (right images) projectile. The main difference is in the extent of deformation occurring ahead of the projectile tip, which is greater in the flat-ended case.

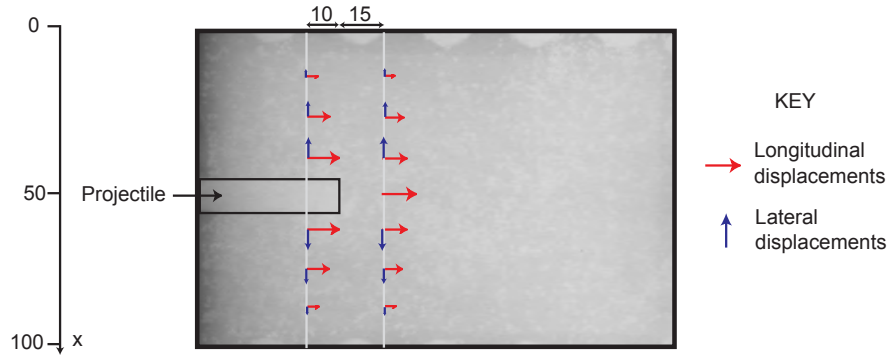


Figure 5.7: An illustration of the lateral and longitudinal displacements along perpendicular lines 15 mm ahead of the projectile tip and 10 mm behind the projectile tip.

material ahead of the projectile. The displacements are not only larger directly in front of the projectile but are larger across the whole width of the sample. Figure 5.9 shows the variation in the lateral and longitudinal displacements along a perpendicular line 10 mm behind the projectile tip, for comparison. In this case, the lateral and longitudinal displacements are very similar for both projectile nose shapes, showing that the extent of disruption behind the projectile tip is similar in both cases. This suggests that the main difference in the behaviour of the two projectile types is explained by the extent of the disruption being caused ahead of the projectile tip during the penetration process.

As for the flat-ended projectile case (see Table 4.2), it is interesting to consider the angle that the cone of longitudinal displacements makes with the projectile axis at the various times, as shown in Table 5.1. As before the angle remains relatively constant at (41 ± 2) degrees as the penetration develops. This value is in good agreement with the value obtained for the flat-ended case, which was (40 ± 2) degrees. The fact that this angle is unaffected by the nose shape suggests that it is determined by the properties of the sand or the diameter of the projectile or the initial penetration velocity, all of which are held constant here. The projectile nose shape has a greater effect on how far this cone of disrupted material extends ahead of the projectile tip, rather than the shape of the cone.

5. EFFECT OF PROJECTILE NOSE SHAPE

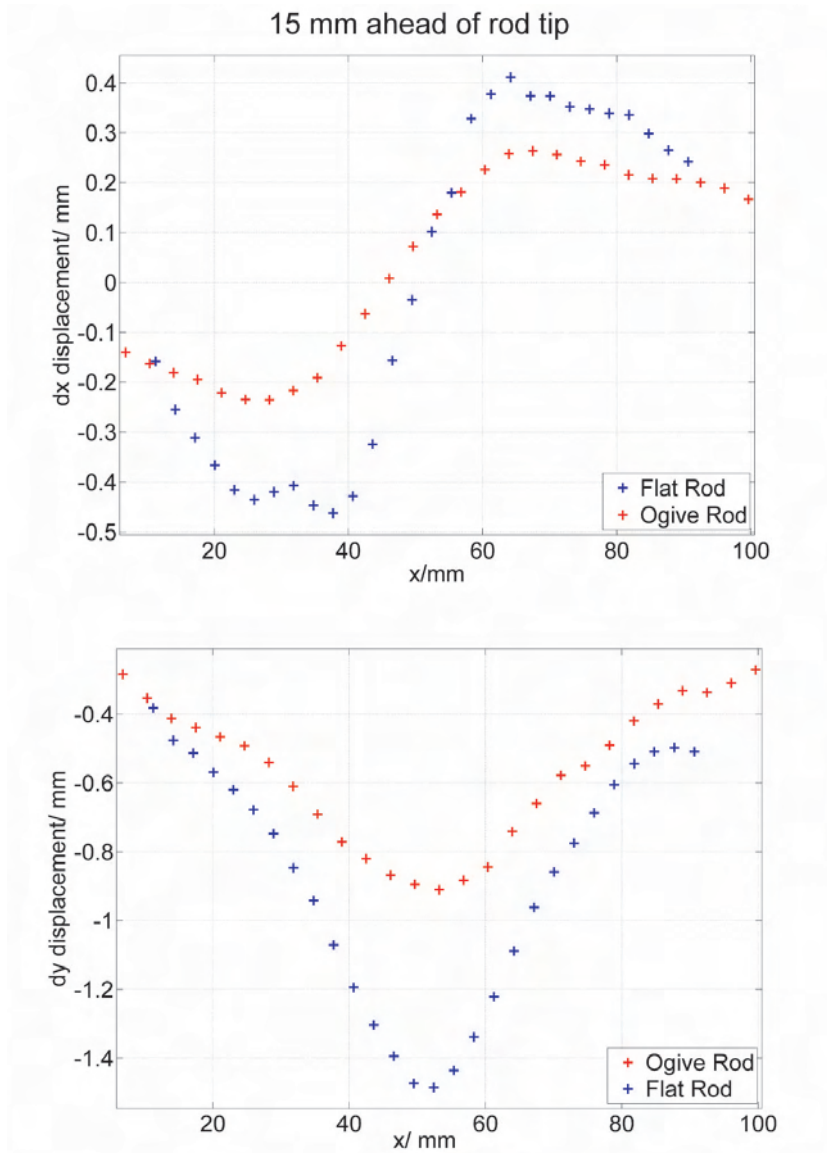


Figure 5.8: Comparing the magnitude of the lateral (dx, top image) and longitudinal (dy, bottom image) displacements along a perpendicular line 15 mm ahead of the projectile tip for the ogive (red) and flat-ended (blue) projectile. As shown schematically in Figure 5.7. Both the lateral and longitudinal displacements are greater in magnitude and extent for a flat-ended projectile.

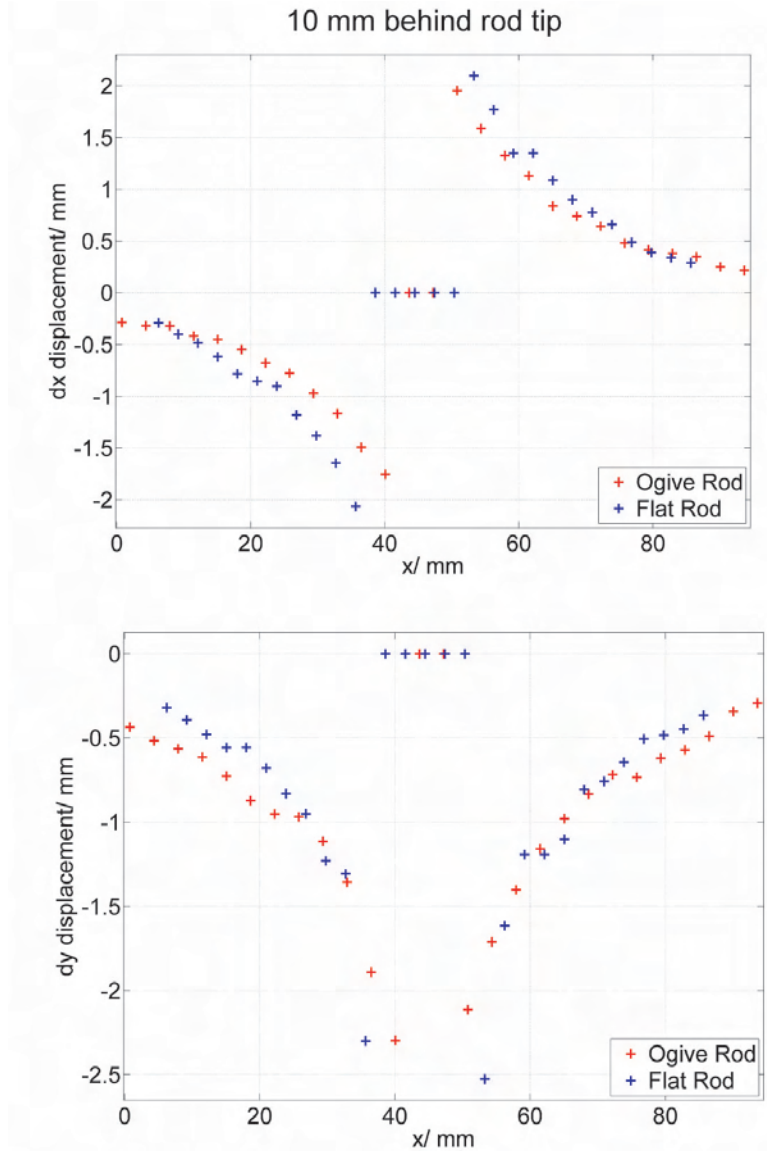


Figure 5.9: Comparing the magnitude of the lateral (dx , top image) and longitudinal (dy , bottom image) displacements along a perpendicular line 10 mm behind the projectile tip for the ogive (red) and flat-ended (blue) projectile. There is little difference in the displacements between the two nose shapes. No displacement, or displacements of zero, are recorded around $x = 50$ as this area of the image is covered by the projectile.

5. EFFECT OF PROJECTILE NOSE SHAPE

Delay/ μs	Angle/ degrees
150 ± 2	41.3 ± 1.0
250	42.1
350	39.0
450	40.5
550	42.0

Table 5.1: The angle of the envelope of longitudinal displacements relative to the projectile axis for ogive nose shapes.

5.2.1 Penetration Velocity Profiles

The instantaneous projectile velocity as a function of penetration depth is shown in Figure 5.10 for the three different nose shapes. The velocity for the ogive projectile was calculated in the same way as discussed in the previous chapter for the flat-ended projectile. The velocity data for the hemispherical nose shape was obtained by measuring the position of the projectile during the penetration on high speed video images (the initial impact velocity was slightly higher in this case). This velocity data was found to be consistent with the velocity profile for the hemispherical projectiles measured using the X-ray images.

With all three projectile types, there is a significant initial drop in velocity between a penetration depth of 0 and 30 mm. Subsequently, there is far less variation in the velocity. However, the final plateau velocity varies with the nose shape. For projectiles with flat ends, a roughly steady state velocity of around $(137 \pm 4) \text{ ms}^{-1}$ is obtained. For the ogive and hemispherical projectiles, considerably higher final velocities of $(167 \pm 5) \text{ ms}^{-1}$ and $(164 \pm 8) \text{ ms}^{-1}$ are reached. Assuming the velocity is entirely constant for the final four to five data points (for comparative purposes), the final velocities are as shown in Table 5.2.

The final velocities measured for the projectile with an ogive tip are generally higher than those measured for the projectile with a hemispherical tip (although the errors are significant). The final velocities for the flat-ended projectile are significantly lower than for the other two nose shapes. This result suggests that the ogive and hemispherical projectiles interact less strongly with the sample and transfer less energy to the surrounding material. This may be because the more

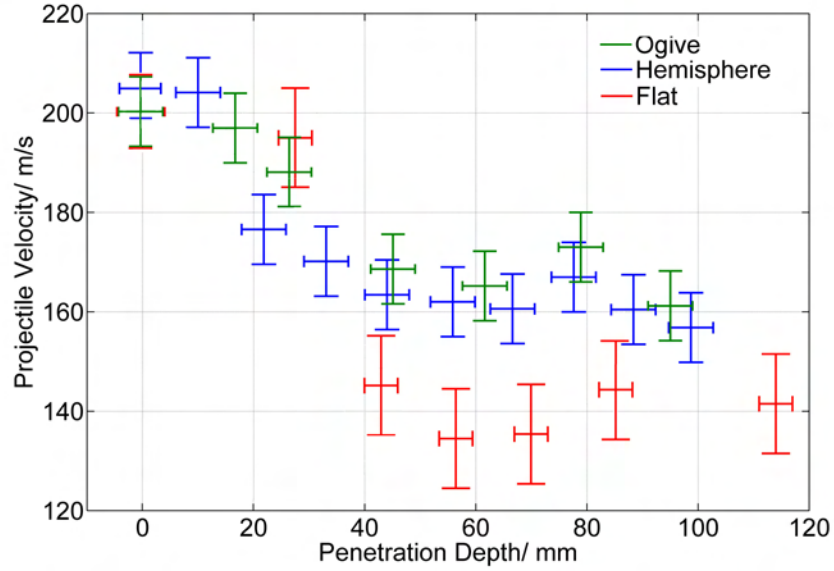


Figure 5.10: Velocity versus penetration depth for the three different nose shapes. For the flat and ogive cases the initial impact velocities were $(200 \pm 4) \text{ ms}^{-1}$. For the hemispherical case the velocity was $(203 \pm 4) \text{ ms}^{-1}$.

Tip shape	Final velocity/ ms^{-1}
Ogive 2	167 ± 5
Hemispherical	164 ± 8
Flat	137 ± 4

Table 5.2: Final 'steady-state' velocities for the three projectile types. For the flat and hemispherical cases the initial impact velocity was $(200 \pm 4) \text{ ms}^{-1}$. For the ogive case the velocity was $(203 \pm 4) \text{ ms}^{-1}$.

5. EFFECT OF PROJECTILE NOSE SHAPE

Tip shape	Energy loss/ J
Flat 2	610 ± 90
Hemispherical	370 ± 70
Ogive	350 ± 70

Table 5.3: The energy lost by each projectile during the early stages of penetration, until the plateau in velocity is reached around $250 \mu\text{s}$.

streamlined nose shape of these projectiles minimises the disruption caused during impact and reduces the size of the body of sand that is set in motion during the early stages (before $250 \mu\text{s}$) of impact. The ogive projectile maintains the highest velocity during the penetration process, which is consistent with it having the sharpest and most streamlined nose shape of the three types of projectile.

The energy lost by the projectiles during this early stage of penetration (before $250 \mu\text{s}$) can be calculated using the final plateau velocities recorded above. The energy loss is listed in Table 5.3 for the three different nose shapes. The flat-ended projectile loses almost twice as much energy during this period as the other two projectile types.

It is interesting to note that for all three types of projectile, the velocity increases slightly at a penetration depth of around 80 mm. Currently, it is difficult to assign a physical reason for this phenomenon, or indeed to say with confidence, given the size of the error bars, that this is a real effect, rather than an experimental system effect. A potential explanation is that at this penetration depth the compaction front has reached and interacted with the confinement. However, the effect of reflected waves from the confinement reaching and interacting with the projectile is difficult to predict.

The combined sets of velocity and displacement data suggest that penetration of the sand at this velocity can be considered as consisting of two distinct phases over the time period studied. During the early stages of penetration (before $250 \mu\text{s}$), phase one, the impact of the penetrator on the front surface of the sample and the effects of the first 20-30 mm of penetration, cause a compaction front to be produced which sets a body of sand in motion. Due to the high forces experienced by the sand grains, and the subsequently high level of friction, the motion of the sand grains is constrained to be in the direction of the applied

force. This leads to material ahead of the projectile tip moving further into the sample, causing compaction. Setting a body of sand in motion requires a significant amount of energy. The projectile therefore experiences a considerable decelerating force, causing the velocity to drop significantly in a short period of time.

The streamlined shape of the ogive projectile means that the initial impact with the front surface generates a smaller resistive force than for the flat-ended projectile, which acts initially more in the manner of a plate impact [2]. As a result the ogive and hemispherical projectiles cause less deformation ahead of the projectile tip (see Figure 5.8) and lose less energy during this phase, losing 350 to 370 J as compared to 610 J for the flat-ended case. They therefore experience a smaller drop in velocity during phase one of the penetration (see Figure 5.10).

The second phase of the penetration process is an effectively steady-state penetration. After the initial drop in velocity associated with phase one, we see that the velocity of the projectiles plateaus in all three cases. During this phase, projectiles penetrate through material that has been disturbed and set in motion by the travelling compaction front which precedes the projectile tip. Since the surrounding material moves in the same direction as the projectile motion, the resistive forces, both the normal forces on the tip and the drag forces along the shaft, are significantly reduced. There is little further energy exchanged between the projectiles and the sand, leading to the velocities remaining relatively constant. The flat-ended projectiles lose more energy during phase one, as a result the velocity at which they plateau is significantly lower than for the ogive and hemispherical projectiles. If the penetration were followed for a longer period of time, dissipative processes such as compaction and shearing of the sand would slow the moving area of sand and the projectile would experience significant further resistive forces. This does not appear to have occurred to any great extent by $750 \mu\text{s}$.

5.3 Summary

To summarise the experimental conclusions on the effect of nose shape:

5. EFFECT OF PROJECTILE NOSE SHAPE

- Within the limits of the DSR technique, the displacements arising from hemispherical and ogive projectiles are the same.
- The general pattern of displacements arising from an ogive projectile is similar to that arising from a flat-ended projectile.
- The main differences occur ahead of the projectile tip, where the flat-ended projectile causes greater disruption, in terms of the magnitudes of both the lateral and longitudinal displacements.
- These displacements are larger across the whole width of the sample ahead of the projectile.
- Penetration of the sand at this velocity can be considered as two distinct phases over the time period studied.
- In phase one, the early stages of the penetration (up to 250 μs) lead to a compaction front and a body of sand being set in motion.
- This causes a considerable resistive force on the projectiles and the velocity drops significantly in a short period of time.
- The force experienced by the projectile during this stage is smaller for the more streamlined ogive and hemispherical nose shapes than for the flat-ended projectile. The flat-ended projectile loses (610 ± 90) J of kinetic energy in this phase, as compared to only (350 ± 70) and (370 ± 70) J for the ogive and hemispherical projectiles. These projectiles therefore maintain a higher velocity.
- In phase two of the penetration, the projectiles travel through material that has been set into motion by the compaction front. The normal forces on the tip and the drag forces on the projectile shaft are therefore significantly reduced.
- Little further energy is transferred between the projectile and the sand and the velocities plateau for a period. As the flat-ended projectiles lost more energy during phase one, the velocity at which they plateau is less than with the ogive projectiles.

- If we were to follow the penetration for a longer period of time, dissipative processes, such as friction, would lead to the decay of the compaction front and further energy from the projectile would be required to support the penetration process.

References

- [1] Chin, S.S., *Missile configuration design*, McGraw-Hill, US (1961)
- [2] Chapman, D.J., Proud, W.G., Tsembelis, K. and Collins, A., *Hard Target Research: Final Progress Report*, Internal Report SP 1184, University of Cambridge (2007)

REFERENCES

Chapter 6

Quasi-Static Penetration

6.1 Introduction

In the preceding chapters, we discussed the behaviour of a cylindrical sample of sand during dynamic penetration experiments at a velocity of 200 ms^{-1} . In this and the following chapters, the rate dependence of the penetration process is investigated. The experimental setup is kept as constant as possible throughout the experiments discussed. In particular, the same sample holder (cylindrical geometry, 150 mm long, 10 mm diameter), sand and projectiles are used throughout. The purpose of these experiments is to investigate any rate dependence in the response of the sand to penetration. An understanding and awareness of any such rate dependence is vital when attempting to fully explain the behaviour of granular materials, or for producing appropriate computational simulations.

Penetration at lower rates to those considered in the previous chapters, at velocities of under ten metres per second, is important in a number of fields. Penetration at effectively quasi-static rates (mm per min) provides information regarding the response of granular materials, such as sand or soil, to localised static loads. This is relevant to the construction and transportation industries. The penetration behaviour of granular materials at velocities of the order of a metre per second is important in mining or construction (consider, for example, the use of pile drivers when setting the foundations for buildings). At both rates, the data provided will be useful in understanding the flow of granular materials at low to medium velocities. An increased knowledge of the internal flow of granular

6. QUASI-STATIC PENETRATION

materials at such rates is vital for our understanding of a number of situations, including the transportation of granular media, such as grains or pills, in factories.

There appears to have been little previous research into the low rate penetration of granular materials or more generally into any rate dependence in the behaviour of such materials during penetration. Researchers have generally restricted themselves to considering dynamic penetration behaviour [1–3], or more general flow of the material at low rates, such as material moving through a silo [4].

In this chapter we consider the internal flow fields within a granular material during effectively quasi-static penetration, at a rate of 1.5 mm/min ($2.5 \times 10^{-5} \text{ ms}^{-1}$). This is a reduction in the penetration velocity by a factor of 8×10^6 relative to the previously discussed dynamic experiments. In the following chapter we will consider penetration at intermediate rates, ranging from 5 ms^{-1} up to 200 ms^{-1} .

6.2 Experimental Setup

The quasi-static penetration experiments were performed using an Instron compressive tester [5]. The Instron machine is designed to smoothly compact materials between two cylindrical anvils at rates ranging from fractions of a millimetre per minute (less than 10^{-5} ms^{-1}) up to a few hundred millimetres per minute (10^{-3} ms^{-1}). A load cell mounted above the projectile measures the vertical reaction force experienced by the upper anvil, up to a maximum load of 2 kN. A penetration velocity of 1.5 mm/min was chosen as the lowest rate, so that penetration up to the full depth of the projectile took approximately one hour.

The sample was prepared in the same manner as discussed in detail in Chapter 4, including the internal layer of scattered lead shot, and was mounted on the Instron machine below the anvil, as shown in the front view in Figure 6.1. The projectiles were secured to the anvil using epoxy, such that they were vertical. An alignment rig was used to ensure that the sample was positioned so that penetration would occur along its central axis, as with the previous gas-gun experiments (to an accuracy of a few mm). The X-ray head was mounted horizontally at a distance of approximately one metre from the front face of the sample (a face that

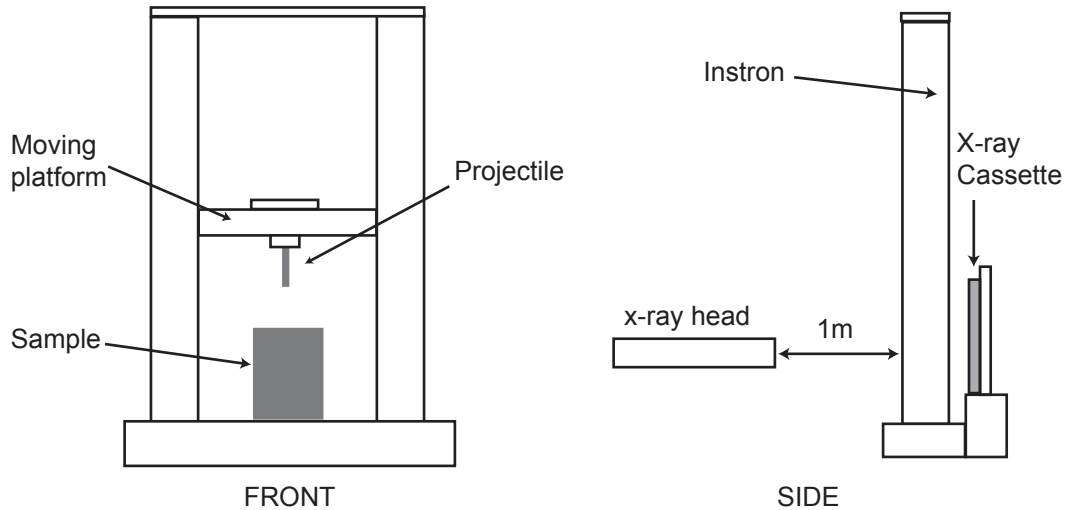


Figure 6.1: The Instron machine with the projectile attached and the sample loaded. The sample was penetrated at a uniform rate of 1.5 mm/min.

runs length-ways parallel to the central axis of the cylindrical bore, and in the same orientation as the plane of lead). The X-ray cassette was mounted immediately behind the sample, as close as experimentally possible, which in practice was approximately 50 mm from the rear face of the sample. The X-ray head and X-ray cassette were aligned so that their faces were in approximately the same orientation as the plane of scattered lead, to within a few degrees. Unlike in the dynamic experiments, the face of the target being penetrated was unconfined. Preliminary experiments suggest that light confinement of the upper surface has little effect on the measured displacements.

As with the dynamic experiments, a reference X-ray image of the sample was taken before the penetration. Subsequent flash X-ray images were taken during the penetration process. Since the penetration rate was much slower than in the gas-gun experiments, it was possible to take up to three X-ray images from a single experiment - limited by the number of X-ray cassettes and the developing time for the X-ray film. By repeating the experiment a number of times, and carefully aligning the sample in each repetition, it was possible to build up a sequence of images showing the temporal progression of the penetration process.

6. QUASI-STATIC PENETRATION

A list of the DSR experiments carried out for this chapter is given in Table A.4 in Appendix A.

It is important to note that there are some differences between these experiments and the previously discussed dynamic penetration experiments. Perhaps the most important difference is that in these experiments the penetration velocity is constant throughout, while in the dynamic penetration experiments the velocity of the projectile varied during the penetration process. This is likely to affect the displacements to some extent, but is unlikely to change the global form of the deformation occurring. Other differences include the penetration occurring vertically, rather than horizontally as in the dynamic experiments, which is also unlikely to have much of an effect on the displacements, and the lack of confinement on the front surface, which preliminary experiments suggest does not noticeably affect the measured displacements.

6.3 Penetration by Flat-Ended Projectiles

Initial experiments were carried out using a flat-ended projectile. The projectile was pushed into the sample at a uniform rate of 1.5 mm/min, up to a maximum depth of 90 mm. The reaction forces experienced by the projectile during the penetration process for four separate experiments are shown in the plots in Figure 6.2. There is some variation between these plots, which arises from the intrinsically inhomogeneous nature of the sand and the natural variations in packing arrangement between the experiments. In each experiment, the density and porosity of the sample will be slightly different, leading to a noticeable variation of up to 20% in the reaction force on the projectile tip between the repetitions. The fact that the differences are noticeable suggests that small changes in the packing order and the number and size of the pores have a considerable effect on how the material interacts with the penetrator.

The measured displacement fields within the material at a selection of different depths of penetration are shown as quiver plots in Figures 6.3 and 6.4. Comparing these displacement quiver plots with those obtained during dynamic penetration experiments, shown in Chapters 4 and 5, there are some clear and significant differences in the response of the material. In Figure 6.5, example quiver plots

6.3 Penetration by Flat-Ended Projectiles

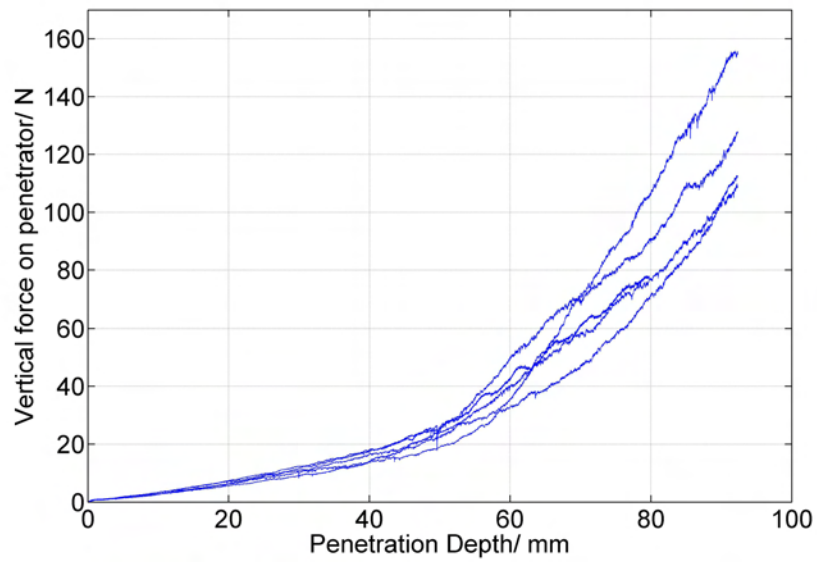


Figure 6.2: The vertical force experienced by the penetrator as a function of penetration depth depth for penetration of the sample at 1.5 mm/min by flat-ended projectiles

6. QUASI-STATIC PENETRATION

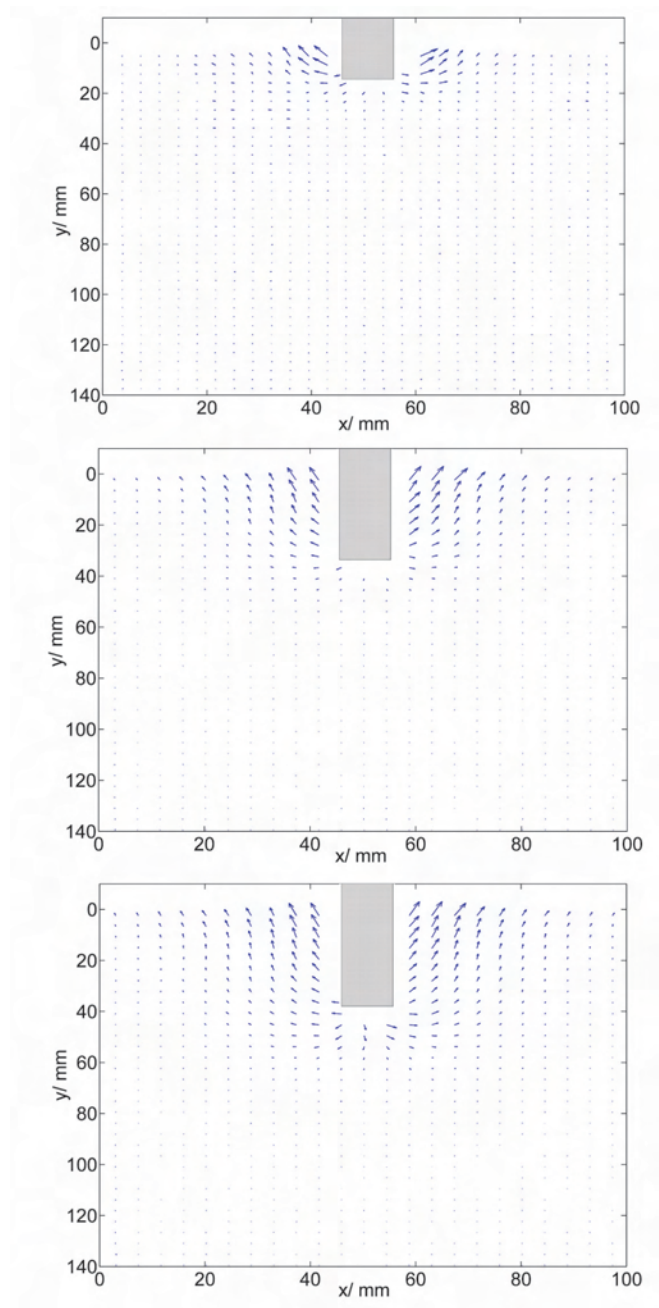


Figure 6.3: Three quiver plot images, showing displacements measured during penetration of the sample at 1.5 mm/min in the Instron

6.3 Penetration by Flat-Ended Projectiles

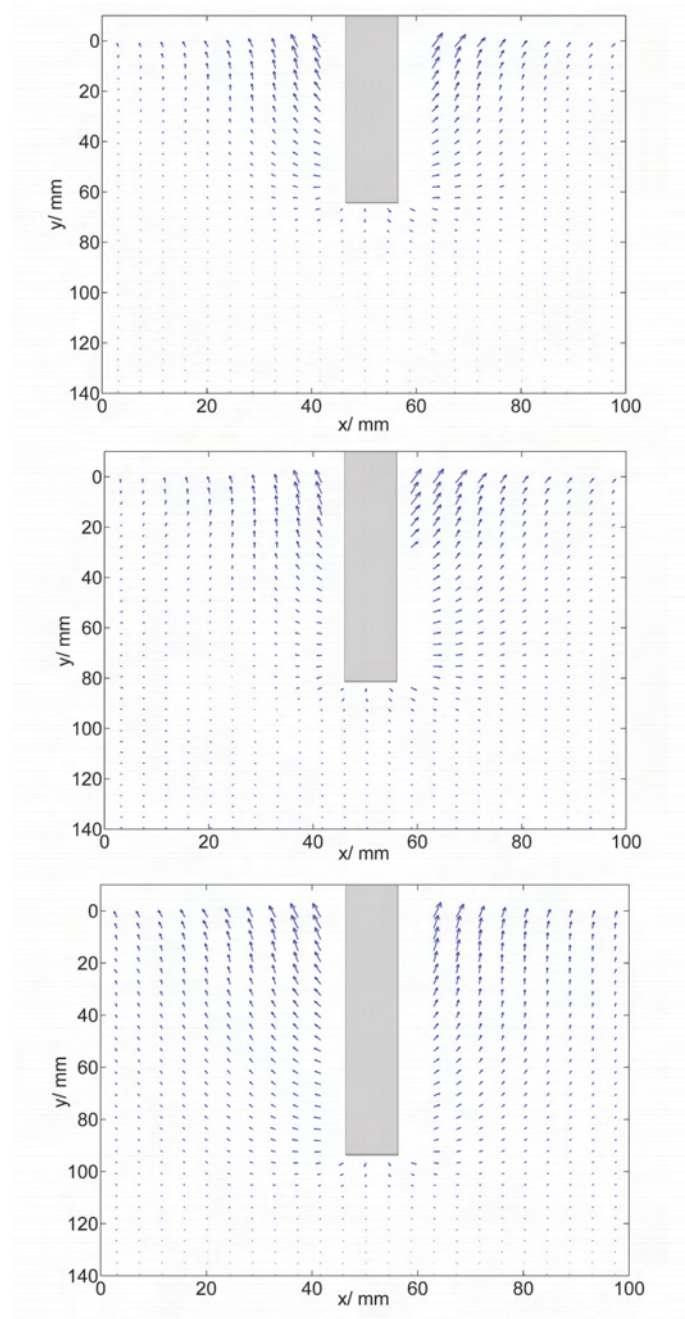


Figure 6.4: Three further quiver plot images, showing displacements measured during penetration of the sample at 1.5 mm/min in the Instron

6. QUASI-STATIC PENETRATION

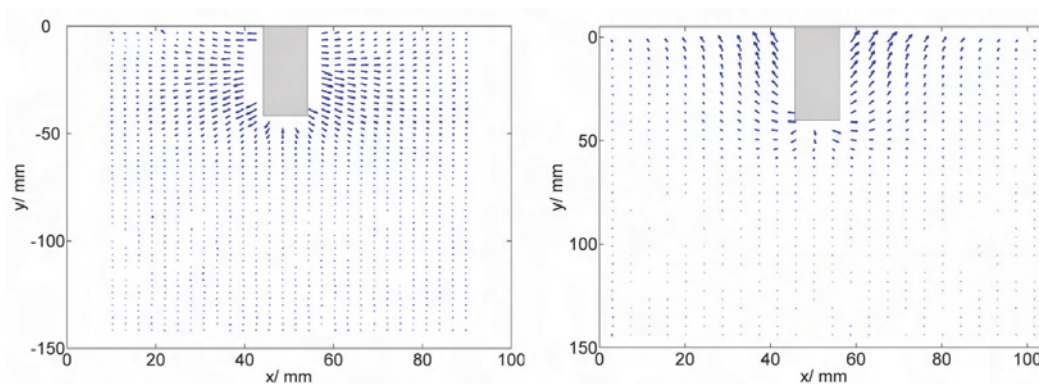


Figure 6.5: Comparing the displacements generated during penetration experiments at 200 ms^{-1} (left image) and 1.5 mm/min (right image), for similar extents of penetration - 45 and 43 mm respectively.

of the displacements measured during the small-gun and Instron experiments for similar extents of penetration (approximately 45 mm) are shown side by side for comparison. There is significantly less disruption of the material occurring ahead of the projectile during the quasi-static penetration. There also appears to be a significantly larger amount of material moving upwards, in the opposite direction to the projectile motion. In order to consider these differences in more detail it is informative to plot the lateral (dx) and longitudinal (dy) displacements separately as contour plots. This is shown for a selection of different depths of penetration in Figures 6.6 and 6.7.

Figures 6.6 and 6.7 show that the type of deformation occurring during low rate, effectively quasi-static, penetration is very different to that observed during the dynamic penetration experiments discussed in Chapters 4 and 5. The plots in Figures 6.6 and 6.7 show that little of the material ahead of the projectile is being deformed or affected by the penetration in the quasi-static case. From the plots of the lateral displacements, we see that the material directly ahead of the projectile is being split laterally. This was also observed for the dynamic case, and appears to be an important mechanism by which projectiles penetrate granular materials. There is also localised longitudinal displacement directly ahead of the projectile, but these displacements are less wide-spread than for dynamic penetration. These

6.3 Penetration by Flat-Ended Projectiles

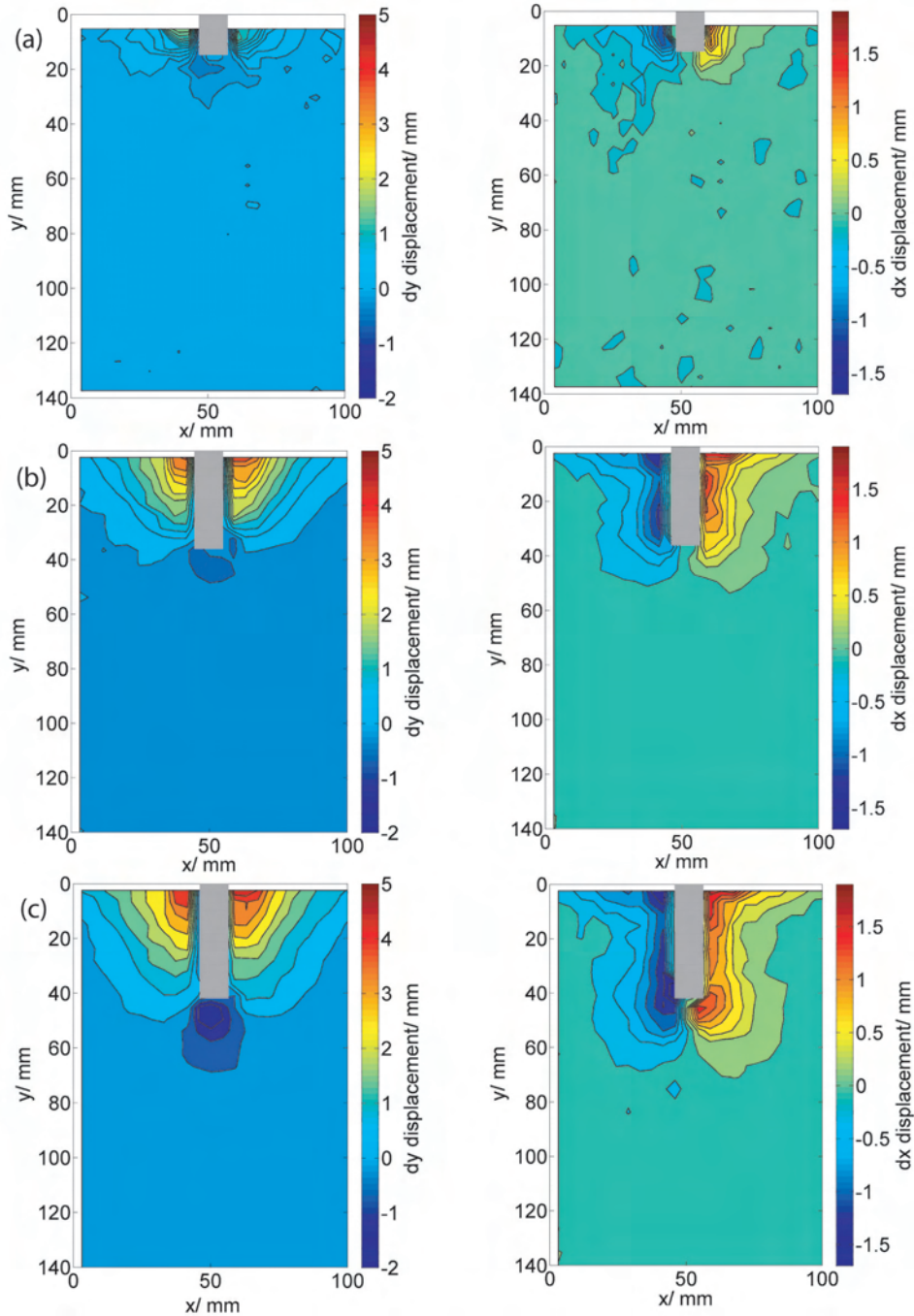


Figure 6.6: Contour plots of the longitudinal displacements (dy , left images) and lateral (dx , right images) displacements for three different extents of penetration. (a) 16 mm, (b) 38 mm, (c) 43 mm.

6. QUASI-STATIC PENETRATION

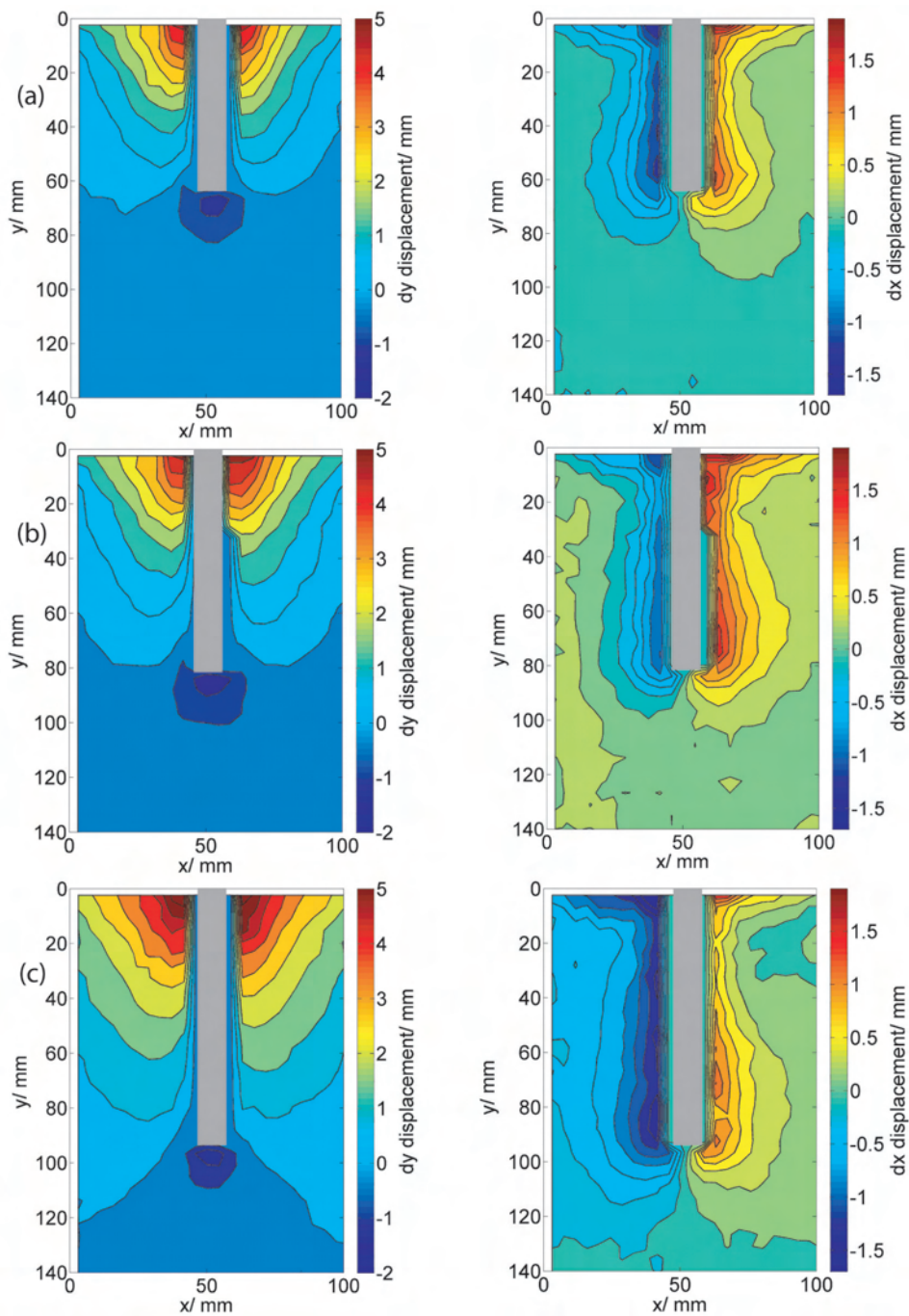


Figure 6.7: Contour plots of the longitudinal displacements (dy , left images) and lateral (dx , right images) displacements for three different extents of penetration. (a) 62 mm, (b) 82 mm, (c) 93 mm.

observations are discussed in more detail in the following sections.

6.3.1 Longitudinal Displacements

The plots of longitudinal displacement in Figures 6.6 and 6.7 show that there is an area directly in front of the projectile that is being displaced longitudinally. The extent to which this displacement stretches ahead of the projectile tip appears to increase between the three images shown in Figure 6.6. Unlike for the dynamic case, there is no wide-spread disruption of material ahead of the projectile. The disruption is generally localised to the area directly ahead of the projectile and extends at most 30 to 40 mm from the tip.

The longitudinal displacements measured during the low-rate Instron experiments and the higher rate gas-gun experiments at a similar extent of penetration (approximately 60 mm) are compared directly in Figure 6.8, where the data sets are plotted as contour plots. The large differences in the response of the material between the two rates are immediately clear. For the low-rate case, the displacements are primarily positive (upwards), showing that the material is releasing out of the impact face. With a higher penetration rate the displacements are primarily negative (downwards), showing that the material is being compacted ahead of the projectile, and that significant disruption of the material ahead of the projectile tip is occurring.

During low-rate penetration, the maximum longitudinal displacements in the same direction as the projectile motion are found directly in front of the projectile tip. When the projectile has penetrated to a depth of 58 mm, the material directly ahead of the projectile has moved by up to 1.5 mm longitudinally. This compares with the maximum longitudinal displacement of 2.6 mm measured ahead of the flat-ended projectile during dynamic penetration for a similar depth of penetration. Clearly, during the low-rate penetration, significantly less material is pushed ahead of the projectile.

Figure 6.9 compares the longitudinal displacement of material directly ahead of the projectile (along a line uniaxial with the projectile) for penetration at 200 ms^{-1} and 1.5 mm/min , for a similar extent of penetration - around 60 mm. The displacements are generally greater by around 50% for the dynamic case.

6. QUASI-STATIC PENETRATION

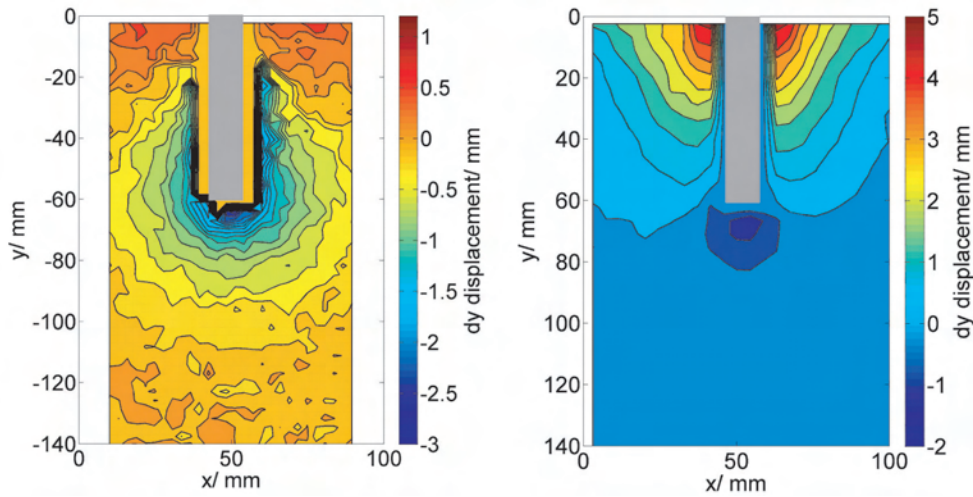


Figure 6.8: Comparing the longitudinal displacements generated during penetration experiments at 200 ms^{-1} (left image) and 1.5 mm/min (right image), for similar extents of penetration of approximately 60 mm. Note that the displacement scales are different.

The gradient of the displacements close to the projectile tip is also much greater during dynamic penetration, suggesting that the material directly in front of the rod is compacted to a greater extent.

The most significant difference between the longitudinal displacements observed here and those observed in the dynamic penetration experiments is the amount of material that moves in the opposite direction to the projectile motion. The quiver plots and the contour plots in Figure 6.6 show that there is a cone shaped area of sand, with the tip of the penetrator at the apex and the impact face as its base, that is moving vertically upwards. Interestingly, even the material directly to the sides of the penetrator, which in the dynamic case was all moving with the penetrator, is seen to be moving in the opposite direction. Indeed, the largest longitudinal displacements are found on the upper face directly to the sides of the point of penetration. Once the projectile has penetrated to around 80 mm, the material in this location has moved in the opposite direction to the projectile by as much as 6 mm.

The displacements at the impact surface lead to the formation of a raised

6.3 Penetration by Flat-Ended Projectiles

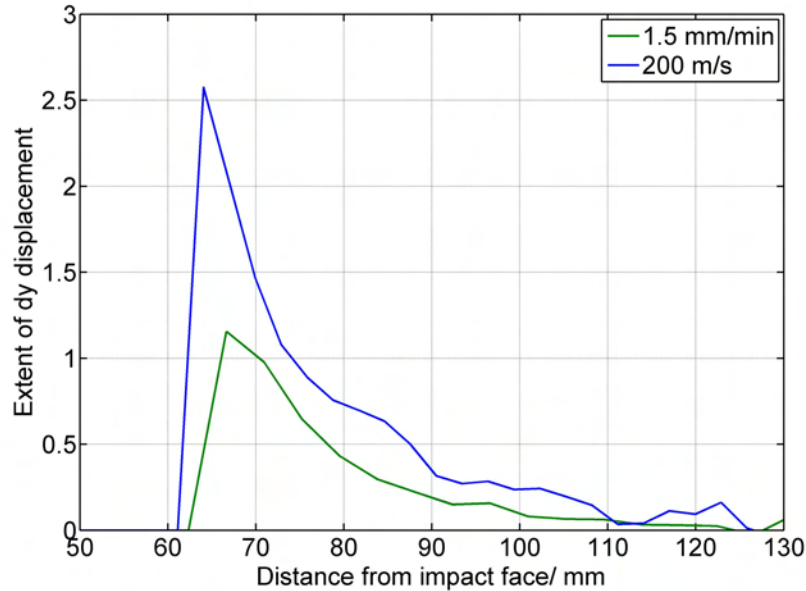


Figure 6.9: Comparison of the longitudinal displacement ahead of the projectile, at a similar extent of penetration, for penetration at 200 ms^{-1} and 1.5 mm/min .

crater which surrounds the shaft of the projectile. To investigate the growth of this surface feature, 2D cross-sections of the surface profiles for various extents of penetration are plotted in Figure 6.10. These plots show that the shape of the crater changes between a penetration of 15 mm and 30 mm, but subsequently the physical shape of the crater appears to change little. Instead, the whole upper surface of the sample rises, causing the crater to rise. By the time the projectile has penetrated to a depth of 90 mm, the entire surface has risen by 2.5 mm relative to the original surface position.

The fact that the whole upper surface of the sample rises suggests that less compaction of the material occurs than in the dynamic case, where instead a lot of material around the projectile was clearly being compacted. During dynamic penetration, the pressures caused by the penetration process were released mainly through compaction of the porous material directly ahead of the projectile, and to some extent through compaction of the material to the sides of the projectile. During low-rate penetration the pressure is instead released through bulk reverse-flow of the material in the opposite direction to the projectile motion, towards the

6. QUASI-STATIC PENETRATION

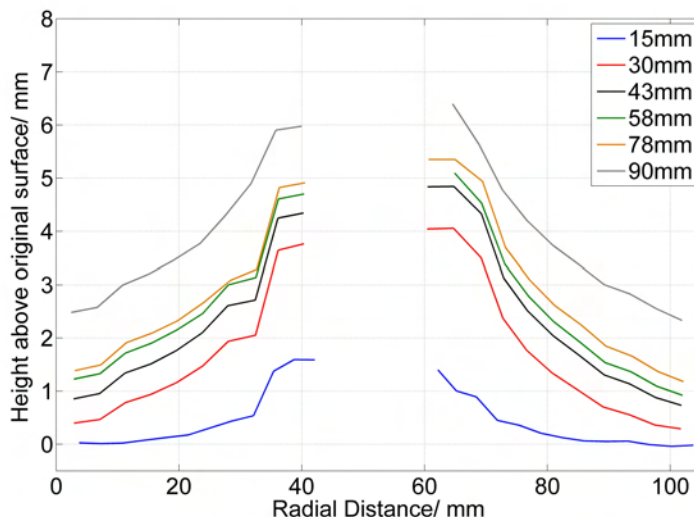


Figure 6.10: Graphs showing the surface profile, in 2D, of the sample versus various penetration depths

impact face, causing the impact face to rise. There is less evidence for significant compaction of material.

This change in the response of the material is most likely due to the increase in the magnitude of the inter-granular friction with penetration velocity, as well as a change from a static friction regime to a dynamic friction regime. The magnitude of the inter-granular friction will be related to the forces experienced by the grains. The maximum force experienced vertically by the rod during the low-rate penetration process was around 140 N. During the dynamic penetration the rod (mass 55 g) was slowed from approximately 200 to 140 ms^{-1} in a distance of 40 mm, requiring an average resistive force during the deceleration of 14 kN, roughly two orders of magnitude greater than with the low rate penetration.

It appears that at a low rate of penetration, where there is a relatively low force on the individual sand grains, the grains are able to move relatively freely. This enables them to move in the direction of least resistance, which may involve moving in a direction different to that in which the force is applied, for example to move sideways into a void. If the porosity is sufficiently low the forces will be transmitted between grains, so that grains at any unconfined boundaries, in

6.3 Penetration by Flat-Ended Projectiles

this case the impact face, will move. This causes the upper surface to rise as the penetration continues and more material is forced out of the way of the projectile. In the dynamic case, however, the forces are sufficiently large and applied over a sufficiently short time period that the frictional forces confine the motion of the sand grains. The sand grains are unable to move as freely as before and are instead constrained to move in the direction of the applied force, causing compaction of the material directly ahead of the projectile tip and to the side of the projectile. Only the material close to the impact face can move upwards to release through the upper surface in response to the applied forces.

In Figure 6.11 the longitudinal displacements along a perpendicular line 15 mm ahead of the projectile tip are compared for dynamic and quasi-static penetration by flat-ended projectiles. For the quasi-static case, the magnitude of the displacements is significantly less than for the dynamic case. It is also apparent that in the quasi-static case the majority of the displacement occurs within 15 - 20 mm of the projectile axis. The dynamic penetration causes significantly more widespread deformation ahead of the projectile tip, the lateral displacements being significant all the way out to the edges of the sample. This wide-spread disruption of the material in the dynamic case is caused by the action of the expanding compaction front, something that is not found in the quasi-static case.

6.3.2 Lateral Displacements

In Figure 6.12, the lateral (dx) displacements at the two penetration rates, 1.5 mm/min and 200 ms⁻¹, for a similar extent of penetration of approximately 60 mm, are compared. There are significant differences in the way in which the material is responding to the penetration. In both cases the displacements are roughly symmetric around the central axis of the projectile, which is to be expected due to the conservation of momentum. The maximum magnitude of the lateral displacements is noticeably lower for the Instron experiments, being of the order of 1 mm compared to over 2 mm for the dynamic case. In the dynamic case, the lateral displacements are effectively uniform along the length of the rod. This suggests that the majority of the lateral displacement is caused by the motion of the projectile tip.

6. QUASI-STATIC PENETRATION

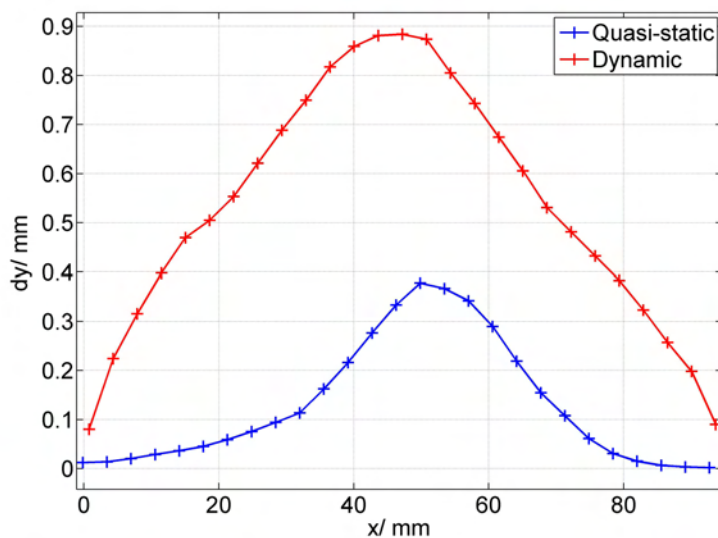


Figure 6.11: Comparing the longitudinal (dy) displacements along a transverse line 15 mm ahead of the projectile tip for the dynamic and quasi-static case, with a flat-ended projectile. The penetration extent was (60 ± 5) mm in both cases.

In the case of the Instron experiments, the lateral displacements are no longer uniform along the length of the rod. Wide-spread lateral displacement occurs in the material within ten to fifteen millimetres of the penetration face. The entire upper surface moves laterally (and indeed longitudinally also), contributing to the formation of the surface crater. Below this disrupted surface layer, the extent to which the deformation extends outward from the projectile axis increases with distance down the projectile. Near the projectile tip, the lateral deformation of the material extends to a distance of around 30 mm from the projectile axis, compared to only 15-20 mm nearer to the surface layer.

Although a small amount of material is pushed ahead of the projectile, the majority of the material is split laterally ahead of the projectile tip and then moves upwards towards the front face, in the opposite direction to the projectile motion. If, rather than considering the local displacement of the sub-images, we consider the material to be flowing as a fluid and consider the flow-field, the flow lines would look similar to those shown as red lines in Figure 6.13. In order for material near the projectile shaft to move towards the penetration surface, it

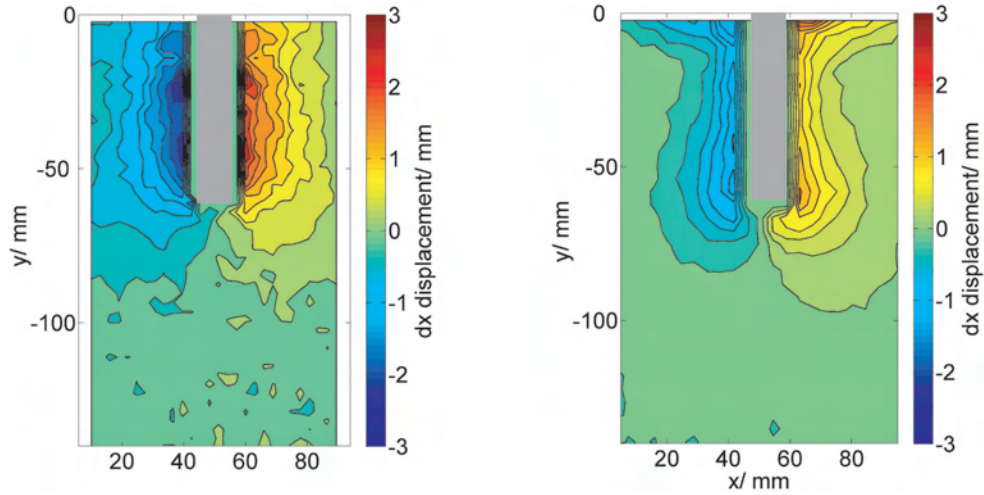


Figure 6.12: Comparing the lateral displacements generated during penetration experiments at 200 ms^{-1} (left image) and 1.5 mm/min (right image), for a similar extent of penetration of approximately 60 mm (displayed as contour plots with the same displacement scale for comparison).

must first move out sideways to move around the material vertically above it that has also been pushed sideways. The deeper the depth at which the material was originally disturbed by the projectile, the further out sideways this deformation extends. Thus the extent to which the lateral displacements extend from the projectile axis increases with distance down the projectile. In the dynamic case, the larger forces cause the material to the sides of the projectile to be compacted. The magnitude of these forces and therefore the extent of the compaction decay rapidly to zero about 40 mm out from the rod axis.

6.3.3 Decay of the Displacements

We saw in Figure 6.9 that the longitudinal displacements ahead of the projectile tip appear to decay with longitudinal distance in a similar manner in both the dynamic and quasi-static penetration experiments (although the decay begins at different starting displacements in the two cases). As for the dynamic experiments in Chapter 4, it is interesting to consider how these displacements vary during the penetration process for quasi-static penetration. In Figure 6.14, the longitudinal

6. QUASI-STATIC PENETRATION

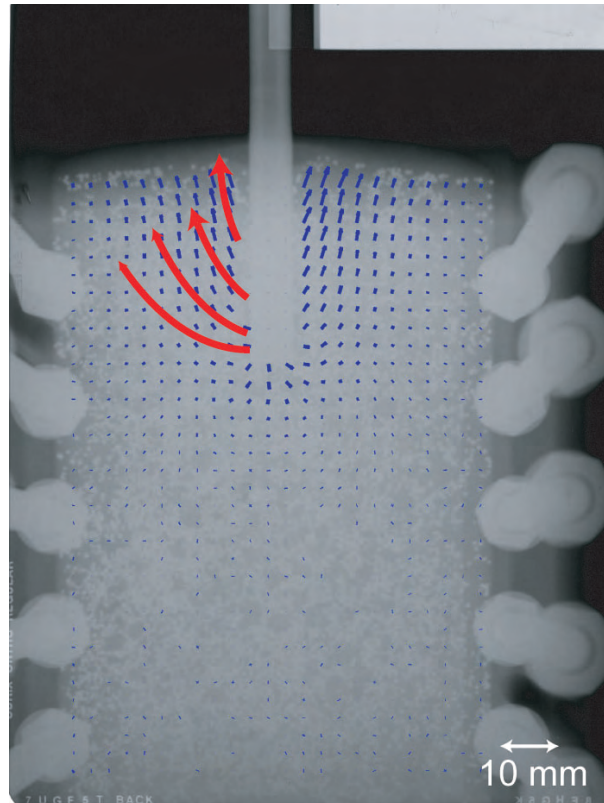


Figure 6.13: A schematic illustrating the flow-field within the sample, to the left of the projectile only, during the penetration process. The red arrows show the direction of flow of material to the left of the projectile. In order to move upwards towards the impact face material must first move out sideways further than the material above has moved sideways. This leads to the extent of the lateral displacement of the material increasing with distance down the projectile shaft.

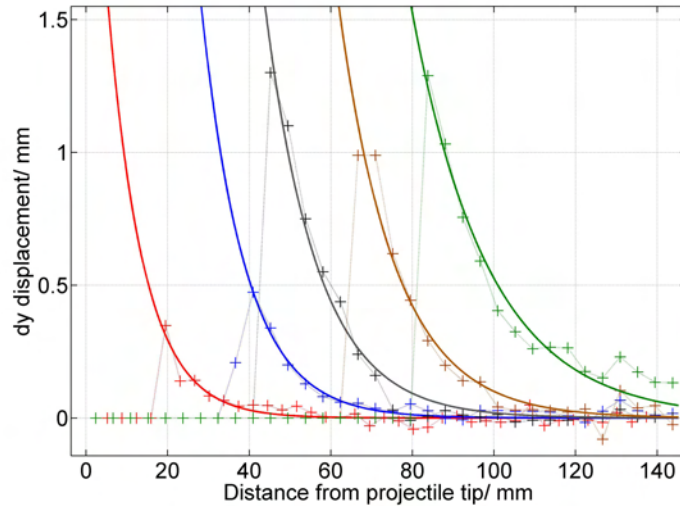


Figure 6.14: Plots showing how the longitudinal displacement varies with distance in front of a flat-ended projectile tip, for a series of different penetration depths (16, 38, 43, 62 and 82 mm). The displacements all decay with a similar exponential factor, with the exception of the first data set (red).

displacements are plotted for a number of different extents of compaction. A single decaying exponential has been fitted to the data in each case, showing that the displacements appear to decay exponentially with distance from the projectile tip.

The first set of data, at a very low extent of penetration, has an exponential decay constant of -0.114 . The subsequent four data sets have very similar exponential decay constants, with a mean of (-0.069 ± 0.010) . This value is consistent with the decay constant found for decay of the displacements ahead of the projectile and to the sides of the projectile during dynamic penetration experiments, discussed in Chapter 4. The implications of these results are discussed in Chapter 4.

6.3.4 Extent of Compaction

Figure 6.15 shows the extent of compaction occurring throughout the sample, resolved in two perpendicular directions, for both dynamic and quasi-static pen-

6. QUASI-STATIC PENETRATION

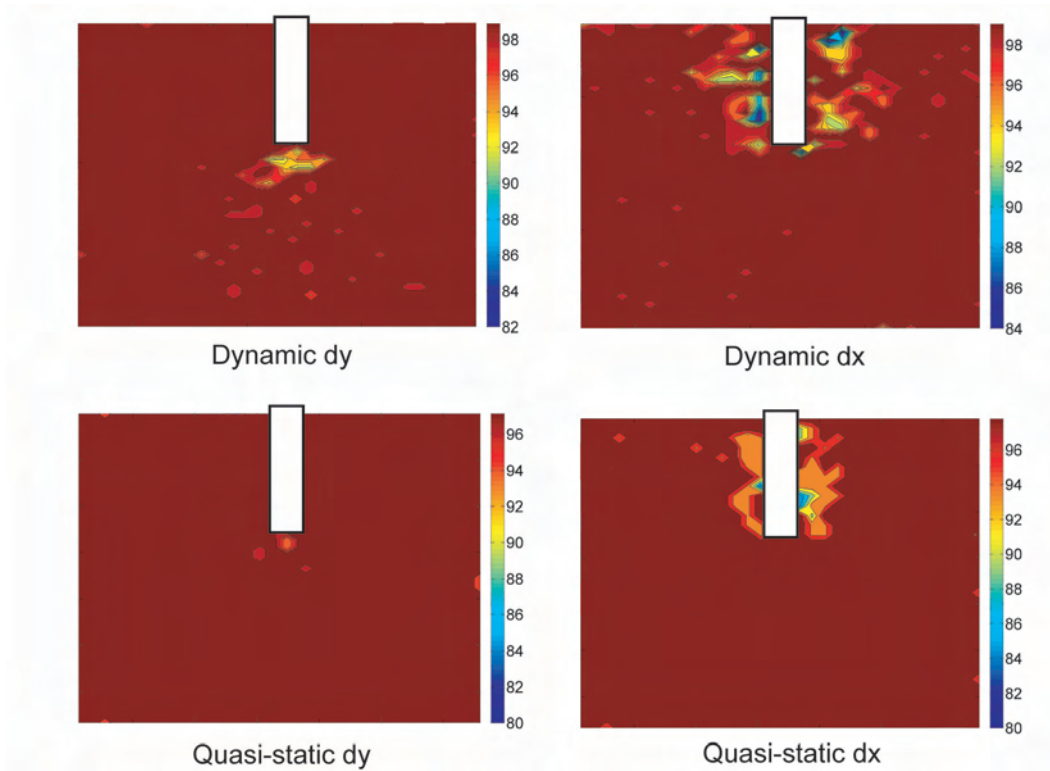


Figure 6.15: Comparing the extent of compaction in the longitudinal (dx , right images) and lateral (dy , left images) directions during dynamic (top images) and quasi-static (bottom images) penetration. The colour in the plot shows the compaction factor multiplied by 100.

etration by flat-ended projectile. In both cases, the majority of the material is not significantly compacted. What compaction there is occurs in the area directly surrounding the projectile. There is more wide-spread compaction of the material occurring directly ahead of the projectile tip in the dynamic case. Considering the extent of lateral (dx) compaction occurring, it can be seen that while the magnitudes are similar in both cases the extent to which the lateral compaction extends from the projectile axis is greater in the dynamic case. These results confirm that more material is being compacted in the dynamic case, while in the quasi-static case more of the material seems to be flowing as a bulk, rather than being compacted.

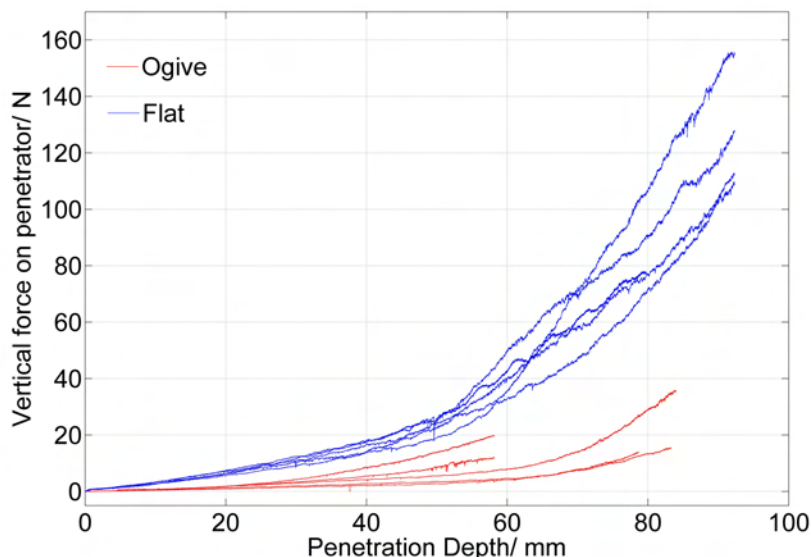


Figure 6.16: The vertical force experienced by the penetrator as a function of penetration depth for penetration of the sample at 1.5 mm/min by flat-ended (blue traces) and ogive-tipped (red traces) projectiles.

6.4 Penetration by Ogive-Tipped Projectiles

The red plots in Figure 6.16 show that if identical Instron experiments (1.5 mm/min penetration rate) are performed using a projectile with an ogive-2 nose shape (details of which are given in Chapter 4) the vertical forces felt by the projectile are reduced by over a factor of four. This difference must be due to the interaction between the projectile and the sand and the subsequent dynamics of the surrounding material.

Three quiver plots showing selected stages of the penetration process with an ogive nose-cone are shown in Figure 6.17. The form of deformation is very similar to that observed with the flat-ended projectiles, shown in Figures 6.3 and 6.4. The majority of the material down to the projectile tip is moving upwards towards the front face, where a crater is formed around the projectile shaft. The projectile nose shape does not have a significant effect on the overall shape of the displacement field, as was found with the dynamic experiments where the

6. QUASI-STATIC PENETRATION

displacement fields were a similar shape for three different nose shapes.

To investigate the difference in response more closely, the lateral (dx) and longitudinal (dy) components of the displacements, at similar extents of penetration, are compared for ogive and flat-ended projectiles in Figure 6.18. While the global similarity in the displacement fields is evident, there are also clear differences in the material response between the two nose shapes. Considering the longitudinal (dy) displacements first, we can see that the flat-ended projectile causes more wide-spread deformation of the material directly ahead of the projectile tip. A larger area of sand is displaced by a greater extent (up to 1.5 mm versus up to 1 mm) than with the ogive nose-shape.

It is also clear that with a flat-ended projectile, the longitudinal displacements at the penetration surface, in the opposite direction to the projectile motion, are larger, which can be seen by considering the relative sizes of the red areas, representing larger magnitude displacements. This suggests that the ogive projectile causes less displacement of the material in the opposite direction to the projectile motion than with a flat-ended projectile. Considering the lateral (dx) displacements, we can see that the ogive projectile causes slightly more lateral displacement than the flat-ended projectile. The envelope of lateral displacement extends further from the projectile axis for the ogive rod and the maximum lateral displacement is slightly larger (1.8 mm versus 1.5 mm).

These results show that the ogive rod causes less deformation of the material ahead of the projectile tip. Rather than pushing material ahead of the projectile, leading to compaction and disruption of the sample ahead of the projectile, more material is split laterally and pushed to the sides. The increased lateral displacement, and the reduction in the amount of sand being pushed in front of the ogive tip, is logical given its shape. The sharp nose cone is likely to push material away from the tip at a considerable angle relative to the projectile axis. This reduces the volume of material being propelled ahead of the rod and increases the extent of the lateral displacements. The reduction in the longitudinal displacements in the opposite direction to the rod motion at the surface of the sample is less obvious. The flat-ended projectile pushes a larger body of sand to a greater extent in the longitudinal direction. This inevitably leads to compaction of the material ahead of the projectile, a process which generates a larger resistive force than

6.4 Penetration by Ogive-Tipped Projectiles

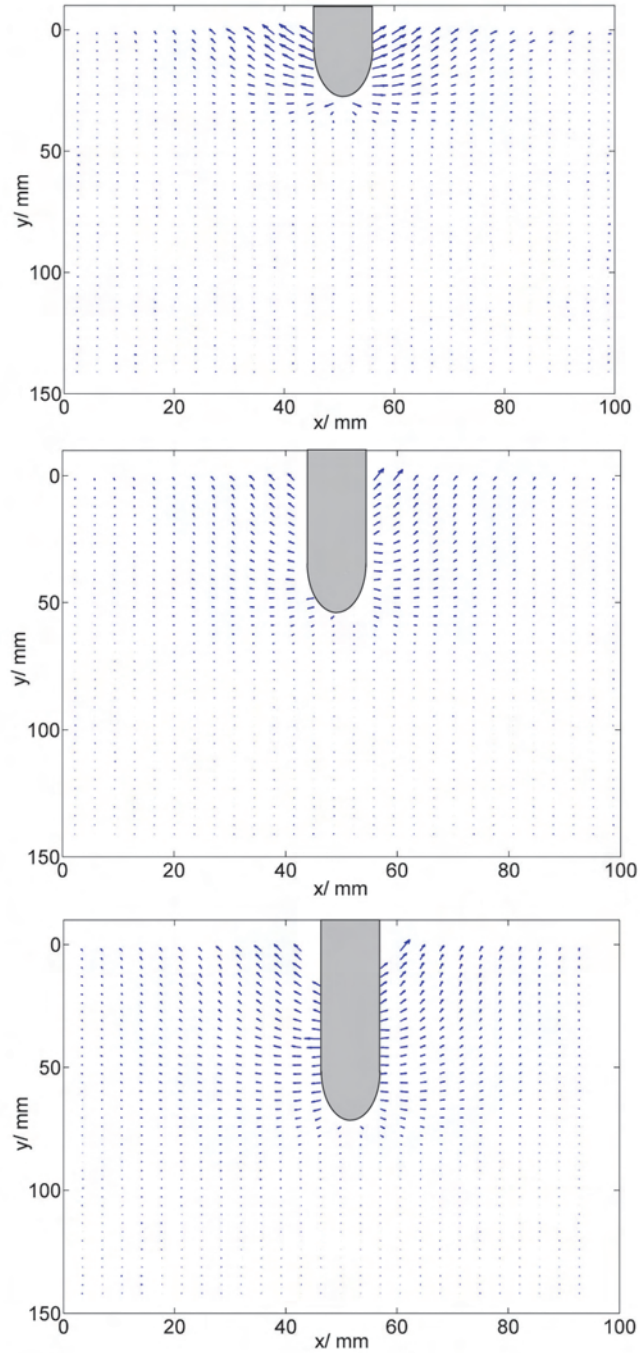


Figure 6.17: Three quiver plots showing the penetration of a sample at 1.5 mm/min by an ogive nosed projectile.

6. QUASI-STATIC PENETRATION

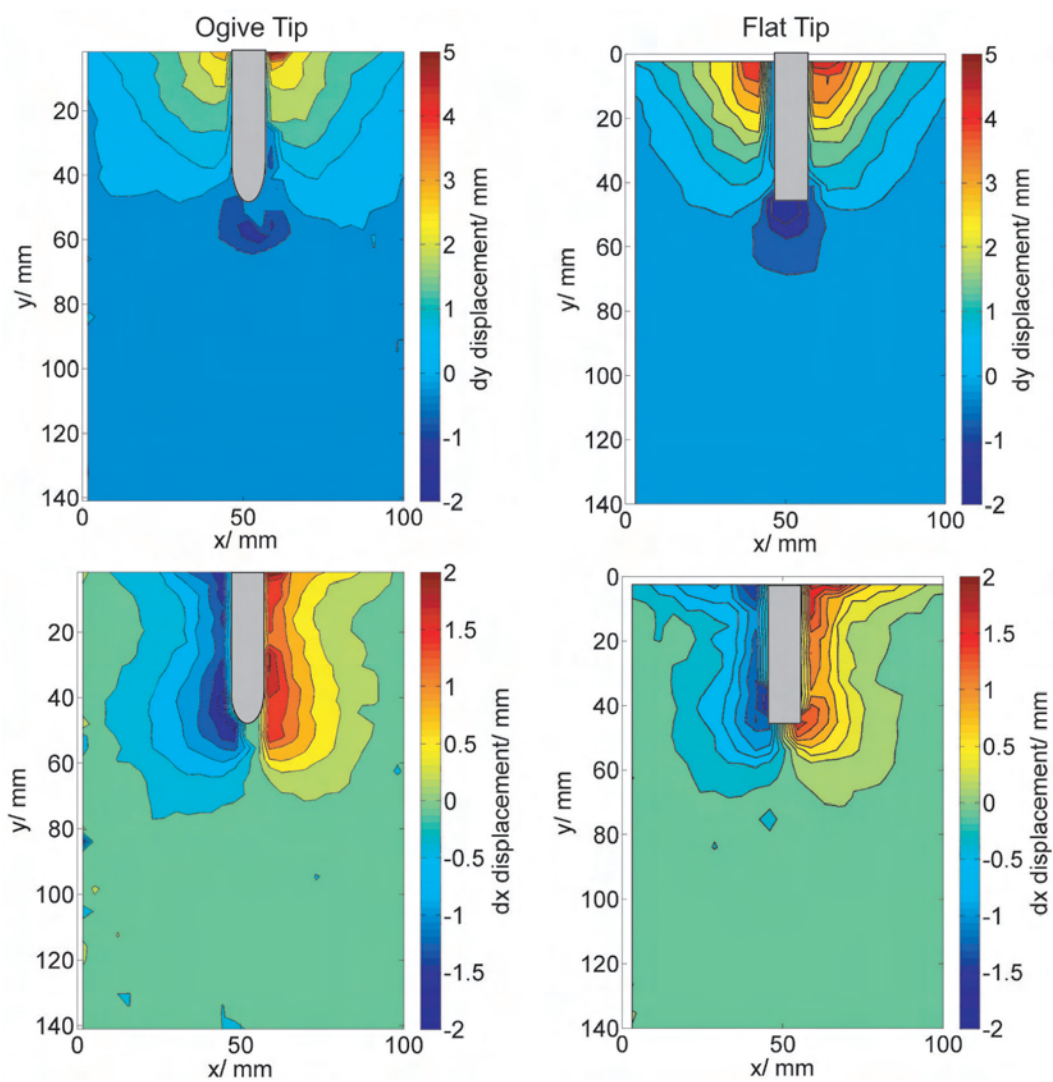


Figure 6.18: Comparing the longitudinal (top images) and lateral (bottom images) displacements for penetration by ogive (left) and flat-ended (right) rods at a penetration depth of approximately 43 mm.

splitting the material - it being more difficult to compact material than to cause it to flow. The reduced reaction force experienced by the projectile with an ogive nose cone during the penetration is therefore likely caused by the way in which it more effectively splits the material ahead of the nose tip, rather than compacting it.

6.5 Summary

In summary:

- The displacements generated during quasi-static penetration at a velocity of 1.5 mm/min are substantially different to those found with dynamic penetration (at a velocity of 200 ms⁻¹).
- At the quasi-static rate there is significantly less disruption of the material ahead of the projectile tip, both in terms of extent and magnitude, than in the dynamic case. What deformation there is, is localised to the area directly ahead of the projectile tip, rather than spread across the width of the sample as for dynamic penetration.
- Large areas of material, down to the projectile tip, are found to be moving upwards towards the upper face of the sample by as much as 6 mm, leading to the formation of a crater around the projectile shaft on the penetration face.
- The different response is likely due to the relative importance of friction between the two cases. At a low rate, the forces on individual sand grains are low (up to 140 N ignoring force-chains). The grains are therefore able to move relatively freely in response to the force, including moving to fill voids. Where grains are in contact the forces are transmitted towards the surface causing material at the surface to rise.
- At a high rate, the forces experienced by the grains are much higher (up to 14 kN). Friction between the grains is therefore more significant and the grains are constrained to move more in the direction of the applied force,

REFERENCES

as they are not freely able to move to fill neighbouring voids. This leads to significant amounts of material moving in the direction of the projectile and causes compaction of material ahead of the projectile.

- At a low rate of penetration, ogive nose cones are found to be more effective at penetrating granular materials, in the sense that they experience a smaller force and would therefore maintain a higher velocity. This is due to the way in which the nose cone efficiently splits the material ahead of the rod, leading to smaller displacements and a smaller extent of disruption ahead of the projectile tip.

References

- [1] Allen, W.A., Mayfield, E.B. and Morrison, H.L., “Dynamics of a Projectile Penetrating Sand”, *Journal of Applied Physics*, **28(3)**, (1957), 370–376
- [2] Borg, J.P. and Vogler, T.J., “Mesoscale simulations of a dart penetrating sand”, *Int. Journal of Impact Engineering*, **35**, (2008), 1435–1440
- [3] Grantham, S.G., Proud, W.G. and Field, J.E., “Internal Displacements in Cement During Ballistic Impact”, *Shock Compression of Condensed Matter*, **706**, (2003), 1335–1338
- [4] Grantham, S.G. and Forsberg, F., “Measurement of granular flow in a silo using digital speckle radiography”, *Powder Technology*, **146**, (2004), 56–65
- [5] Burr, G.S., *Controlling in Materials Testing*, US Patent No. 3391572, US (1966)

Chapter 7

Intermediate Rate Penetration

7.1 Introduction

We saw in the previous chapter that there is a significant difference in the response of the material to penetration at effectively quasi-static and dynamic rates. This is perhaps unsurprising due to the large difference in the rate of the penetration (a factor of 10^7 in the penetration velocity). It is suggested that the change in the response of the sand to penetration between the two rates is explained by the magnitude of the force felt by individual grains, and the change from static to dynamic friction. An interesting question to consider is whether the transition between these two types of deformation happens rapidly, and if so at what velocity, or whether there is a more gradual transition over a larger range of velocities.

The experiments presented in this chapter aim to answer this question. For consistency, projectiles with ogive-2 nose cones are used in all of the experiments (refer to Chapter 4 for details of the projectile geometry). Initial experiments performed to measure the force experienced by the projectile during penetration at rates ranging from 4 mm/min ($7 \times 10^{-5} \text{ ms}^{-1}$) to 400 mm/min ($7 \times 10^{-3} \text{ ms}^{-1}$) using the Instron machine showed no significant variation in the force with penetration velocity. Graphs detailing the measured forces for four different rates of penetration are shown in Figure 7.1. At each penetration rate, four different experiments were carried out and the results were averaged. At a given penetration

7. INTERMEDIATE RATE PENETRATION

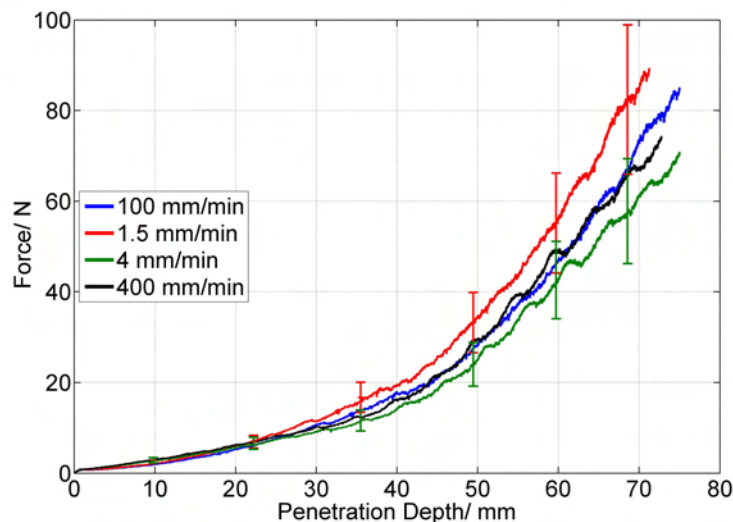


Figure 7.1: The effect of penetration velocity on the normal force experienced by the projectile during Instron experiments. The error at each velocity was estimated from the variations in the force between four repetitions.

rate, there were variations of up to 20% in the response of the material for nominally identical repetitions with the same mass of sand, density and sample size. These variations are caused by the differing grain arrangements in the samples and variations in packing and porosity, demonstrating the significant impact that grain arrangement and porosity can have on the behaviour of a granular sample (these factors will be discussed in more detail in Chapters 9 and 10).

Within the errors (estimated from the variations between the repetitions), the plots are consistent with there being no velocity dependence on the measured force, suggesting that the material response is the same at all four velocities of penetration. The displacement fields are therefore unlikely to differ from the displacements measured during penetration at 1.5 mm/min. This was confirmed for the 400 mm/min case by performing DIC on X-ray images of the penetration. The measured displacements were consistent with those observed at the lower rate of penetration. Any transition between deformation regimes must therefore occur at higher velocity.

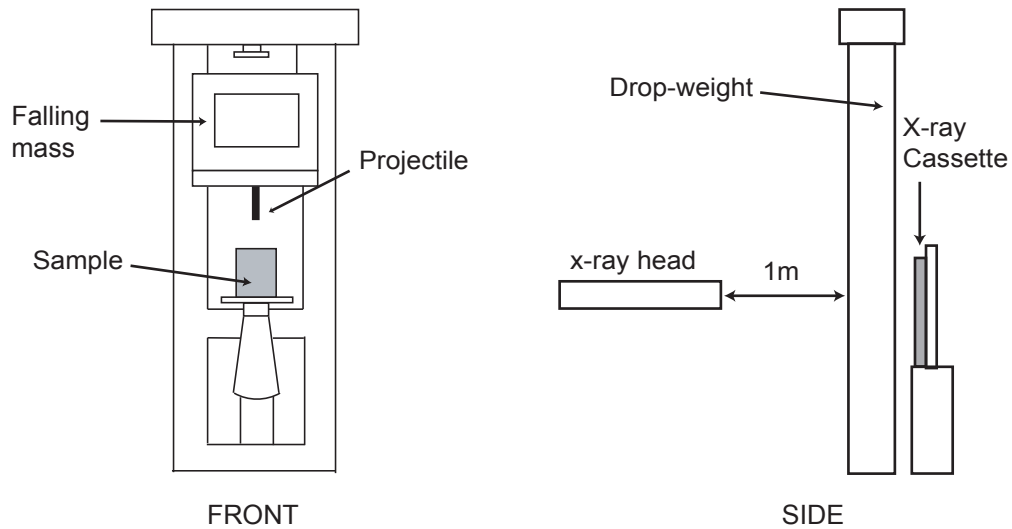


Figure 7.2: A schematic of the Cavendish drop-weight facility, showing a front view of the apparatus and a side view with the X-ray system set up.

7.2 Drop-Weight Experiments

To investigate penetration at a higher velocity, the Cavendish drop-weight apparatus was used to achieve a penetration velocity of $(5.0 \pm 0.2) \text{ ms}^{-1}$. The drop-weight consists of a 6.414 kg mass dropped from a height of 1.2 m. The apparatus is discussed in more detail in Chapter 9. The falling mass is guided by two external steel guide rods, so that it is constrained to only move in the vertical direction. An ogive-2 projectile was secured in the centre of the falling mass and an alignment rig was used to align the sample at the impact point so that the penetration would occur along the central axis of the cylindrical sample. A schematic of the drop-weight facility with the sample set up is shown in Figure 7.2.

It is important to recognise that these experiments differ somewhat from the dynamic penetration experiments. While in the dynamic experiments the velocity of the projectile varied significantly, in these experiments the projectile is attached to a mass of 6.4 kg. The large mass of the combined mass and projectile means that the velocity of the projectile varies little during the penetration process. As

7. INTERMEDIATE RATE PENETRATION

for the Instron experiments, the penetration occurs along a vertical axis rather than a horizontal axis.

In these experiments the X-ray head was mounted at a distance of 65 cm from the front of the sample holder (limited by the available space). The X-ray cassette was mounted at a distance of 50 mm behind the back of the sample holder and was arranged so that its face was in the same orientation at the sample holder.

Six separate drop-weight experiments were performed to investigate the temporal progression of the penetration, the details of which are listed in Table A.5 in the Appendix. Some examples of the measured displacements calculated using DICC are shown as contour plots in Figure 7.3 for penetration depths of 22, 43 and 56 mm. The form of displacement occurring within the samples appears fairly similar to that observed with the lowest penetration rates achieved using the Instron machine. The longitudinal displacements measured at the same depth of penetration for penetration at low rates (using the Instron), and the higher rate of 5 ms^{-1} achieved with the drop-weight, are compared side by side in Figure 7.4. The contours of longitudinal displacement have a similar form in both cases. In particular, there is a similar shaped area of material down to the tip of the projectile that is moving upwards towards the penetration face with a similar level of displacement (up to 4 mm).

The main difference in the longitudinal displacements is the extent of deformation occurring ahead of the projectile tip. In the quasi-static case, the maximum displacements ahead of the projectile reach 0.55 mm in magnitude. For the higher velocity penetration of 5 ms^{-1} , using the drop-weight, the displacements ahead of the projectile tip are larger, reaching 1.6 mm in magnitude. There is also a larger area ahead of the projectile that is affected in the drop-weight case. The larger displacements ahead of the projectile tip suggest that more compaction occurs in this region. The maximum measured displacements ahead of the projectile tip are a little lower than those measured with the higher velocity dynamic penetration experiments. The extent to which these displacements extend ahead of the projectile tip is also smaller, as is the lateral extent of the deformation ahead of the projectile tip. Although there is more compaction going on ahead of the projectile, there has been no significant transition to the form of displacement observed for dynamic rates.

7.2 Drop-Weight Experiments

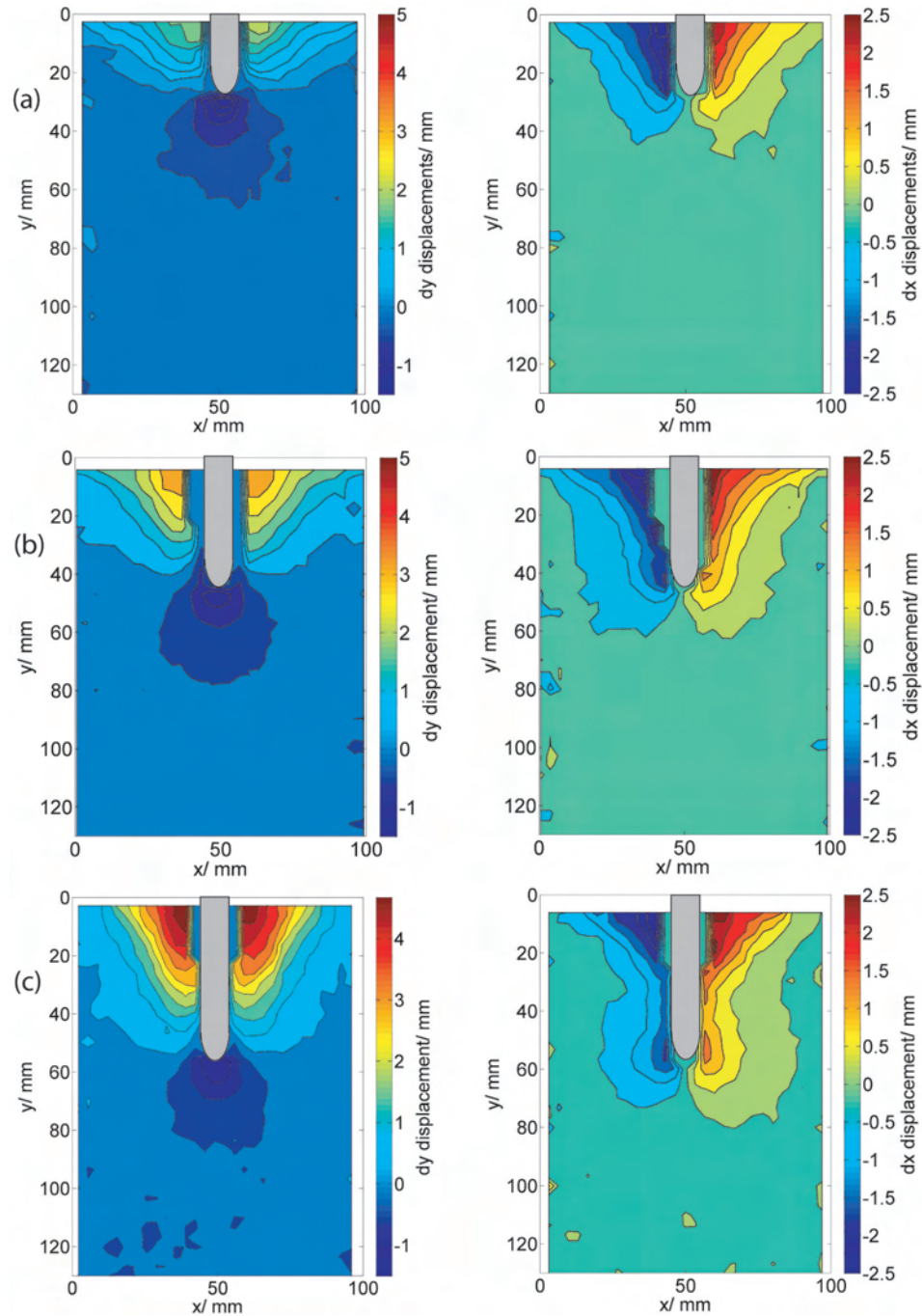


Figure 7.3: Contour plots showing the longitudinal (left) and lateral (right) displacements occurring during dropweight penetration experiments for penetration depths of (a) 22, (b) 43 and (c) 56 mm.

7. INTERMEDIATE RATE PENETRATION

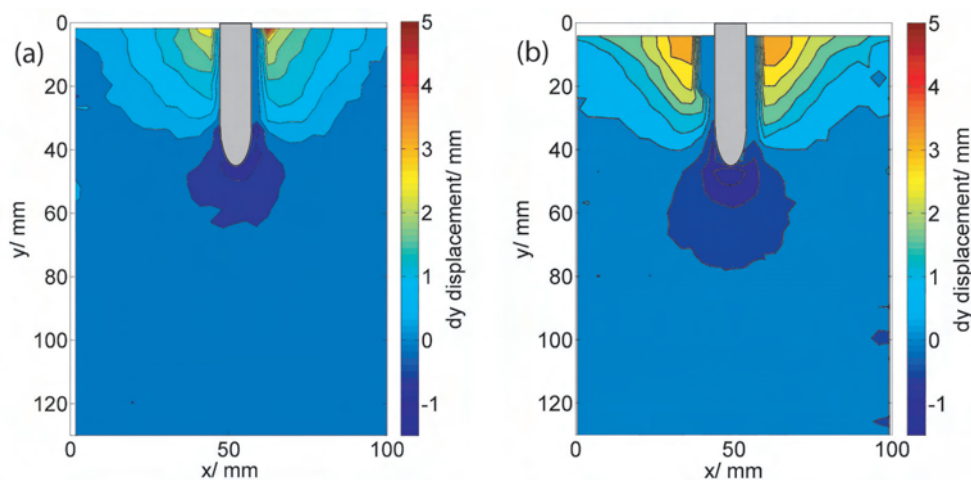


Figure 7.4: Contour plots comparing the longitudinal displacements, for the same extent of penetration, for the Instron (a) and drop-weight (b) experiments.

7.3 Light Gas-Gun Experiments

The behaviour of the sample has been shown to be ‘quasi-static’ in form for velocities of 5 ms^{-1} and under and ‘dynamic’ in form at 200 ms^{-1} . To continue investigation of the transition between these two regimes, the light gas-gun discussed in Chapter 4 was used to generate ogive projectiles with velocities ranging from 8 ms^{-1} up to 200 ms^{-1} . Lower velocity projectiles were generated by using a lower firing pressure of the light gas-gun than for the experiments discussed in Chapters 4 and 5. The experimental set-up was identical to that used in the previous gas-gun experiments discussed in Chapters 4 and 5. Penetration experiments were carried out at velocities of 150, 100, 55, 30, 19, 12 and 8 ms^{-1} . Due to the un-reliability of the light gas gun at low velocity (the velocity can vary by $5\text{-}10 \text{ ms}^{-1}$ when firing the projectiles at low velocity), the depth of penetration varies somewhat between the experiments. Although it is therefore not necessarily possible to directly compare the magnitude of the displacements between the experiments, they will clearly show any transition in the form and shape of the displacement occurring. The results are presented as contour plots showing the longitudinal (dy) and lateral (dx) displacements in Figures 7.5, 7.6 and 7.7.

7.3 Light Gas-Gun Experiments

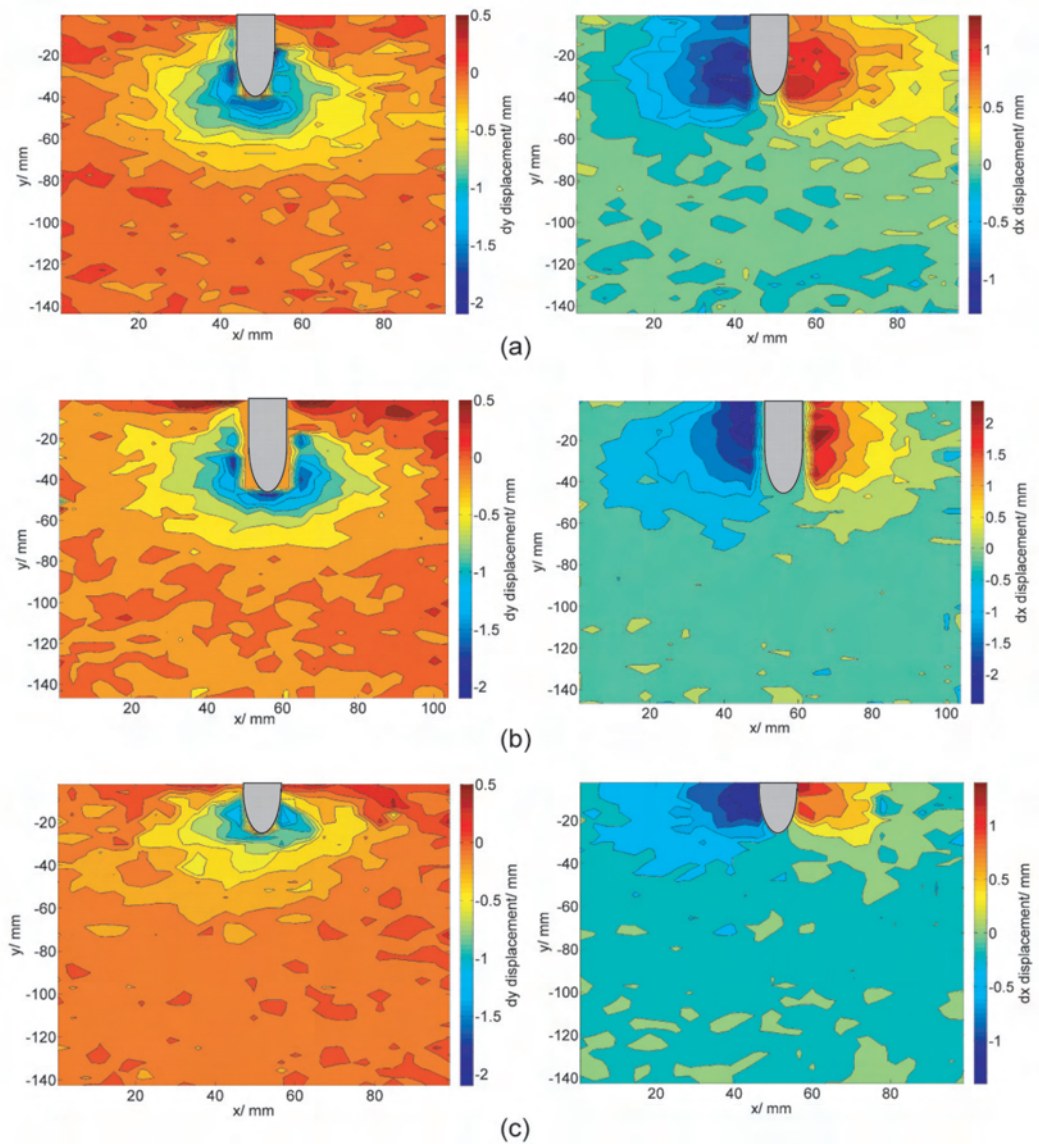


Figure 7.5: Contour plots showing the measured longitudinal (left) and lateral (right) displacements with a penetration velocity of (a) 150 ms⁻¹, (b) 100 ms⁻¹ and (c) 55 ms⁻¹. The extent of penetration varies between the images for reasons discussed in the text.

7. INTERMEDIATE RATE PENETRATION

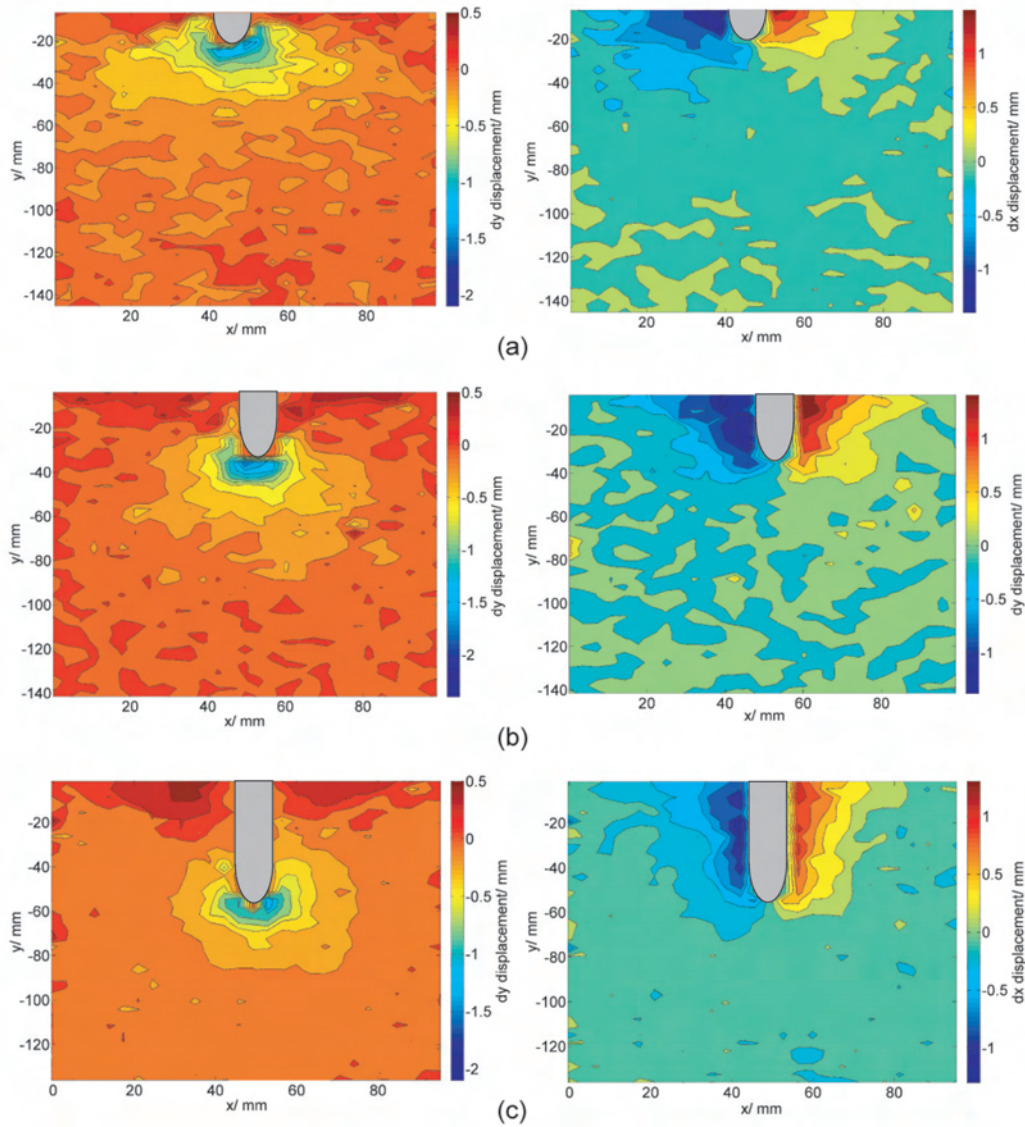


Figure 7.6: Contour plots showing the measured longitudinal (left) and lateral (right) displacements with a penetration velocity of (a) 30 ms⁻¹, (b) 19 ms⁻¹ and (c) 12 ms⁻¹. The extent of penetration varies between the images.

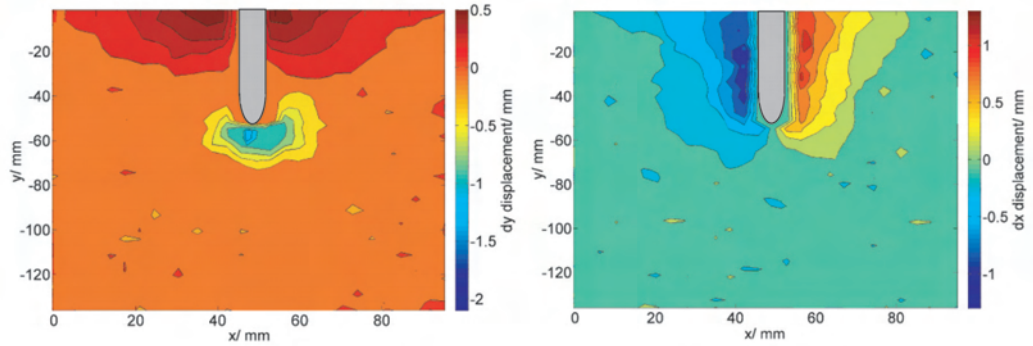


Figure 7.7: Contour plots showing the measured longitudinal (left) and lateral (right) displacements with a penetration velocity of 8 ms^{-1} .

The contour plots presented in these three figures show the effect of penetration velocity on the response of the sand to penetration. The first four images, covering a velocity range of 200 ms^{-1} to 30 ms^{-1} , show a similar behaviour to that observed with dynamic penetration. In particular, the longitudinal displacements show a cone shaped region of material, with the position of impact on the front surface at the point, moving longitudinally and causing wide-spread deformation of the material ahead of the projectile tip. This feature was observed in the dynamic penetration experiments discussed in Chapters 4 and 5. There is some evidence in (c) of Figure 7.5 and (a) of Figure 7.6 of an increase with velocity of the angle that the outside of this cone makes with the vertical, leading to a flatter appearance of the longitudinal displacements around the projectile tip. The magnitude of the longitudinal displacements directly ahead of the projectile tip decreases somewhat with the impact velocity, falling from 2 mm at 200 ms^{-1} to around 1.3 mm at 30 ms^{-1} . To the sides of the projectile axis on the impact face are lobes of material moving upwards by up to 0.4 mm . The lateral displacements show that the lateral deformation is roughly uniform along the axis of the projectile and consistent with that observed with dynamic penetration.

The appearance of the displacement fields begins to change around a velocity of 19 ms^{-1} , shown in (b) of Figure 7.6. The lateral displacement field at a penetration velocity of 19 ms^{-1} is similar to that observed with the 5 ms^{-1} drop-weight penetration experiment at a similar extent of penetration. The envelope

7. INTERMEDIATE RATE PENETRATION

of lateral displacements is cone shaped, with more material near to the surface having been disturbed laterally than near the projectile tip. The longitudinal displacements appear to have become more localised to the region in front of the projectile tip.

The differences become more significant for an impact velocity of 12 ms^{-1} , shown in (c) of Figure 7.6. At this velocity, the amount of material moving longitudinally in the same direction as the projectile is significantly reduced. In particular, the material to the side of the projectile axis no longer all moves in the same direction as the projectile. Instead, most of the material to the side of the projectile, down to half the penetration depth, is moving upwards towards the impact face, in the opposite direction to the projectile motion. The lobes of material moving upwards through the penetration face are larger and extend to a greater depth into the material, although still not to the projectile tip, as was observed for the quasi-static penetration experiments. The longitudinal deformation ahead of the projectile tip is no longer spread across the width of the sample. Instead, only material within 20 mm laterally of the projectile axis is deformed ahead of the projectile tip.

For a penetration velocity of 8 ms^{-1} , shown in Figure 7.7, the displacement fields more closely resemble those observed at quasi-static penetration rates than those observed at dynamic rates. The extent to which material ahead of the projectile tip has been deformed is significantly reduced relative to the higher velocity penetration. Only material within 10-15 mm of the projectile tip has been displaced longitudinally ahead of the projectile. Significantly larger amounts of material are moving upwards, releasing through the penetration face. The upwards displacements reach 0.5 - 1 mm in magnitude. This is still significantly smaller than the maximum displacements observed in this area at the quasi-static rate, which reached 5 mm in magnitude. It is possible that this difference may be due to the low momentum of the penetrator at this velocity (8 ms^{-1}) for the light gas-gun experiment. In the quasi-static penetration experiments, the velocity of the projectile was held constant.

These experiments show that there is a transition in the appearance of the displacements occurring during penetration of the sample between a velocity

of 5 ms^{-1} and 19 ms^{-1} . During this velocity range, the form of the displacement changes from a ‘dynamic’ regime to a ‘quasi-static’ regime. In the dynamic regime, the dominant form of deformation is compaction of the material around the projectile and ahead of the projectile tip through the action of a travelling compaction front. In the quasi-static regime, the dominant form of deformation involves splitting of the material ahead of the projectile tip and subsequent fluid-like, bulk reverse-flow of material in the opposite direction to the projectile motion, towards the penetration face.

The determining factor as to which process is dominant (bulk flow or compaction) is likely to be the magnitude of the frictional forces between the grains. When the frictional forces between grains are low, they are able to freely rotate and move relative to each other. This allows individual grains to move in directions other than that in which the force is applied, for example to move laterally into a pore or packing defect. This causes the material to behave in a more fluid-like manner, and causes the observed flow of material towards the penetration face, where the forces applied by the projectile can be released. Where the frictional forces between grains are high, the grains are unable to freely move or rotate relative to each other. Instead, the grains lock together and are constrained to move in the direction of the applied force. This leads to the material ahead and to the sides of the projectile moving in the direction of penetration, which causes a compaction front in the material.

A rough estimate of the forces experienced by the sand grains during the penetration can be determined by calculating the average force required to decelerate the projectile. If an X-ray is taken during the penetration at a time Δt after impact, and the projectile is found to have penetrated to a depth D in the sample, the average penetration velocity over this period, v_a , is

$$v_a = \frac{D}{\Delta t}. \quad (7.1)$$

If the initial velocity of the projectile is v_i , an estimate of the energy lost by the projectile during the penetration process is (to be fully correct the final velocity should be the instantaneous velocity at this time rather than the average velocity over the time period)

7. INTERMEDIATE RATE PENETRATION

$$E = \frac{m(v_i^2 - v_a^2)}{2}. \quad (7.2)$$

An estimate of the average resistive force acting to decelerate the projectile during this period can then be calculated as,

$$F_r = \frac{E}{D}. \quad (7.3)$$

This mean resistive force has been calculated for a number of different initial penetration velocities and the results are displayed in the graph in Figure 7.8. The X-ray delay times range from 350 μs at 200 ms^{-1} to 4500 μs at 8 ms^{-1} and the penetration depths range from 64 mm to 29 mm. The graph shows that the approximate average resistive force experienced by the projectile varies significantly with the initial impact velocity, with the average force rising from 35 N to 2500 N as the impact velocity increases. Although it is difficult to predict the forces experienced by individual sand grains using this data, it is sensible to assume that the forces on the grains will be greater when the projectile feels a greater resistive force, as the sand sample generally must feel an equal and opposite force to that experienced by the projectile. This assumption ignores the effects of force chains and voids within the material, which would cause localised areas of higher stress.

As the frictional force between two sand grains is directly related to the normal force between the two grains (R),

$$F_{friction} = \mu R, \quad (7.4)$$

the frictional forces between the grains will roughly increase with the force experienced by the projectile. The graph in Figure 7.8 therefore suggests that the frictional forces between sand grains will increase significantly (by almost two orders of magnitude) over the velocity range of 8 - 200 ms^{-1} . It should be recalled that the formation of force chains in the system can lead to the concentration of pressure along chains of particles, leading to normal and frictional forces between particles significantly larger than the estimates presented in Figure 7.8.

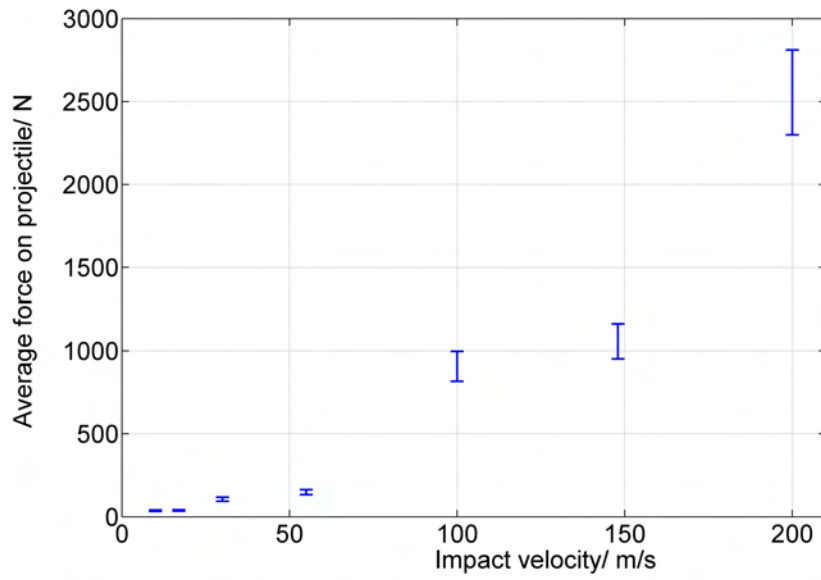


Figure 7.8: The approximate average force experienced by the projectile, averaged over the early stages of penetration (up to 60 mm), as a function of the initial impact velocity.

7. INTERMEDIATE RATE PENETRATION

There is no evidence in the graph in Figure 7.8 for a significant or sharp decrease in the average resistive force around 19 ms^{-1} . It is around this velocity that the form of the displacement began to change noticeable between the dynamic and quasi-static regimes. What is clear though is that at velocities of 30 ms^{-1} or under, the frictional forces are likely to be significantly reduced relative to those at higher velocity. This suggests that the magnitude of the frictional force is important in determining what form of deformation will occur during the penetration process.

7.4 Summary

- With a penetration velocity of 5 ms^{-1} , obtained using the drop-weight, the displacement fields are similar to those observed with quasi-static penetration rates.
- At 5 ms^{-1} , there are larger magnitude displacements directly ahead of the projectile tip (1.6 mm versus 0.6 mm) and more significant lateral displacement for the first few cm of penetration than was observed for the quasi-static penetration.
- For initial impact velocities between 30 ms^{-1} and 200 ms^{-1} , the deformation fields are similar to those observed with dynamic penetration at 200 ms^{-1} , although the magnitude of the displacements ahead of the projectile tip falls with the impact velocity.
- As the impact velocity is further reduced there is a transition between the dynamic and quasi-static regimes of deformation. This occurs between 5 ms^{-1} and 19 ms^{-1} .
- Below 19 ms^{-1} , the deformation occurring ahead of the projectile tip decreases significantly, as does the lateral extent of the deformation ahead of the tip. The amount of material moving towards the impact face, in the opposite direction to the projectile motion, increases.

- The main mode of deformation appears to change from compaction of the material at high rates (a compaction front is clearly visible) to a more fluid-like behaviour where bulk reverse-flow of material towards the impact face occurs.
- The force experienced by the projectile increases significantly with initial impact velocity, with estimates of the average force ranging from 35 N at 8 ms^{-1} to 2500 N at 200 ms^{-1} .
- The force experienced by the material around the projectile tip is likely to scale with the force experienced by the projectile (ignoring force localisation through the formation of force chains). Therefore the normal force between grains, and the subsequent frictional force, will likely increase with penetration velocity.
- When the impact velocity and therefore the frictional forces between grains are high, the material locks-up and is constrained to move in the direction of the applied force - the grains cannot rotate or move freely relative to each other. This leads to the observed compaction front.
- When the impact velocity and the frictional forces are low, the grains are able to move and rotate more freely relative to each other. This leads to a more fluid-like behaviour of the material, where the grains are not constrained to move in the direction of the applied force and the stresses can instead be released by material flowing towards the impact face.

7. INTERMEDIATE RATE PENETRATION

Chapter 8

Simulation and Comparison with Other Materials

8.1 Comparison with Other Materials

In the past, a number of researchers have tried to model the flow of granular materials using a hydrodynamic approach [1, 2]. The models are hydrodynamic in the sense that they are based on continuum theories consisting of partial differential equations, analogous to the Navier Stokes equations found with Newtonian fluids [3]. The viability of a hydrodynamic state of evolution of a granular system is determined by factors such as particle density, particle roughness and the coefficients of friction and restitution. In the flow of granular materials, the collisions between particles are inherently inelastic. A hydrodynamic state will exist only if the coefficient of restitution exceeds some critical value [4]. This is more likely to occur during rapid flow of particles at low density, in which the particles interact mainly through infrequent and fast impacts. At a slower rate of flow or a greater density, the inter-particle friction forces are likely to be more dominant. The particles will be continually moving and rotating relative to the surrounding particles, leading to significant energy dissipation.

Fluid dynamic equations are derived using time and length-scale averaging processes that are not necessarily appropriate for granular materials. Such length scales are by definition larger than the size of the particles. The size of the system being analysed may only be of the order of hundreds or thousands of particles.

8. SIMULATION AND COMPARISON WITH OTHER MATERIALS

This may frequently be insufficient to assume that the sample behaves homogeneously on the chosen scale, particularly as force chains may span hundreds of particles. By failing to consider the grain level behaviour of the material, hydrodynamic approximations break down where the number of particles in the sample, or the size of a column of flow, is small. Effects such as jamming and locking of the particles to form a blockage in a narrow opening are impossible to predict with such models. Other phenomena, such as the instability of projectiles during penetration cannot be modelled. During penetration, the heterogeneous structure of the granular material can lead to asymmetric loading of the projectile tip, which can cause the projectile to deviate from its original path and lead to phenomena such as tumbling and bending of the projectile [5].

Despite these inherent flaws, hydrodynamic based models have been used with some success to analyse the behaviour of granular materials in motion [1]. A good review of this subject is given by Heinrich *et al.* in [2]. An early example is the research of Byers *et al.*, who produced a Lagrangian wavecode to investigate the stresses and resultant velocities generated in simulated earth penetrations [3]. The code treated the target material as homogeneous and split it into a grid of cells. Masses within these cells were modelled as moving in response to local stress gradients. By solving the partial differential equations of motion the resulting velocities and displacements within the material could be determined.

A guide to whether the sand discussed in the preceding chapters is behaving in a hydrodynamic sense during penetration can be determined by experimentally comparing the displacements with those measured during experiments on a material that is known to behave hydrodynamically. If the displacement fields are found to be similar, it is likely that the behaviour of the sand can be modeled hydrodynamically. If there are significant differences in the displacement fields this would confirm that the observed displacements are caused by the heterogeneous granular structure.

8.1.1 Gelatine

The obvious choice for a material that behaves hydrodynamically is water. Experimental limitations, however, such as trying to include a plane of visible contrast

8.1 Comparison with Other Materials

variation, rule this out. Ideally, a significantly more viscous or even solid material would be more suitable for experimentation. A suitable substitute is to use a Gelatine based sample. As the resulting mixture is homogeneous and composed mostly of water, it will behave in a similar manner to water.

For the purposes of comparison with the earlier displacement data measured during penetration of sand, it is helpful to use the same cylindrical sample holder. A liquid gelatine sample was produced by mixing one litre of hot water and 45 g of gelatine powder. This was added to the cylindrical sample holder in stages to produce a sample containing a horizontal layer of lead filings, for the purposes of DSR. The completed sample was mounted in the catch chamber of the light gas-gun using the alignment rig discussed in Chapter 4 and was aligned so that it was uniaxial with the gun barrel. The same experimental procedure as discussed in Chapter 4 was used to generate flash X-ray images of the penetration occurring for a flat-ended projectile with an initial velocity of 200 ms^{-1} . Initially, the displacement fields were measured for a penetration depth of 36 mm. The measured lateral and longitudinal displacements are shown in Figure 8.1.

At this relatively low depth of penetration of approximately 40 mm, the entire sample has been noticeably disturbed. The contour plot of the lateral displacements shows that the material down to the tip of the projectile has been pushed sideways, causing compaction of the material. Unlike with the sand there is little obvious splitting of the material ahead of the projectile tip. The contour plot of the longitudinal displacements presents a considerably more confusing picture. There is a hemispherical area around the impact point where the material has been displaced longitudinally. This makes sense as the projectile will obviously displace a volume of material during the penetration. The situation ahead of the projectile tip is more complicated. The entire sample has moved longitudinally by up to 4 mm. The longitudinal displacements initially decrease in magnitude upon moving away from the rod tip but then apparently increase in magnitude again when nearing the rear surface. It appears that there has been some oscillation in the longitudinal displacements.

This oscillation is likely due to travelling pressure waves generated upon impact. The oscillation of these waves within the sample, including reflection from

8. SIMULATION AND COMPARISON WITH OTHER MATERIALS

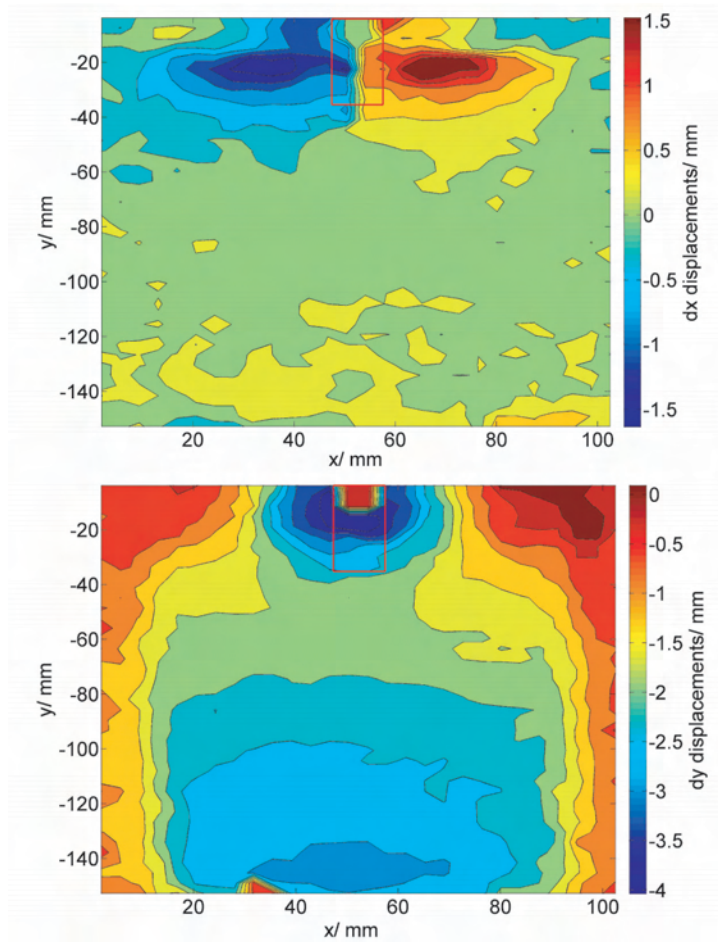


Figure 8.1: Lateral (top image) and longitudinal (bottom image) displacements measured in a cylindrical Gelatine sample during penetration by a flat-ended projectile with an initial velocity of 200 ms^{-1} , at a penetration depth of 36 mm.

8.1 Comparison with Other Materials

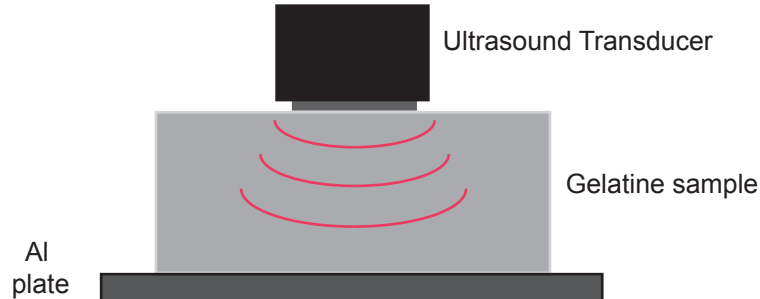


Figure 8.2: A diagram of the ultrasound transducer mounted above a sample of Gelatine. The ultrasound pulse is reflected at the boundary with the Al plate due to the impedance mismatch.

the sample boundaries, would cause considerable variation in the measured displacements. To investigate this in more depth, ultrasound transducers were used to measure the longitudinal sound speed within the gelatine. A 5 MHz Panametrics ultrasound transducer/receiver attached to a variable height stand was used to generate longitudinal ultrasound pulses in various thicknesses of gelatine, as shown in Figure 8.2. The gelatine samples were mounted on an aluminium sheet, where the ultrasound pulse is reflected due to the large difference in impedance. The reflected wave is detected by the ultrasound transducer/receiver, allowing the travel time of the pulse to be measured. The exact travel time is difficult to measure, due to some ambiguity as to the start point on the pulse, but by comparing the relative travel time for a variety of samples of known difference in thickness an accurate estimate of the longitudinal sound speed can be calculated.

A plot of the variation of the travel time of the pulse as a function of the thickness of the sample, taking into account that the pulse travels twice the thickness of the sample before being detected by the transmitter/receiver, is shown in Figure 8.3. A straight line has been fitted to the data and the gradient, which is the longitudinal sound speed of the gelatine, is $(1481 \pm 5) \text{ ms}^{-1}$. This value is very close to the sound speed in water which is 1497 ms^{-1} at room temperature (25°C) and pressure.

A second experiment with an X-ray delay time of $50 \mu\text{s}$ was performed, so that any pressure waves generated in the sample would be visible. With a longitudinal

8. SIMULATION AND COMPARISON WITH OTHER MATERIALS

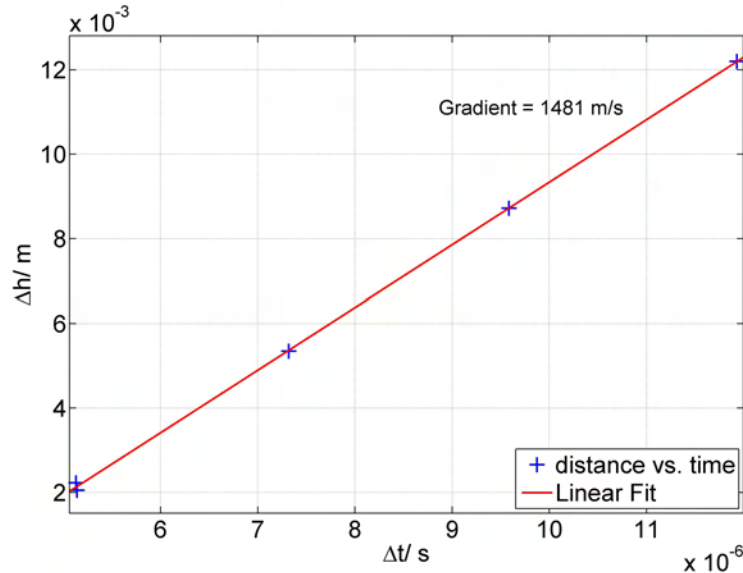


Figure 8.3: A plot of the increase in height of the gelatine sample against the increase in travel time of the ultrasound pulse. The gradient of the fitted straight line gives the longitudinal sound speed in the material.

sound speed in the material of 1481 ms^{-1} the pressure waves should have reached a depth of around 70 mm. Figure 8.4 shows the longitudinal (dy) displacements measured at $50 \mu\text{s}$ after impact. There is a roughly hemispherical shaped area extending to 60-70 mm into the sample, behind which the material has been displaced longitudinally. At this point the projectile had penetrated to a depth of around 10 mm. This confirms that there is a pressure wave travelling through the sample at the sound speed of the material and expanding radially from the point of impact.

The displacements observed here are very different to those observed in the sand samples. For a hydrodynamic material, two main forms of deformation occur. As the projectile must physically occupy some volume of the sample, localised displacement of the material directly around its location occurs. This can be observed in the plot of longitudinal displacements shown in Figure 8.1. The second main cause of deformation is a pressure wave travelling at the speed of sound within the material. The action of this pressure wave means that by

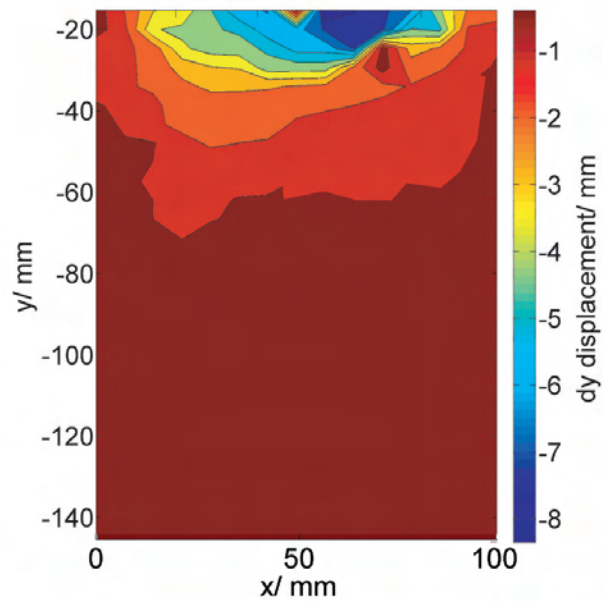


Figure 8.4: Longitudinal displacements generated in a cylindrical Gelatine sample during penetration by a flat-ended projectile with an initial velocity of 200 ms^{-1} . Dynamic image taken $50 \mu\text{s}$ after impact. There is a travelling pressure wave that has reached a distance of 60 - 70 mm into the sample at this time. The position of the projectile tip is just visible in the small area of failed correlation at the top of the image.

8. SIMULATION AND COMPARISON WITH OTHER MATERIALS

only 100 μs after impact the whole sample will have been affected and significant displacements will be measurable even at the rear surface, as observed for a later time in Figure 8.1 where the action of this pressure wave has caused significant variations in displacement throughout the sample.

It is the action of these pressure waves that seems to differentiate the behaviour of a hydrodynamic material from the behaviour of the sand. Because of dissipative processes, such as friction between grains and void filling, a loosely packed sample of sand is unable to sustain a pressure wave for any significant length of time. Indeed, even a small thickness of sand is sufficiently dissipative that it is not possible to measure the sound speed of the material using the ultrasound technique used for the gelatine, as no significant transmitted or reflected wave can be detected. Rather than the displacements in sand being caused by a pressure wave travelling at the speed of sound in the material, they are instead caused by bulk flow of material into the sample in the form of a compaction front.

8.1.2 Concrete

Another interesting comparison is to compare the behaviour of sand during penetration with that of concrete, an inhomogeneous solid which contains various grains, inclusions and pores. Concrete samples were made up using the same sand used in the previous penetration experiments. The exact composition of the concrete is shown in Table 8.1. Cylindrical samples of concrete containing a layer of scattered lead shot were produced by first making a larger square sample in stages and then turning it down on a lathe. To confine a sample, a cylindrical acrylic tube with a diameter slightly larger than the sample was used. Epoxy was used to fill the small gap between the sample and the tube, securely holding and confining the sample. The samples were mounted in the catch chamber in an identical manner to that discussed in Chapter 4 and penetration was carried out using flat-ended projectiles with initial velocities of $(200 \pm 4) \text{ ms}^{-1}$.

At 200 ms^{-1} , the depth of penetration achieved by the projectiles was relatively small, the terminal penetration depth generally being at most 25 - 30 mm. There was also an obvious crater formed in all of the shots where the material in the immediate vicinity of the projectile had been fractured and left the front

8.1 Comparison with Other Materials

Constituent	Percentage of Mass %
Portland Cement	16.8
Sand	67.3
Bentonite Clay	0.6
Water Reducer	0.01
Water	15.3

Table 8.1: The composition of the concrete used in the experiments.

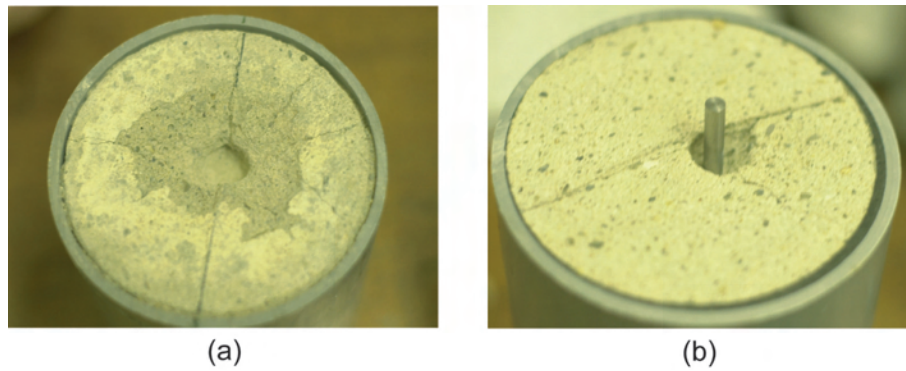


Figure 8.5: Cylindrical concrete samples after impact by flat-ended projectiles at 200 ms^{-1} . In (a) the sample has been impacted by a 10 mm diameter projectile, cratering and compaction in the area directly impacted are clearly visible. In (b) a thinner penetrator with a width of 5 mm has penetrated the sample to a depth of roughly 40 mm.

surface of the sample. This can clearly be seen in the photographs of recovered samples shown in Figure 8.5. Also apparent are radial cracks running outwards from the point of impact, showing that wide-spread fracturing of the material has occurred

The measured displacements at a penetration depth of (15 ± 5) mm are shown in Figure 8.6, firstly as a quiver plot super-imposed on the second X-ray image and secondly as a contour plot showing the total magnitude of the displacement. The displacement data show that measurable disruption of the material only occurs in the immediate vicinity of the projectile, forming a hemispherical shaped region of disturbed material around the projectile tip. The measured displacements are

8. SIMULATION AND COMPARISON WITH OTHER MATERIALS

also relatively small - the maximum is 1.4 mm, but the majority of disturbed material has moved significantly less than this. This suggests that only limited compaction of the material ahead of the projectile tip occurs. Outside of the deformed region immediately around the projectile the material is undisturbed. The sound speed in concrete is in the region of $(3400 \pm 200) \text{ ms}^{-1}$ (depending on composition), so pressure waves would have travelled throughout the entire sample a number of times by this point, reflecting from the confinement. The displacement data show that these travelling pressure waves do not generate any measurable displacement in the concrete.

The response to these pressure waves seems to be the main difference in behaviour between the gelatine and concrete samples. In both cases, there is a region around the projectile where the material is forced to deform in order to incorporate the volume of the projectile. This region is generally hemispherical in shape and does not extend far beyond the projectile tip. The strength of the concrete sample means that the material is not measurably deformed by the passing of the pressure waves. The lack of strength in the gelatine sample means that the material is noticeably affected by traveling pressure waves, so that only a short time after impact the entire sample has been heavily disturbed.

8.1.3 Comparison

These experiments strongly suggest that it is unsuitable to model penetration of granular materials at this velocity as being either hydrodynamic or solid-like in behaviour. In the sand, the majority of the longitudinal displacement is caused by a travelling compaction wave, rather than by displacement of material to incorporate the volume of the projectile or by pressure waves travelling at the speed of sound. In contrast to a pressure wave moving through the gelatine, loading and releasing the material, a compaction wave in a granular material consists of a body of moving material, in this case set in motion during the initial stages of impact. This moving body of sand precedes the projectile tip and pushes into the material ahead of the projectile, causing compaction and displacement. The heterogeneities present in a granular material mean that the velocity fields are not constrained to have the same form as the force or pressure fields in the

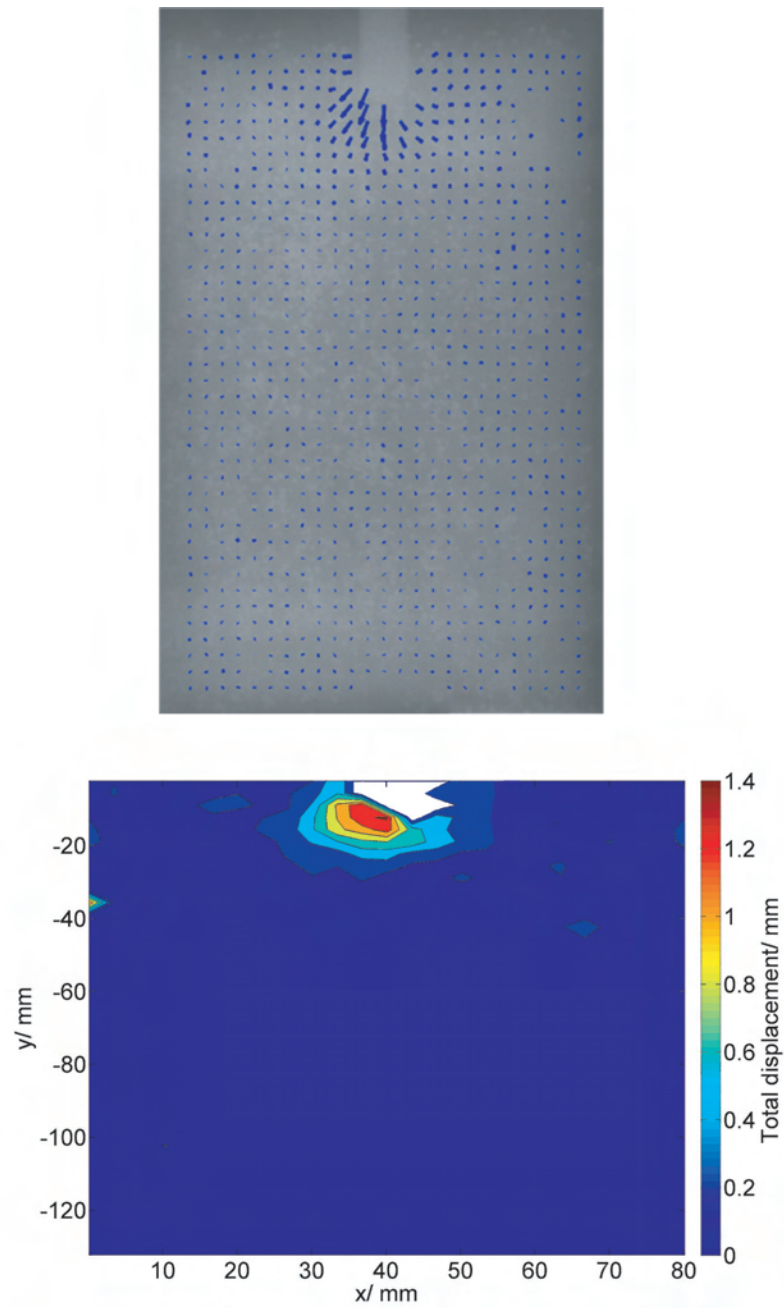


Figure 8.6: Measured displacements during penetration of a concrete sample displayed as a quiver plot and a contour plot.

8. SIMULATION AND COMPARISON WITH OTHER MATERIALS

material. Flaws such as voids and packing defects open up new directions of slip and motion. These defects mean that the only kind of travelling wave that can be supported in a granular material for any extent of time are compaction waves which involve bulk motion of sand into the sample, particularly if supported by the motion of a projectile.

The data suggest that in order for computational simulations to recreate the observed deformations during the dynamic penetration experiments, it is necessary to consider the interactions between particles, including damping terms to account for inelastic interactions such as collisions and rolling friction. It is necessary to consider heterogeneous effects such as void filling and reorganisation of particles in order to fully account for the behaviour of the material. A hydrodynamic approach is not able to account for these processes and other collective phenomena, such as jamming of the material or size segregation.

8.2 Computational Simulations

8.2.1 Simulation Details

To investigate the inner mechanisms responsible for the behaviour of granular materials, Bobaru *et al.* have developed a programme called BobKit, which combines Discrete Element Method (DEM) and Finite Element Method (FEM) approaches [6, 7]. The code currently contains two contact models which can be used to model the contact forces between 2D particles. The first is a simple linear spring and dash-pot model which involves an elastic term (the spring) and a damping term (the dash-pot) in parallel. This is shown schematically in Figure 8.7. The other is a nonlinear spring-dashpot model based on the Hertz model for 2D elastic disks. These models allow the force experienced by individual particles (2D disks) within the material to be resolved, and therefore the subsequent velocities and displacements to be determined.

This code was applied by Bobaru *et al.* to investigate the deformation observed during the experiments reported in this thesis. The aim was not to recreate the experiments exactly, but to see if the general deformation features observed, for example the curved traveling compaction front, could be reproduced. The

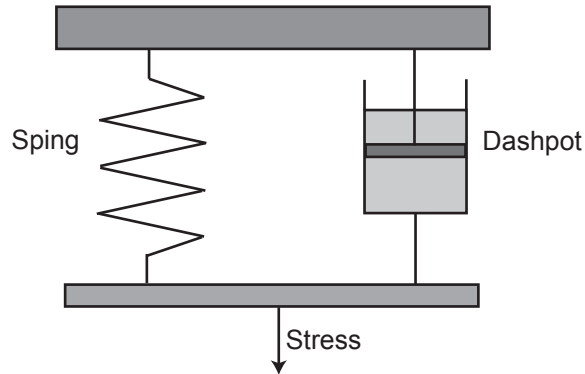


Figure 8.7: A schematic of the spring and dash-pot model. Particle contacts are treated as consisting of a spring (elastic component) and a dash-pot (damping term) in parallel.

simulation results were supplied as videos by Florin Bobaru showing the particle motion, force network and velocity network. Selected images were extracted from these videos by myself, and were then interpreted and compared with the experimental data by myself. The following interpretation and discussion of the simulation results, and the comparison with the experimental results, is my own.

The penetrator for the simulations was chosen, for ease of implementation, to be a disk (radius 10 mm, 0.5 mm thickness). For the stages of the impact in which we are interested, no material moves into the area behind the disk. The same displacement fields would be observed therefore, within a plane, for a hemispherical nosed projectile. Experimentally, the behaviour of hemispherical and ogive-2 nosed projectiles was shown to be very similar.

Computationally it is not currently feasible to model samples of the same size as those used during the experiments, which consisted of millions of particles. Instead, samples consisting of up to 3000 particles were studied. Therefore there are some significantly different factors between the simulations and the experiments. In particular, the ratio of the size of the projectile to the particles is much smaller in the simulations, as is the number of particles across the width of the sample. Despite these differences, such simulations are likely to provide useful information to help explain the types of deformation observed in the experiments.

8. SIMULATION AND COMPARISON WITH OTHER MATERIALS

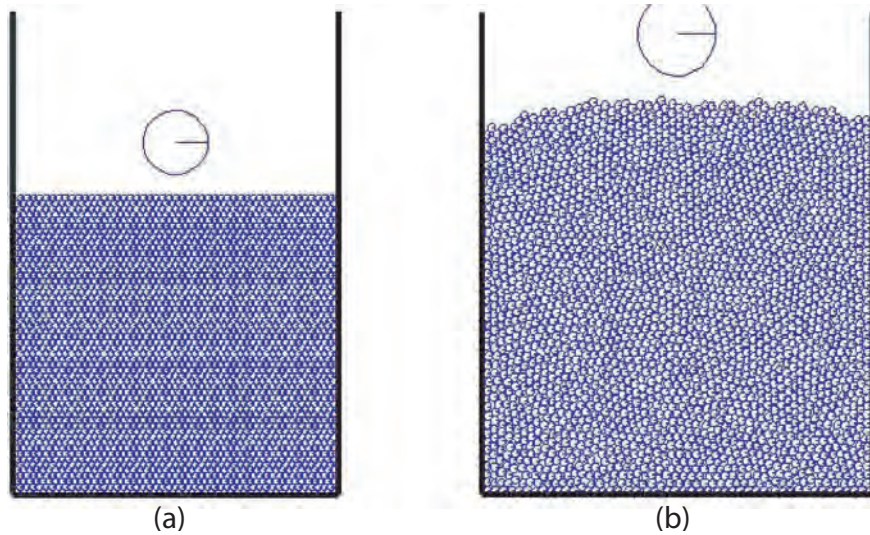


Figure 8.8: (a) A close-packed mono-disperse sample and (b) a randomly-packed poly-disperse sample.

The program was used to investigate the particle size dependence of the penetration process and also the influence of the type of packing of the particles, either close-packed or randomly-packed. Examples of a mono-disperse close-packed sample and a poly-disperse randomly-packed sample are shown in Figure 8.8. The results of the simulations allow the structure and profiles of the network of normal contact forces between particles (force chains) and the velocity fields to be visualised. The non-linear spring-dashpot model was determined to be the more realistic model for the behaviour of granular materials during dynamic impact. The linear spring-dashpot model was found to not work as effectively for high speed dynamic impacts [6]. Material properties for the simulations were chosen to be representative for a coarse grained sand and were as follows: density 2600 kg/m^3 (note that this is the density of a single grain rather than the composite granular material), Young's modulus 50 GPa, Poisson's ratio 0.3 and friction coefficient 0.3. The restitution coefficient is 0.9 and all problems were run for a maximum time of 300 microseconds from the initial position [6].

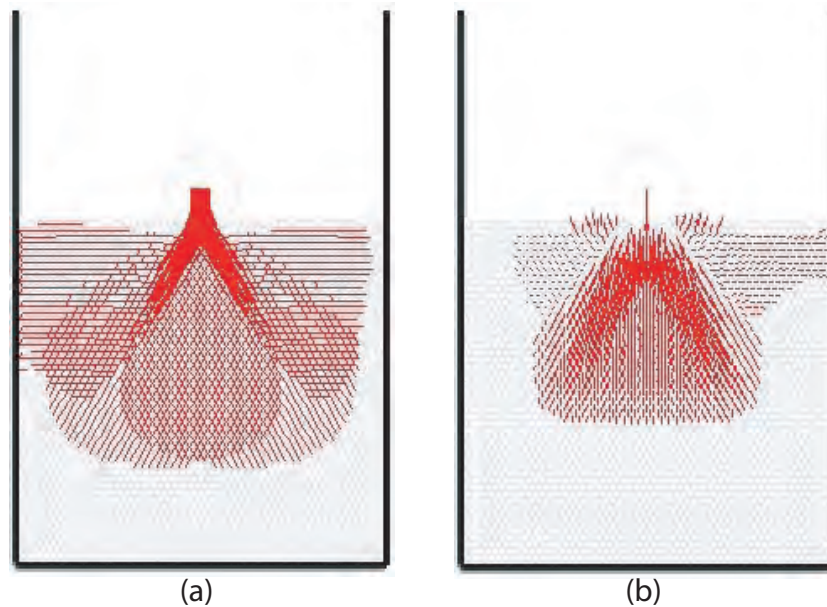


Figure 8.9: (a) Force and (b) velocity networks for a close-packed mono-disperse sample, containing 2674 disks 1 mm in diameter, during impact by a larger disk 10 mm in size.

8.2.2 Close-Packed, Mono-Disperse Samples

Figure 8.9 shows firstly the network of reaction forces between particles and secondly the resultant particle velocities for a close-packed mono-disperse sample being impacted at 100 ms^{-1} . This particle arrangement is shown in the left image of Figure 8.8. This simulation involved 2674 particles, each 1 mm in diameter. Close packing involves the centres of three particles in mutual contact forming an equilateral triangle, as illustrated in figure 8.10. It is the densest possible formation of mono-size disks or spheres in a granular system.

The network of forces is highly symmetric around the central penetration axis, which is perhaps to be expected given the symmetrical nature of the packing. A cone shaped area of force pushing material in a longitudinal direction forms in front of the projectile. This resembles the cone of displaced material seen in the experimental speckle and contour images. The forces are greater around the outsides of the cone, producing an arch of force which shields the material ahead

8. SIMULATION AND COMPARISON WITH OTHER MATERIALS

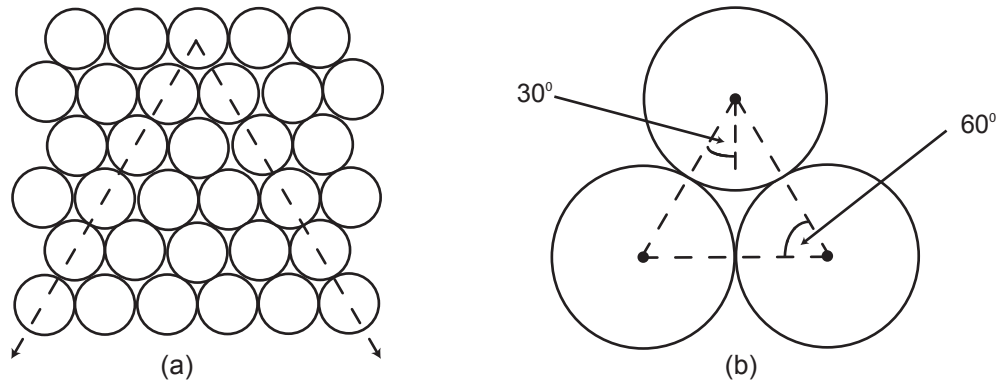


Figure 8.10: (a) A close-packed arrangement of equal size spheres. Two potential shear directions are shown with arrows. (b) A close-packed arrangement of three equal size spheres. The centres form an equilateral triangle.

of it to some extent. This arch makes an angle of (30.5 ± 0.9) degrees relative to the vertical. This represents a shear direction for a close-packed, mono-disperse material. Figure 8.10 shows a close-packed arrangement of equal size spheres. Any three neighbouring spheres are arranged so that their centres form an equilateral triangle. The main shear directions are therefore at an angle of 30 degrees relative to the vertical, the same angle as the cone of force seen in the simulations.

Comparing the arrangement of forces in the first image of Figure 8.9 with the plot of velocities, shown in the second image, it is clear that they are very similar in shape and direction. There is a large cone-shaped area of sand moving ahead of the projectile. This differs significantly from the experiments in that the largest longitudinal velocities are not along the centre of this cone, but instead are generally found near the edges along the main shear planes of the system (this is where the maximum forces are located also). The dense close packing arrangement restricts the motion of the particles, such that only a small distance in front of the impactor, the largest displacements are found along the shear directions, rather than along the direction of motion of the impactor. It is clear that although there are similarities with the experimental data, a mono-disperse close-packed system gives some significantly different responses.

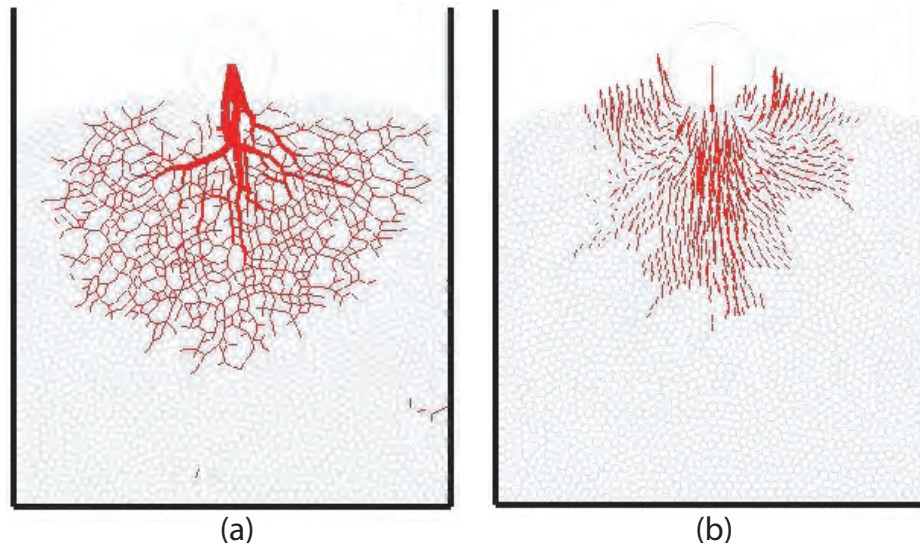


Figure 8.11: (a) Force chain network and (b) velocity for a randomly-packed poly-disperse sample. The sample contains 2000 particles with diameters ranging from 0.9 - 1.1 mm.

8.2.3 Randomly-Packed, Poly-Disperse Sample

Similar force and velocity plots for a randomly-packed poly-disperse sample of 2000 particles, with particle sizes of 0.9 - 1.1 mm, similar to the sand used in the experiments, are shown in Figure 8.11. A randomly-packed sample was simulated by randomly dropping particles into the container and then letting the system relax for two seconds [6]. It is clear from Figure 8.11 that both the network of forces and the subsequent velocities calculated here are significantly different to those found with a close-packed, mono-disperse sample. The network of forces develops through a series of branching chains of force, transmitted at particle contact points, into a tree shaped structure which is not symmetric. Generally, the largest forces occur along a line directly ahead of the projectile, but significant forces are seen at times branching off of this line. Unlike the close-packed case, there is no apparent preferred direction in which the force is transmitted (the forces were generally transmitted at 30 degrees to the vertical for the close-packed sample).

Comparing the appearance of the second image in Figure 8.11, which shows

8. SIMULATION AND COMPARISON WITH OTHER MATERIALS

the velocities of the particles, with the network of forces, it can be seen that they are very different. This is in contrast to the mono-disperse, close-packed case, for which the patterns of force and velocity were very similar. The fact that the pattern of velocities is so different to the force network strongly suggests that there is significant reorganisation, sliding and void-filling taking place in the randomly-packed samples. The presence of pores and packing defects in the geometrical structure induces frictional slip lines that allow different kinds of motion inside the system when compared to a close-packed system. The velocity distribution seen in the second image of Figure 8.11 closely resembles the pattern of displacements seen in the experimental data presented earlier, although the extent of penetration is less.

The cone-shaped area of material moving ahead of the projectile in Figure 8.11 grows in size as the penetration progresses. The angle made relative to the vertical remains roughly constant though at (32 ± 1) degrees. Interestingly, this is very similar to the 30 degree value found with the close-packed case. For the close-packed system, the angle of 30 degrees was caused by the close-packed arrangement of the particles, which lead to shear directions at an angle of 30 degrees relative to the vertical. A suggested reason for this is that, as the initial porosity in the simulated poly-disperse samples is low, it takes little rearrangement of the particles to reach a packing arrangement similar to the close-packed form. The porosity, and presence of packing defects, allows the particles to move when they experience a force and not necessarily in the direction that the force is acting, so that they pack together better. The higher density arrangement is then similar in form to the close-packed arrangement, leading to a similar angle for the cone of material moving ahead of the impactor.

8.2.4 Randomly-Packed, Mono-Disperse

Figure 8.12 shows force and velocity data from a simulation on a randomly-packed mono-disperse sample consisting of 2400 particles each 1 mm in diameter. The differences between the data shown here and that calculated for the randomly-packed, poly-disperse case are minor, suggesting that there is some particle size

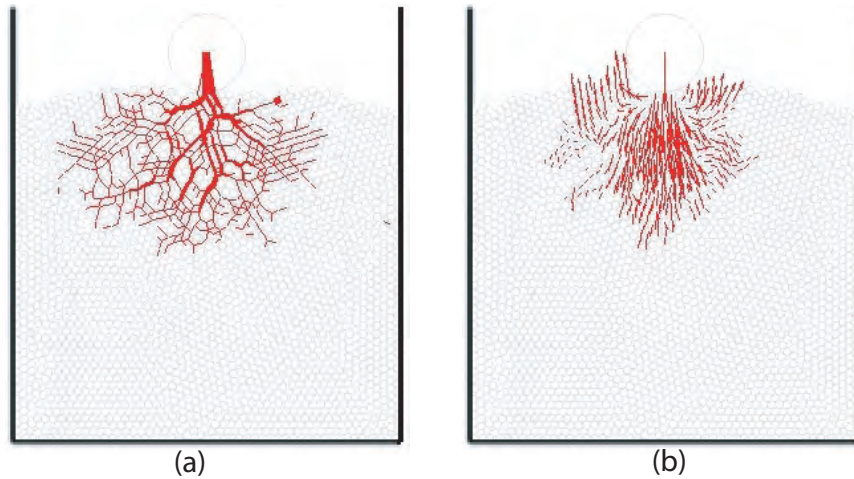


Figure 8.12: (a) Force chain network and (b) velocity for a randomly-packed poly-disperse sample. The sample contains 2400 particles each 1 mm in diameter.

dependence in the behaviour but that these effects are secondary to the effects of particle packing.

8.2.5 Discussion

The results of the three simulations suggest that it is the randomly arranged nature of the sand grains in the experiments that leads to the observed displacement patterns. A sequence of images showing in more detail the forces generated by the penetration of a poly-disperse (0.9 - 1.1 mm), randomly-packed sample are shown in Figure 8.13. The corresponding velocity networks are shown in Figure 8.14. Comparing the general shape of the velocity patterns with the displacement quiver plots obtained from penetration experiments using ogive-tipped projectiles (Figures 5.2 and 5.3), it can be seen that they are very similar in form. The longitudinal displacements measured during penetration of sand at 200 ms^{-1} by an ogive tipped projectile and the velocity field calculated for penetration of a randomly-packed, poly-disperse sample of disks are compared in Figure 8.15. There are some strong similarities in the shape of the displacement and velocity fields.

8. SIMULATION AND COMPARISON WITH OTHER MATERIALS

Both the simulations and experiments show a growing cone shaped area of material that moves longitudinally and stretches ahead of the projectile. In the experiments, this envelope has a clearly curved front. This is less well defined in the simulations. This is perhaps not too surprising, as the significantly smaller number of particles in the simulations means that random variations in packing density will cause more significant variations than in the experiments. There is an area of material to the sides of the impact point on the impact face in the simulations that is moving in the opposite direction to the projectile. This area grows in size as the penetration proceeds. This feature is also observed in the experimental data. The main difference between the experimental data and the simulations is the extent to which the deformation extends ahead of the projectile for a given penetration depth. Because of the small number of particles used in the simulations, it takes little penetration (less than 10 mm) before most of the sample has been disturbed. In the experiments significant penetration (90 mm) is required to cause a majority of the sample to be disturbed.

8.2.6 Modelling Conclusions

It has been demonstrated that the DEM-FEM code of Bobaru *et al.* can provide useful information to help explain the mechanisms behind the deformation phenomena observed in the penetration experiments discussed in this thesis. Simulations run on randomly-packed, poly-disperse samples (as would be found in the experimental sand samples) show similar features in the generated velocities and displacements as were observed experimentally.

When looking at a randomly-packed, poly-disperse material, the simulated velocity patterns closely resembled the patterns of displacement that were seen in the experiments. The simulated velocity patterns were significantly different to the simulated force-chain network, which had a branched root-like system. The fact that the resultant velocity pattern is so different to the network of forces suggests that there is significant reorganisation, sliding and void-filling taking place in the randomly-packed samples (therefore allowing for release of pressure by particles moving into voids, rather than necessarily moving in the direction that the force is acting). As the material is randomly-packed, it is significantly

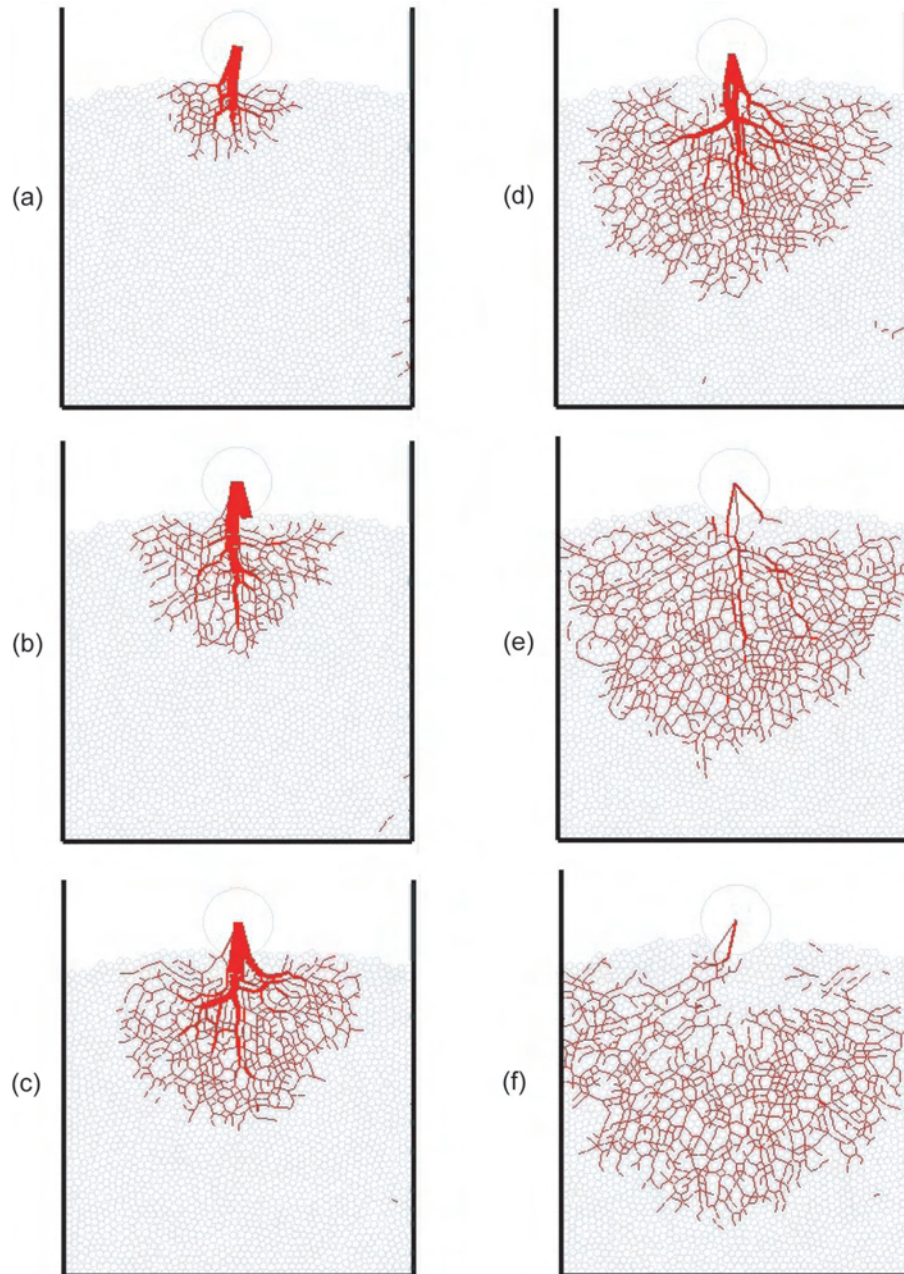


Figure 8.13: Six images showing the force networks during penetration of a randomly-packed, poly-disperse sample. The penetration depth increases from (a) to (f).

8. SIMULATION AND COMPARISON WITH OTHER MATERIALS

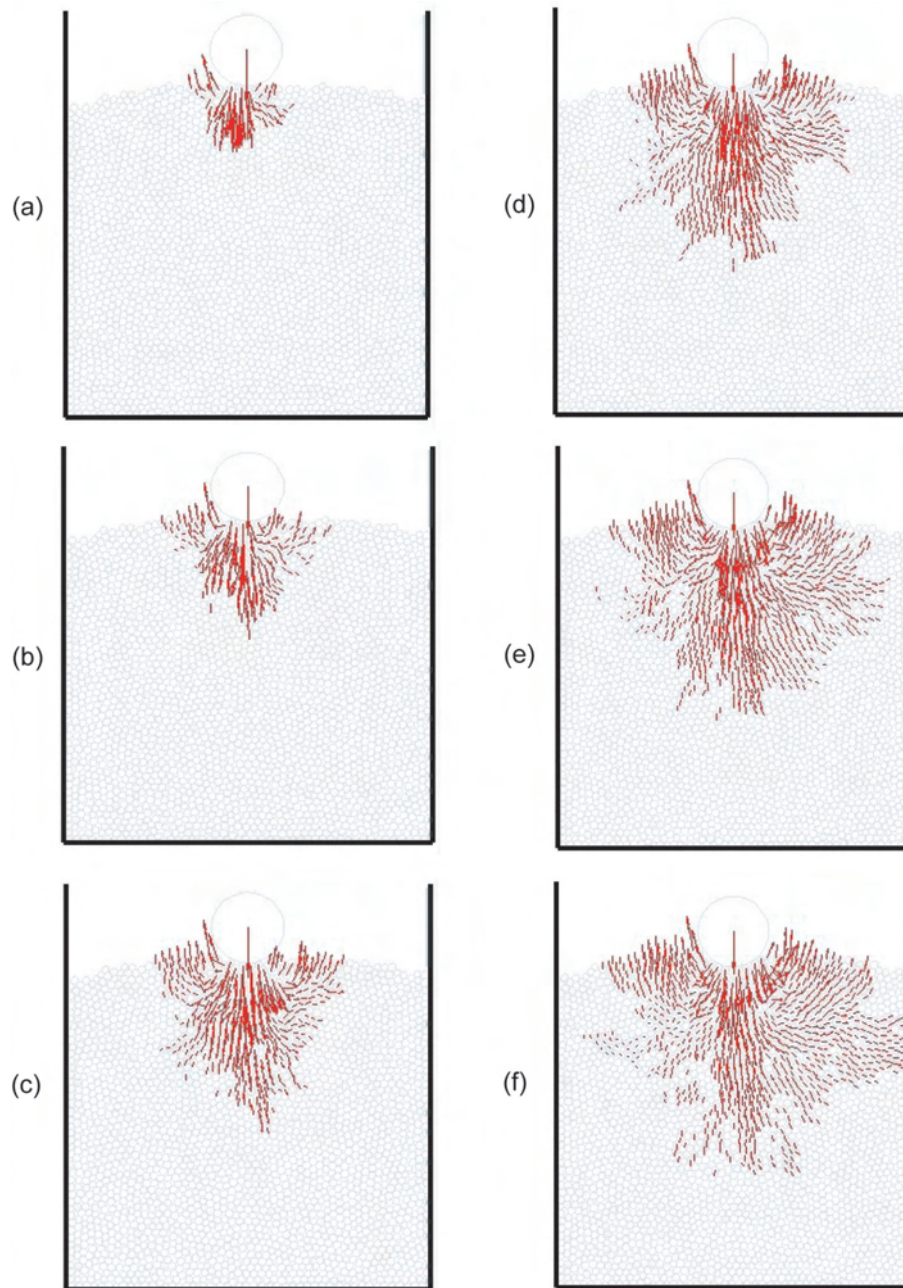


Figure 8.14: Six images showing velocities during the penetration of a randomly-packed, poly-disperse sample. The penetration depth increases from (a) to (f).

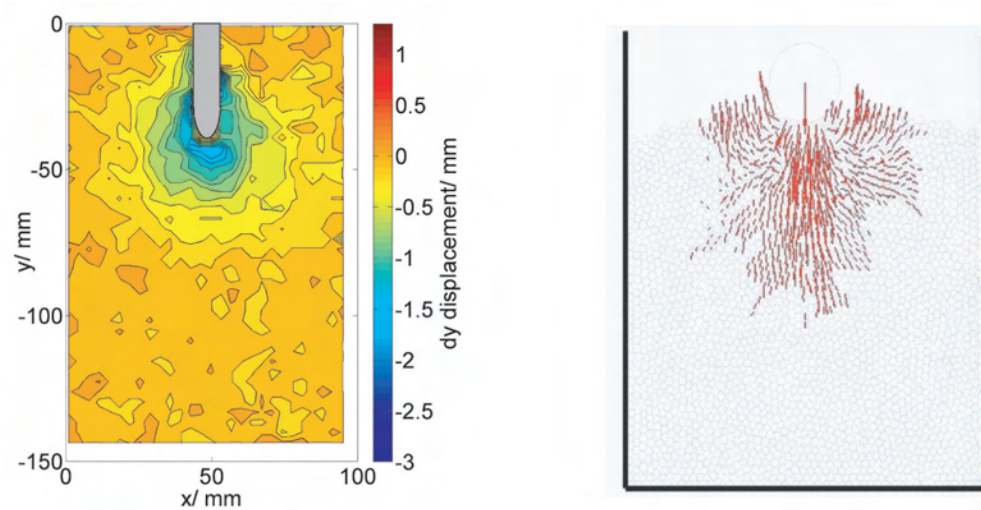


Figure 8.15: Comparing the longitudinal displacement field from a dynamic penetration experiment with the velocity field calculated from a simulation.

less dense than in the close-packed case and contains a large number of voids and packing defects. These introduce additional frictional slip lines, allowing a very different kind of motion to occur to the simple shearing observed in the close-packed system. This suggests that the main processes involved in producing the types of displacement observed experimentally, including the cone shaped area ahead of the projectile moving longitudinally, are related to the material flowing and rearranging itself so as to more closely pack together and reduce the number and size of the voids.

The fact that the angle of the cone of material moving ahead of the projectile was the same as with the close-packed case in these simulations suggests that global shearing of the material may still have a role in describing the type of deformation observed. It is possible that this plays a role in explaining the shape of the cone of material that was observed experimentally moving in the same direction as the projectile in the dynamic impacts. Potentially, densification of the material directly ahead of the projectile may lead to a packing order in which shearing becomes important.

In terms of using granular materials to slow or stop penetration by projectiles,

8. SIMULATION AND COMPARISON WITH OTHER MATERIALS

for example in sandbags, the modelling data suggest that a mono-disperse close-packed sample is most suitable. The close-packed structure, and the lack of packing defects and voids, limits the types of deformation of the material that are possible. The forces generated by the projectile can be released only through material escaping from the sample, for example through the impact face, or by compaction of the grains themselves. This requires significant forces and therefore strongly decelerates the projectile.

Although in reality it would be very difficult to arrange for a close-packed arrangement of material in sandbags, it is not unfeasible that the material could be sieved to reduce the range of particle sizes. Compacting the material would also help to reduce the number and size of pores, and therefore improve its ability to resist penetration.

8.3 Summary

To summarise the conclusions of this chapter:

- A granular material responds in a noticeably different manner to hydrodynamic materials and inhomogeneous solids.
- For concrete, an inhomogeneous solid consisting mainly of sand, displacement occurs only in the immediate area around the projectile. This localised compaction is necessary to incorporate the volume of the projectile.
- The strength of the concrete means that the high-velocity pressure waves generated at impact do not cause measurable deformation of the material.
- For gelatine, a hydrodynamic material, the same localised displacement around the projectile is observed. Significant bulk displacement of the material is also caused by pressure waves generated at impact. At only a small time after impact the whole sample has been measurably disrupted.
- The porous nature of sand means that it is unable to sustain a pressure wave for any significant length of time. The main cause of deformation is

instead a travelling compaction front, consisting of a bulk of sand set in motion during the early stages of impact.

- It is this intermediate behaviour, between the very localised displacement around the projectile in a solid and the wide spread displacement caused by pressure waves in a hydrodynamic material, that characterises the response of a granular sample to penetration.
- With a close-packed mono-disperse material the predicted force and velocity distributions are very similar. The largest forces and velocities are found along the main shear directions, at 30 degrees to the projectile axis. An arch of force is formed which shelters the material ahead of the projectile.
- With a randomly-packed arrangement, the calculated forces look very different. The forces are transmitted into the sample through a growing root-like system of force chains.
- In this case the velocity distribution looks very different to the force distribution. This suggests that processes such as reorganisation, sliding and void filling are taking place, allowing the grains to move in directions other than the applied force.
- The resulting velocity distribution bears a strong resemblance to the experimentally measured displacement fields. In particular, there is a growing cone-shaped region behind which material is in motion.
- The velocity distribution is similar for a close-packed arrangement of mono-sized particles, suggesting that the packing arrangement has a more significant effect than variations in particle size.
- The simulations suggest that the inhomogeneities present in the sand are responsible for the types of deformation experimentally observed.

REFERENCES

References

- [1] Goldhirsch, I., “Rapid Granular Flows”, *Annu. Rev. Fluid Mech.*, **35**, (2003), 267–293
- [2] Jaeger, H.M., Nagel, S.R. and Behringer, R., “Granular solids, liquids and gases”, *Review of Modern Physics*, **68(4)**, (1996), 1259–1273
- [3] Byers, R.K., Yarrington, P. and Chabai, A.J., “Dynamic Penetration of Soil Media by Slender Projectiles”, *Int. J. Engng Sci.*, **16**, (1978), 835–844
- [4] Goldshtein, A. and Shapiro, M., “Mechanics of collisional motion of granular materials. Part 1. General hydrodynamic equations”, *J. Fluid. Mech.*, **282**, (1995), 75–114
- [5] Dwivedi, S.K., Teeter, R.D., Felice, C.W. and Gupta, Y.M., “Two Dimensional Mesoscale Simulations of Projectile Instability During Penetration in Dry Sand”, *Journal of Applied Physics*, **104**, (2008), 083,502–1
- [6] Promratana, K., *Granular Materials Behavior under Dynamic Excitations*, Phd, University of Nebraska-Lincoln (2008)
- [7] Rattanadit, K., *Coupled DEM-FEM simulations for the analysis of 2D granular materials under quasi-static bending deformation and bending vibrations on an elastic foundation*, Phd, University of Nebraska-Lincoln (2008)

Chapter 9

High Strain-Rate Behaviour of PTFE/Al/W Composites

9.1 Introduction

The previous chapters have considered the behaviour of granular materials during penetration. In this chapter we move on to consider the behaviour of particulate materials, in a polymer matrix, during compaction. The materials discussed are mixtures of Aluminium (Al), Polytetrafluoroethylene (PTFE) and Tungsten (W). Mixtures of PTFE and Al are known to be energetic under mechanical or thermal loading [1–3]. They are similar in composition to thermites [4], a sub-group of the class of pyrotechnics. Thermites are formulated to generate a large quantity of heat during reaction. The addition of tungsten (W) in this study increases the density and overall strength of the samples.

Thermites and similar materials have both civilian and military applications. They produce a very high temperature (up to 2500°C) in a localised area, and can therefore be used to cut or weld steel, for example *in-situ* during the laying of railway tracks [5]. Thermite hand grenades are used by the military to destroy or damage equipment and papers, particularly in time-sensitive situations where a more thorough destruction is not possible [6].

Tailoring the mechanical and thermal properties of reactive materials is important for a number of applications. Varying particle size and morphology in

9. HIGH STRAIN-RATE BEHAVIOUR OF PTFE/AL/W COMPOSITES

pressed explosives can be used to tailor the shock sensitivity of the material [7–9]. The sensitivity of explosive materials has been shown to vary significantly with factors such as the grain size, particle shape and the surface roughness of grains [8, 9]. Varying the pressing conditions introduces different porosities and component configurations within a sample. The presence and size of pores has been shown to be an important variable in determining the sensitivity to reaction of energetic materials, and in determining the rate of burning in pyrotechnics [10–12]. The formation of stress/force chains within a granular or particulate energetic material can be related to the location and frequency of ignition sites [13]. The sensitivity of energetic materials is therefore often closely linked to the mechanical response of the material to applied stresses.

The experiments discussed in this chapter contribute to a larger research project by Nesterenko *et al.* [14–16] into the effect of strain rate on the compaction of mixtures of Al and PTFE powders. The materials consist of 77% W (Teledyne, 44 μm or Alfa Aesar, < 1 μm), 5.5% Al (Valimet, 2 μm) and 17.5% PTFE (Dupont, approximately 100 nm diameter powder size) by weight. The samples were provided in a pressed form by V. Nesterenko, University of California San Diego, US. The samples were produced by cold isostatic pressing of the powder mixtures at a variety of pressures. Three different batches were provided, giving a variety of porosities and W particle sizes, details of which are in Table 9.1. This allowed for comparison of the behaviour of samples with the same density but different W particle sizes, and with the same size of W particles but different densities. Notice that for the same pressing pressure the samples containing fine W particles result in a lower density than the samples containing coarse W particles (6.0 versus 7.1 gcm^{-3}). This suggests that the samples containing fine W particles have a greater resistance to compaction.

To investigate the mechanical properties of these materials, including the ultimate compressive strength, small cylindrical samples (height 8 mm, diameter 10.5 mm) were compacted at $(5.0 \pm 0.2) \text{ms}^{-1}$ using a drop-weight machine. The main features of the Cavendish drop-weight are discussed in the following section.

Name	W particle size/ μm	Pressing conditions	Average density/ gcm^{-3}	Porosity / %
Porous mixture, fine W	$< 1.0 \pm 0.1$	350 MPa for 20 min	6.0 ± 0.2	14.3 ± 0.4
Porous mixture, coarse W	44.0 ± 0.5	20 MPa for 20 min	6.1 ± 0.3	14.3 ± 0.3
Dense mixture, coarse W	44.0 ± 0.5	350 MPa for 20min	7.1 ± 0.2	1.6 ± 0.2

Table 9.1: Details of the three mixtures which were investigated. The mixtures allow comparison of the behaviour of samples with the same density but different W particle sizes, and with the same size of W particles but different densities. The samples were provided in a pressed form by V. Nesterenko, University of California San Diego, US.

9. HIGH STRAIN-RATE BEHAVIOUR OF PTFE/AL/W COMPOSITES

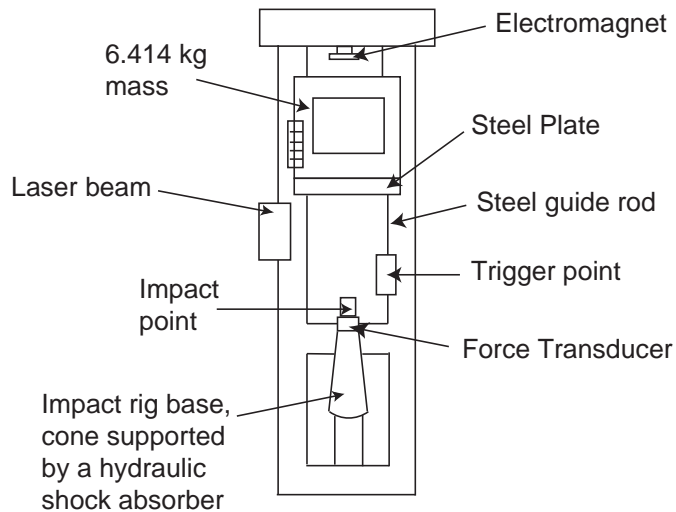


Figure 9.1: The Cavendish drop-weight apparatus. The mass is guided to the impact point where velocities of up to 5 ms^{-1} are achievable (depending on drop height). A more detailed description is given in the text.

9.2 Experimental Method

9.2.1 Cavendish Drop-Weight Machine

The Cavendish drop-weight consists of a 6.414 kg mass which is dropped from a height of up to 1.2 m. The falling mass is guided by two external steel guide rods to the impact plane, where impact velocities of up to 5 ms^{-1} can be achieved. Typically, strain rates of the order of a few 100 s^{-1} are reached in samples during impact, depending on the sample properties. The main features of the drop-weight are shown in Figure 9.1. The drop-weight has previously been used to investigate the properties of polymers [17], metals [18], and the sensitivity of granular explosives [19].

The velocity of the mass upon impact is measured by two different techniques. Attached to the mass is a grid of fine lines with a spacing of 2 mm. When the grid passes between a laser beam and a photo-diode, situated just above the impact plane, an oscillating square wave is produced with a period equal to the time taken for the mass to travel 2 mm. This trace is recorded on an oscilloscope at

a time resolution of 1 μs , allowing the velocity to be calculated to within a few percent. The advantage of this method is that the rebound velocity of the mass after impact can also be determined. This value is needed when calibrating the force transducer. In the second technique, the velocity at impact is measured using a pair of sequentially broken light gates (mounted just above the impact plane) and a counter/timer. The advantage of this technique is that the light-gate system can easily be moved along the steel guide rods, which is useful when using a more complicated geometry at the impact plane.

The transmitted force at the impact plane is determined using a force transducer, located directly below the sample. The transducer consists of four strain gauges attached to a cylindrical steel anvil, two aligned parallel with the anvil, in order to measure the axial strain, and two aligned perpendicular, in order to measure the circumferential strain. The gauges are connected together in a Wheatstone bridge arrangement. A calibration factor is required to convert the voltage output of the Wheatstone bridge into a force. This is determined by impacting the mass onto the anvils when no sample is present. The impulse imparted to the mass can be equated to its change in momentum due to the impact, as shown in equation (9.1).

$$I = \int F dt = k \int V dt = m\Delta v. \quad (9.1)$$

Rearranging this equation gives an equation for the calibration factor, k , in terms of known or measurable quantities:

$$k = \frac{m\Delta v}{\int V dt}. \quad (9.2)$$

Five calibration drops (with no sample present) were carried out from a height of 112 cm. The mean calibration factor was calculated to be $(8.5 \pm 2) \times 10^4 \text{ N/V}$. By carrying out subsequent calibration drops, three each from heights of 80, 60, 40, 20 and 5 cm, the calibration factor was found to be independent of height, and therefore impact velocity, with a mean value of $(8.5 \pm 3) \times 10^4 \text{ N/V}$.

The strain, or density if the sample is a granular material, can be determined from the force as a function of time data and from the impact velocity. Rearranging Newton's second law gives the instantaneous deceleration of the mass

9. HIGH STRAIN-RATE BEHAVIOUR OF PTFE/AL/W COMPOSITES

as

$$a(t) = \frac{F(t)}{m}. \quad (9.3)$$

Subtracting the integral of this with respect to time from the initial velocity gives the instantaneous velocity of the mass as

$$v(t) = v_i - \int_0^t a(t) dt. \quad (9.4)$$

The distance, $x(t)$, by which the sample has been compressed at any given time is then given by integrating this velocity with respect to time, as shown in equation (9.5).

$$x(t) = \int_0^t v(t) dt. \quad (9.5)$$

This allows the strain, or the extent of compaction, of a sample to be determined as a function of time.

As the samples are compacted between two steel anvils, it is important to consider the effects of friction at the sample-anvil interfaces. The extent of the friction at these interfaces can influence the dominant form of deformation. For example if the friction is high, barrelling of the sample, where the diameter at the centre increases by more than the diameter at the ends, may be more likely as the top and bottom of the sample will be less able to deform. The samples discussed in this chapter contain large amounts of PTFE which will act as a lubricant. The addition of a petroleum jelly based lubricant to the top and bottom of the sample reduces the friction further. Research by Walley *et al.* suggests that petroleum jelly is effective at reducing the friction at the sample-anvil interface [17, 20].

9.2.2 Soft Drop-Weight Experiments

In previous experiments using the Cavendish drop-weight the voltage traces were found to be obscured by large amounts of oscillatory noise [18]. This noise was frequently of greater magnitude than the signal of interest, making it difficult to extract useful information from a single trace, although some information could be obtained by performing a large number of experiments and averaging the

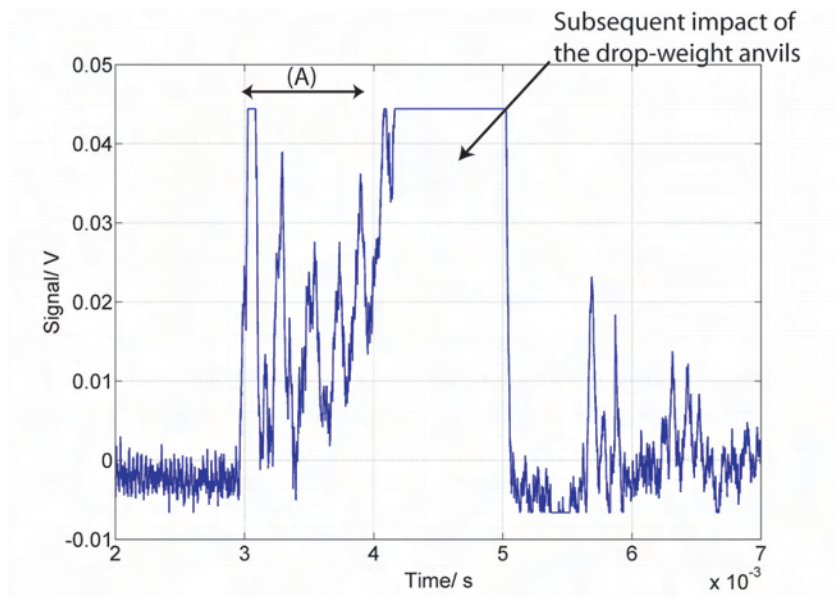


Figure 9.2: A drop-weight trace for a dense sample with coarse W particles showing significant oscillatory noise. The signal of interest, which occurs between 3 - 4 ms in the region labelled as (A), is entirely obscured by oscillatory noise, likely caused by vibrations within the drop-weight apparatus. The later region, where the signal is cut off, is due to the subsequent impact of the drop-weight anvils after the sample has failed.

results [18]. The noise is likely caused by vibrations inevitably excited in the drop-weight machine by the impact of the mass. Consequently, when testing low strength materials in which the signal of interest is low relative to the amplitude of the oscillatory noise, it is difficult to extract any meaningful information.

The problem is illustrated by the drop-weight trace shown in Figure 9.2 from an experiment on a low-strength, dense sample containing coarse W particles. The signal of interest, occurring between 3 and 4 ms, has been obscured by larger amplitude oscillatory noise. Some limited recovery of the signal can be achieved by filtering the data in Fourier space, but there is often no single frequency obviously responsible for the oscillations.

In the following experiments, the oscillations were damped by including an o-ring on the anvil above the sample, as illustrated in Figure 9.3. An o-ring above

9. HIGH STRAIN-RATE BEHAVIOUR OF PTFE/AL/W COMPOSITES

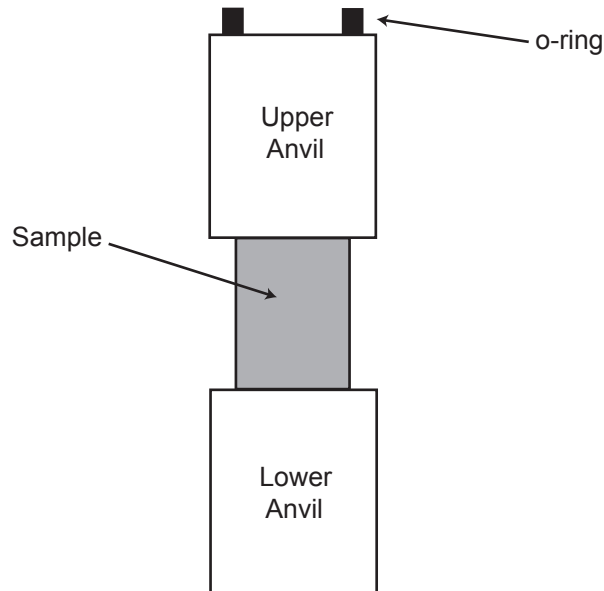


Figure 9.3: Diagram showing the location of the o-ring during 'soft' drop-weight experiments. The o-ring is mounted above the upper anvil.

the sample acts to soften the impact by increasing the rise time of the force. The effectiveness of Nitrile BS201NI70 (-201) and 310 - Silicone o-rings at damping the oscillations was investigated by performing experiments on samples of pure PTFE. Two experiments were performed with each type of o-ring. The Nitrile BS201NI70 o-rings were found to be more effective at removing the noise. Figure 9.4 shows the voltage trace from an identical drop-weight experiment to that in Figure 9.2, but with a -201 o-ring included on the upper anvil. The oscillatory noise is no longer present and the signal due to the sample is clearly visible between 2 and 3.5 ms. Measurements can now be made regarding the voltage (and therefore the force) at which the material fails.

In order to determine the strain of the sample in a 'soft' drop-weight experiment of this kind it is necessary to take into account the deformation of the o-ring. As the force transducer directly measures the force transmitted through the sample, regardless of what is occurring above the sample, the presence of the o-ring does not affect the accuracy of the force measurements. Since the extent of the compaction is determined by calculating the displacement of the mass after

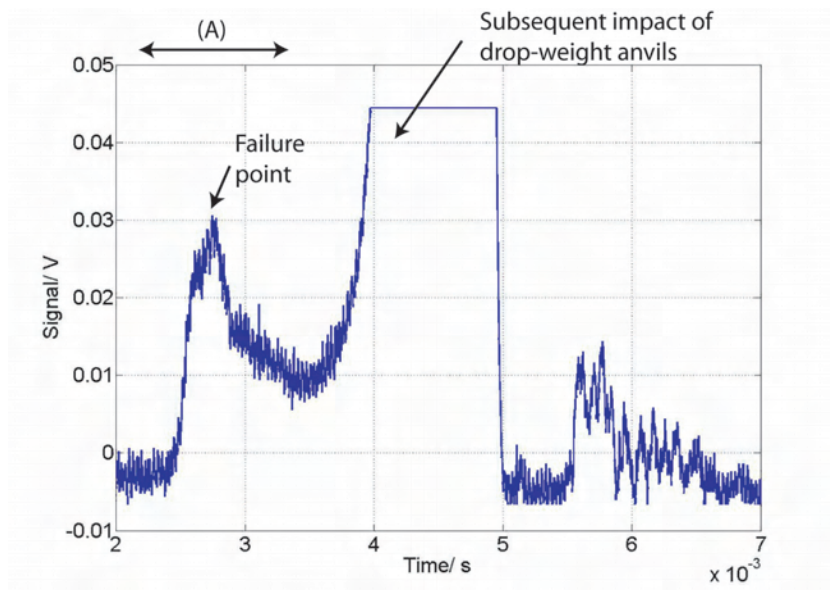


Figure 9.4: Drop-weight trace for an experiment on a dense sample with coarse W particles with an o-ring on the upper anvil. The large oscillations visible in region (A) in Figure 9.2 have been removed and the signal, located in region (A) of this figure, is now clearly visible.

9. HIGH STRAIN-RATE BEHAVIOUR OF PTFE/AL/W COMPOSITES

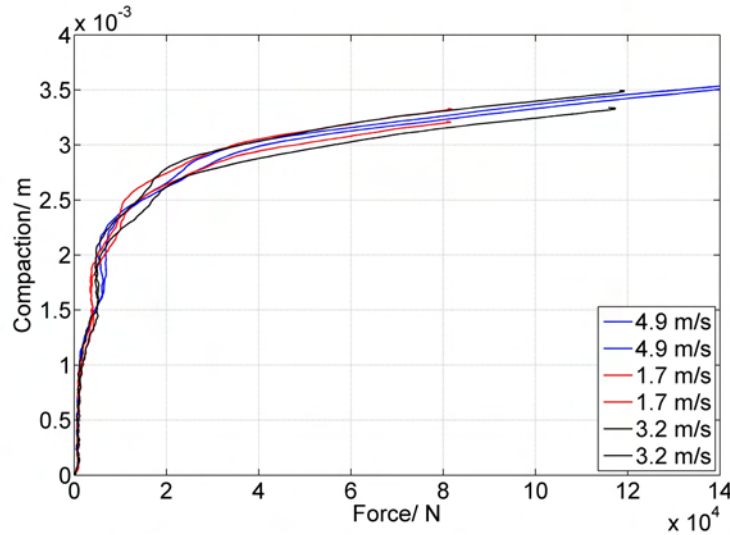


Figure 9.5: Extent of compaction versus force for o-rings in drop-weight experiments from a range of heights. There is no velocity dependence in the response of the o-rings in the velocity range 1.7 - 5 ms^{-1} .

impact, which includes the distance moved in compacting the o-ring, it is necessary to correct for the compaction of the o-ring. The relationship between the force measured at the transducer and the extent of compaction of the o-ring can be determined from drop-weight experiments performed with an o-ring, but with no sample present. Figure 9.5 shows typical traces of o-ring compaction versus force for a variety of mass drop-heights, and therefore a range of impact velocities. In the velocity range of 1.7 - 5 ms^{-1} there is no significant dependence of the extent of compaction as a function of force relationship on the impact velocity.

Using these traces it is possible to determine an average trace showing the extent of compaction of a Nitrile BS201NI70 o-ring as a function of force, valid over a wide range of impact velocities. Figure 9.5 shows that there are variations of up to 4% between the traces. This variation, and the subsequent errors in the average trace, lead to errors of the order of 5% in the corrected sample strains.

When analysing data from a 'soft' drop-weight experiment, where an o-ring has been included above the sample, Figure 9.6 (A) shows that the total measured displacement includes the extent of compaction of both the sample and the o-ring.

At a given time the o-ring component of the displacement (d_o) at the current force (F_T) can be determined from the average compaction as a function of force trace for a -201 o-ring, as shown in (B) of Figure 9.6. Subtracting this value from the total measured compaction leaves just the component due to the sample, d_s . Once the extent of compaction of the sample is known the strain is straight-forward to calculate.

9.2.3 Validation of the Soft Drop-Weight Technique

To verify that the ‘soft’ drop-weight technique correctly calculates the sample strain, a series of experiments was performed using the drop-weight with both the standard and ‘soft’ techniques. PTFE was used rather than actual samples due to their limited supply. As PTFE is a relatively weak material, it will allow validation of the technique over the stress ranges likely to be experienced with actual samples. Figure 9.7 compares typical traces measured for PTFE using the standard technique (shown in blue) and the soft technique (shown in red). The damping of the oscillations in the soft technique is clearly apparent. There is an initial oscillation, but following this there are no further oscillations. In the trace from the standard technique there are significant oscillations that distort the stress-strain relationship. The trace measured with the soft technique passes approximately through the centre of these oscillations, suggesting that the underlying stress-strain relationship has not been altered.

To further validate the technique, the stress-strain relationship determined from a ‘soft’ drop-weight experiment on PTFE was compared to that obtained from a split-Hopkinson bar experiment on the same material. A split-Hopkinson pressure bar is a piece of apparatus for determining the dynamic stress-strain response of a material by deforming a sample between two symmetrical bars, one of which is impacted by a striker bar fired from a gas-gun. A good review of Hopkinson bar theory is given in [21].

Example traces for the two experiments are shown in Figure 9.8. Up to the strains achievable in the split-Hopkinson bar (the strain at which the red line stops), the two curves are in relatively good agreement, taking into account the initial oscillation in the drop-weight trace and the difference in strain-rate between

9. HIGH STRAIN-RATE BEHAVIOUR OF PTFE/AL/W COMPOSITES

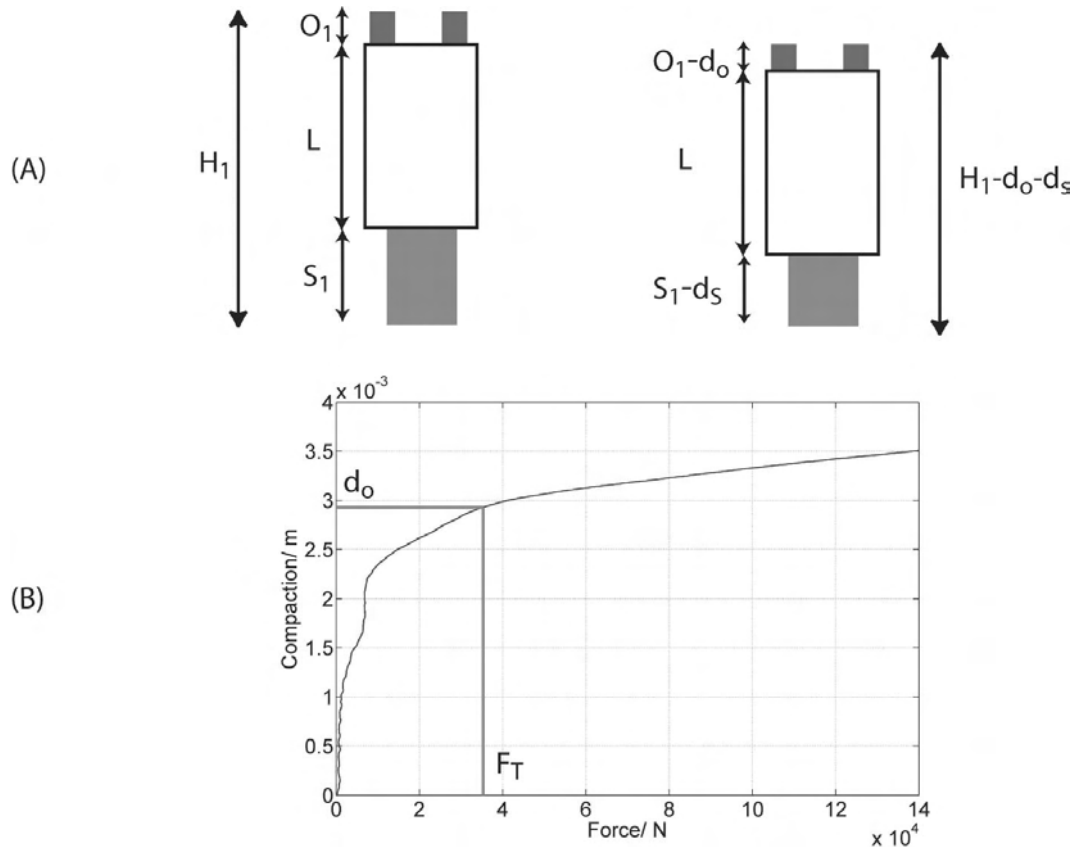


Figure 9.6: (A) The measured displacement of the mass at a given time includes the compaction of the o-ring, d_o , and the compaction of the sample, d_s . The compaction of the o-ring at any given time can be determined using a plot of the average compaction as a function of force for the o-ring. The force at any given time, F_T is known as it is measured directly by the force transducer below the sample. By subtracting the o-ring compaction value (d_o) from the measured displacement of the mass, we are left with the compaction of the sample, d_s .

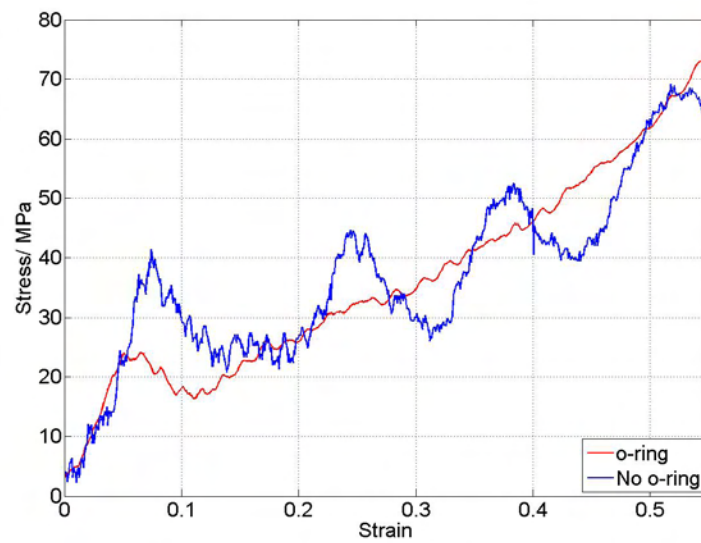


Figure 9.7: Comparison of stress-strain data for PTFE obtained from normal (blue trace) and ‘soft’ (red trace) drop-weight experiments. The blue trace suffers from significant oscillations that mask the underlying stress-strain relationship. These have mostly been removed using the soft technique, leaving a cleaner trace with only one early oscillation. The red trace passes through the oscillations of the blue trace, suggesting the underlying stress-strain relationship has not been altered and only the oscillations have been removed.

9. HIGH STRAIN-RATE BEHAVIOUR OF PTFE/AL/W COMPOSITES

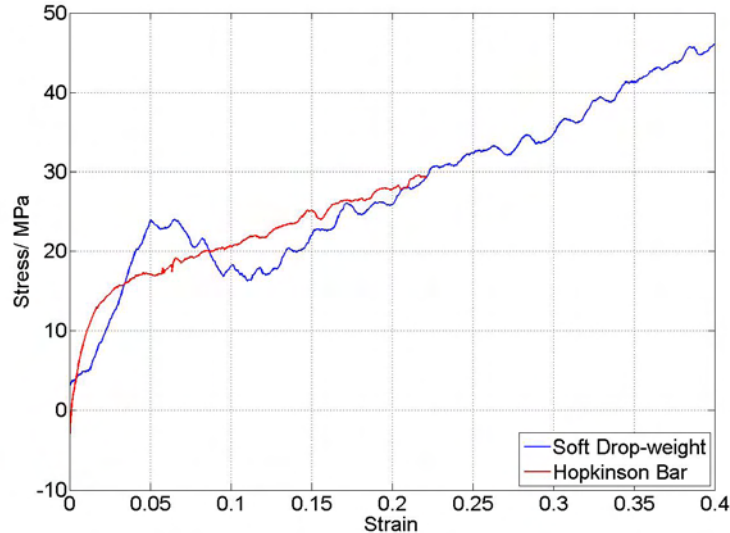


Figure 9.8: Comparison of stress-strain data for PTFE obtained from 'soft' drop-weight (blue) and Hopkinson bar (red) experiments. The two plots are in quite good agreement, although there is still an early oscillation in the drop-weight trace.

the two techniques (the strain-rate is roughly three times as great with the split-Hopkinson bar, so some strain-rate difference in the response of the material is likely). These results confirm that the method used to correct for the effect of the compaction of the o-ring on the measured displacement of the drop-weight is appropriate.

These experiments demonstrate the success of 'soft' drop-weight experiments in determining the properties of low strength materials. The results are significantly better than those obtained during standard drop-weight experiments, where the signal from a low-strength sample is swamped by oscillatory noise.

9.2.4 Interrupted Experiments

Soft materials have low strength and are therefore severely damaged during drop-weight experiments. The samples investigated in this chapter are completely destroyed during a standard drop-weight experiment, making it difficult to in-

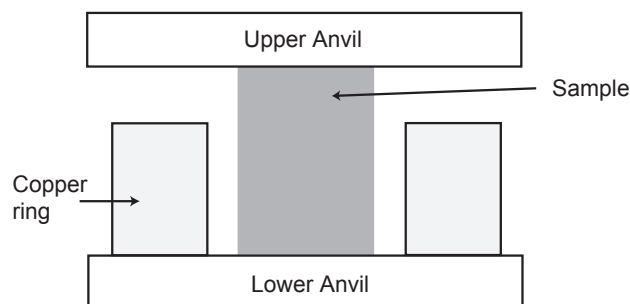


Figure 9.9: Set-up for an interrupted drop-weight experiment. The copper ring placed around the sample terminates the compaction at a chosen extent, while allowing for the lateral expansion of the sample.

investigate the mode of failure of the samples. This problem was overcome using interrupted drop-weight experiments. A copper ring was placed around some of the samples, with a height chosen so as to interrupt the compaction of the sample at a chosen strain. The internal diameter of the rings was sufficient to allow for lateral expansion of the sample. This allows for recovery of a partially deformed sample at any chosen strain, so that the mode of failure can be more closely investigated. Recovered samples were investigated using optical microscopy and the analysis of photographic images.

9.3 Results

Approximately 30 drop-weight experiments were carried out using the three materials presented in Table 9.1. A list of these experiments, as well as those performed on PTFE and o-rings in order to develop the soft drop-weight technique, is given in the Appendix in Tables A.6, A.7 and A.8. Firstly, we will discuss the behaviour of the porous samples containing fine W particles.

9.3.1 Porous Samples with Fine W Particles

A typical voltage as a function of time trace produced by the force transducer for an experiment on a porous sample with fine W particles ($< 1 \mu\text{m}$) is shown in

9. HIGH STRAIN-RATE BEHAVIOUR OF PTFE/AL/W COMPOSITES

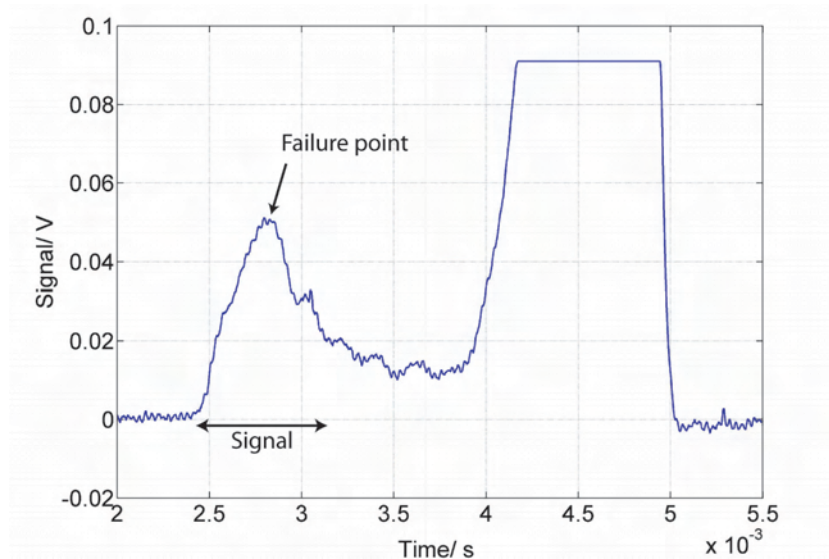


Figure 9.10: A typical drop-weight voltage trace for an experiment on a porous sample with fine W particles. The failure point of the material is clearly visible, as is an apparent change in gradient during the loading section of the trace.

Figure 9.10. The signal due to the sample appears between 2.5 and 3.5 ms. The signal between 4 and 5 ms is caused by the eventual impact of the upper and lower anvils, after the sample has been entirely destroyed. This figure demonstrates once again the success of the ‘soft’ drop-weight technique in removing the parasitic oscillations found in standard drop-weight experiments on weak materials. The point at which the material fails is clearly visible, as are other features such as an apparent change in gradient on the loading part of the trace.

The corresponding engineering stress as a function of logarithmic strain plot for this drop-weight experiment is shown in Figure 9.11. The logarithmic strain is the natural log of the final length divided by the original length. The stress at which the material fails, the ultimate compressive stress, is roughly 48 MPa. There is an apparent change in the gradient of the stress as a function of strain relationship at a stress of around 25 MPa, suggesting that the effective stiffness of the material has altered. This apparent change in stiffness was observed with two other samples, their stress as a function of strain relationships being shown in blue in the plot in Figure 9.12. For two further samples this change in stiffness

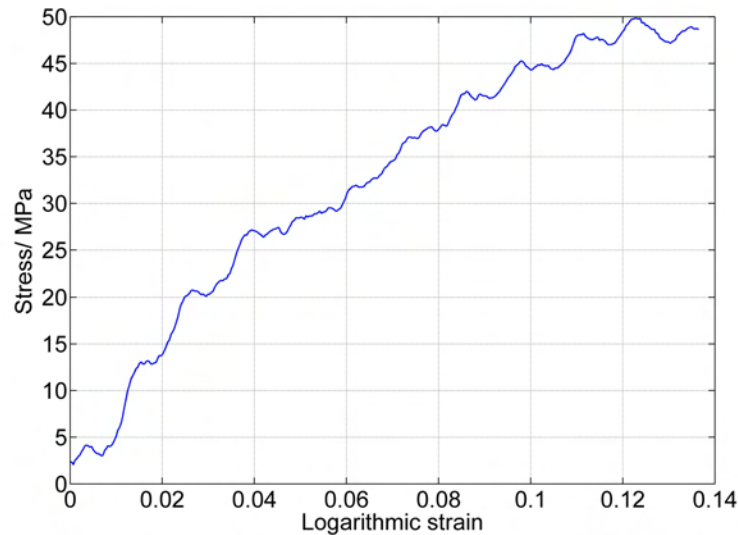


Figure 9.11: Engineering stress as a function of logarithmic strain relationship for the voltage trace in Figure 9.10.

was not observed. The stress as a function of strain relationships for these samples are shown in red in Figure 9.12.

A change in stiffness of this kind would suggest a change in the dominant mode of deformation. Additional interrupted drop-weight experiments were carried out to investigate the dominant mode of deformation at two different extents of strain. The strain at which the experiment was interrupted was changed by altering the height of the copper ring around the sample. At a logarithmic strain of 0.02 (this involved some elastic recovery of the sample, the calculated maximum strain was 0.028), the sample was found to have barrelled, in that the diameter in the center increased more than the diameter at the ends. The central diameter increased from 10.53 mm to 10.62 mm and its height decreased from 8.24 mm to 8.12 mm. A strain of 0.02 - 0.028 lies to the left of the change in gradient in the plot shown in Figure 9.11. Samples recovered at strains of 0.1 - 0.15 (around the failure point) were seen to have deformed through shearing. A possible suggestion therefore for the change of gradient observed in many of the traces is a change from a barreling type of deformation to a shear-based form of deformation.

The ultimate compressive strength of the samples was between 50 and 65 MPa,

9. HIGH STRAIN-RATE BEHAVIOUR OF PTFE/AL/W COMPOSITES

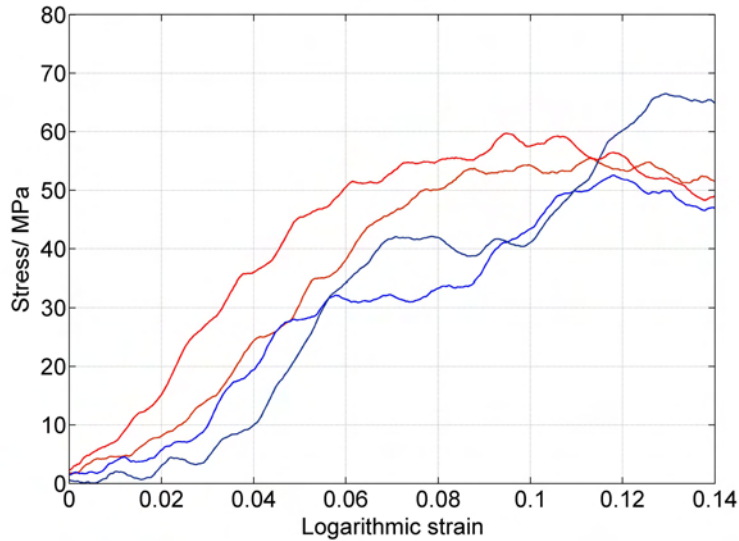


Figure 9.12: Some further example engineering stress as a function of logarithmic strain relationships for porous samples with fine W particles. Changes in gradient were observed in the blue plots.

the mean being (55 ± 4) MPa. The failure stress for each experiment is listed in Table 9.2. The failure stress was not reached in the interrupted experiments.

9.3.2 Porous Samples with Coarse W Particles

For the porous material with coarse W particles ($44 \mu\text{m}$) there were some more significant variations in material properties between experiments. Figure 9.13 shows two stress as a function of strain relationships obtained for this type of material. The plots are very different. One of the materials has failed at a stress of around 18 MPa while the other has failed at roughly twice the strain and at a significantly higher stress of around 30 MPa. This very large difference in response between the two samples implies that the type of deformation occurring is very different between the two repetitions. In further experiments, more examples of both types of behaviour were seen. Further stress as a function of strain relationships are plotted in Figure 9.14.

These plots suggest that there are two ways in which the porous material

Sample	ρ / kgm^{-3}	UCS/ MPa
59	5.91 ± 0.02	49.0 ± 0.4
60	5.91	55.2
63	5.67	53.1
62	5.91	53.3
65	5.91	57.8
102	5.89	63.4

Table 9.2: Density and ultimate compressive strength of the porous samples with fine W particles.

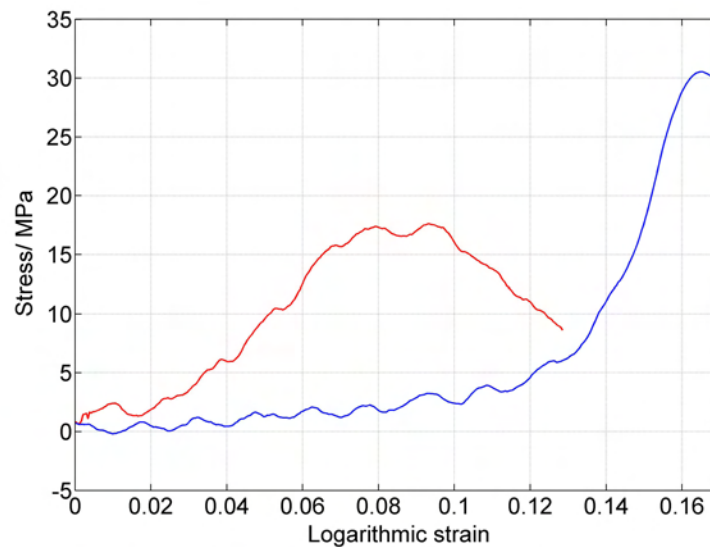


Figure 9.13: Example engineering stress as a function of logarithmic strain relationships for porous samples with coarse W particles, showing the two different types of deformation. The red trace shows a sample that has failed at a stress of 17 MPa. The blue trace is from a sample that failed at a much larger stress of 30 MPa after a slow rise in stress with strain that most likely represents densification of the material.

9. HIGH STRAIN-RATE BEHAVIOUR OF PTFE/AL/W COMPOSITES

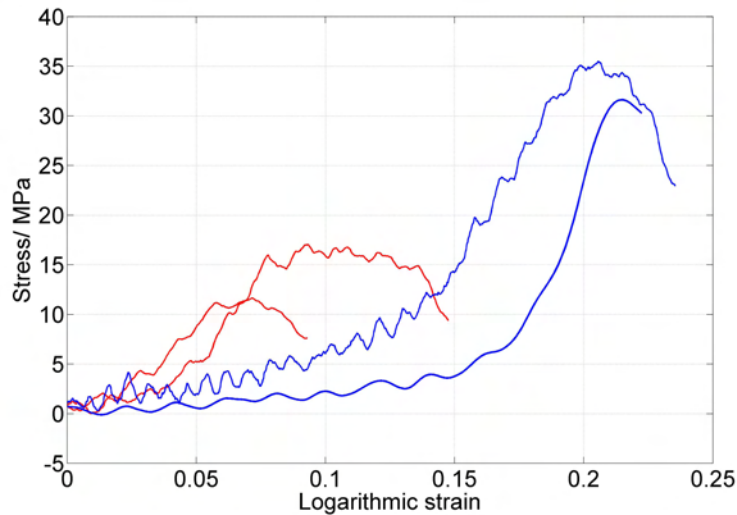


Figure 9.14: Further engineering stress as a function of strain relationships for porous samples with coarse W particles. Two different types of behaviour can be seen between the blue and red curves.

with coarse W particles can deform. Some samples exhibit a very low strength and fail at a stress of around 15 MPa. Other samples exhibited considerably greater strength, failing at 30 MPa or above. The stress as a function of strain relationships for the stronger samples show a long slow rise in stress during the early stages of the compaction, which is not observed with the weaker samples. It is likely that the higher compressive strength can be attributed to a gradual densification of the sample during this initial stage of deformation. This would lead to a considerably increased strength relative to those samples which fail almost immediately upon impact, without the initial densification stage observed in other samples.

The ultimate compressive strength of the samples which display this densification stage is around 30 MPa. As we will see shortly, this is comparable to the ultimate compressive strength of the dense samples with coarse W particles. The pressing pressure for the porous materials with coarse W particles was 20 MPa, as shown in Table 9.1. The ultimate compressive strength of the material is therefore close to the pressing pressure. As the stronger samples fail at a stress

Sample	ρ / kgm^{-3}	UCS/ MPa
72	5.90 ± 0.02	35.0 ± 0.4 , precursor
76	5.80	12.3
93	6.01	33.1, precursor
96	6.06	16.9, plateau
97	6.14	17.2
99	6.11	14.6
103	6.01	30.1, precursor

Table 9.3: Density and ultimate compressive strength of the porous samples with coarse W particles.

greater than this pressing pressure it is logical that some further densification is occurring. The failure stress for each experiment on this material, excluding the interrupted experiments, is listed in Table 9.3.

Using additional interrupted drop-weight experiments, the weak samples were found to fail almost immediately through shearing. For the stronger samples, it was observed that the material had been effectively strained uniaxially, leaving a flat surface flush with the surface of the copper ring. The recovered sample had an unchanged diameter, showing that the density of the sample had been increased. The stronger samples eventually failed in a similar way to the weaker ones, through shear localisation. Figure 9.15 shows a sample that failed in this manner.

This shear localisation leads to de-bonding of the metal particles from the PTFE matrix and the fracture of the matrix itself [22]. It is not known why some samples fail at a low strain while others acquire an increased strength through densification. There is clearly some closely balanced competition between compaction of the soft visco-elastic matrix and fracture during the deformation process. Which process is more significant is clearly sensitive to the particle arrangement and packing within the sample. Small natural variations between samples can lead to significantly different material responses.

9. HIGH STRAIN-RATE BEHAVIOUR OF PTFE/AL/W COMPOSITES

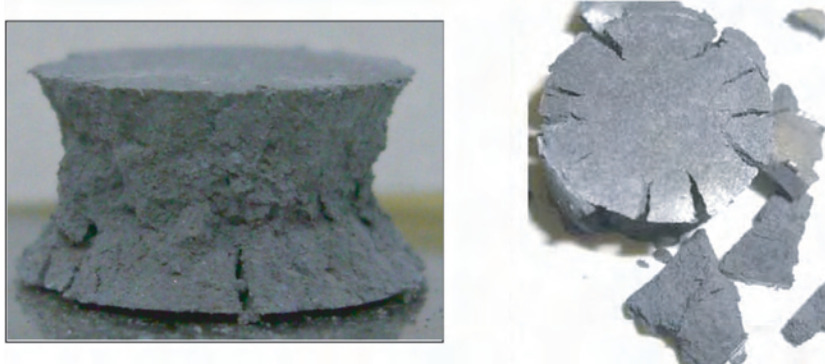


Figure 9.15: A recovered porous sample with coarse W particles. The sample has failed through shear localisation. A symmetrical pattern of cracks could be seen in the fractured samples.

9.3.3 Dense Samples with Coarse W Particles

Example stress as a function of strain relationships for the dense samples with coarse W particles are shown in Figure 9.16. Their failure stress was measured from the traces as between 25 and 33 MPa, the mean being (28 ± 3) MPa. The traces in Figure 9.16 demonstrate a considerable plateau in the stress prior to sample failure. This suggests that considerable plastic deformation of the samples occurs before failure, in comparison to the porous materials with fine W particles for which most of the traces had a clear peak in the stress versus strain relationship, suggesting a more brittle failure. The failure stress in each experiment is shown in Table 9.4.

9.4 Discussion

Characteristic stress as a function of strain relationships for all three materials are shown in Figure 9.17 for ease of comparison. Comparing the two samples containing coarse W particles, the porous samples are significantly weaker than the dense samples. The porous samples generally failed at a stress of around 15 MPa, although we saw in some cases that densification led to an increased ultimate compressive strength. The denser samples generally failed at a higher

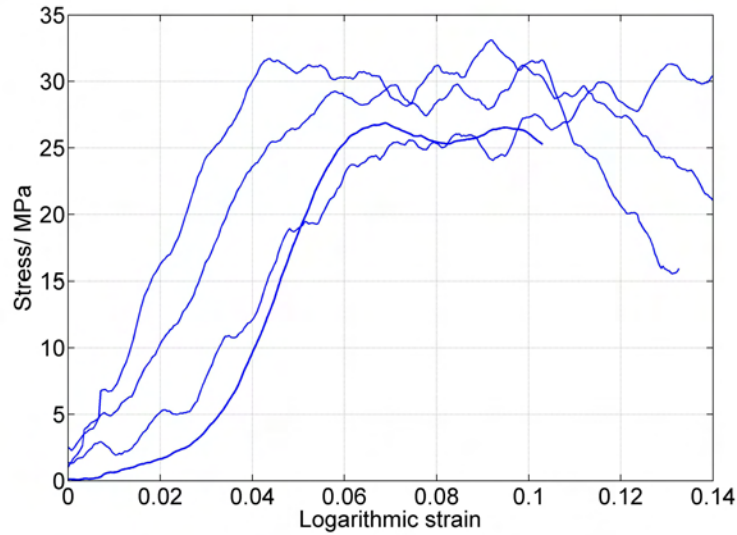


Figure 9.16: Example stress versus strain relationships for dense samples with coarse W particles. All of the samples demonstrated a significant plateau in the stress, suggesting significant plastic deformation occurred before failure.

Sample	ρ / kgm^{-3}	UCS / MPa
71	7.16 ± 0.02	28.1 ± 0.4
75	7.16	32.0, plateau
79	7.14	30.9, plateau
81	7.07	25.1, plateau
83	7.18	26.2, plateau
84	7.11	28.8
85	7.06	28.1

Table 9.4: Density and ultimate compressive strength of the dense samples with coarse W particles.

9. HIGH STRAIN-RATE BEHAVIOUR OF PTFE/AL/W COMPOSITES

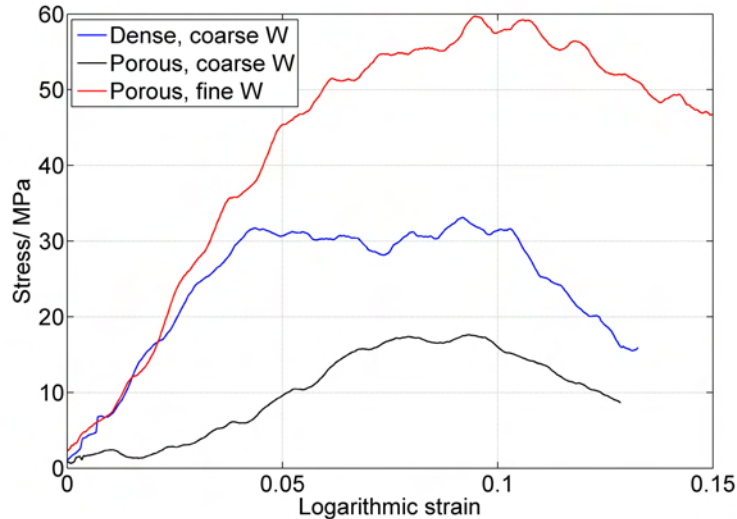


Figure 9.17: Example stress versus strain traces for all three materials. The porous material with fine W particles (red) is the strongest, failing at over 50 MPa. The dense material with coarse W particles (blue) is the next strongest and the traces frequently contain a large plateau before failure, suggesting significant plastic deformation is occurring. The porous material with coarse W particles (black) is generally the weakest, although some samples were strengthened through densification during the deformation.

stress of around 30 MPa. For a given size of W particle it therefore appears that a higher porosity reduces the strength of the material. This is because pores are points of weakness, around them stresses are concentrated and the material is therefore likely to fail at a lower global stress.

It might be expected therefore that the dense material with coarse W particles would be stronger than the porous material with fine W particles, due to the lower porosity. Instead, the porous material with fine W particles has the highest ultimate compressive strength of the three materials, failing at an average stress of (55 ± 4) MPa. The large strength of this material relative to the others is unexpected given its high porosity.

It appears that the unexpectedly high strength of the porous samples with fine W particles, relative to the dense samples with coarse W particles, is caused

	Dense PTFE-Al- coarse W	Porous PTFE-Al-fine W	Porous PTFE-Al- coarse W	Pure Dense PTFE	
Size of W Particles (μm)	<44	<1	<44	-	
CIPing Pressure (MPa)	350	350	20	350	
Experimental Density (g/cm^3)	~ 7.05	~ 6.00	~ 6.00	~ 2.1	
Porosity relative to the theoretical dense composite (%)	1.6	14.3	14.3	4.5	
Ultimate Compressive Strength (MPa)	Quasi-static tests (10^{-3} s^{-1})	18	24	5	3
	Hopkinson bar tests ($\sim 500 \text{ s}^{-1}$)	24	44	18	20
	Drop-weight tests ($\sim 500 \text{ s}^{-1}$)	32	55	12 (35)	-

Figure 9.18: A table showing the variation in material properties with load and strain rate, taken from [15]. The drop-weight values were derived from the experiments performed by the author and reported here.

by the presence of the fine ($< 1\mu\text{m}$) W particles. This relatively large dependence of the strength of the composites on the size of the W particles was somewhat unexpected as it was thought that the majority of the strength would come from the PTFE matrix. It appears that adding fine W particles to a porous matrix leads to a stronger composite than adding coarse W particles to a dense composite. The increased resistance to compaction in the porous samples with fine W particles must be caused by the interaction between the fine W particles and the porous matrix. Table 9.18 is taken from a paper by Herbold *et al.* [15] and shows similar mechanical data obtained by Nesterenko *et al.* [14] for samples of the same material using an Instron machine and a Hopkinson bar. The data show that the surprisingly high strength of the porous samples with fine W particles is repeated across all three strain rates, as is the general order of strength of the three materials.

9.5 Simulations

The simulations of the drop-weight experiments discussed here were performed by Herbold [15]. In this section I interpret the results of these simulations in light

9. HIGH STRAIN-RATE BEHAVIOUR OF PTFE/AL/W COMPOSITES

of the experimental results.

To investigate the effect on the PTFE matrix of the inclusion of Al and W particles, Herbold used two-dimensional numerical simulations to simulate compaction of composite materials of this kind. A two-dimensional Eulerian Hydrocode was implemented to simulate behaviour of the samples at the high strain-rates achieved in the drop-weight. More details on the modelling approach, and details of the simulations, can be found in papers by Herbold *et al.* [15, 23, 24]. Simulations were performed on mixtures of fine W ($1\ \mu\text{m}$) and Al particles ($2\ \mu\text{m}$), and mixtures of coarse W ($10\ \mu\text{m}$) and Al particles ($2\ \mu\text{m}$), embedded in a PTFE matrix. The weight and ‘volume’ fractions (the simulations were performed in 2D) were set to be similar to the drop-weight experiments discussed here (although the number of particles is significantly lower in the simulations).

Selected images from a simulation of the compaction of a Al/W/PTFE sample with $1\ \mu\text{m}$ W particles, taken from [15], are shown in Figure 9.19. During the early stages of the compaction several force chains that span the length of the sample are apparent. These force chains contributed to a significant rise in the resistance of the sample to further compression. As the deformation continues, and the sample begins to locally fail, particle rearrangement leads to the formation of new force chains that again increase the resistance of the sample to compression. The continual breaking of force chains due to localised failure, followed by subsequent activation of force chains elsewhere in the sample, leads to the damage being more evenly distributed throughout the sample. The subsequent failure of the samples, through shear localisation, is in qualitative agreement with the observed failure modes in the experiments.

A different behaviour was observed in simulations of compaction of Al-W-PTFE samples with $10\ \mu\text{m}$ W particles. Again selected images from the simulation, taken from [15], are shown in Figure 9.20. The initial particle distribution in this sample is not conducive to the formation of force chains. Activation of force chains spanning the length of the sample was not as strong as in the previous sample. Instead, only weak localised force chains were developed through small groups of particles. The predicted strength of this type of sample, shown in the curve labelled as (2) in figure 9.21, was significantly lower than that for the first type (labelled as (1)). The simulated stress-strain behaviour was very similar to

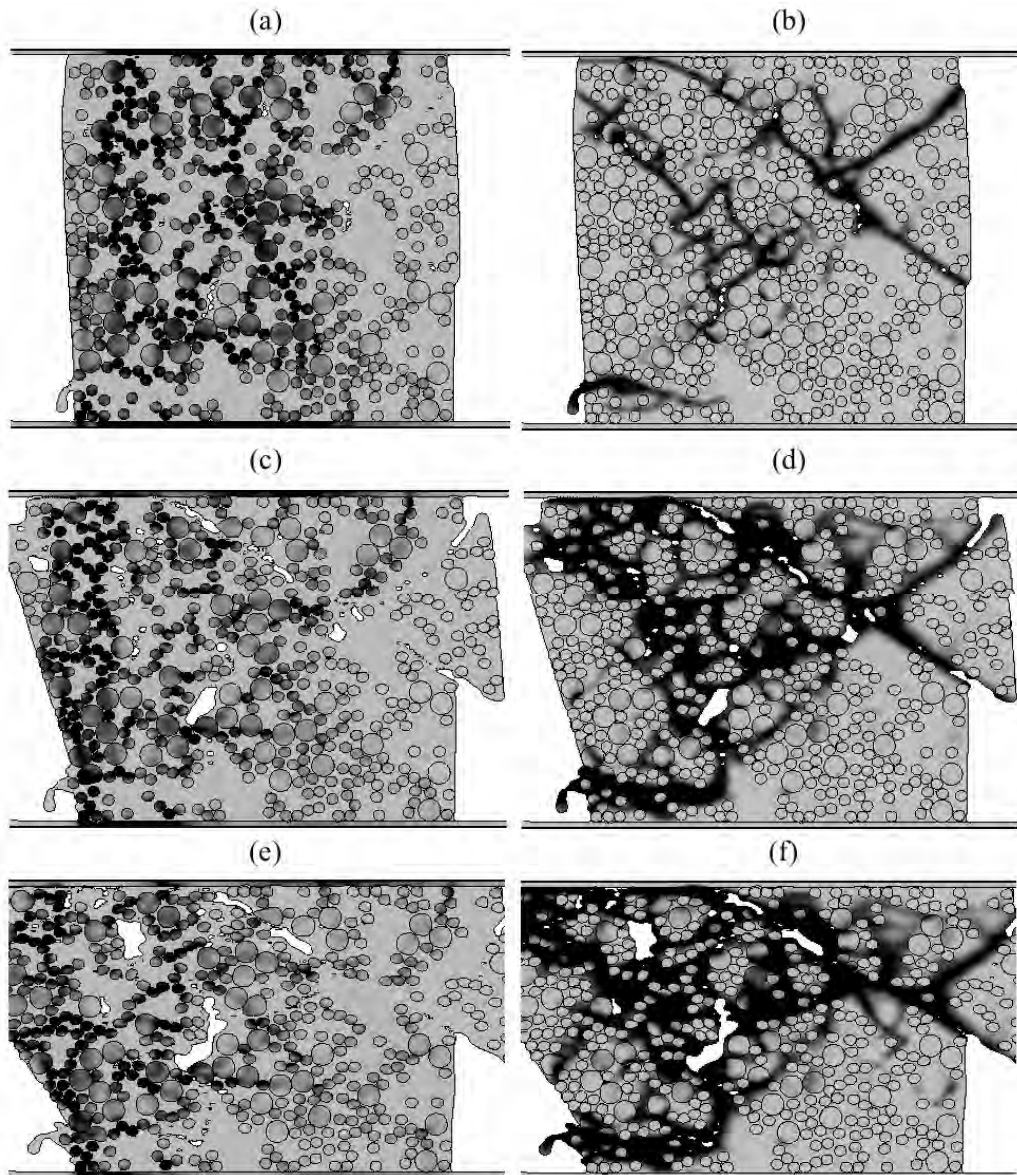


Figure 9.19: The left images show the simulated von Mises stress, from light grey = 0 MPa to dark grey (greater than 500 MPa), at strains of (a) 0.022, (c) 0.043 and (e) 0.238 global strain for the sample with 1 μm W particles. The right images (b), (d) and (f) show the local effective plastic strain (0 to ≥ 0.05) at these corresponding global strains. Figure is taken from Herbold [15]

9. HIGH STRAIN-RATE BEHAVIOUR OF PTFE/AL/W COMPOSITES

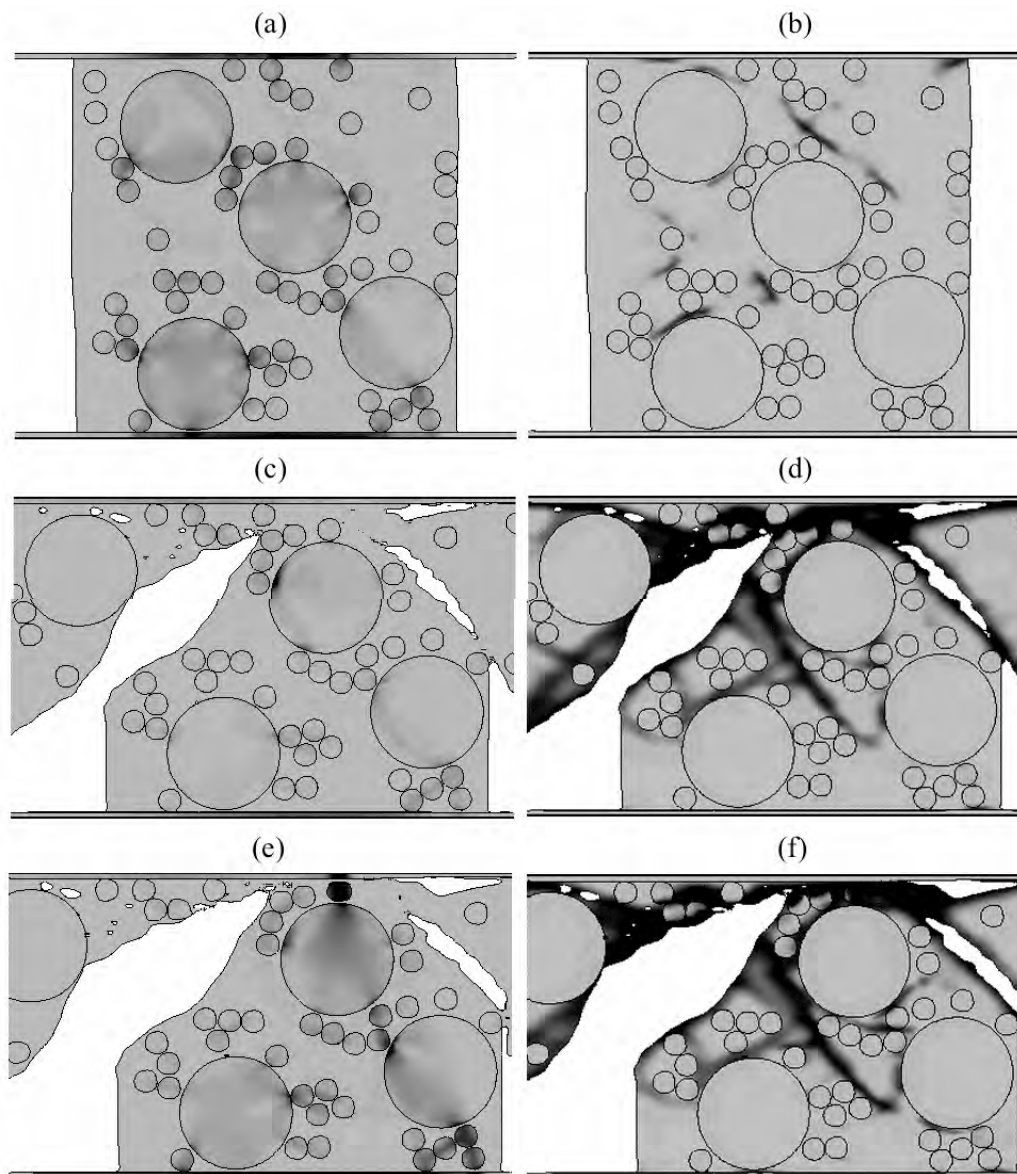


Figure 9.20: The left images show the simulated von Mises stress, from light grey = 0 MPa to dark grey (greater than 500 MPa), at strains of (a) 0.014, (c) 0.186 and (e) 0.23 global strain for the sample with 10 μm W particles. The right images (b), (d) and (e) show the local effective plastic strain (0 to ≥ 0.05) at these corresponding global strains. Figure is taken from Herbold [15]

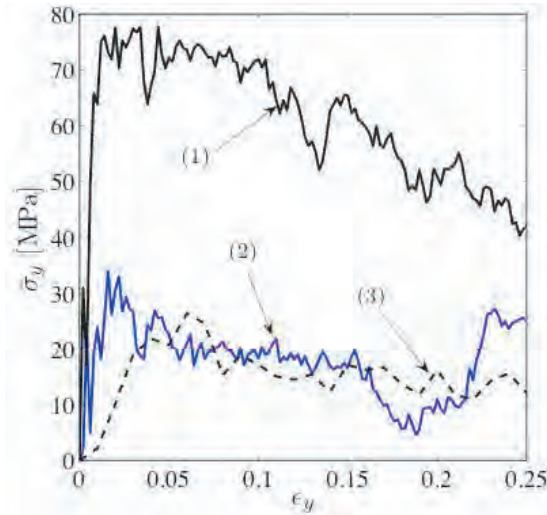


Figure 9.21: Simulated stress-strain relationships for (1) the sample in Figure 9.19, (2) the sample in Figure 9.20 and (3) pure PTFE. The behaviour of (2) and (3) are very similar suggesting that with 10 μm W particles the majority of the load is born by the PTFE matrix.

that predicted for pure PTFE, labelled as (3) in figure 9.21, suggesting that the PTFE matrix is bearing most of the load, rather than any force chains between the metal particles [15].

The simulation results therefore agree with the experimental results in indicating that a PTFE/Al/W mixture containing fine W particles can be significantly stronger than one containing larger W particles, even at a higher porosity. The simulations suggest that the network of fine W particles and Al particles is more suited to the formation of force chains. Indeed, these force chains may have already been activated during the pressing process, where for a given pressure the samples with small W particles ended with a lower density than those with large W particles, suggesting there was more resistance to compaction.

9.6 Conclusions

The technique of ‘soft’ drop-weight experiments, where polymer o-rings are included above the sample, has been developed and shown to be generally successful at removing oscillatory noise from drop-weight traces. This is particularly important for low strength materials, such as those discussed here. Previously, the signals would have been distorted by noise and measurements of the ultimate compressive strength would have been impossible. This technique is likely to prove useful in the future for investigating the high-rate compaction of soft materials. The main advantage over the split-Hopkinson pressure bar is the extent of deformation that can be achieved. Whereas the Hopkinson bar generally only provides small strains (generally under 10%), ‘soft’ drop-weight experiments can be used to produce considerably larger strains (of over 50%).

The unusual phenomenon of the significantly higher strength ((54 ± 4) MPa) of porous composite with small W particles in comparison with the strength ((28 ± 3) MPa) of dense composites with larger W particles was observed. This is attributed to the formation of force chains within the network of small W and Al particles, a mechanism which is supported and reproduced by numerical simulations. It appears that the smaller W particles in a porous matrix are more able to form an arrangement conducive to the formation of force chains than larger W particles in a dense matrix. These force chains may already have been activated during the pressing of the powders to form the samples.

Porous samples containing coarse W particles were found to deform by two significantly different mechanisms. Some samples failed at low stresses of approximately 15 MPa. Other samples failed at considerably higher stresses of around 35 MPa, and much larger strains. The stronger samples displayed an initial slow rise in stress with strain that is attributed to gradual densification of the samples, leading to a much increased strength relative to the original material. It is suggested that this variation in response is only observed for this sample type as the ultimate compressive strength of the material, if it fails without any densification, is close to the original pressing density (20 MPa). This means that any samples that reach a pressure greater than the pressing density before failing, for example because the particle arrangement is such that the material is stronger than

average, are likely to undergo some further densification before failure. These stronger samples subsequently fail in a similar manner and at a similar stress to the initially dense samples with coarse W particles. Clearly some close competition between compaction of the visco-elastic matrix and fracture occurs during the compaction process. This result demonstrates the significant influence that small changes in particle arrangement can have on the subsequent mechanical properties of the sample.

For a given W particle size (coarse W, 44 μm) porosity is detrimental to the material strength. Porous samples had strengths of around 15 MPa (unless densification occurred), while dense samples had strengths of around 35 MPa. This demonstrates the effect that voids and pores have in terms of localisation of forces and introducing points of weakness into a material.

The results provide useful information regarding the tailoring of such materials. In situations where material strength is important, the porous samples with fine W particles would be most appropriate. These samples also allow for the investigation of the formation of force chains, a phenomenon which is important in determining the frequency and location of ignition sites in some reactive materials [13]. Although the sensitivity of the materials was not investigated, the localisation of stress in force chains, particularly in the porous material with fine W particles where force chains appear more important, will lead to localised high temperature regions which may then act as ignition sites within the material, leading to reaction.

The inclusion of copper rings around the sample in interrupted drop-weight experiments was shown to be an effective method of recovering partially deformed materials. This allows for investigation of the mode of deformation occurring at a given strain. Using interrupted experiments the majority of the samples were found to have failed by shear localisation. Earlier types of deformation were observed, including barrelling of some samples and densification of others.

9.7 Summary

To summarise the conclusions of this chapter:

REFERENCES

- The soft drop-weight technique effectively removes the oscillatory noise experienced with standard drop-weight experiments on weak materials, allowing material properties such as the failure stress to be determined.
- Porous composites of Al and PTFE with fine W particles are significantly stronger ((55 ± 4) MPa) than dense Al/PTFE composites with larger W particles ((28 ± 3) MPa). The higher strength is attributed to the formation of force chains by the fine W particles and the Al particles.
- For mixtures of Al and PTFE with coarse W particles, the dense composite is stronger than the porous composite ((28 ± 3) MPa versus (15 ± 2) MPa). This is due to the weakening effect of pores and voids, at which the stresses become localised and magnified.
- Porous Al/PTFE samples with coarse W particles can experience two different forms of deformation. Some samples fail at low stresses (15 MPa) through shearing, while others experience a significant densification period before failing at a larger stress (35 MPa).
- This difference is attributed to a competition between compaction of the visco-elastic matrix and fracture. Which process is dominant appears very sensitive to the particular arrangement of particles within the sample.

References

- [1] Davis, J.J., Lindfors, A.J., Miller, P.J., Finnegan, S. and Woody, D.L., “Detonation like phenomena in metal-polymer and metal/metal oxide-polymer mixtures”, *11th Int. Det. Symp.*, (1998), 1007–1013
- [2] Holt, W.H., Mock, W. and Santiago, F., “X-ray photo-electron spectroscopy indication of decomposition species in the residue of shocked polytetrafluoroethylene powder”, *Journal of Applied Physics*, **88(9)**, (2000), 5485–5486
- [3] Ames, R., “Energy release characteristics of impact-initiated energetic materials”, *Mater. Res. Soc. Symp. Proc.*, **896**, (2006), 123–132

REFERENCES

- [4] Field, J.E., Walley, S.M., Proud, W.G., Balzer, J.E., Gifford, M.J., Grantham, S.G., Greenaway, M.W. and Siviour, C.R., “The Shock Initiation and High Strain Rate Mechanical Characterization of Ultra-fine Energetic Powders and Compositions”, *Mater. Res. Soc. Symp. Proc.*, **800**, (2004), 179–190
- [5] Meric, C. and Engez, T., “Understanding the thermitic welding process”, *Welding Journal*, **78(1)**, (1999), 33–36
- [6] Lumsden, *Incendiary Weapons*, Stockholm International Peace Research Institute, SIPRI monograph (1975)
- [7] Czerski, H., *Ignition of HMX and RDX*, Phd thesis, University of Cambridge (2006)
- [8] Czerski, H. and Proud, W.G., “Relationship between the morphology of granular cyclotrimethylene-trinitramine and its shock sensitivity”, *Journal of Applied Physics*, **102**, (2007), 113,515
- [9] Pergeot, F. and Watt, D., *RS-RDX: Literature review and discussions*, NIMIC Report L102, US (2002)
- [10] Bowden, F.P. and Yoffe, A.D., *Ignition and growth of explosion in liquids and solids*, Cambridge University Press, UK (1952)
- [11] Bourne, N.K. and Field, J.E., “Bubble collapse and the initiation of explosion”, *Proc. R. Soc. Lond. A*, **435**, (1991), 423–435
- [12] Khasainov, B.A., Ermolaev, B.S., Presles, H.N. and Vidal, P., “On the effect of grain size on shock sensitivity of heterogeneous explosives”, *Shock Waves*, **7**, (2007), 89–105
- [13] Foster, J.C.J., Glenn, J.G. and Gunger, M., “Meso-scale Origins of the Low-Pressure Equation of State and High Rate Mechanical Properties of Plastic Bonded Explosives”, *Shock Comp. of Cond. Matt.*, **505**, (2000), 703

REFERENCES

- [14] Cai, J., Nesterenko, V.F., Vecchio, K.S., Jiang, F., Herbold, E.B., Benson, D.J., Addiss, J.W., Walley, S.M. and Proud, W.G., “The influence of metallic particle size on the mechanical properties of polytetrafluoroethylene-AlW powder composites”, *Applied Physics Letters*, **92**
- [15] Herbold, E.B., Nesterenko, V.F., Benson, D.J., Cai, J., Vecchio, K.S., Jiang, F., Addiss, J.W., Walley, S.M. and Proud, W.G., “Particle size effect on strength, failure, and shock behavior in polytetrafluoroethylene-Al-W granular composite materials”, *Journal of Applied Physics*, **104(103903)**
- [16] Addiss, J.W., Cai, J., Walley, S., Proud, W.G. and Nesterenko, V.F., “High strain and strain-rate behaviour of PTFE/Aluminium/Tungsten mixtures”, *Proc. Shock Compression of Condensed Matter*, **955**, (2007), 773–776
- [17] Walley, S.M., Field, J.E., Pope, P.H. and Safford, N.A., “The rapid deformation behaviour of various polymers”, *J. Phys. III France*, **1**, (1991), 1889–1925
- [18] Radford, D.D., Walley, S.M., Church, P. and Field, J.E., “Dynamic upsetting and failure of metal cylinders: Experiments and analysis”, *J. Phys. IV France*, **110**, (2003), 263–268
- [19] Balzer, J.E., Proud, W.G., Walley, S.M. and Field, J.E., “High-speed photographic study of the drop-weight impact response of RDX/DOS mixtures”, *Combustion and Flame*, **135**, (2003), 547–555
- [20] Walley, S.M., Field, J.E., Pope, P.H. and Safford, N.A., “A Study of the Rapid Deformation Behaviour of a Range of Polymers”, *Pilos. Trans. Royal. Soc. Lon.*, **328(1597)**, (1989), 1–33
- [21] Grey, G.T., “Classic Split-Hopkinson Pressure Bar Testing”, *OH: ASM International*, **1**, (2000), 462–476
- [22] Cai, J., Walley, S.M., Hunt, R.J.A., Proud, W.G., Nesterenko, V.F. and Meyers, M.A., “High-strain, high-strain-rate flow and failure in PTFE/Al^W granular composites”, *Mat. Sci. and Eng. A*, **472**, (2008), 308–315

REFERENCES

- [23] Herbold, E.B., Cai, J., Benson, D.J. and Nesterenko, V.F., “Simulation of particle size effect on dynamic properties and fracture of PTFE-W-Al composites”, *Shock Comp. of Cond. Matter*, **955**, (2007), 785–788
- [24] Cai, J., Nesterenko, V.F., Vecchio, K.S., Jian, F., Herbold, E.B., Benson, D.J., Addiss, J.W., Walley, S.M. and Proud, W.G., “The influence of metallic particle size on the mechanical properties of PTFE-Al-W powder composites”, *Shock Comp. of Cond. Matter*, **955**, (2007), 785–788

REFERENCES

Chapter 10

Compaction of Soils

10.1 Introduction

In previous chapters we considered the response of sand to penetration by long-rod projectiles and discussed the importance of the response of the material to an applied force. In this chapter, the properties of sand, silt and soils (a combination of sand and silt) during dynamic compaction are investigated using the drop-weight apparatus described in Chapter 8. The effect of varying concentrations of water content on the compaction properties of the materials is also investigated. This research forms part of a larger study of the dynamic compaction behaviour of geological materials, including concretes and mixtures of sand and silt, carried out by researchers at the University of Cambridge and elsewhere [1, 2].

The compaction properties of materials formed of sand and silt (soil, for example) are relevant to a wide range of applications, including mining, seismology and the construction industry. Sand and silt are also major components of concrete and consequently are of importance to a wide range of engineering applications. How the properties of such materials vary with water content is of obvious significance.

Previous experiments investigating the effect of moisture content on the high strain-rate behaviour of sand suggest that partially wet sand is more compressible than dry sand [3]. When compacting a confined sand sample in a split-Hopkinson pressure bar, the softest behaviour of the material was observed for a moisture content of $(7.0 \pm 0.5)\%$ and any level of saturation between 3 and 20% made the

10. COMPACTION OF SOILS

material softer. The behaviour of dry sand has been investigated at high rates (impacts of the order of 1 km/s) [4] using a 50 mm diameter gas-gun. At somewhat lower rates, the compressive response of sand has been investigated using a split-Hopkinson pressure bar [5]. The results suggested that the compressive response of dry sand was not sensitive to strain rate under the chosen loading conditions, but was significantly dependent on the initial density and the extent of lateral confinement of the sample. Data from Hopkinson bar studies are limited by the short loading time and by the maximum achievable level of compaction, which is found to be relatively low for experiments on granular materials - strains of only a few percent are likely given the low momentum of the rod impactor.

In the research presented here, a drop-weight is used to investigate the dynamic compactability of mixtures of sand and silt up to strains of 50%. The effect of varying the ratio of the two components will be discussed (specifically: pure sand, 2:1 sand to silt, 1:1, 1:2 and pure silt) as will the effect of adding varying percentages of water by mass (0%, 5% and 10%). Using the drop-weight apparatus allows the properties of the material to be studied up to significantly larger strains than with the Hopkinson bar.

10.2 Sample Characterisation and Preparation

The sand used in these experiments is a quartz based sand provided by the Concrete Structures Section, Department of Civil Engineering, Imperial College, London. Some characterisation of this sand was also carried out by David Chapman for the research in his thesis [6]. The mean particle size of the sand was found, using the same laser scattering technique discussed in Chapter 4, to be $270 \pm 30 \mu\text{m}$. The measured particle size distribution is shown in red in Figure 10.1. The silt used in the following experiments was also provided by Imperial College. The average particle size is $60 \pm 20 \mu\text{m}$ and the measured particle size distribution is shown in black in Figure 10.1.

In addition, the mineral content of the two materials has previously been investigated using a mineral analyser at the School of Chemical and Environmental Engineering, Nottingham University. The results obtained using a Mineral Liberation Analyser (MLA) (produced by JKTech) for the sand and silt are shown

10.2 Sample Characterisation and Preparation

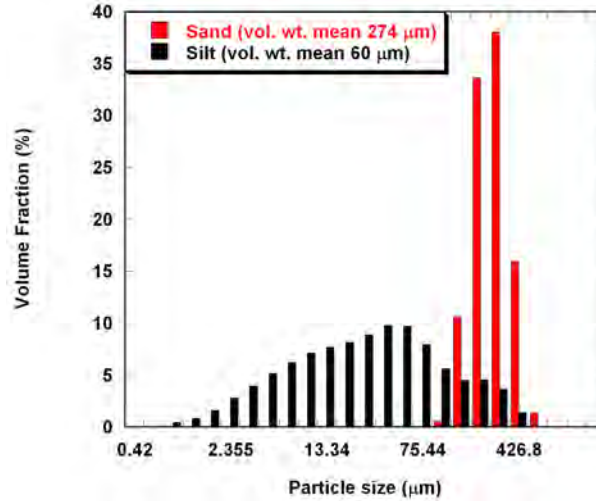


Figure 10.1: The particle size distributions of the sand (red) and silt (black) materials, as measured using a laser particle sizer. Figure taken from [6].

in Figures 10.2 and 10.3 respectively. The mineral analysis technique involves the analysis of back-scattered electrons to identify the minerals present. The relative proportions of the different minerals are calculated from the relative magnitudes of the surface areas involved in the back-scattering of the electrons.

Figure 10.2 shows that the sand is almost 100% Quartz, with only minor impurities of Zircon, Rutile and Titanate. The composition of the silt material is more complicated, with significant fractions of Orthoclase (45%), Quartz (35%) and Chlorite (17%), as well as minor impurities of Calcite and Iron.

The sand has a tapped density of $(1530 \pm 30) \text{ kgm}^{-3}$. The “tapped” density of the sample is the density achieved by vigorously tapping the sample on a hard surface to allow the material to settle. Since the sand is almost 100% quartz, the theoretical maximum density (TMD) of the sample is approximately that of quartz, which is 2650 kgm^{-3} for α -quartz [7].

The porosity, ϕ , of a granular material is defined as,

$$\phi = \frac{V_V}{V_T}, \quad (10.1)$$

where V_V is the volume of the voids and V_T is the total volume of the sample.

10. COMPACTION OF SOILS

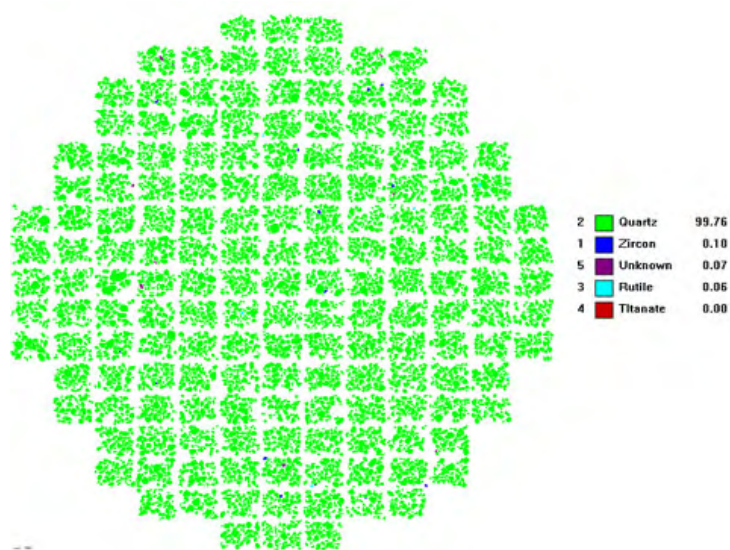


Figure 10.2: Results of the mineral analysis carried out by Nottingham University on the sand. The colours in the figure show the percentage of the various minerals present (percentages are of the total electron back-scattering area). Here, the dominant constituent of the sand is Quartz. Image courtesy of Dr S. Plint, Prof. S. Kingman and D. Chapman [6].

10.2 Sample Characterisation and Preparation

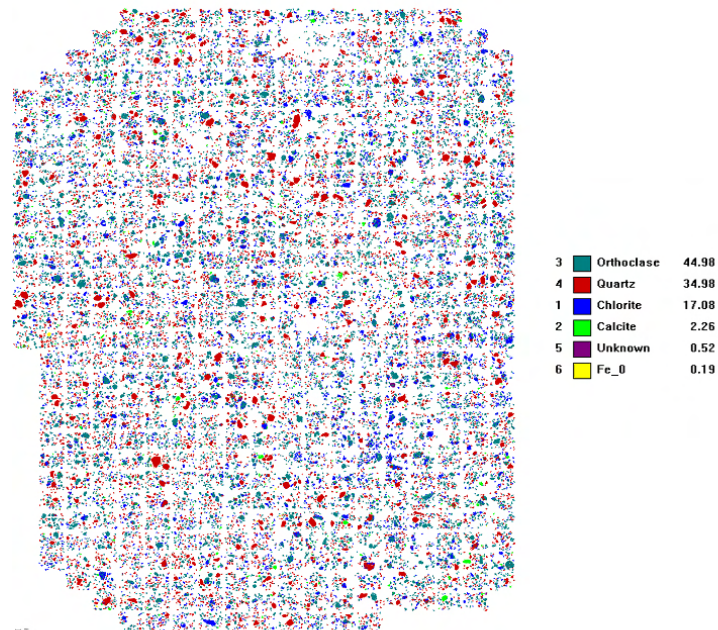


Figure 10.3: Results of the mineral analysis carried out by Nottingham University on the silt material. The colours in the figure show the percentage of the various minerals present (percentages are of the total electron back-scattering area). The silt has a more complex composition than the sand, with significant fractions of Orthoclase, Quartz and Chlorites. Image courtesy of Dr S. Plint, Prof. S. Kingman and D. Chapman [6].

10. COMPACTION OF SOILS

Mineral	Fraction	Density/ kgm^{-3}
Orthoclase	44.98	2563
Quartz	34.98	2650
Chlorite	17.08	2600 - 3300

Table 10.1: Densities of the three main mineral components of the silt material.

Alternatively, the porosity can be written as,

$$\phi = 1 - \frac{\rho_{sample}}{\rho_{TMD}}, \quad (10.2)$$

where ρ_{sample} is the tapped density of the sample. Comparison of the tapped density and the TMD of the dry sand suggests that it is 42% porous by volume. Estimating the porosity of the silt material is more complicated as it consists of a number of different minerals. Since the proportions in Figures 10.2 and 10.3 are related to the back-scattering area, only the relative magnitude of the surface areas is known, not the volume ratio of the minerals in the mixture. The densities of the three main component minerals in the silt material are shown in Table 10.1.

An approximate estimate of the theoretical maximum density of the silt material can be made by averaging the densities shown in Table 10.1, weighted by the relevant fraction. This gives an approximate theoretical maximum density for the silt of $(2660 \pm 30) \text{ kgm}^{-3}$. The measured tapped density of the dry silt is $(1300 \pm 30) \text{ kgm}^{-3}$, suggesting that the dry material is $(51 \pm 2)\%$ porous by volume.

Five different mixtures of the sand and silt were prepared by thoroughly mixing together the proportions, by volume, shown in Table 10.2. The samples were stirred vigorously to ensure thorough mixing of the components. Some separation of the components was observed during transport, so regular subsequent stirring of the mixtures was performed. The wet samples were prepared by adding the required mass of water to the dry mixtures, as measured using a balance accurate to $\pm 1 \text{ mg}$. Experiments were performed on each mixture of sand and silt in their dry state, after being dried in an oven for 24 hours, and with $(5.0 \pm 0.3)\%$ added water by mass and with $(10.0 \pm 0.3)\%$ added water, such that the water makes up 5% or 10% of the total mass of the resulting sample. The wet samples were

10.2 Sample Characterisation and Preparation

Name	Mixture (by volume)
C	Pure silt
CCS	Two thirds silt and one third sand
CS	One half silt and one half sand
CSS	One third silt and two thirds sand
S	Pure sand

Table 10.2: The five mixtures of sand and silt. Experiments were performed on the dry material, and with 5% and 10% added water by mass. For each combination, three experiments were performed so an average could be obtained. 45 dropweight experiments were performed in total.

thoroughly stirred by hand so that the water was evenly distributed throughout the material.

The porosity of the dry sand was calculated earlier as 42% by volume. Therefore, a fully saturated sample of sand would consist of a mixture of 58% quartz by volume, at a density of 2650 kgm^{-3} , and 42% water by volume, at a density of 998.2 kgm^{-3} . The density of the saturated sample would therefore be 1960 kgm^{-3} . This corresponds to 21% added water by mass, as calculated by:

$$\frac{M_w}{M_T} = \frac{V_w \rho_w}{V_w \rho_w + V_s \rho_s}, \quad (10.3)$$

where M_w and M_T are the mass of the added water and the total sample mass, and V_w , V_s , ρ_w and ρ_s are the volumes and densities of the water and sand components of the mixture. All of the sand samples used in this research are therefore significantly less than fully saturated. The density of a fully saturated silt sample would be 1810 kgm^{-3} , corresponding to 28% added water by mass.

If a mass fraction of quartz, f_q , and a mass fraction of water, f_w , are mixed the total volume of quartz and water, V_m , is given by:

$$V_m = \frac{\rho_{\text{sample}} \times f_w \times V_T}{\rho_{\text{water}}} + \frac{\rho_{\text{sample}} \times f_q \times V_T}{\rho_{\text{quartz}}}. \quad (10.4)$$

More generally we can say that:

$$V_m = V_T \rho_{\text{sample}} \sum_i \frac{f_i}{\rho_i}, \quad (10.5)$$

10. COMPACTION OF SOILS

Material	Water/ %	Density/ gcm ⁻³	Porosity/ %
Silt	0.0 ± 0.3	1300 ± 30	51.1 ± 0.8
Silt	5.0 ± 0.3	1370 ± 40	44.2 ± 0.7
Silt	10.0 ± 0.3	1406 ± 40	38.3 ± 0.7
Sand	0.0 ± 0.3	1530 ± 30	42.3 ± 0.9
Sand	5.0 ± 0.3	1633 ± 40	33.2 ± 0.8
Sand	10.0 ± 0.3	1656 ± 40	27.1 ± 0.9

Table 10.3: Porosity of the pure sand and silt with various amounts of added water. The silt is significantly more porous than the sand.

where f_i and ρ_i are the mass fraction and density of each constituent. The porosity of the sample is then given by:

$$\phi = \frac{V_T - V_m}{V_T}. \quad (10.6)$$

The densities and porosities of the pure sand and silt mixtures with the different water contents, calculated in this way, are shown in Table 10.3.

Table 10.3 shows that the silt samples are all significantly more porous than the corresponding sand samples. Adding water to the samples increases the density of the material, which suggests that the water is being contained within the porous granular structure, for example, within voids, or coating the outside of the particles. In mixtures containing silt the silt grains may also absorb some of the water.

Three experiments were performed on each mixture of sand, silt and water (15 distinct mixtures in total) so that an average density as a function of pressure relationship could be obtained. The inherent variability of granular materials means there is a spread in the starting densities and the subsequent response of the samples. In total 45 drop-weight experiments were performed.

10.3 Experimental Method

For the experiments, the samples were constrained in the holder shown in Figure 10.4. This consists of a hollow cylindrical steel jacket which is sealed at one

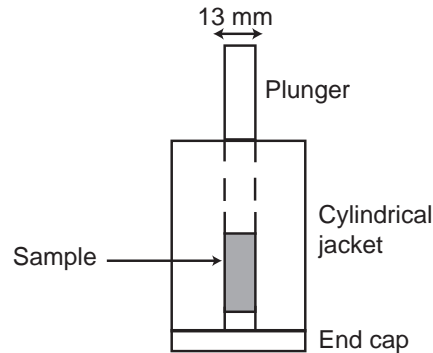


Figure 10.4: The sample holder used in these experiments. The sample is held in a cylindrical jacket, sealed at one end with an end cap. The plunger is placed in the open end and is driven by the drop-weight into the sample.

end with a removable cap. The central bore of the cylinder has a diameter of (13.0 ± 0.1) mm. For each experiment, approximately 6 g of material (6.01 ± 0.08) g was weighed out and added to the holder in stages, interspersed with tapping the holder on a hard surface to allow the material to settle.

A close fitting plunger was machined to match the size of the bore of the jacket to within $100 \mu\text{m}$, so that it would slide freely within the holder. This was inserted in the open end of the sample holder so that it was resting on the sample. In each experiment the sample holder was mounted vertically on the force transducer of the drop-weight, so that the falling mass would drive the plunger into the sample to compact it.

10.4 Preliminary Results

A characteristic voltage as a function of time trace recorded for an experiment on a sand sample is shown in Figure 10.5. There is a large amount of oscillatory noise in the signal, thought to be caused by vibrations excited in the drop-weight by the impact of the large mass. The oscillations have a mean frequency of 5550 ± 50 Hz and cover a range from 5200 to 6500 Hz. As the oscillations cover a relatively narrow range of frequencies, and occur at a distinct frequency from the useful

10. COMPACTION OF SOILS

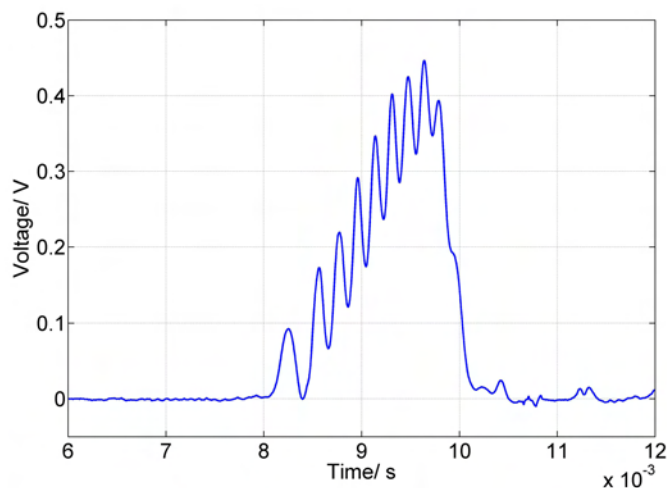


Figure 10.5: A voltage time trace recorded for a drop-weight experiment on a dry sand sample. There are large oscillations in the signal with a frequency ranging from 5200 to 6500 Hz, with a mean of 5550 ± 50 Hz.

information about the sample, it should be possible to remove them by filtering the Fourier transform power spectrum.

Figure 10.6 shows the Fourier transform power spectrum of the voltage-time trace displayed in Figure 10.5. Most of the information about the sample behaviour occurs in the 0 - 2000 Hz range. The secondary peak around 5500 Hz mostly corresponds to the oscillatory noise observed in the voltage trace. By filtering out this secondary peak in the power spectrum, by setting a narrow region of the frequency spectrum covering the peak to zero, and then performing an inverse Fourier transform, the filtered voltage-time trace shown in red in Figure 10.7 results. The filtered voltage-time trace passes through the centre of the oscillations as would be expected, suggesting that the noise has been successfully removed without significantly affecting the signal of interest. There is little additional oscillation of the filtered trace, suggesting that the chosen filtering method is appropriate.

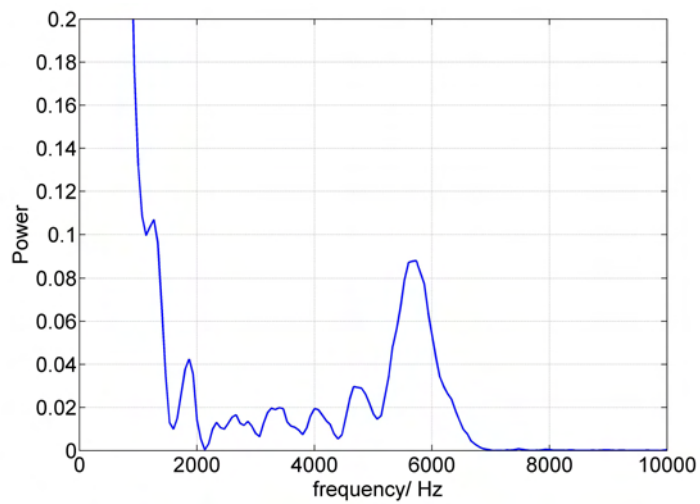


Figure 10.6: Fourier transform power spectrum for the voltage-time signal shown in Figure 10.5. There is a clear secondary peak around 5500 Hz.

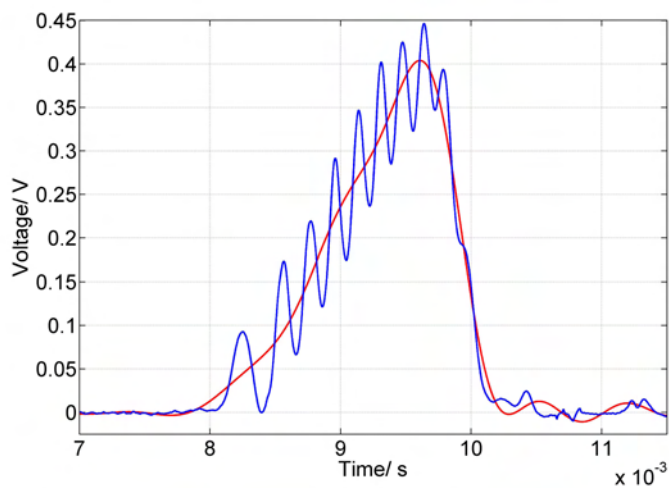


Figure 10.7: Original voltage-time trace for an experiment on sand (blue), and the voltage-time trace recovered after filtering out the secondary peak in the Fourier transform power spectrum (red).

10. COMPACTION OF SOILS

Type	ρ_i / kgm^{-3}	TMD/ kgm^{-3}	Porosity i/%	$\rho_{relative}$	Porosity f/%
S	1530	2650	42	1.13 ± 0.04	35 ± 2
CSS	1490	2653	44	1.33	25
CS	1407	2655	47	1.37	27
CCS	1394	2657	47	1.34	30
C	1300	2660	51	1.48	28

Table 10.4: A table of the densities and porosities of the samples before compaction (ρ_i and Porosity i), and at a pressure of 220 MPa ($\rho_{relative}$, Porosity f)

10.5 Results

The experimental results allow comparison of a number of factors, specifically: the effect of varying water content for a given mixture of sand and silt, and the effect of varying the relative proportions of sand and silt for a given water content.

10.5.1 Comparison of Dry Materials

The average calculated density as a function of pressure curves for the five mixtures with no added water are shown in Figure 10.8. The mixtures have a range of starting tapped density, ranging from a maximum of $(1530 \pm 30) \text{ kgm}^{-3}$ for the sand to a minimum of $(1300 \pm 30) \text{ kgm}^{-3}$ for the silt. The tapped densities of the mixtures are shown in Table 10.4. Despite the range of starting densities, the subsequent behaviour of the material is very similar for all of the mixtures, with the exception of the dry sand. For a given pressure the dry sand remains at a lower density than the other mixtures, which all have similar densities at higher pressures. As we are interested in the ‘compactability’ of the materials, it may be more informative to plot the density, relative to the starting density, as a function of pressure. This is shown in Figure 10.9 for the dry mixtures.

Figure 10.9 shows that the silt material is the most compactable, reaching a maximum relative density of 1.47 ± 0.03 , and that the sand is easily the least compactable, reaching only 1.14 ± 0.02 . The relative density reached by each of the materials at a pressure of 220 MPa is shown in Table 10.4. Also listed in Table 10.4 are estimates of the TMD of each mixture and the approximate initial

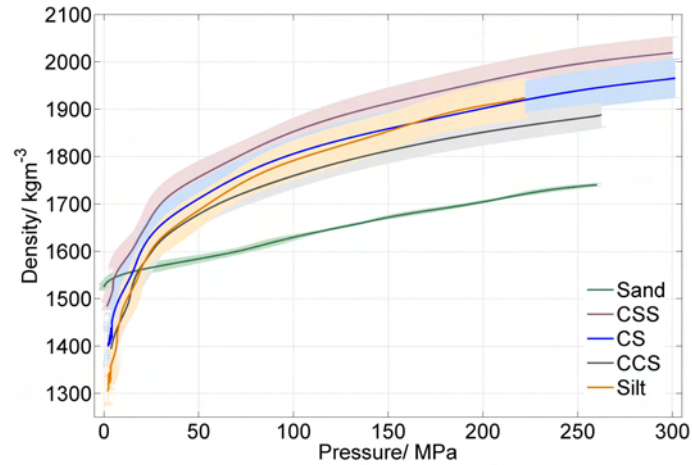


Figure 10.8: Average density as a function of pressure relationships for the five dry mixtures in Table 10.2. The average values are shown with solid lines and the errors are shown in a lighter shade of the same colour. Despite the range of starting density, the mixtures have similar behaviour at higher pressures, with the exception of the dry sand.

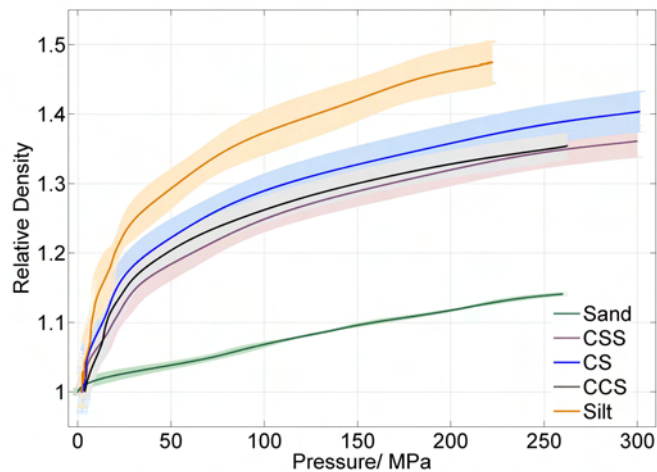


Figure 10.9: Relative density as a function of pressure relationships for the five mixtures with no added water. Determined by dividing each of the traces in Figure 10.8 by the starting density.

10. COMPACTION OF SOILS

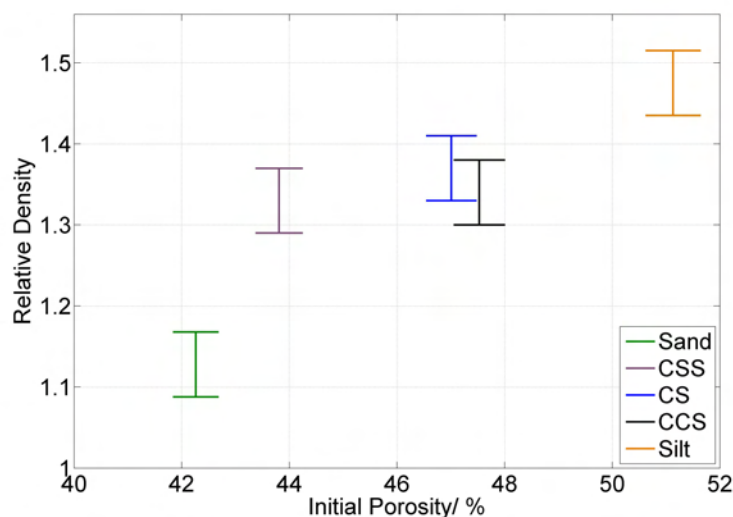


Figure 10.10: A plot of the relative density reached at a pressure of 220 MPa for each of the materials, as a function of their estimated initial porosity. There is a reasonable correlation between compactability and initial porosity.

porosity of the materials. The order of starting porosity correlates quite well with with the order of compactability, as shown in the plot in Figure 10.10. The porous nature of the silt material means that little force is required to densify the material, leading to a high compactability. Mixtures containing large amounts of silt behave in a similar manner, although with a somewhat reduced compactability due to the lower porosity. The sand has the lowest initial porosity, and the larger grains means that it is more difficult for the porosity to be reduced without fracturing of the grains. This leads to a reduced compactability relative to the silt material.

10.5.2 The Effect of Water

We now consider the effect of water on the mixtures. Figure 10.11 shows the effect on the relative density as a function of pressure relationship of varying the water content of the sand. Adding 5% by mass of water to the sand significantly increases the compactability relative to the dry sand. Adding 10% by mass of

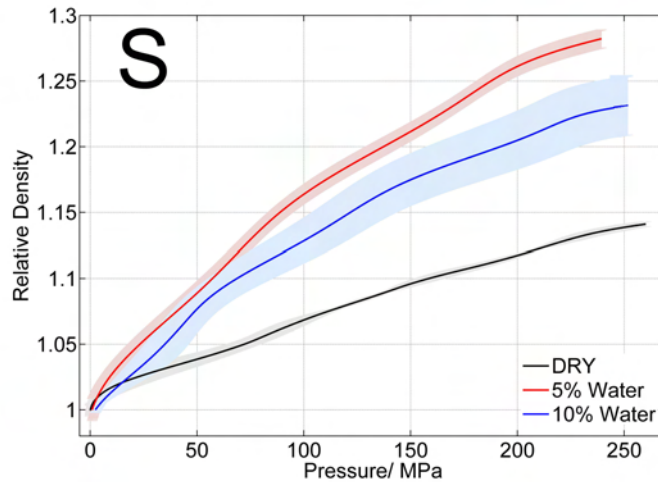


Figure 10.11: Relative density as a function of pressure relationships for sand at three different water contents - 0% (black), 5% (red), and 10% (blue).

water also increases the compactibility, but by less of an extent than adding 5% water.

When we consider the corresponding results for the CSS mixture, shown in Figure 10.12, we see that that adding 5% water again makes the material more compactable. In this case though, adding 10% water actually makes the material less compactable than the dry material. The same effect was found for the silt material and the CCS mixture, shown in Figures 10.14 and 10.15. For the CS mixture, shown in Figure 10.13, it appears that varying the water content has little effect on the compactibility of the material.

Figures 10.14 and 10.15 show unusual behaviour of the silt and CSS mixture with 10% added water (shown in blue). In both cases, the material with 10% water is significantly less compactable than the dry material. There is an initial rapid increase in density with pressure, followed by a much flatter and slower increase in density, suggesting that the compactibility of the material changes significantly during the compaction. These materials also reach a much lower final pressure than might otherwise be expected.

The effect of varying the relative amounts of sand and silt in the mixtures, in the presence of water, is illustrated in Figures 10.16 and 10.17, showing the

10. COMPACTION OF SOILS

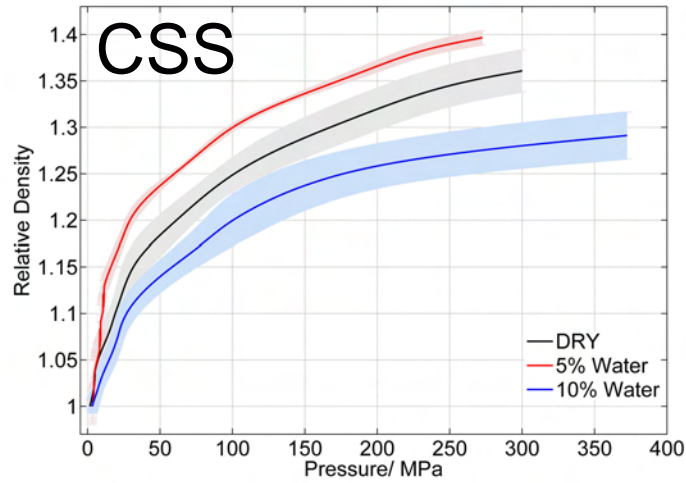


Figure 10.12: Relative density as a function of pressure relationships for the CSS mixture at three different water contents - 0% (black), 5% (red), and 10% (blue).

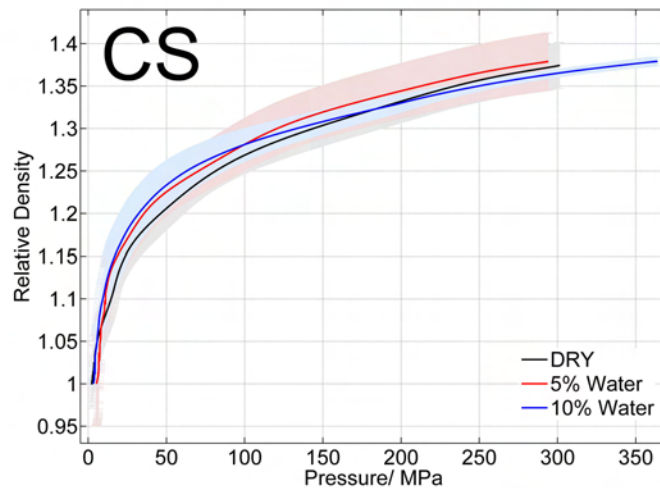


Figure 10.13: Relative density as a function of pressure relationships for the CS mixture at three different water contents - 0% (black), 5% (red), and 10% (blue).

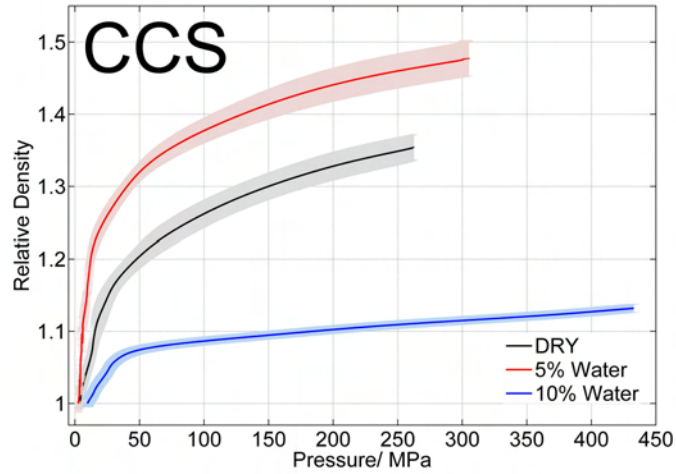


Figure 10.14: Relative density as a function of pressure relationships for the CCS mixture at three different water contents - 0% (black), 5% (red), and 10% (blue).

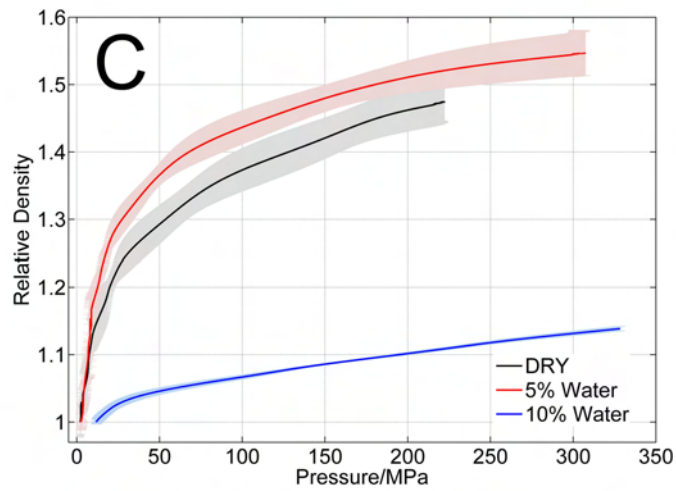


Figure 10.15: Relative density as a function of pressure relationships for the silt material at three different water contents - 0% (black), 5% (red), and 10% (blue).

10. COMPACTION OF SOILS

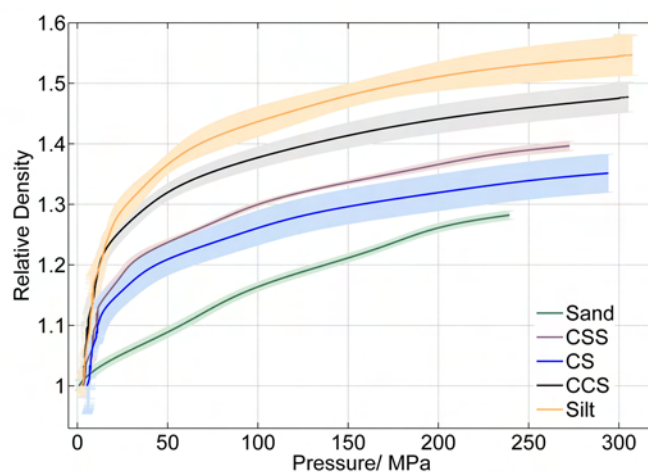


Figure 10.16: Relative density as a function of pressure relationships for the five mixtures with 5% added water by mass.

situation with 5% and 10% added water respectively. With 5% added water the situation is similar to with the dry material. Increasing the relative proportion of silt in the mixtures generally appears to increase the compactibility of the samples, although the CS mixture appears a little less compactable than the CCS mixture. The situation is considerably different with 10% added water. With the sand, CSS and CS mixtures, the compactibility increases with the relative proportion of silt. The silt and CCS mixtures, though, are significantly less compactable than the others.

10.6 Discussion

The dry specimens investigated in this research consist of a skeleton structure of sand and silt particles surrounding pores filled with air. During compaction the grains move to fill the pores, leading to a reduction in porosity and an increase in density. Even at 300 MPa, none of the samples is sufficiently compacted to remove all of the porosity. Indeed, Table 1.4 shows that the final porosities are still significant, being at least 25% by volume. It is therefore unlikely that the air in the voids is bearing any of the load. Instead, when a void is partially filled,

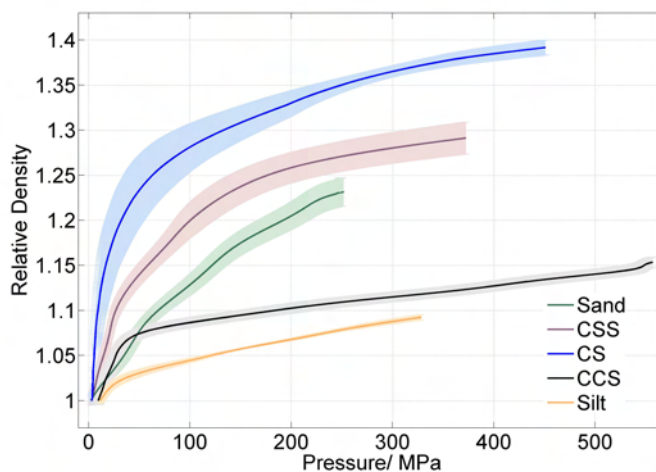


Figure 10.17: Relative density as a function of pressure relationships for the five mixtures with 10% added water by mass.

the air is displaced to elsewhere in the volume.

Adding a small quantity of water to the samples might be expected to have little effect on their response to compaction, since the pores would still mostly be filled with air. The particles would still be able to move to fill voids and displace the air contained in those voids. However, the data presented here shows that adding a relatively small amount of water (5%) to the materials actually increases their compactability. A possible explanation of this effect is that the presence of the water around the grains helps to lubricate the system, and reduces the friction between grains, relative to the dry state. The presence of water around the inter-particle contact areas will reduce the shear stresses between particles and enable them to move and rearrange more freely in response to the applied load. This situation is illustrated in the middle panel of Figure 10.18.

For most of the mixtures, excluding the sand, adding a larger amount of water (10% by mass) actually acts to reduce the compactability of the material relative to the dry state. This can be understood by considering the extreme case, where the samples are fully saturated with water. In this case, very little rearrangement of the grains is possible before the water in the pores is loaded. This means the sample would rapidly stiffen, relative to the dry material, and become relatively

10. COMPACTION OF SOILS

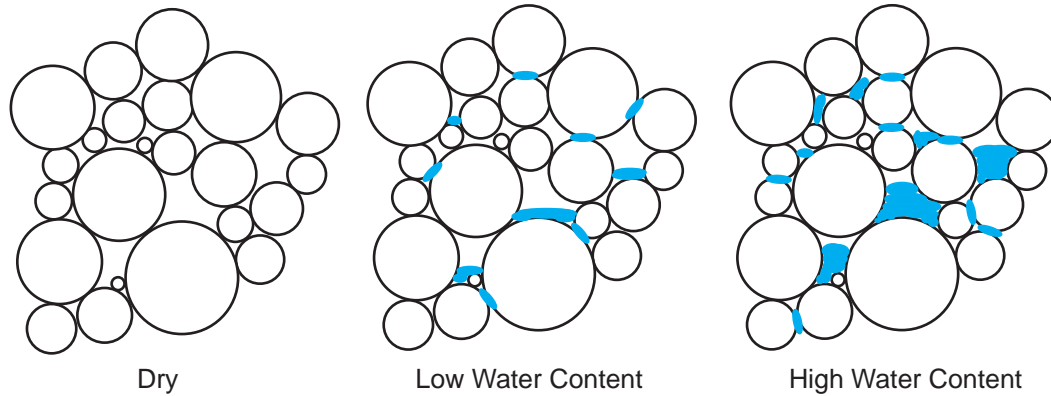


Figure 10.18: Schematic diagrams showing the effect on the grain structure of adding water. For a low water content, the water acts to lubricate grain motion without preventing displacement of the gas in the pores. At a higher water content the pores begin to fill significantly with water, reducing the compactability of the sample.

incompactable after only a small initial compaction. With a moderate amount of added water (less than saturation), there would be significant water content within the pores as well as at the inter-particle contact points. This increased water content acts both to restrict the displacement of the air within the voids during the early stages of compaction, and also to bear some load during the later stages of compaction. Both of these processes restrict the ability of the material to densify and therefore reduce the compactability of the samples relative to the dry state.

This stiffening of the material as the water begins to bear a significant load may explain the traces for the silt and CCS mixtures with 10% added water, shown in blue in Figures 10.14 and 10.15. The CCS material in particular shows a dramatic change in gradient after a small initial compaction, after which the material becomes significantly less compactable. This behaviour can be understood by noting that during dynamic loading the sample is not uniformly loaded. Instead, as illustrated in Figure 10.19, a compaction front is generated in the sample, leading to a compaction zone separating the compacted material from the

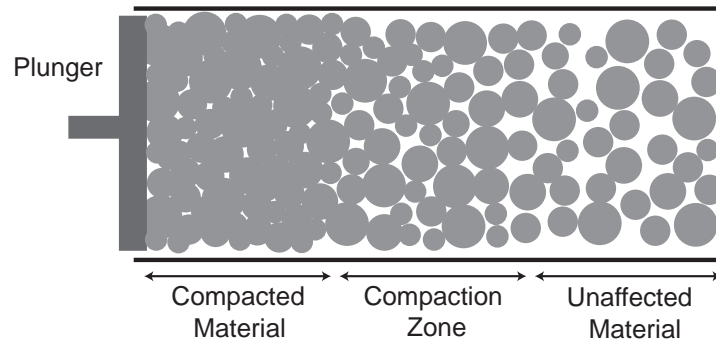


Figure 10.19: A diagram illustrating the non-uniform loading of a granular sample during dynamic compaction. The un-compacted bed and compacted material are separated by a traveling compaction zone. Based on Fig. 1. in [8].

un-compacted granular bed [8]. For a partly saturated granular sample, water displaced from pores in the compaction zone will build up in the unaffected region, causing the material to rapidly become less compactable as the compaction continues.

An alternative explanation for the behaviour of the silt with 10% added water is that the silt grains absorb water, causing them to swell. As the grains swell, the porosity in the sample will be reduced relative to the dry material. This would make the wet material less compactable than the dry material (Figure 10.10 shows that the compactability of the dry materials increases with the porosity). However, this explanation does not account for the increased compactability of the silt with 5% added water. In reality, the variation in the behaviour of the silt between the three moisture levels is probably best described by a combination of the two effects.

The amount of water required to transit between the lubrication regime and stiffening regime will likely depend on factors such as the pore size (and therefore by extension the grain size), the shape of the grains and the friction between grains. Figure 10.11 demonstrates that the sand material with 10% added water is actually more compactable than the dry material, but less so than with 5% added water. This agrees with similar data obtained by testing sand samples with various different moisture contents using a Hopkinson pressure bar [3]. This

10. COMPACTION OF SOILS

is a very different result to the silt material, for which the silt with 10% added water was much less compactable than the dry material.

This difference in behaviour may stem from the difference in size of the silt and sand particles. The sand particles are over four times larger on average than the silt particles (274 μm compared to 60 μm). The sand sample is therefore likely to contain larger pores than the silt material. To reduce the porosity in the sand sample, in which the grains are larger, fracturing of the grains is likely to be as important a process as rearrangement of the particles. If fracturing of the grains is an important process, it matters less if the voids are partially full with water.

The silt material consists of much smaller grains, and consequently smaller voids. The initial starting density is considerably less than the sand, and the initial porosity is higher (see Table 10.4). Rearrangement of the grains to reduce the number of voids and the porosity is therefore likely to be the most important process in the compaction. In this case, it is more important whether the pores contain significant amounts of water, as this would act to prevent the displacement of the air in the voids and would act to increase the resistance of the material to compaction.

Some of these trends can be seen in more detail in Figures 10.16 and 10.17. With 5% added water the silt, and the mixtures containing large amounts of silt, are the most compactable, while the mixtures consisting mainly of sand are less compactable. With 10% added water the same trend exists for the sand, CSS and CS materials, but the silt and CCS mixtures have an abnormally low compactability. This lack of compactability is likely due to a combination of swelling of the silt grains in the presence of water, and the partial filling of the small pores.

10.7 Conclusions

- When dry, samples containing a large proportion of silt are more compactable than samples containing large amounts of sand.

- Silt samples are more compactable as they are very porous (51% air by volume) and have small particles which are able to move relatively freely.
- Sand samples are not as compactable as they are less porous (42% air by volume) and contain larger grains which move less freely. This means that fracturing of the grains, which requires a relatively high stress, is likely to be a more important process during the compaction.
- Adding a small quantity of water (5% by mass) to any of the samples makes them more compactable. The most likely explanation is that the water acts to lubricate the system, reducing the friction at particle contacts and therefore increasing the particle mobility.
- Generally, adding a larger amount of water (10% by mass) makes the materials less compactable than the dry material, with the exception of pure sand. When larger amounts of water are added, the voids become partly full. This water acts to restrict the displacement of the air within the voids during the early stages of compaction, and also bears some load during the later stages of compaction, therefore resisting the compaction to a greater extent.
- Silt, and a mixture of silt and sand in the ratio 2:1, with 10% added water has an anomalously low compactability relative to the dry material. This is likely to be a combination of the water significantly filling the voids and bearing some of the load, and the silt particles absorbing some of the water and swelling, causing the porosity to be reduced relative to the dry material. A lower porosity would most likely reduce the compactability, as observed from Table 10.4 for the dry samples.
- The sand material is the only mixture for which the samples with 10% added water are more compactable than the dry material. This agrees with other research carried out using Hopkinson bars [3]. In contrast to the silt material, it is likely that fracturing of the grains plays a significant role in the compaction properties alongside rearrangement of the particles. In that case it is less important if the pores are partly filled with water than

REFERENCES

with the silt material. Lubrication of the particle contact points still acts to increase the mobility of the particles, allowing them to more easily perform the limited possible rearrangement before fracturing of the grains becomes significant.

References

- [1] Chapman, D.J., Proud, W.G., Tsembelis, K. and Collins, A., *Hard Target Research: Final Progress Report*, Internal Report SP 1184, University of Cambridge (2007)
- [2] Proud, W.G., Chapman, D.J., Williamson, D.M., Tsembelis, K. and Addiss, J., “The dynamic compaction of sand and related porous systems”, *Shock Comp. of Cond. Matter.*, **955**, (2007), 1403–1408
- [3] Martin, B.E., Chen, W.N., Song, B. and Akers, S.A., “Moisture effects on the high strain-rate behaviour of sand”, *Mechanics of Materials*, **41(6)**, (2009), 786–798
- [4] Brown, J.L., Volger, T.J., Grady, D.E., Reinhart, W.D., Chhabildas, L.C. and Thornhill, T.F., “Dynamic compaction of sand”, *Shock Comp. of Cond. Matter.*, **955**, (2007), 1363–1366
- [5] Song, B., Chen, W.N. and Luk, V., “Impact compressive response of dry sand”, *Mechanics of Materials*, **41(6)**, (2009), 777–785
- [6] Chapman, D.J., *Shock Compression of Distended Materials*, Phd, University of Cambridge (2009)
- [7] Deer, W.A., Howie, R.A. and Zussman, J., *Rock-forming minerals, Volume 4*, Wiley, US (1962)
- [8] Cochran, M.T. and Powers, J.M., “Computation of compaction in compressible granular material”, *Mechanics Research Comm.*, **35(1-2)**, (2007), 96–103

Chapter 11

Conclusions

The research reported in this thesis considers the internal response of granular media during compaction and penetration. The challenge was to produce high-resolution displacement data on the internal flow of material within a large opaque sample using the technique of Digital Speckle Radiography (DSR). The research addressed three main areas:

1. Optimisation of the technique of DSR for application to large, non-ideal samples, so that significant improvements are achieved in the accuracy of the displacement fields. It was found that when existing DIC algorithms are used to analyse X-ray images of large samples, the errors in the measured displacements and the regions of false correlation are unacceptably large. These problems were attributed to the variations in contrast present in experimental X-ray images, arising from the Gaussian profile of the X-ray beam, the sample geometry and the presence of metal projectiles or regions of densified material. Improved normalisation techniques were investigated to determine their effects on the correlation coefficients and the accuracy of the subsequent displacements.

Suitable normalisation of the contrast in the X-ray images was found to give a much more successful correlation. An optimised DIC algorithm was produced, which was shown to more accurately measure the displacement fields within large samples of granular material undergoing penetration or compaction. This new algorithm allows larger samples to be studied than could

11. CONCLUSIONS

previously be investigated. It was shown that these techniques are applicable to both spatial and Fourier domain DIC algorithms when applied to non-ideal speckle patterns, or in situations where there are large variations in illumination.

2. An experimental investigation of the internal flow of material within a large sample of sand during penetration using DSR and the optimised DIC algorithm. An improved experimental setup for DSR experiments was designed and produced, including a new catch-chamber and alignment rig, which allowed for more accurate alignment of the sample. The data enabled quantitative study of the way in which the disturbance was transmitted through the sample.

Factors such as the effect of penetration velocity (1.5 mm/min to 200 ms⁻¹) and the projectile nose shape (flat-ended, hemispherical and ogive-2) were considered. The dominant material response at low rates (1.5 mm/min) was found to be splitting of the material ahead of the projectile tip, followed by bulk reverse-flow of material towards the penetration face. At the higher rates (200 ms⁻¹) the dominant response was compaction of the material ahead of the projectile tip. The dynamic experimental results agreed qualitatively with the simulations by Bobaru. In particular, the observed compaction front was reproduced.

3. An investigation of the effect of particle size, density, force chain formation and water content on the mechanical behaviour of granular systems and particulate composites during compaction. It was shown that the formation of force chains spanning a porous particulate composite can significantly increase the material strength, relative to dense composites in which force chains are not activated. These force chains can increase the strength of a porous composite such that the material is stronger than a similar more dense composite, even with the weakening effect of the concentration of stress around the pores.

For a granular material, a small concentration of added water (5% water by mass) was found to increase the compactability, which was attributed

to the water lubricating the grain contact points, reducing the friction and shear stresses and increasing the particle mobility. Larger concentrations of added water (10% water by mass) were found to reduce the compactability of the material. This was attributed to the water partially filling the voids and restricting the displacement of the air during the early stages of the compaction and bearing some of the load during the later stages.

11.1 Future Work

Considering the penetration of granular samples by a projectile, there are still a number of factors which could usefully be investigated to build upon the research presented in this thesis, including the width of the projectile, the projectile momentum and the effect of the moisture content of the granular material. There is also scope for more detailed investigation of the effect of nose shape on the penetration process. At low rates of penetration, the dominant mode of deformation was splitting of the material ahead of the projectile tip, followed by reverse-flow of material towards the penetration face. It is possible that penetrators designed to aid this reverse-flow, for example those that narrow above the projectile face, might penetrate more effectively at these lower rates.

The research reported here has provided a large amount of experimental data on the behaviour of a granular material during penetration and compaction. Researchers producing simulations of granular materials could test or optimise their simulations by trying to recreate the experimental data. Further experiments on simple systems, such as a small number of spheres of a well characterised material, would help this process. Further experiments could also be performed on individual grains of the sand used in the penetration experiments discussed here, to better characterise the material properties and to investigate whether fracturing of the grains is likely to be occurring during the penetration.

11. CONCLUSIONS

Appendix A

A.1 Published Papers

Parts of the research discussed in this thesis have also been reported in the following papers:

1. Herbold, E.B., Nesterenko, V.F., Benson, D.J., Cai, J., Vecchio, K.S., Jiang, F., Addiss, J.W., Walley, S.M. and Proud, W.G. Particle size effect on strength, failure, and shock behavior in polytetrafluoroethylene-Al-W granular composite materials, *Journal of Applied Physics*, **104(10)**, (2008), 103903.
2. Cai, J., Nesterenko, V.F., Vecchio, K.S., Jiang, F., Herbold, E.B., Benson, D.J., Addiss, J.W., Walley, S.M. and Proud, W.G. The influence of metallic particle size on the mechanical properties of polytetrafluoroethylene-Al-W powder composites, *Applied Physics Letters*, **92(3)**, (2008), 031903.
3. Addiss, J.W., Collins, A. L. and Proud, W.G., Measurement of the internal flow fields in granular materials using digital speckle radiography, submitted to: *Journal of Strain Analysis*, (2009).
4. Addiss, J.W., Collins, A., Bobaru, F., Promratana, K. and Proud, W.G., Dynamic behaviour of granular materials at impact, *Proc. of DYMAT 2009*, **1**, (2009), 59-65.
5. Addiss, J.W., Cai, J., Walley, S.M., Proud, W. G. and Nesterenko, V. F. High strain and strain-rate behaviour of PTFE/aluminium/tungsten mixtures, *Proc. Shock Compression of Condensed Matter*, **955**, (2007), 773-776.

A.

6. Addiss, J.W., Collins, A.L. and Proud, W.G., Optimisation and use of a digital speckle radiography algorithm for investigation of long rod penetration of granular media, *Proc. Shock Compression of Condensed Matter*, (2009) accepted for publication.
7. Addiss, J.W., Collins, A.L. and Proud, W.G., Investigation of the rate dependence of long-rod penetration of granular media using an improved DSR algorithm, *Proc. Shock Compression of Condensed Matter*, (2009) accepted for publication.

Some of the results were presented in the following poster:

- Addiss, J.W., Collins, A.L. and Proud, W.G., Optimisation and use of a digital speckle radiography algorithm for investigation of long rod penetration of granular media, Presented at the American Physical Society Shock Compression of Condensed Matter Conference in Nashville, Tennessee, June 2009.

A.2 Lists of Experiments

The following tables include lists of the experiments reported in selected chapters. The lists generally show most of the experiments performed in that chapter, but they are not comprehensive.

Shot name	Projectile mass/ g	Projectile length/ mm	Projectile speed/ ms^{-1}	Delay/ μs	Comments
hs1107a	57.21 ± 0.08	100.1 ± 0.1	230 ± 4	2000	X-rays triggered late Phantom
hs1107b	57.15	100.0	185	2000	projectile gone through
fs1607a	56.52	100.2	203	150	Successful experiment Phantom Samples now dried
fs1707a	56.98	100.2	202	150	X-ray trigger failed X-ray head now raised
fs1807a	57.07	100.0	203	250	20keV X-rays - V. poor contrast Phantom
fs2107a	55.72	100.0	198	250	X-ray trigger failed
fs2107b	57.37	101.5	199	250	Successful experiment 29keV X-rays - better contrast
fs2207a	57.30	100.9	201	350	Successful experiment
fs2207b	57.10	101.0	unknown	500-700	X-ray trigger failed unknown real delay
fs2207c	57.32	100.1	199	450	Successful experiment Using better make triggers

Table A.1: A list of the gas-gun penetration experiments carried out using ogive (o), flat (f) and hemispherical (h) projectiles and discussed in Chapters 4 and 5. In some experiments high-speed video (Phantom) was taken.

Shot name	Projectile mass/ g	Projectile length/ mm	Projectile speed/ ms ⁻¹	Delay/ μ s	Comments
fs2807a	57.32	100.0 \pm 1	200 \pm 4	550	Experiment worked X-ray did not develop
fs2807b	57.33	101.0	unknown	550	X-ray triggered early due to dirty barrel? Phantom
fs2907a	54.98	100.0	195	550	Successful experiment Phantom looking at front
fs2907b	57.14	101.8	203	750	Successful experiment
fs3007a	55.09	101.8	204	1500	Successful experiment Projectile leaving sample
os0808a	53.33	100.1	202	350	Successful experiment Phantom
os2609a	53.44	100.0	202	550	Successful experiment
os2609a	53.44	100.0	202	550	Successful experiment
os1711a	54.06	100.2	unknown	150	velocity measurement failed X-rays okay
os1711b	53.95	100.1	201	150	Successful experiment Phantom on back face

Table A.2: A list of the gas-gun penetration experiments carried out using ogive (o), flat (f) and hemispherical (h) projectiles and discussed in Chapters 4 and 5. In some experiments high-speed video (Phantom) was taken.

A.

Shot name	Projectile mass/ g	Projectile length/ mm	Projectile speed/ ms^{-1}	Delay/ μs	Comments
os2011a	56.03	99.8	203	250	Experiment successful X-ray developing problems
os2011b	54.89	100.0	204	250	Successful experiment
os2411a	53.32	100.1	202	450	Successful experiment
os2811a	55.03	100.1	180	550	Velocity too low dirt in barrel?
os2811b	54.96	100.0	201	550	Successful experiment
os1112a	55.04	99.9	201	60	Successful experiment Phantom on front
hs1112b	56.15	100.0	202	250	Successful experiment Phantom on front for velocity
hs1512a	54.83	100.1	201	550	Successful experiment Phantom on front for velocity
hs1712a	56.19	100.2	unknown	450	No velocity measurement
hs1812a	55.47	99.8	199	450	Successful experiment Phantom on front for velocity

Table A.3: A list of the gas-gun penetration experiments carried out using ogive (o), flat (f) and hemispherical (h) projectiles and discussed in Chapters 4 and 5. In some experiments high-speed video (Phantom) was taken.

A.

Nose	Rate/ mm/min	Depth of Penetration/ mm
Flat	1.500 ± 0.001	$16 \pm 2, 38 \pm 2$
Flat	1.5	43, 63
Flat	1.5	82, 93
Ogive	1.5	17, 38
Ogive	1.5	42, 67
Ogive	1.5	82, 92
Ogive	15.00 ± 0.01	15, 39
Ogive	15	43, 65
Ogive	400.0 ± 0.1	16, 38
Ogive	400	42, 66

Table A.4: A list of the DSR penetration experiments carried out using the Instron machine and discussed in Chapter 7.

Nose-shape	Rate/ ms^{-1}	Depth of penetration/ mm
Ogive	5.0 ± 0.2	13 ± 2
Ogive	5	22
Ogive	5	31
Ogive	5	43
Ogive	5	56
Ogive	5	84

Table A.5: A list of the DSR penetration experiments carried out using the drop-weight machine and discussed in Chapter 8.

A.2 Lists of Experiments

Sample	Type	O-ring	h/ mm	d/ mm	m/ g	ρ/ kgm^{-3}	Details
55	D, C	None	8.15 ± 0.02	10.50 ± 0.02	4.9638 ± 0.0001	7.03 ± 0.02	Scope Sensitivity too low
57	D, C	None	8.21	10.49	4.9327	7.01	V. Large oscillations
-	PTFE	None	8.16	10.23	-	-	Significant oscillations
-	PTFE	-310	8.10	10.20	-	-	Fewer oscillations
-	PTFE	-310	8.11	10.19	-	-	Fewer oscillations
-	PTFE	-201	8.11	10.21	-	-	Better than -310 o-ring
-	PTFE	-201	8.11	10.21	-	-	Better than -310 o-ring
71	D, C	-201	8.27	10.49	5.1163	7.16	Good signal, UCS=28MPa
59	P, F	-201	8.16	10.53	4.2019	5.91	UCS=49MPa
72	P, C	-201	8.13	10.52	4.1705	5.90	UCS=35MPa, precursor
60	P, F	-201	8.14	10.53	4.1877	5.91	UCS=55MPa
63	P, F	-201	8.12	10.53	4.1275	5.67	UCS=53MPa
61	P, F	-201	8.22	10.53	4.2686	5.96	Scope sensitivity wrong
62	P, F	-201	8.25	10.52	4.2276	5.91	UCS=53MPa
76	P, C	-201	8.26	10.51	4.1412	5.80	UCS=12MPa
75	D, C	-201	8.24	10.50	5.1099	7.16	UCS=32MPa, plateau
79	D, C	-201	8.20	10.50	5.0678	7.14	UCS=31MPa, plateau
80	D, C	None	8.10	10.50	5.0881	7.25	V. Large oscillations

Table A.6: A table of experiments carried out in Chapter 9. P= porous, D= dense, F= fine W particles ($< 1\mu m$), C= coarse W particles ($44\mu m$), -201 = Nitrile BS201NI70 o-ring, UCS = Ultimate Compressive Strength.

Sample	Type	O-ring	h/ mm	d/ mm	m/ g	ρ/ kgm^{-3}	Details
80	D, C	None	8.10 ± 0.02	10.50 ± 0.02	5.0881 ± 0.0001	7.25 ± 0.02	V. Large oscillations
81	D, C	-201	8.22	10.50	5.0306	7.07	UCS=25MPa, plateau
82	D, C	-201	8.21	10.48	5.1198	7.23	Strain gauge failed
83	D, C	-201	8.13	10.50	5.0549	7.18	UCS=26MPa, plateau
84	D, C	-201	8.23	10.50	5.0670	7.11	UCS=29MPa, oscillation
85	D, C	-201	8.16	10.51	4.9876	7.06	UCS=28MPa
78	P, C	-201	8.21	10.53	4.1315	5.79	3 oscillations
92	P, C	-201	8.22	10.52	4.2049	5.89	3 oscillations
93	P, C	-201	7.93	10.48	4.1125	6.01	UCS=33MPa, precursor
94	P, C	-201	7.93	10.51	4.1704	6.06	oscillations present
-	O-ring	-201	-	-	-	-	112 cm height drop
-	O-ring	-201	-	-	-	-	112 cm height drop
-	O-ring	-201	-	-	-	-	112 cm height drop
-	O-ring	-201	-	-	-	-	112 cm height drop
-	O-ring	-201	-	-	-	-	60 cm height drop
-	O-ring	-201	-	-	-	-	60 cm height drop
-	O-ring	-201	-	-	-	-	45.5 cm height drop
-	O-ring	-201	-	-	-	-	45.5 cm height drop

Table A.7: A table of experiments carried out in Chapter 9. P= porous, D= dense, F= fine W particles ($< 1\mu\text{m}$), C= coarse W particles ($44\mu\text{m}$), -201 = Nitrile BSS201NIT70 o-ring, UCS = Ultimate Compressive Strength.

A.

A.2 Lists of Experiments

Sample	Type	O-ring	h/ mm	d/ mm	m/ g	ρ/ kgm^{-3}	Details
-	O-ring	-201	-	-	-	-	15.5 cm height drop
-	O-ring	-201	-	-	-	-	15.5 cm height drop
-	O-ring	-201	-	-	-	-	3.8 cm height drop
-	O-ring	-201	-	-	-	-	3.8 cm height drop
-	PTFE	-201	8.13	10.20	-	-	Interrupted exp.
-	PTFE	-201	8.08	10.22	-	-	Interrupted exp.
63	P, F	-201	8.17 ± 0.02	10.52 ± 0.02	4.2420 ± 0.0001	5.97 ± 0.02	Interrupted exp.
63	P, F	-201	8.17	10.52	4.2420	5.97	Interrupted exp.
64	P, F	-201	7.94	10.53	4.1353	5.98	Interrupted exp.
98	P, C	-201	8.01	10.48	4.1504	6.01	Interrupted exp.
88	D, C	-201	8.08	10.50	4.9490	7.06	Interrupted exp.
65	P, F	-201	8.32	10.53	4.2786	5.91	UCS=59MPa
96	P, C	-201	8.05	10.51	4.2343	6.06	UCS=16MPa, plateau
97	P, C	-201	8.01	10.47	4.2312	6.14	UCS=17MPa
99	P, C	-201	8.02	10.43	4.2234	6.11	UCS=17MPa
87	P, C	-201	8.14	10.53	3.9833	5.62	Interrupted
102	P, F	-201	8.12	10.51	4.1395	5.89	UCS=63MPa
103	P, C	-201	8.09	10.51	4.2213	6.01	UCS=30MPa, precursor

Table A.8: A table of experiments carried out in Chapter 9. P= porous, D= dense, F= fine W particles ($< 1\mu m$), C= coarse W particles ($44\mu m$), -201 = Nitrile BS201NI70 o-ring, UCS = Ultimate Compressive Strength.